29th edition

ISSN 1454 - 8003

Proceedings of International Conference on HYDRAULICS, PNEUMATICS, SEALING ELEMENTS, TOOLS, PRECISION MECHANICS, SPECIFIC ELECTRONIC EQUIPMENT & MECHATRONICS

HERVEX 2025

November 19-21 | Băile Govora, ROMANIA

November 2025
29th Edition

INTERNATIONAL CONFERENCE

HERVEX 2025

Hydraulics| Pneumatics| Sealing Elements| Tools| Precision Mechanics| Specific Electronic Equipment & Mechatronics

Baile Govora, ROMANIA | November 19 - 21, 2025

HERVEX 2025

ORGANIZERS

HYDRAULICS AND PNEUMATICS RESEARCH INSTITUTE
BUCHAREST, ROMANIA

CHAMBER OF COMMERCE AND INDUSTRY VALCEA, ROMANIA

ORGANIZING PARTNERS

WROCLAW UNIVERSITY OF SCIENCE AND TECHNOLOGY, POLAND

KOMAG INSTITUTE OF MINING TECHNOLOGY, POLAND

TECHNICAL UNIVERSITY OF MOLDOVA IN CHISINAU, REPUBLIC
OF MOLDOVA

NATIONAL INSTITUTE OF RESEARCH & DEVELOPMENT FOR MACHINES
AND INSTALLATIONS DESIGNED TO AGRICULTURE AND FOOD INDUSTRY
– INMA BUCHAREST, ROMANIA

"POLITEHNICA" BUCHAREST NATIONAL UNIVERSITY
OF SCIENCE AND TECHNOLOGY

"POLITEHNICA" UNIVERSITY OF TIMISOARA, ROMANIA

TECHNICAL UNIVERSITY OF CLUJ-NAPOCA, ROMANIA

"DUNAREA DE JOS" UNIVERSITY OF GALATI, ROMANIA

MEDIA PARTNERS

INTERNATIONAL CONFERENCE

HERVEX 2025

HELD UNDER HONORARY AEGIS OF

Comité Européen des Transmissions Oléohydrauliques et Pneumatiques

cetop
The Voice of the European Fluid Power Industry

SUPPORTED BY

National Professional Association of Hydraulics and Pneumatics in Romania - "FLUIDAS"

Conference Proceedings is **indexed by**

EBSCO PUBLISHING Google scholar TIB LEIBNIZ INFORMATION CENTRE FOR SCIENCE AND TECHNOLOGY UNIVERSITY LIBRARY

Published by Hydraulics and Pneumatics Research Institute, Bucharest, Romania

COMMITTEES

ORGANIZING COMMITTEE

Dipl. Eng. Gheorghe RIZOIU – General Manager of Chamber of Commerce and Industry Valcea, Romania

PhD. Eng. Gabriela MATACHE – Hydraulics and Pneumatics Research Institute in Bucharest, Romania

Prof. PhD. Eng. Krzysztof KĘDZIA – Wroclaw University of Technology, Poland

Prof. PhD. Eng. Dan OPRUȚA – Technical University of Cluj-Napoca, Romania

PhD.Eng. Petrin DRUMEA – President of National Professional Association of Hydraulics and Pneumatics – FLUIDAS, Romania

Prof. PhD. Eng. Ilare BORDEAȘU – Politehnica University of Timisoara, Romania

Dipl.Eng. Valentin CISMARU – President of Chamber of Commerce and Industry Valcea, Romania

PhD.Eng. Nicolae-Valentin VLĂDUȚ – General Manager of National Institute of Research and Development for Machines and Installations Designed to Agriculture and Food Industry – INMA Bucharest, Romania

Prof. PhD. Eng. Adrian CIOCĂNEA – National University of Science and Technology POLITEHNICA Bucharest, Romania

PhD.Eng. Sergiu NICOLAIE – General Manager of R&D National Institute for Electrical Engineering ICPE-Advanced Researches, Bucharest, Romania

PhD.Eng. Ioan LEPĂDATU – Hydraulics and Pneumatics Research Institute in Bucharest, Romania

PhD.Eng. Cătălin DUMITRESCU – Director of Hydraulics and Pneumatics Research Institute in Bucharest, Romania

SCIENTIFIC PROGRAMME COMMITTEE

Prof. PhD.Eng. Zygmunt DOMAGALA – Wroclaw University of Technology, Poland

Prof. PhD.Eng. Valeriu DULGHERU – Technical University of Moldova, Republic of Moldova

PhD.Eng. Cătălin DUMITRESCU – Director of Hydraulics and Pneumatics Research Institute in Bucharest, Romania

Prof. D.Sc. Eng. Dariusz PROSTAŃSKI – KOMAG Institute of Mining Technology, Gliwice, Poland

Ph.D. Eng. Bartosz POLNIK – KOMAG Institute of Mining Technology, Gliwice, Poland

Prof. PhD. Eng. Paweł ŚLIWIŃSKI – Gdańsk University of Technology, Gdansk, Poland

Prof. PhD. Eng. Ryszard JASINSKI – Gdańsk University of Technology, Gdansk, Poland

Prof. PhD.Eng. Mihai AVRAM – National University of Science and Technology POLITEHNICA Bucharest, Romania

Prof. PhD. Eng. Katharina SCHMITZ – Director of Institute for Fluid Power Drives and Systems (ifas) - RWTH Aachen University, Germany

Assoc. Prof. PhD. Eng. Tatiana MINAV – Tampere University, Finland

Assoc. Prof. PhD.Eng. Nicuşor BAROIU – "Dunarea de Jos" University of Galati, Romania

PhD.Eng. Marin ŞENILĂ – Director of Research Institute for Analytical Instrumentation INCDO INOE 2000 - ICIA Cluj-Napoca, Romania

Prof. PhD. Eng. Marius PARASCHIVOIU – Concordia University, Montréal , Quebec, Canada

Prof. PhD. Eng. Călin VAIDA – Technical University of Cluj-Napoca, Romania

Lect. PhD. Eng. Dorin BORDEAŞU – Politehnica University of Timisoara, Romania

PhD. Eng. Daniela-Doina CIOBOATĂ – Scientific Manager of National Institute of Research and Development in Mechatronics and Measurement Technique (INCDMTM), Bucharest, Romania

Conf. PhD.Eng. Bogdan GRĂMESCU – National University of Science and Technology POLITEHNICA Bucharest, Romania

PhD. Eng. Cătălin VIŢELARU – National Institute of Research and Development for Optoelectronics - INOE 2000, Romania

PhD. Eng. Alina DRAGOMIR – National Institute of Research and Development for Optoelectronics - INOE 2000, Romania

Conf. PhD.Eng. Oana TONCIU – Technical University of Civil Engineering in Bucharest, Romania

Conf. PhD.Eng. Cătălin FRÂNCU – Technical University of Civil Engineering in Bucharest, Romania

Conf. PhD.Eng. Mihail SAVANIU – Technical University of Civil Engineering in Bucharest, Romania

PhD.Eng. Cornelia MURARU-IONEL – National Institute of Research and Development for Machines and Installations Designed to Agriculture and Food Industry – INMA Bucharest, Romania

Assoc. Prof. PhD.Eng. Andrei DRUMEA – National University of Science and Technology POLITEHNICA Bucharest, Romania

Prof. PhD.Eng. Sorin CĂNĂNĂU – National University of Science and Technology POLITEHNICA Bucharest, Romania

Prof. PhD.Eng. Ion DAVID – Technical University of Civil Engineering in Bucharest, Romania

Prof. PhD.Eng. Edmond MAICAN – National University of Science and Technology POLITEHNICA Bucharest, Romania

PhD.Eng. Mihai Gabriel MATACHE – National Institute of Research – Development for Machines and Installations Designed to Agriculture and Food Industry – INMA, Bucharest- Romania

PhD.Eng. Mircea PRICOP – S.C. HESPER S.A., Bucharest, Romania

Lect. PhD.Eng. Ioan Lucian MARCU – Technical University of Cluj-Napoca, Romania

Lect. PhD.Eng. Daniel-Vasile BANYAI – Technical University of Cluj-Napoca, Romania

Lect. PhD.Eng. Iulian-Claudiu DUŢU – National University of Science and Technology POLITEHNICA Bucharest, Romania

Dipl. Eng. Nicolae TASU – HANSA FLEX Romania

EXECUTIVE SECRETARIAT

MSc. Stud. Ana-Maria POPESCU – Hydraulics and Pneumatics Research Institute in Bucharest, Romania

PhD.Eng. Liliana DUMITRESCU – Hydraulics and Pneumatics Research Institute in Bucharest, Romania

Dipl. Eng. Ioana ILIE – Hydraulics and Pneumatics Research Institute in Bucharest, Romania

Dipl. Eng. Carmen NECULA – Hydraulics and Pneumatics Research Institute in Bucharest, Romania

PhD. Stud. Eng. Ștefan-Mihai ȘEFU – Hydraulics and Pneumatics Research Institute in Bucharest, Romania

SPECIALIZED REVIEWER COMMITTEE

PhD.Eng. Petrin DRUMEA – President of National Professional Association of Hydraulics and Pneumatics – FLUIDAS, Romania

Prof. PhD.Eng. Valeriu DULGHERU – Technical University of Moldova, Republic of Moldova

PhD. Eng. Teodor Costinel POPESCU – Hydraulics and Pneumatics Research Institute in Bucharest, Romania

PhD. Eng. Marian BLEJAN – Hydraulics and Pneumatics Research Institute in Bucharest, Romania

Prof. Dr.h.c. mult. Ph.D. Paul Mugur SVASTA – National University of Science and Technology POLITEHNICA Bucharest, Romania

PhD. Eng. Gheorghe ȘOVĂIALĂ – Hydraulics and Pneumatics Research Institute in Bucharest, Romania

PhD. Eng. Alexandru-Polifron CHIRIȚĂ – Hydraulics and Pneumatics Research Institute in Bucharest, Romania

PhD. Eng. Radu Iulian RĂDOI – Hydraulics and Pneumatics Research Institute in Bucharest, Romania

EDITORIAL STAFF

Editor-in-Chief

- PhD. Eng. Gabriela MATACHE - Hydraulics and Pneumatics Research Institute in Bucharest, Romania

Executive Editor

- MSc. Stud. Ana-Maria POPESCU - Hydraulics and Pneumatics Research Institute in Bucharest, Romania

CONTENTS

ISSN 1454 - 8003
Proceedings of 2025 International Conference on Hydraulics and Pneumatics - HERVEX
November 19-21, Băile Govora, Romania

ANALYSIS OF A LOW-PRESSURE HYDROSTATIC DRIVE SYSTEM

Nicușor BAROIU[1,2], Georgiana-Alexandra MOROȘANU[2,3], Andrea MIRON[4], Florin-Ioan MOROȘANU[1], Florin CHIRIȚĂ[5]

[1] Department of Manufacturing Engineering, ”Dunarea de Jos” University of Galati, Romania
Nicusor.Baroiu@ugal.ro; morosanuflorinioan@gmail.com

[2] Research Center in Manufacturing Engineering Technology (ITCM), ”Dunarea de Jos” University of Galati, Romania

[3] Center of Continuous Training and Technological Information, Danubius International University, Galati, Romania
georgianaalexandra.morosanu@univ-danubius.ro

[4] Department of Mechanical Engineering, ”Dunarea de Jos” University of Galati, Romania
mironandrea04@gmail.com

[5] Chif Technology SRL, Bucharest, Romania
florin.chirita@chif.ro

Abstract: *Hydrostatic drive systems are an important component of modern power transmission technology, using fluids to transform mechanical energy into hydraulic energy and then back into mechanical energy. These systems are valued for their ability to provide forces with high precision, for functional flexibility and for energy efficiency in various technological applications. In particular, low-pressure drive systems present significant economic and operational advantages, offering increased component durability, reduced energy losses and simplified maintenance. In this paper, a low-pressure hydrostatic drive system is analyzed, presenting the operating principles and essential elements of hydrostatic drives. The main components, such as the hydraulic pump, the directional control valve, are described, along with the energy conversion processes. A simulation is also performed using the Omegon Fluid software, which offers the possibility of configuring the main circuit parameters and analyzing the behavior of the hydrostatic system under controlled conditions. The program's graphical interface allows investigating interactions between components, evaluating response to electrical actuation, and examining system stability over pressure and flow variations.*

Keywords: *Hydrostatic system, Omegon Fluid, low-pressure, simulation*

1. Introduction

Hydrostatic drive systems are widely used in industrial, agricultural, construction or transportation applications. These systems are based on the conversion of mechanical energy into hydraulic energy and then back into mechanical energy, allowing precise control of movement, the provision of high forces and high adaptability to load variations. Unlike other types of drives, such as hydraulic drives used in industry for the circulation of fluids with high viscosity or mechanical drives, which require greater attention to the profiling of the surfaces of hydraulically driven constituent components and working at high pressures [1,2], low-pressure hydrostatic drive systems focus precisely on the optimal balance between performance, cost and reliability. They allow for reduced energy consumption, reduced internal losses, simplified construction and maintenance, while being, at the same time, safer from an operational point of view. Their applicability extends especially to agricultural equipment, low and medium power machinery, testing equipment, where working pressures (below 10 bar) are sufficient to perform functional loads [3,4].
Research in the field has highlighted an orientation towards volumetric optimization and intelligent control of hydraulic flow. Ma et al. [3] analyzed the behavior of an experimental hydrostatic system, demonstrating the importance of numerical simulation for the optimal configuration of pressure and flow parameters. In a complementary approach, Baroiu et al. [5] developed a constructive-functional

model of hydraulic filters, providing a practical basis for the analysis of pressure losses and filtration efficiency in low-pressure circuits.
The yield optimization and the reduction of energy losses in hydrostatic drives have been treated by complex dynamic models. Takosoglu et al. [4], showed that the use of variable displacement pumps can increase volumetric yield by over 15%. In parallel, the generation of progressive cavity pump screws has been studied by graphical and geometric methods, proposing constructive solutions that ensure uniform flow transmission and reduce pressure pulsations [2].
Another active area of research is that of hybrid drives and coordinated control systems, in which mechanical and hydraulic components are managed simultaneously to improve the stability and energy efficiency of the assembly. Kahandawa et al. [6] presented this concept in which hydraulic and mechanical systems act synchronously to increase the dynamic stability of vehicles. Similarly, in other research, double-acting hydraulic cylinders were analyzed, highlighting how the constructive parameters influence the dynamic behavior of the assembly in the reduced pressure regime [7].
Also, Wos et al. [8] demonstrated that forced flow regulation allows a faster reaction of the system to load variations. Similarly, Costin et al. [9] showed that pressure regulation through hydraulic control circuits ensures superior process uniformity and increased stability of operating parameters.
Developments in the field of hydrostatic system diagnostics have led to the integration of smart sensors and failure prediction algorithms. Also, some studies propose graphical models for studying the variation of operating parameters of hydraulic pumps, demonstrating the importance of correlating simulation data with experimental measurements [10,11,12].
A significant contribution towards improving performance belongs to the research on variable structures and adaptive control. Wang et al. [13] highlighted the influence of pressure on the dynamic behavior of the system and on its stability. In parallel, Berbinschi et al. [14] highlighted the importance of surface and profile modeling in the design process, a method that can be extended to the analysis of geometric elements in hydrostatic drives.
Also, Zhang et al. [15] proposed a modular drive architecture, optimized for large agricultural machinery, which uses gear pumps and proportional directional control valves for movement control.
A complementary approach is found in papers [16], [17] and [18], where reverse engineering techniques are used to generate helical hydraulic drive components. This research provides a basis for evaluating functional surfaces and optimizing manufacturing processes of hydraulic transmission elements. Modern development trends are increasingly oriented towards hybrid electro-hydraulic systems. Helduser et al. [19] presented the advantages of the combination of electrical and hydraulic sources, demonstrating the possibility of reducing global energy consumption by up to 25%.
A significant contribution to the understanding and dynamic modeling of hydrostatic drives is brought by paper [20], in which the authors provide an analysis of current trends in hydrostatic system architecture, adaptive control strategies and energy efficiency optimization. The study emphasizes the fact that modern systems tend to be treated as nonlinear, self-regulating entities, in which the interaction between flow, pressure and internal losses must be analyzed simultaneously for a correct prediction of dynamic behavior.
This theoretical approach correlates with the research of Rundo [21], who proposes advanced mathematical models for simulating flow and evaluating volumetric losses in gear pumps, thus providing a solid basis for the development of control algorithms and strategies for optimizing the overall yield of hydrostatic drive systems.
Overall, research is converging towards the development of modular, energy-efficient and intelligently controlled drives, in which low-pressure is no longer a limitation, but an advantage in optimizing system performance. Thus, the analysis of a low-pressure hydrostatic drive system, performed using software tools such as Omegon Fluid, becomes a necessary step in validating theoretical models and identifying correlations between operating parameters - pressure, flow and power - under the influence of variable loads.
The paper aims to investigate these aspects through an integrated approach, which combines the constructive-functional analysis of the main components with numerical simulation and the evaluation of the system's behavior in low-pressure regime.

2. Description of the low-pressure hydrostatic drive system

Figure 1 shows the low-pressure hydrostatic drive system, used as an experimental model to highlight the operating principles of hydraulic elements under reduced pressure conditions. The system is placed on a modular platform and has the role of reproducing, in a functional way, a linear drive circuit, being composed of real components, dimensioned according to the experimental requirements.

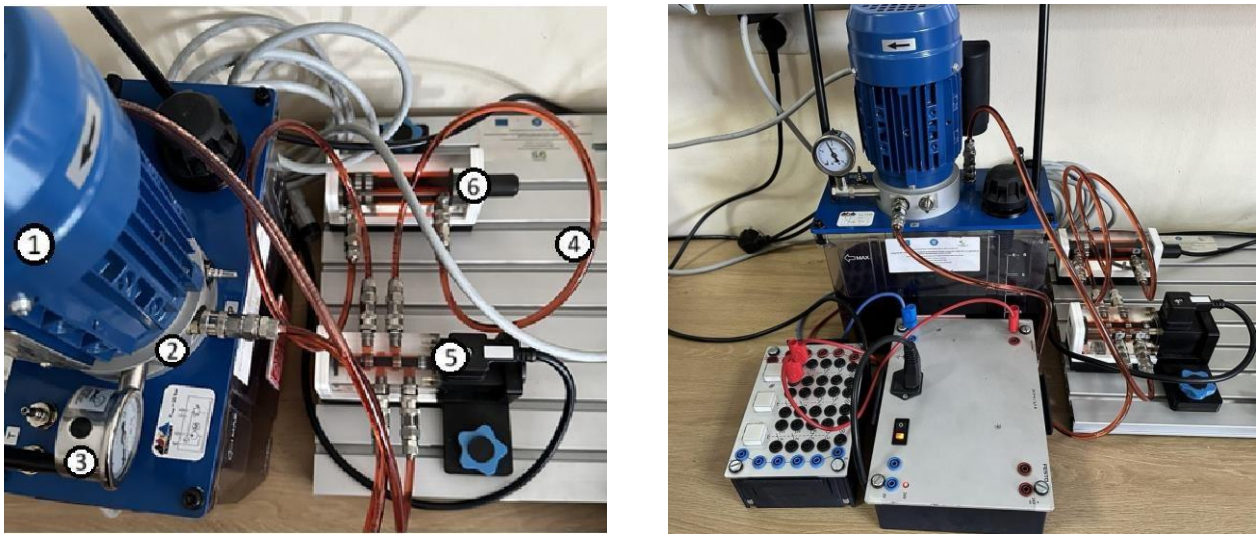

Fig. 1. Assembly of the low-pressure hydrostatic system: electric motor (1); hydraulic pump (2); pressure gauge (3); flexible hydraulic pipes (4); 4/2-type directional control valve (5); hydraulic cylinder (6)

Figure 1 shows the functionality of a simple circuit in which the following components are found:
- *the pumping gr*oup, consisting of an electric motor (1) and a hydraulic pump (2), which ensures the circulation of the fluid in the circuit at a reduced pressure; the pressure is monitored using a pressure gauge (3) mounted on the pump housing;
- *the flexible hydraulic pipes* (4), made of a transparent material, which allow visual observation of the fluid circulation and facilitate the connection between the elements;
- *the 4/2 type directional control valve* (5), which controls the movement direction of the fluid and, implicitly, the direction of the hydraulic cylinder operation;
- *the linear hydraulic motor (hydraulic cylinder)* (6), which has the role of transforming the hydraulic energy of the working fluid into linear mechanical energy, achieving the translational movement required by the drive system.

Figure 2 shows the symbolic diagram of the hydrostatic system operation, which provides a logical, standardized and easy-to-interpret representation of the working principle of the low-pressure hydrostatic drive system.

This diagram allows highlighting the connections between the components, illustrating how hydraulic energy is transmitted and controlled within the hydrostatic circuit. Through this representation, the fluid flow paths, the positions, as well as the functional states of the directional control valve and the operating mode of the linear hydraulic motor can be identified, in correlation with the pressure and flow variations.

The operation of the diagram is based on the supply of the circuit by a pump (1) driven by an electric motor (2). The generated flow is directed through a relief valve (3) and controlled by a 4/2-type directional control valve (4).

Depending on its position, the fluid is directed either to chamber A or to chamber B of the linear hydraulic motor (5). Thus, the piston moves in one direction or the other, achieving the necessary mechanical movement. When the directional control valve returns to its original position, the circuit is discharged and the piston movement stops.

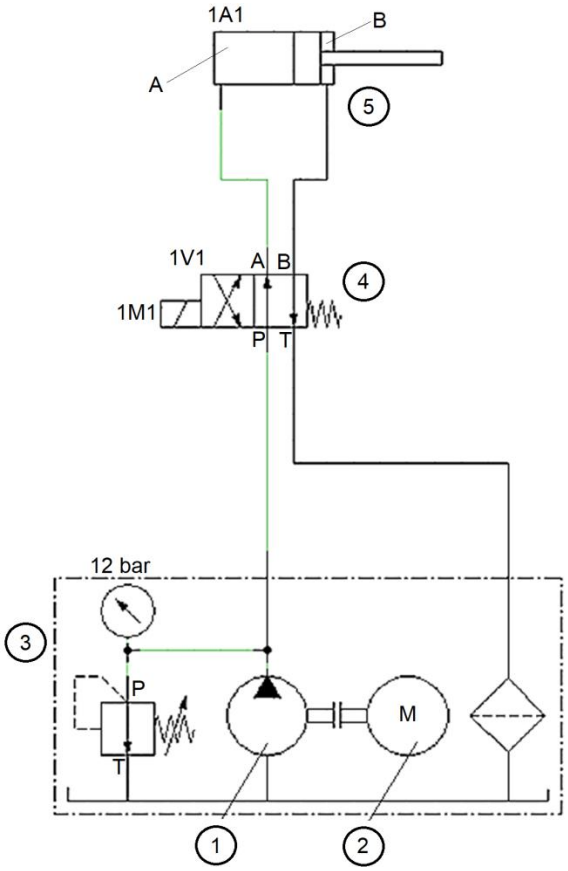

Fig. 2. Symbolic operating diagram of the hydrostatic system: hydraulic pump (1); electric motor (2); relief valve (3); 4/2-type directional control valve (4); linear hydraulic motor (5)

Unlike the physical assembly, which reflects the actual positioning of the equipment, the symbolic diagram eliminates the construction details and highlights only the functional relationships between the elements. This allows a quick analysis of the operating mode, possible losses, critical points in the system and provides support in the design, sizing and diagnosis of the circuit.
The hydraulic pump, Figure 3, is a compact equipment, consisting of a cylindrical metal body in which two gears (one driving and one driven), responsible for transporting the fluid, are mounted. In the figure, both the real shape of the pump and its technical representation with dimensions and fixing points are observed.

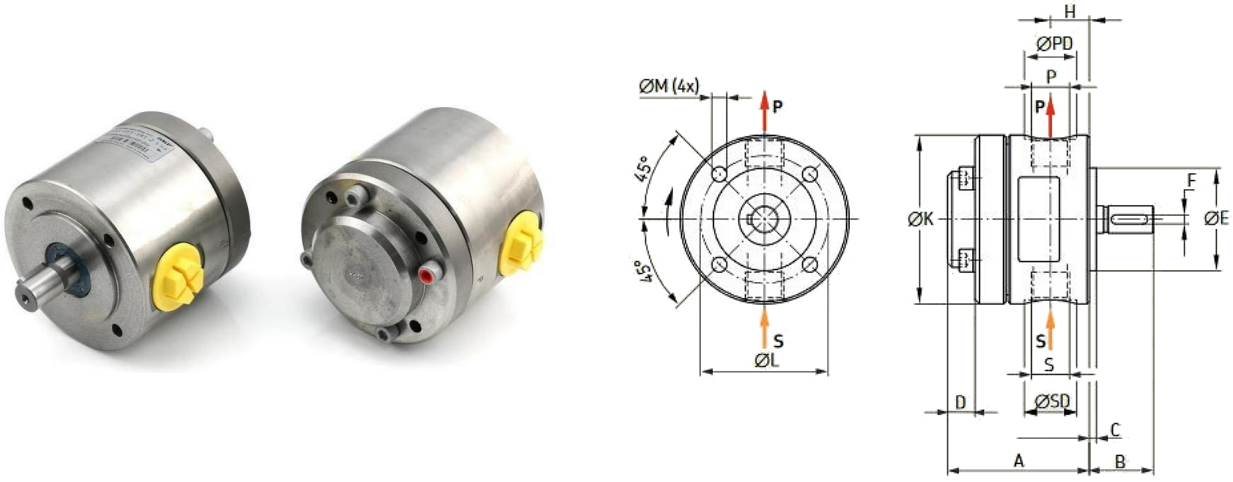

Fig. 3. Gear pump [22]

Through the suction and discharge ports, the liquid is taken in and pumped under pressure, and the drive shaft transmits the movement to the gears. The robust body of the pump indicates its use in industrial applications where reliability and pressure resistance are essential.
The figure highlights the main dimensions and mounting method. The front view shows the positioning of the discharge (P) and suction (S) ports at 45°, as well as the mounting holes. The side view shows the total length of the pump (A, B, C), the position of the drive shaft (ØE) and the essential housing diameters (ØK, ØSD, ØPD).
To characterize the low-pressure hydrostatic drive system, it is necessary to highlight the main technical parameters of the components that make it up. These parameters determine the overall performance of the system, influencing both energy efficiency and dynamic behavior under various operating conditions.
Table 1 summarizes the main technical parameters relevant for the system analysis and sizing process, their values constituting the starting point for the numerical simulations performed during the study.

Table 1: Gear pump technical parameters [22]

Crt. no.	Parameters	Symbol	Value	Unit
1.	Normal pressure	p	10	[bar]
2.	Volume flow	Q	0.48	[l/min]
3.	Nominal rotational speed	n_n	1500	[rot/min]
4.	Viscosity range	-	20-1000	[mm²/s]
5.	Characteristic curve	-	1	-
6.	Nominal volume	V_n	0.61	[cm³]
7.	Actuating power	P	0.20	[kW]

At the same time, measurements were taken to determine the dimensions of the functional components of the hydrostatic system. For the calculation of the operating parameters, standardized values will be adopted for the pressure, p = (2, 4, 6, 8, 10) bar and the rotational speed, n = (700, 900, 1100, 1300, 1400) rot./min. The flow rate, driving moment and power will be determined, taking into account the following characteristics of the gear pump: outer diameter, D_e = 22 mm; inner diameter, D_i = 17 mm; rolling diameter, D_r = 19.5 mm; tooth heigh, h = 2.5 mm; width of the gears, l = 4 mm.
The flow rate of a gear pump indicates the volume of fluid transported in a certain time interval and is an essential parameter for evaluating its performance. It is influenced by the geometric characteristics of the gears, the pump rotation speed and the internal losses in the system.
To determine the theoretical flow rate, the pump's construction dimensions, such as the rolling diameter, the tooth height and the width of the gears, will be used. The volumetric yield will also be taken into account to estimate the actual flow rate of the pump under actual operating conditions. Thus, the flow rate is calculated in the form [11]:

$$Q = V \cdot n \cdot 10^{-6} \left[\text{l/min}\right], \tag{1}$$

where:

$$V = \pi \cdot D_r \cdot h \cdot l \left[\text{mm}^3\right]. \tag{2}$$

$$V = \pi \cdot 19.5 \cdot 2.5 \cdot 4 = 612.3\ \text{mm}^3.$$

Next, the flow rate was calculated for each of the normalized rotational speed values represented in Table 2.

Table 2: Pump rotational speed and flow values

Crt. no.	n [rot/min]	Q [l/min]	
1	n_1 = 700	$Q_1 = V \cdot n_1 = 428610 \cdot 10^{-6}$	Q_1 = 0.43
2	n_2 = 900	$Q_2 = V \cdot n_2 = 551070 \cdot 10^{-6}$	Q_2 = 0.55
3	n_3 = 1100	$Q_3 = V \cdot n_3 = 673530 \cdot 10^{-6}$	Q_3 = 0.67
4	n_4 = 1300	$Q_4 = V \cdot n_4 = 795990 \cdot 10^{-6}$	Q_4 = 0.80
5	n_5 = 1400	$Q_5 = V \cdot n_5 = 857220 \cdot 10^{-6}$	Q_5 = 0.86

The driving moment of a gear pump is the torque force required to turn the gears and move the fluid through the system. It depends on the working pressure, the geometrical dimensions of the gears and the internal losses in the mechanism.
The moment is calculated using the relationship [11]:

$$M = \frac{p \cdot V}{2 \cdot \pi} \cdot 10^{-4} \left[\mathrm{N} \cdot \mathrm{m} \right]. \tag{3}$$

The calculation of the driving moment was performed for several pressure values, Table 3.

Table 3: Values of the moment and pump pressure

Crt. no.	p [bar]	M [N·m]	
1	p_1 = 2	$M_1 = \frac{p_1 \cdot V}{2 \cdot \pi} \cdot 10^{-4}$	M_1 = 0.19
2	p_2 = 4	$M_2 = \frac{p_2 \cdot V}{2 \cdot \pi} \cdot 10^{-4}$	M_2 = 0.38
3	p_3 = 6	$M_3 = \frac{p_3 \cdot V}{2 \cdot \pi} \cdot 10^{-4}$	M_3 = 0.57
4	p_4 = 8	$M_4 = \frac{p_4 \cdot V}{2 \cdot \pi} \cdot 10^{-4}$	M_4 = 0.76
5	p_5 = 10	$M_5 = \frac{p_5 \cdot V}{2 \cdot \pi} \cdot 10^{-4}$	M_5 = 0.96

The power of a gear pump represents the energy transmitted to the system to ensure the movement of fluid under pressure. The determination of the power is based on the relationship between the driving moment and rotational speed, respectively between the pump flow and the pressure difference.
The hydraulic power generated by the pump is given by the relation [11]:

$$P = \frac{p \cdot Q}{612 \cdot \eta} \left[kW \right], \tag{4}$$

where η represents the yield, between 0.5 ÷ 0.9.

To analyze the influence of the working pressure on the power developed by the gear pump, the calculation was performed for different distinct values, Table 4.

Table 4: Values of the power and pump pressure

Crt. no.	p [bar]	P [kW]	
1	p_1 = 2; η = 0.5	$P_1 = \frac{p_1 \cdot Q_1}{612 \cdot \eta} \cdot 1.66$	P_1 = 0.0011
2	p_2 = 4; η = 0.5	$P_2 = \frac{p_2 \cdot Q_2}{612 \cdot \eta} \cdot 1.66$	P_2 = 0.0029
3	p_3 = 6; η = 0.5	$P_3 = \frac{p_3 \cdot Q_3}{612 \cdot \eta} \cdot 1.66$	P_3 = 0.0054
4	p_4 = 8; η = 0.5	$P_4 = \frac{p_4 \cdot Q_4}{612 \cdot \eta} \cdot 1.66$	P_4 = 0.0086
5	p_5 = 10; η = 0.5	$P_5 = \frac{p_5 \cdot Q_5}{612 \cdot \eta} \cdot 1.66$	P_5 = 0.0116

The graphical representation of flow, moment and power is shown in Figure 4.

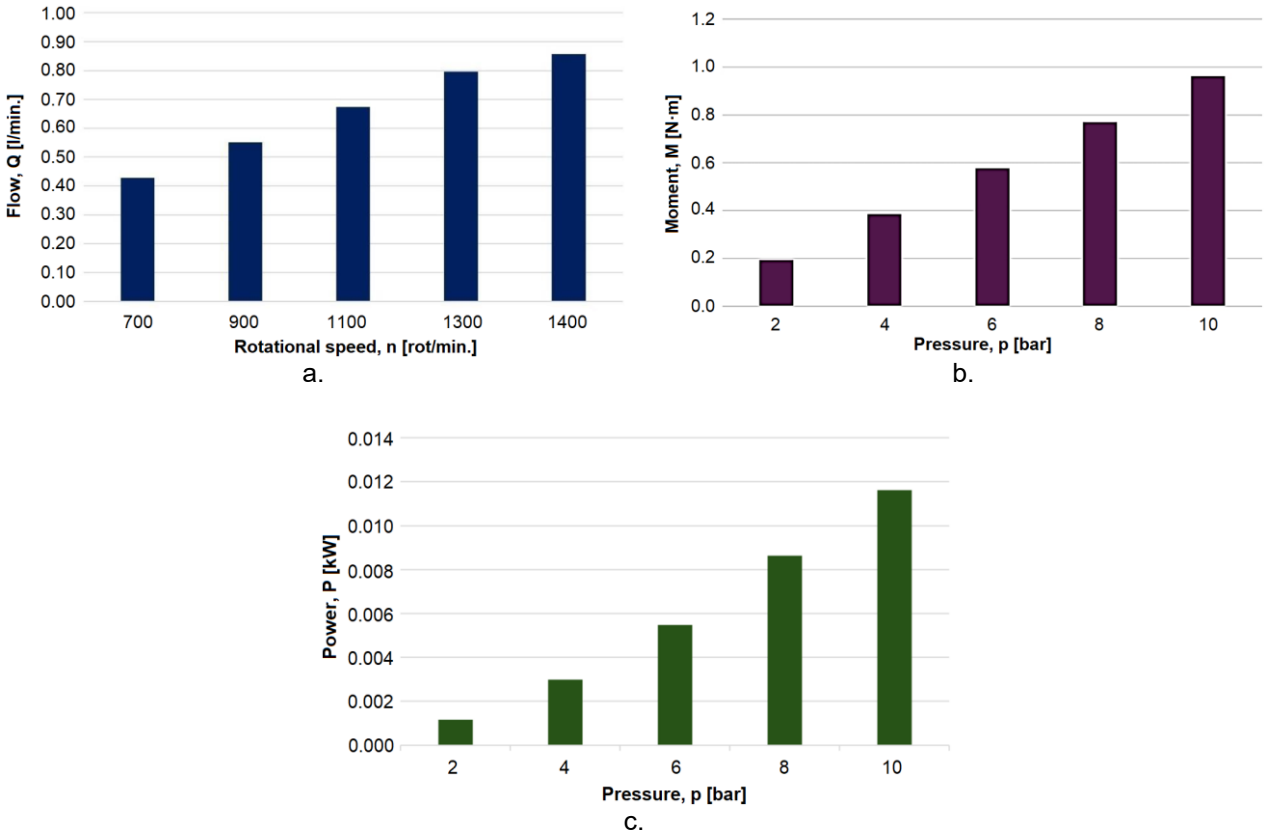

Fig. 4. Graphical representation of flow (a), moment (b) and power (c).

The directional control valve used in the low-pressure hydrostatic drive system is of the 4/2 type, Figure 5.a, with electric drive and elastic return and has the role of switching the direction of fluid flow between the pump, actuator and the tank.
The directional control valve is integrated in a transparent body, which allows direct observation of the position of the spool valve and the fluid path. The connections are made with quick couplings

and the control is provided by an electrical connector. The assembly is fixed on a modular platform and the orange tubes indicate the pressure and return lines.

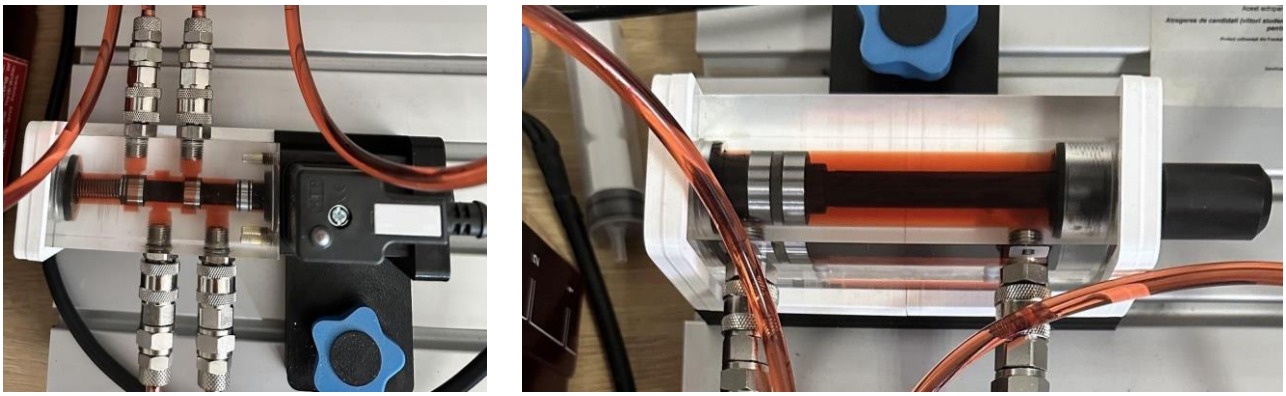

a. b.

Fig. 5. Mounting of the 4/2-type directional control valve (a) and the linear hydraulic motor (b).

The 4/2 type directional control valve has four ports and two switching positions. Depending on the position of the spool, it allows the fluid flow to be directed to one of the chambers of the hydraulic cylinder, while the other is connected to the discharge. The initial position is maintained by a return coil and the switching is done electrically.
Table 5 presents the main characteristics of the 4/2 type directional control valve. These specifications were taken into account in the selection and integration process of the directional control valve within the low-pressure hydrostatic drive system, ensuring the functional compatibility and performance required to achieve directional control of the hydraulic circuit.

Table 5: Technical parameters of the 4/2 type directional control valve [23]

Working fluid	HM class hydraulic oils, viscosity class ISO VG 32, 46 and 68
Liquid temperature range [°C]	-20 ... +60
Maximum ambient temperature [°C]	-20 ... +50
Viscosity range [mm²/s]	10 ... 500
Liquid purity class	Class 21/18/15
Permissible voltage fluctuations [%]	± 10 (alternating current), ± 15 (direct current)
Maximum switching frequency [1/h]	15.000
Working cycle	100 %
Weight [kg]	0.20
Maximum tightening torque - directional control valve [N·m]	30
Flow diameter [mm]	15

In order to analyze the behavior of the directional control valve and the entire low-pressure hydraulic drive system, it is necessary to determine the fluid flow velocity. This is a parameter for evaluating pressure losses, flow rate and geometric dimensions of hydraulic components.
The speed can be determined using the relationship:

$$v = \frac{4 \cdot Q}{\pi \cdot D^2} \left[\text{m/min}\right]. \tag{5}$$

To highlight how the fluid flow rate varies depending on the operating conditions, it will be determined based on the five flow rates previously calculated. Each of these values corresponds to a different operating scenario of the hydraulic system. The results are presented in Table 6.

Table 6: Values of the flow and the directional control valve speed

Nr. crt.	Q [l/min]	v [m/min]	
1	Q_1 = 0.43	$v_1 = \frac{4 \cdot Q_1}{\pi \cdot D^2}$	v_1 = 0.0024
2	Q_2 = 0.55	$v_1 = \frac{4 \cdot Q_1}{\pi \cdot D^2}$	v_2 = 0.0031
3	Q_3 = 0.67	$v_1 = \frac{4 \cdot Q_1}{\pi \cdot D^2}$	v_3 = 0.0037
4	Q_4 = 0.80	$v_1 = \frac{4 \cdot Q_1}{\pi \cdot D^2}$	v_4 = 0.0045
5	Q_5 = 0.86	$v_1 = \frac{4 \cdot Q_1}{\pi \cdot D^2}$	v_5 = 0.0048

The linear hydraulic motor (hydraulic cylinder) is an actuator used to transform hydraulic energy into linear movement. The operating principle is based on the action of fluid under pressure on the surface of a piston, thus generating a force capable of moving loads in one direction or alternatively. The performance of a hydraulic motor depends on several parameters, including: piston diameter, working pressure, fluid flow rate and assembly efficiency.
In this paper, a linear hydraulic motor shown in Figure 5.b was used. The motor contains a transparent cylinder that allows viewing the piston movement during fluid supply. Quick couplings ensure connection to the hydraulic circuit and visible metal seals at the ends of the piston delimit the working chambers.

3. Assembly and simulation schemes with Omegon Fluid

In the design of a low-pressure hydrostatic drive system, simulation of operation plays an essential role in validating the calculated parameters and in anticipating the mechanical behavior of the assembly. Through simulation, it is possible to analyze how the hydraulic energy is transmitted to the mechanical execution elements and how they respond to various loads.
Omegon Fluid [24] is a software dedicated to the simulation of hydraulic and pneumatic circuits, used to analyze the behavior of drive systems. The program allows the configuration of individual parameters for each component and the simulation of the dynamic behavior of the entire circuit. Important quantities such as pressure, flow, speed or force can be analyzed, all in the context of a mechanical system that responds to hydraulic drive.
One of the advantages of using the Omegon Fluid software is the real-time graphical representation of the fluid movement and the driven mechanical components, which allows a clear understanding of the system's operation and its easy adaptation according to the application requirements.
Omegon Fluid is a graphical simulation environment used for modeling and analyzing hydraulic and pneumatic circuits. The program interface is intuitive, based on standardized symbols according to ISO standards, which allows the rapid construction of realistic functional diagrams that are easy to understand and interpret.
The program also provides a visual legend of the colors used in the simulation: for example, red indicates high pressure, blue indicates low pressure and green represents normal fluid circulation. This color code facilitates the rapid interpretation of the circuit behavior.
Another useful aspect is the possibility of placing measurement points inside the pipes, to track real-time values: pressure, flow rate or fluid speed at a specific node. This contributes to a detailed

understanding of the circuit dynamics, which is essential in projects that involve the verification of mechanical components operated by hydraulic forces.
With these functionalities, Omegon Fluid presents itself as a complete tool for functional testing of a hydrostatic system in a visual and interactive way, allowing the simulation of various working scenarios and the rapid adaptation of parameters.
An important aspect in using the program is the possibility of configuring the simulation conditions, as well as the control over the input and output parameters of the system. For example, constant or variable supply pressures, mechanical loads applied to linear actuators, logical or automatic controls via directional control valves can be introduced. For low-pressure systems, Omegon allows testing of behavior in regimes with reduced pressure values, which is ideal for simulating drives where energy efficiency, fine movement control and loss limitation are priorities.

3.1. Low-pressure hydrostatic drive system assembly diagram

In order to analyze the operation of the low-pressure hydrostatic drive system, a schematic diagram was created in Omegon Fluid that reproduces the physical circuit. The hydrostatic system includes the main components, such as: pump, tank, directional control valve, linear hydraulic motor and connecting pipes.
The electrical part has the role of controlling the activation of valves, pump or other drives via signal panels and logic interfaces.
According to Figure 1, the following components can be seen on the front panel: the electrical signal panel, which includes buttons and LEDs for ON/OFF commands, direction reversal, manual or automatic cycle triggering; the modular electrical connectors, which allow the connection of control wires between different devices (such as directional control valve); the areas dedicated to power and safety, where the power supplies, fuses and ground terminals are located. These panels are an integral part of the Omegon Fluid environment and facilitate the simulation of dynamic behavior through manual or automatic commands, allowing real-time observation of the circuit response.
Subsequently, in Figure 6, the diagram created in the Omegon Fluid program is shown, in its initial state, before any action is triggered.

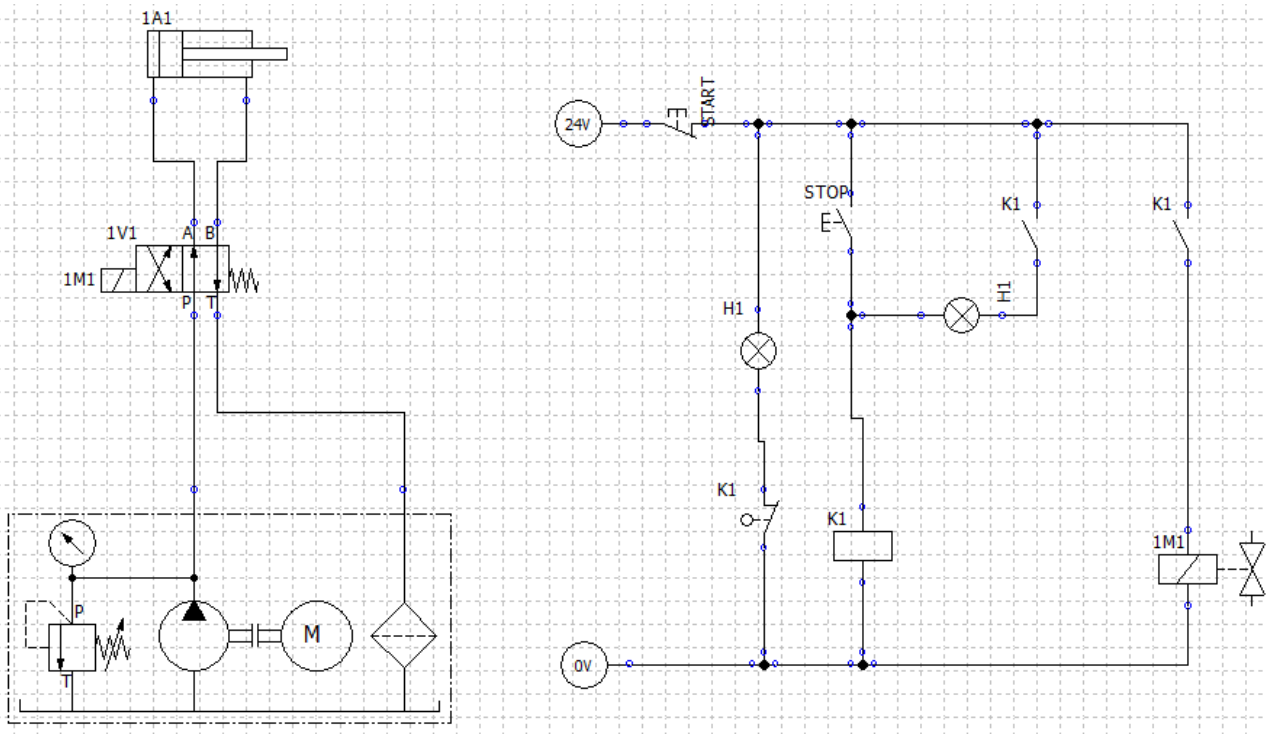

Fig. 6. System diagram, simulated in the Omegon Fluid program

The pipes are positioned between the elements according to the principles of a standard hydraulic circuit and their directional control valve follows logical paths between the tank, pump, directional control valve and hydraulic cylinder. The initial position of the directional control valve is neutral-centered, without directing the flow to the cylinder. The cylinder rod is fixed and the colors of the pipes indicate that there is no active pressure in the system (resting state). This visualization provides a starting point for the analysis of subsequent operation and allows understanding of how the hydraulic and electrical components are connected.

3.2. Configuring parameters in the Omegon Fluid software

In order for the simulation performed in Omegon Fluid to reflect the real behavior of a low-pressure hydrostatic drive system, it is important to correctly configure each component element with precise data. The parameters that describe the system components, from the pump to the directional control valve, cylinder, pipes and protective elements, have a direct influence on the results obtained in the simulation, both from a kinematic, functional and energetic point of view. The values resulted from a detailed analysis presented in the previous chapter, in which the basic system parameters were dimensioned and calculated.
Thus, the data configured in the Omegon Fluid interface is consistent with the theoretical design of the system and ensures complete coherence between the analytical and simulation parts.
A gear pump was used to supply the circuit, configured with a maximum flow rate of 10 l/min and a maximum working pressure of 10 bar. The operating rotational speed set in Omegon Fluid was 1400 rpm and the direction of rotation was set to clockwise.
The directional control valve is a 4/2 type with a centered neutral position, being returnable to the initial position. It was configured in such a way as to allow the correct direction of the hydraulic oil flow to the cylinder, depending on the applied electrical signal. The electrical control has an activation voltage of 24 V, and in the neutral position, the pump is discharged directly to the tank.
The hydraulic cylinder is double-acting and has the following characteristics configured in Omegon: piston diameter: 20 mm; rod diameter: 10 mm; stroke: 58 mm; average force: 14 N; average speed: 2.50 m/min. These dimensions were entered into the software to reproduce the linear movement of the rod during the simulation. The cylinder was connected directly to the directional control valve via rigid pipes, so as to ensure control of the direction of movement.
The hydraulic pipes were configured with the following characteristics: inner diameter: 5 mm; total length: 0.3 m; connection type: rigid, without significant losses; fluid: hydraulic oil. They ensure the connection between the pump, directional control valve and cylinder and in Omegon Fluid, the pipe route was organized so as to respect real assembly principles.
In addition to the hydraulic system, electrical components play a fundamental role in controlling the directional control valve and controlling the operating cycles. To make these connections, work-specific equipment was used. The power supply in the hydrostatic system, Figure 7, has an output voltage of 24 V DC and a maximum current of 4.5 A. It is equipped with standardized output terminals for +24 V (red) and 0 V (blue), a power switch and a light indicator. Connections are easily made via plugs, and the outputs are protected.

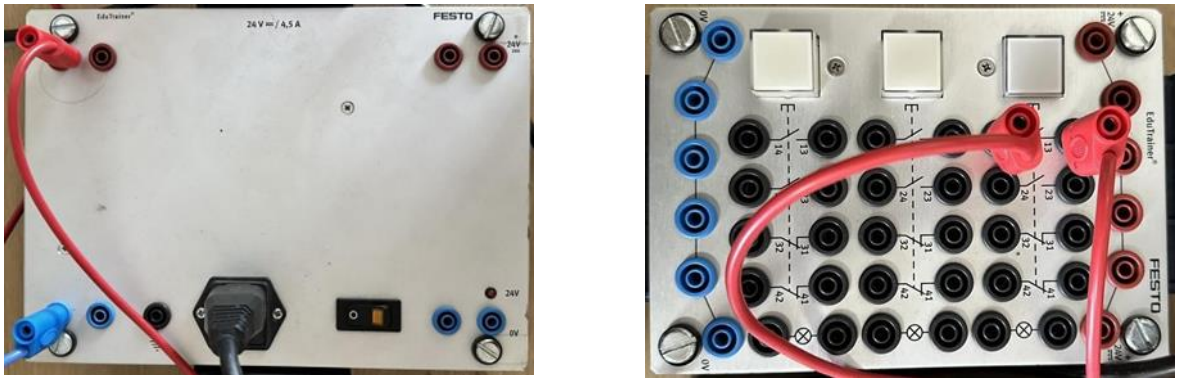

Fig. 7. Power supply and relay

The electrical control module is responsible for activating or deactivating the hydrostatic system circuit. When the start button is pressed, the electrical signal causes the directional control valve to switch, which leads to the supply of hydraulic oil to the cylinder and the start of its stroke. Once the button is pressed to stop, the directional control valve returns to the neutral position. Thus, the module allows precise control of automatic or manual operation, being essential in simulating repeated system cycles.

3.3. Operation of the hydraulic system simulated in Omegon Fluid

To evaluate the dynamic behavior of the low-pressure hydrostatic drive system, it is essential to analyze its operation in a full operating mode. In this stage, the concrete operation of the modeled system is analyzed, following the synchronization of the electrical control with the movement of the hydraulic cylinder and the way in which the main elements of the scheme interact in a full drive cycle. Figure 8 shows the scheme of the low-pressure hydrostatic system at the time of simulation.

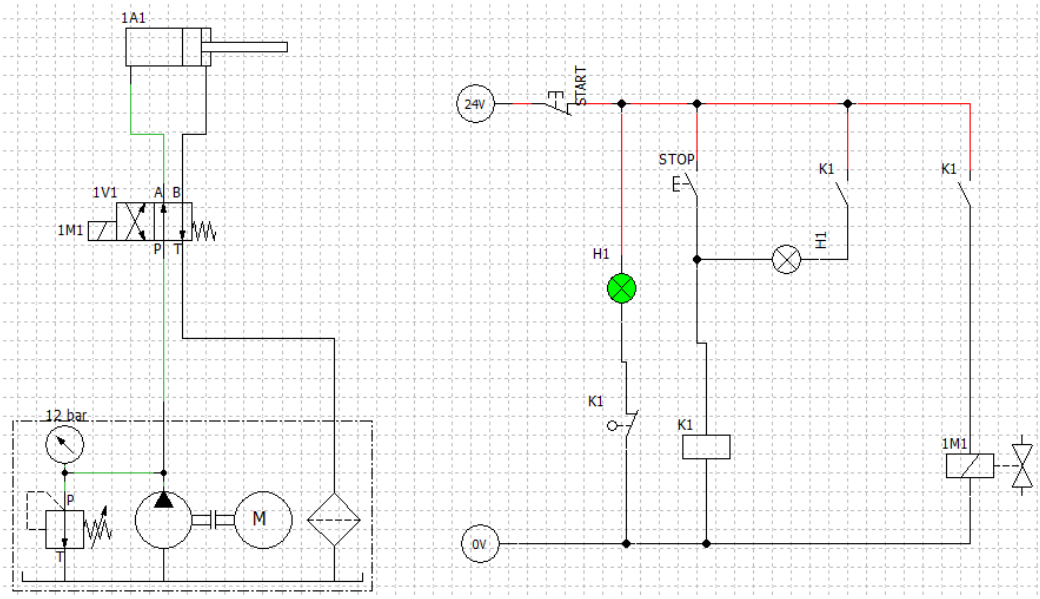

Fig. 8. System diagram at the time of simulation

a. b.

Fig. 9. The pressure gauge that records the pressure during the active stroke of the cylinder (a) and the passive stroke (b)

As the simulation progresses, the flow continues to feed the cylinder and the rod movement occurs in a controlled manner, supported by constant oil pressure. The electrical control is maintained throughout the stroke, ensuring a complete work cycle.

In this phase, the pressure in the circuit increases with the mechanical stress, and this phenomenon is also confirmed by reading the pressure gauge attached to the pumping group, Figure 9.a.
During the active stroke of the cylinder, the pressure gauge indicates a value of approximately 4.2 bars. This value corresponds to the working pressure developed at that moment in the circuit, being in accordance with the specifications of the designed low-pressure system. The pressure gauge, mounted between the pump and the safety valve, allows the pressure to be monitored in real time, thus providing a direct indicator of the system stress in the active phase.
Once the stroke is completed, the pressure in the system also progressively decreases, and the pressure gauge gradually returns to its initial value, indicating a state of hydraulic rest, Figure 9.b. This return confirms the correct functional behavior of the valve and the discharge to the tank.
At the end of the stroke, once the electrical control is interrupted, the distributor automatically returns to its neutral position, according to the internal configuration. This condition is shown in Figure 10, where the connections between the pump and cylinder are broken and the oil is directed back to the tank. At this point, the piston rod remains stationary, marking the completion of a complete operating cycle of the system.

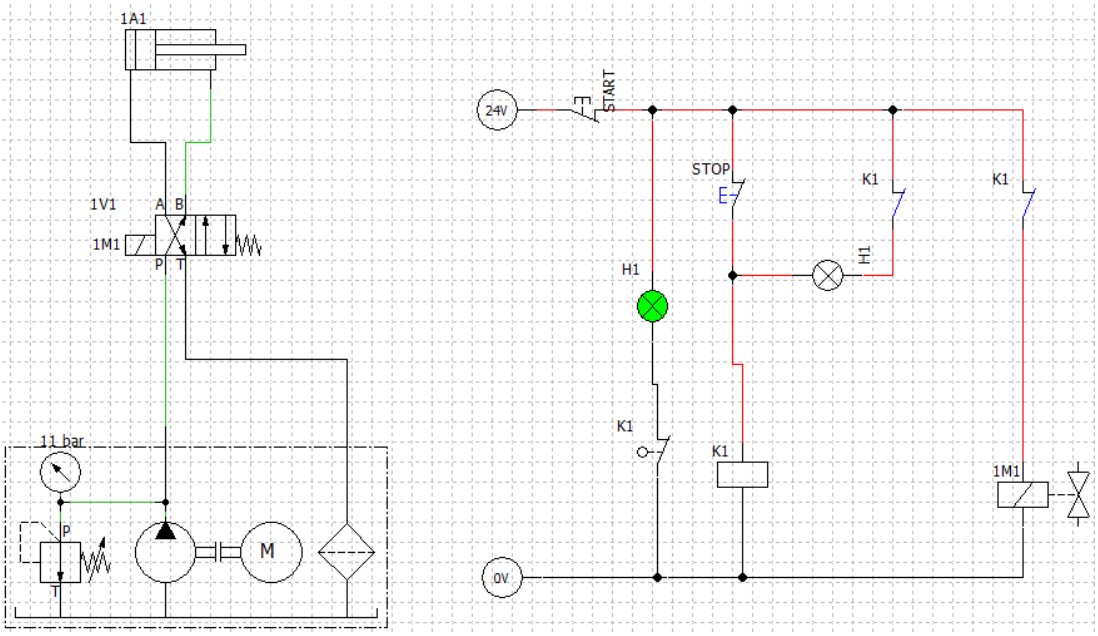

Fig. 10. Returning the system to a resting state during simulation

The entire simulated process highlights the correct synchronization between the electrical control and the mechanical response, with hydraulic parameters adapted to low-pressure operation, thus validating both the theoretical and practical parts of the project.

3.4. Graphical analysis of the operating cycle

To highlight the dynamic behavior of the actuator system simulated in Omegon Fluid, a graphical analysis of the main signals in the circuit was performed.
Figure 11 shows how several successive cylinder strokes are performed, correlated with the directional control valve command. The red curve (1A1 - Hydraulic actuator) represents the position of the cylinder rod over time, expressed as a percentage (0 -100%).
A cyclic variation is observed, with four complete advance and retraction cycles. The increase in the value towards 100% indicates the rod advance, while the decrease to 0% reflects its retraction to the initial position. The duration of each stroke is approximately 4 seconds, the system having a repetitive and stable behavior.

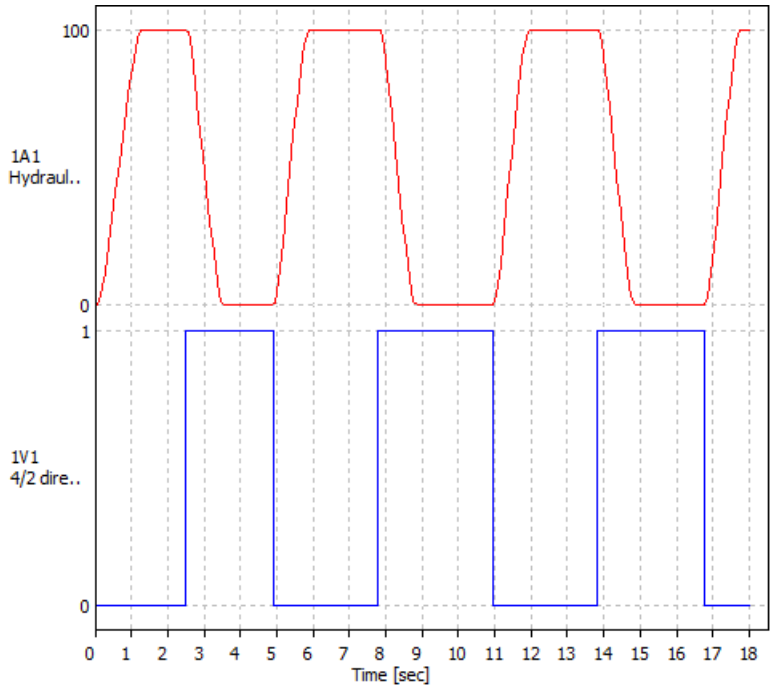

Fig. 11. Diagram of the hydraulic system's cyclic operation in Omegon Fluid

The blue curve (1V1 - 4/2 directional control valve) represents the electrical command applied to the valve. The binary values 0 and 1 indicate the activation state (1 = active, 0 = inactive). It can be seen that the valve is activated (blue line at position 1) during the period in which the rod is in the forward stroke, and upon the complete return of the rod, the command signal is reactivated to initiate a new stroke.
This graph demonstrates the synchronization between the valve command and the position of the hydraulic actuator, in a fully automated system. The operation is cyclical and controlled, and each activation of the valve generates a new work cycle, ensuring the repeatability of the movement and thus validating the correctness of the control logic implemented in the simulation.

4. Conclusions

The paper aimed at the theoretical analysis and functional simulation of a low-pressure hydrostatic drive system, aiming to highlight the advantages that this category of drives offers in industrial and educational applications. By integrating the constructive-functional design stages with the numerical simulation performed in the Omegon Fluid software program, a complete picture of the behavior of the hydraulic system under reduced pressure conditions was obtained, confirming the viability and efficiency of this type of drive.
The obtained results demonstrated that low-pressure hydrostatic drive systems can operate stably and energy-efficiently when the parameters are carefully dimensioned and correlated with each other. These systems ensure a significant reduction in internal losses and energy consumption, extend the life of components and contribute to increasing operational safety, while being easier to maintain and diagnose.
Although the working pressure is relatively low, the analyzed system has proven to be able to generate sufficient actuation forces for the intended practical applications, such as test equipment, laboratory installations or low-power machines. The determined values for flow, torque and power, depending on speed and pressure, were within the calculated theoretical limits, confirming the validity of the analytical model used. The simulation performed in the Omegon Fluid program allowed the verification of the correlation between the electrical controls and the mechanical response of the system.

A precise synchronization between the electrical signal applied to the directional control valve and the movement of the cylinder rod was found, which demonstrates the reliability of the control scheme and the smooth functioning of the interaction between the hydraulic and electrical components. During the simulation, the variations in the pressure in the circuit, monitored with the help of the pressure gauge, revealed a stable evolution, without major fluctuations, confirming the correct behavior of the safety valve and the unloading system.
The graphical analysis of the operating cycle showed a repetitive, stable and controlled behavior of the system, with a constant duration of the successive cylinder strokes. The automatic return of the directional control valve to the neutral position after the end of each cycle demonstrated the dynamic balance of the assembly and the efficiency of the control scheme implemented in the simulation.
This concordance between the theoretical and the practical part emphasizes the high level of accuracy of the modeling and the relevance of the simulation method used.
Through the complete analysis carried out, it was confirmed that low-pressure hydrostatic systems represent high-performance and economical solutions for applications where low energy consumption, high precision and increased reliability are searched.
The Omegon Fluid simulation environment proved to be an effective tool, offering the possibility of detailed parameter configuration, interactive visualization of hydraulic flows and testing of dynamic scenarios under controlled conditions. It allows the study to be extended to more complex systems with electro-hydraulic or adaptive control, opening up research and optimization perspectives in the field of hydraulic drives. In conclusion, the research highlighted the importance of numerical simulation as an indispensable step in the design process of hydrostatic drives.
The obtained results validate both the analytical calculations and the practical configuration of the system, demonstrating the coherence between theory and application. Low-pressure hydrostatic drives are thus emerging as a viable and sustainable option for modern applications, offering an optimal balance between performance, costs, safety and energy efficiency.

References

[1] Moroşanu, G.A., N. Baroiu, V.G. Teodor, V. Păunoiu, and N. Oancea. ”Review on study methods for reciprocally enwrapping surfaces.” *Inventions* 7, no. 1 (2022): 10.
[2] Baroiu, N., G.A. Moroșanu, V.G. Teodor, and N. Oancea. ”Roller profiling for generating the screw of a pump with progressive cavities.” *Inventions* 6, no. 2 (2021): 34.
[3] Ma, J., H. Yan, R. Li, F. Li, and X. Fang. ”Design, simulation, and experimental study of hydrostatic drive system for wide-span farming platform.” *PLoS One* 20, no. 10 (2025): e0334856.
[4] Takosoglu, J., Ł. Chłopek, K. Ziejewski, R. Dindorf, and P. Wos. ”Comparative analysis of the hydrostatic drive system for a midi wheel loader.” Paper presented at the International Scientific-Technical Conference on Hydraulic and Pneumatic Drives and Control NSHP 2023, Piechowice, Poland, October 11-13, 2023. *Lecture Notes in Mechanical Engineering. Advances in Hydraulic and Pneumatic Drives and Control 2023* (2024): 114-127.
[5] Baroiu, N., and G.A. Moroşanu. ”Constructive-functional analysis and sizing of hydraulic filters.” *The Ann. of ”Dunarea de Jos”, Univ. of Galați, Fasc. V, Tech. in Mach. Building* 39 (2021): 6-11.
[6] Kahandawa, G., I. Spark, and A. Jayawardena. ”Vehicles with cooperative redundancy of multiple steering systems: a hybrid shaft/hydrostatic drive system.” *Proc. of the Inst. of Mech. Eng., Part D: J. of Auto. Eng.* 239, no. 6 (2024): 2192 - 2204.
[7] Baroiu, N., V.G. Teodor, and G.A. Costin. ”Constructive-functional analysis of single-rod double-acting hydraulic cylinders.” *Tehnomus J. - New Tech. and Prod. in Mach. Manuf. Tech.* (2017): 126-131.
[8] Wos, P., R. Dindorf, J.E. Takosoglu, and Ł. Chłopek. “Volumetric control of hydrostatic drives system according to the principle of the forced flow.” Paper presented at the International Scientific-Technical Conference on Hydraulic and Pneumatic Drives and Control NSHP 2023, Piechowice, Poland, October 11-13, 2023. *Lecture Notes in Mechanical Engineering. Advances in Hydraulic and Pneumatic Drives and Control 2023* (2024): 83-92.
[9] Costin, G.A., C. Afteni, I. Iacob, V. Păunoiu, and N. Baroiu. ”An overview on sheet metal hydroforming technologies.” *The Ann. of ”Dunarea de Jos”, Univ. of Galați, Fasc. V, Tech. in Mach. Building* 36 (2018): 55-62.

[10] Brand, M., H. Stratmann, H.J. Vagt, R. Rueckert, and G. Geissler. ”Drive system and method of monitoring a hydrostatic drive”. Patent: US8386135B2, 2013.
[11] Baroiu, N., and G.A. Moroșanu. ”Graphical modelling and studies on hydraulic pump parameters.” *J. of Ind. Design and Eng. Graph. - JIDEG* 15, no. 2 (2020): 7-12.
[12] Brand, M. ”Hydrostatic drive system”. Patent: US8862359B2, 2014.
[13] Wang, X., Z. Wang, S. Wang, W. Cai, Q. Wu, and W. Ma. ”Design and control performance optimization of variable structure hydrostatic drive systems for wheel loaders.” *Machines* 12, no. 4 (2024): 238.
[14] Berbinschi, S., V.G. Teodor, N. Baroiu, and N. Oancea. ”The substitutive circles family method - graphical aproach in CATIA design environment.” *The Ann. of ”Dunarea de Jos”, Univ. of Galați, Fasc. V, Tech. in Mach. Building* 31 (2013): 53-56.
[15] Zhang, C., C. Li, C. Zhao, L. Li, G. Gao, and X. Chen. ”Design of hydrostatic chassis drive system for large plant protection machine.” *Agriculture* 12, no. 8 (2022): 1118.
[16] Baroiu, N., G.A. Moroșanu, V.G. Teodor, R.S. Crăciun, and V. Păunoiu. ”Use of reverse engineering techniques for inspecting screws surfaces of a helical hydraulic pump.” *Int. J. of Modern Manuf. Tech.* 14, no. 2 (2022): 20-29.
[17] Berbinschi, S., V.G. Teodor, N. Baroiu, and N. Oancea. ”Profiling methodology for side mill tools for generation of helical compresor rotor using reverse engineering.” *The Ann. of ”Dunarea de Jos”, Univ. of Galați, Fasc. V, Tech. in Mach. Building* 29, no. 2 (2011): 111-116.
[18] Popa, L.C., I. Popa, V.G. Teodor, and N. Baroiu. ”Profiling tool generating method, using the profile measurement of rotor of screw compressor components.” *The Ann. of ”Dunarea de Jos”, Univ. of Galați, Fasc. V, Tech. in Mach. Building* 29, no. 2 (2011): 123-128.
[19] Helduser, S. ”Electric-hydrostatic drive - An innovative energy-saving power and motion control system.” *Proc. of the Ins. of Mech. Eng., Part I: Jo. of Syst. and Control Eng.* 213, no. 5 (1999): 427 - 437.
[20] Fan, Q., J. Zhang, R. Li, and T. Fan. ”Review of research on hydrostatic transmission systems and control strategies.” *Processes* 13, no. 2 (2025): 317.
[21] Rundo, M. ”Models for flow rate simulation in gear pumps: a review.” *Energies* 10, no. 9 (2017): 1261.
[22] Sinntec. *Gear pumps*. Accessed October 31, 2025. https://www.central-lubrication.com/Gear-pumps.
[23] Sinntec. *Distributors*. Accessed October 31, 2025. https://www.central-lubrication.com/Distributors.
[24] Omegon. *Omegon Fluid*. Accessed October 31, 2025. https://en.omesim.com/.

ISSN 1454 - 8003
Proceedings of 2025 International Conference on Hydraulics and Pneumatics - HERVEX
November 19-21, Băile Govora, Romania

OPTIMIZATION OF A SOLAR AGRICULTURAL PRODUCT DRYER FOR NIGHTTIME OPERATION

Alexandru-Polifron CHIRIȚĂ[1,*], Gheorghe ȘOVĂIALĂ[1], Ioan PAVEL[1], Radu-Iulian RĂDOI[1], Alin-Nicolae HARABAGIU[2]

[1] National Institute of Research & Development for Optoelectronics – Subsidiary Hydraulics and Pneumatics Research Institute (INOE 2000 – IHP), * chirita.ihp@fluidas.ro

[2] National Institute of Research & Development for Machines and Installations Designed to Agriculture and Food Industry – INMA

Abstract: *This paper details a numerical analysis of the thermal module with water-air heat exchanger for a continuous ultra-efficient, fully autonomous, net-zero emission agricultural dryer system. The research addresses the critical challenge of maintaining operational continuity during nighttime periods when direct solar radiation is unavailable, ensuring uninterrupted drying processes essential for agricultural product preservation. The study contributes to the global transition toward sustainable food processing technologies by developing a solar dryer capable of functioning independently of variable meteorological conditions, thereby supporting the European Green Deal objectives and renewable energy directive frameworks.*

Keywords: *Numerical simulation, optimization, heat exchanger, solar dryer*

1. Introduction

The 21st-century paradigm is fundamentally characterized by the acceleration of climate change and the imperative necessity of a global energy transition. In this context, the development of renewable energy conversion and storage technologies constitutes a fundamental pillar of sustainability strategies [1]. The IPCC Special Report on Global Warming of 1.5°C highlights the critical need to reduce CO2 emissions by 45% by 2030 compared to 2010 levels, aiming for climate neutrality by 2050 [2]. Within this complex and multidimensional framework, the agri-food sector faces unprecedented challenges, requiring innovative solutions that reconcile food security with decarbonization objectives. This strategic initiative aligns with the European Green Deal and Directive (EU) 2018/2001, which establishes a normative framework for increasing the share of renewables in the European Union's energy mix [3, 4].

Dehydration constitutes an essential thermal process in food processing, with significant implications for nutritional quality, shelf life, and the economic value of final products. According to the Food and Agriculture Organization (FAO), approximately 30-40% of agricultural products deteriorate before reaching consumers; implementing efficient dehydration technologies can substantially reduce these losses [5]. However, traditional drying processes are energy-intensive and carry a significant carbon footprint. Conventional dryers, predominantly powered by fossil fuels, emit an average of 2.5–3.0kg of CO_2 for every kilogram of water evaporated [6]. While solar drying offers a cleaner alternative, literature indicates that the global efficiency of such systems is often limited by intermittent radiation, although advanced thermal modules can improve performance by up to 35% [7].

The project "Ultra-efficient, totally autonomous, net-zero emissions continuous dryer" (UCES) provides a concrete response to these limitations by proposing a holistic integration of solar thermal and photovoltaic technologies. The fundamental innovation of the UCES system lies in its capacity to ensure continuous operation, independent of variable weather conditions, through a hybrid energy collection and storage architecture. The critical component of this architecture is the water-to-air heat exchanger module, which facilitates the efficient transfer of thermal energy stored in accumulation systems to the processed air within the drying chamber [8]. This module is the key element in overcoming the primary disadvantage of traditional solar systems: operational discontinuity during periods of insufficient solar radiation.

Recent studies emphasize the importance of maintaining process parameters within strict limits to ensure product quality; specifically, a minimum temperature of 50°C and relative humidity below 10% are critical values for preventing microorganism growth and undesirable enzymatic reactions [9]. Consequently, the research presented in this report focuses on optimizing the performance of heat exchangers under specific operating conditions, with a special emphasis on nocturnal regimes. By utilizing advanced numerical simulation methods, this study offers a profound understanding of heat transfer and fluid dynamic phenomena [10]. This approach allows for the design of a system that maximizes the energy density extracted from thermal storage while minimizing losses.

The socio-economic context of this research is particularly relevant for Romania and other member states with economies in transition. The Romanian agricultural sector, which contributes approximately 4.3% to the GDP and employs over 25% of the active population, faces major challenges regarding the modernization of processing capabilities [11]. The implementation of technologies developed within the UCES project can significantly contribute to increasing the competitiveness of local producers and reducing dependence on imported fuels. Therefore, this research is not merely an academic exercise in thermodynamic optimization but a substantial contribution to the energy transition of the agri-food sector [12]. The numerical simulation results presented provide the scientific foundations necessary for designing an industrial prototype capable of autonomous 24-hour operation, ensuring maximum energy efficiency and net-zero emissions throughout its life cycle.

2. Material and Method

Numerical simulation was implemented using Simcenter Amesim software, a specialized multidomain simulation platform capable of analyzing complex thermal and hydraulic processes. The simulation model presented in Fig. 1 contain a 200L solar collector reservoir with defined thermal capacity and convective heat loss coefficients to ambient conditions.

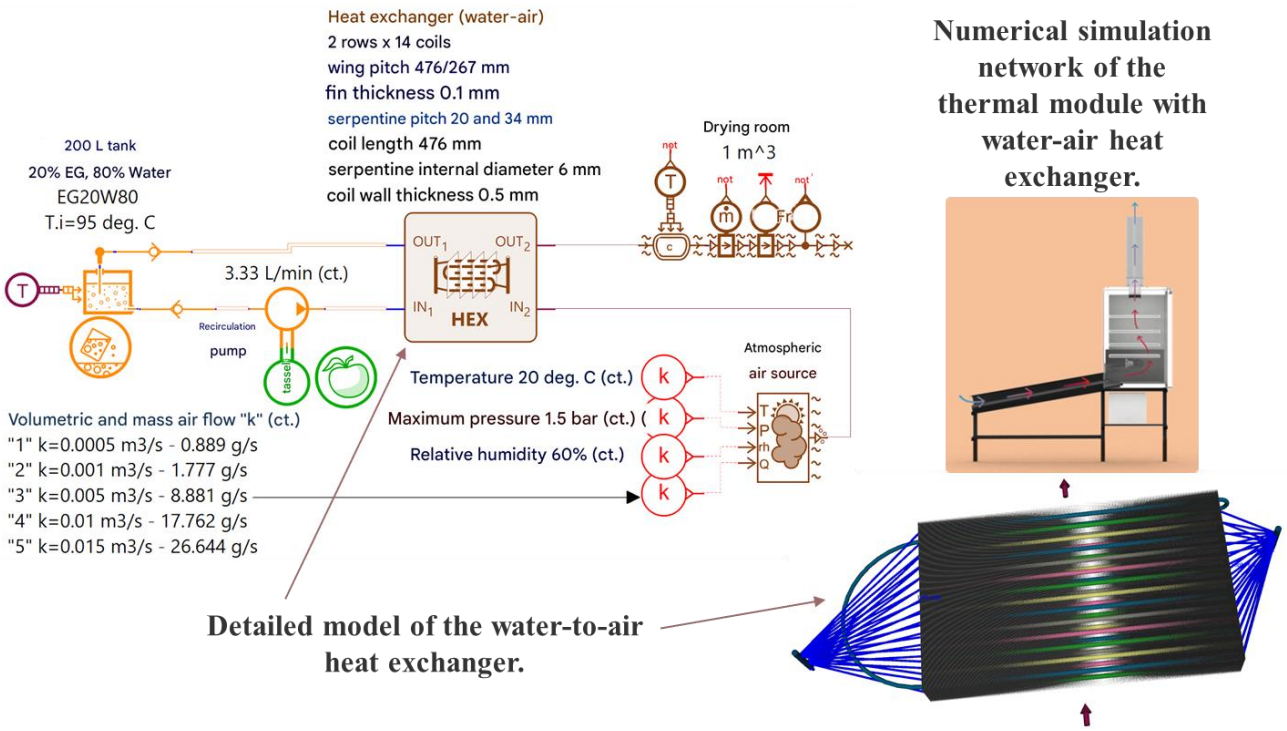

Fig. 1. Simulation network and physical model

The heat transfer fluid consisted of ethylene glycol 20% and water 80% mixture with a total volume of 204L and initial temperature of 95°C. The hydraulic network was dimensioned using DN25

pipes, with detailed modeling of linear head losses and pump energy consumption. The water-air heat exchanger was represented by a detailed 3D model featuring 28 serpentine tubes arranged in 2 rows with 6 mm internal diameter and 0.5 mm wall thickness. The atmospheric air source was modeled with constant mass flow rates ranging from 0.0005 to 0.015m^3/s, at 20°C with 60% relative humidity. The drying chamber was represented as a controlled 1m^3 volume where complex thermodynamic processes including evaporation, condensation, and humidity dynamics were simulated.

The parametric simulation was structured as a systematic experimental protocol consisting of 5 simulation runs, with the volumetric air flow rate serving as the independent variable. The boundary conditions were established to simulate nighttime operational conditions, where the sole thermal energy source was the heat stored in the solar collector reservoir. The initial conditions were defined with the heat transfer fluid at 95°C, the drying chamber environment at 20°C ambient temperature, and 60% initial relative humidity. The performance evaluation was based on 5 critical optimization criteria: the heat exchanger efficiency must exceed 90%; the final temperature within the drying chamber must reach or exceed 50°C; the relative humidity must be maintained at or below 10%; the air flow rate must be sufficiently low to prevent displacement of agricultural products within the chamber; and the continuous operation duration must cover the entire 10 hour nighttime period. This comprehensive evaluation framework ensured the identification of optimal operating parameters that simultaneously satisfy technical, product quality, and operational requirements.

3. Results and Discussion

The temperature of the heat transfer fluid within the reservoir and the temperature within the drying chamber (presented in Fig. 2.) demonstrate a complex relationship with the air flow rate.

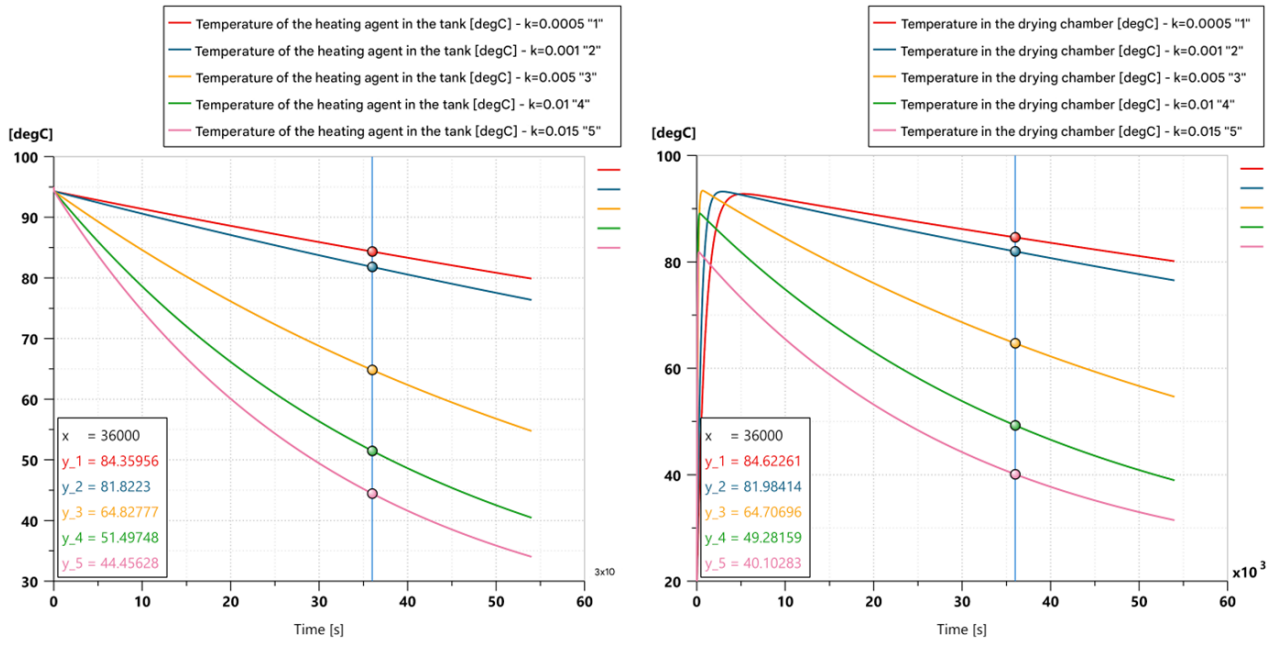

Fig. 2. Dynamic evolution of temperatures

The reservoir temperature figure shows a progressive decline from the initial 95°C over the 10 hours simulation period, with the highest air flow rate producing the most rapid temperature decrease to 44.45°C at 10 hours, while the lowest air flow rate maintains a significantly higher temperature of 84.36°C. The drying chamber temperature figure reveals that all air flow rates except the highest successfully maintain temperatures above the critical 50°C threshold, with the lowest air flow rate achieving 84.62°C after ten hours, while the highest flow rate drops to 40.1°C.

The air flow rate of 0.01 m3/s represents an optimal compromise, maintaining the drying chamber temperature at 49.28°C after 10 hours of operation. These thermal profiles confirm the direct correlation between air flow rate and thermal energy extraction rate, with significant implications for the operational duration and product quality.

Fig. 3. show the dynamic evolutions of heat flux through the heat exchanger and the thermal efficiency of the heat transfer process, these provide critical insights into the system's energy conversion performance. The heat flux figure demonstrates that the maximum heat transfer rate occurs at the beginning of the process and progressively declines as the heat transfer fluid cools, with the highest air flow rate achieving a maximum heat flux of 540W, while the lowest air flow rate maintains a minimum heat flux of 58W. This confirms the direct relationship between air flow rate and thermal energy transfer intensity. The thermal efficiency figure reveals that all air flow rates maintain efficiency within a relatively narrow range of 0.82 to 0.99, with the lowest flow rates achieving values closest to the maximum. Notably, the highest air flow rate produces an efficiency of 0.82, which falls below the required 90 percent threshold, while all other flow rates exceed this critical performance benchmark. The graph confirms that the value of the convection coefficient is between 321 and 341 W/m²/K. At higher air flows, an increased variability of the coefficient is observed. This instability is a consequence of the heat transfer relationships, being correlated with the temperature differences between the supply and return flows, which become more significant at high flow rates.

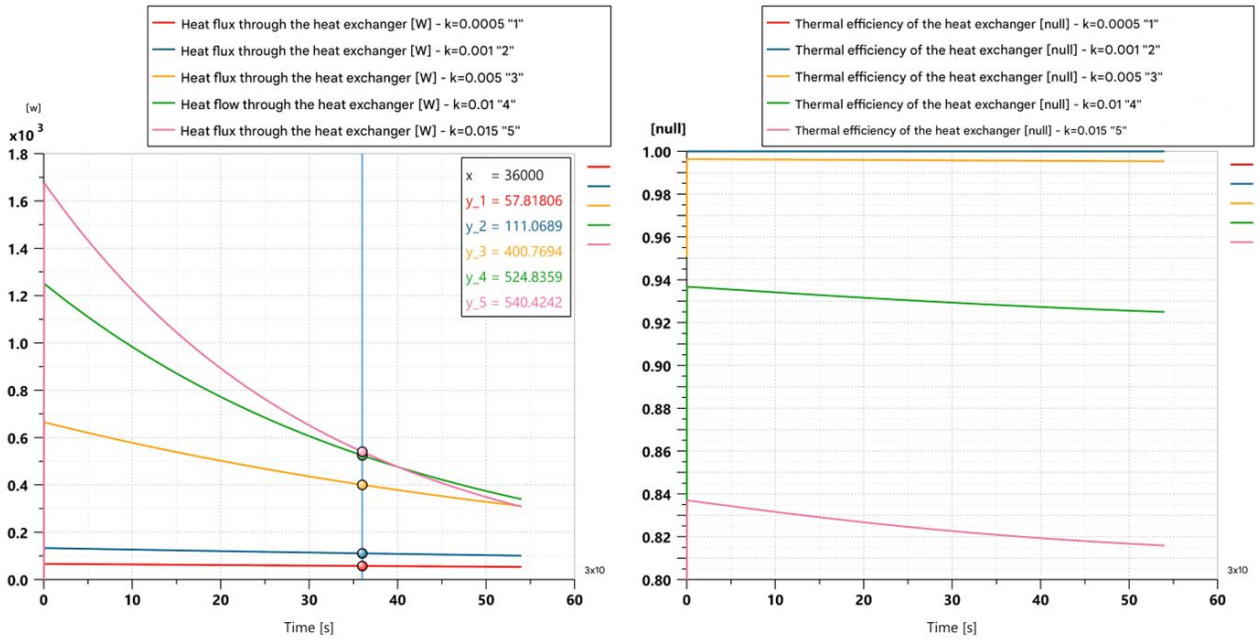

Fig. 3. Heat transfer characteristics

Fig. 4. show the dynamic evolutions of the relative humidity within the drying chamber and the cumulative energy transferred to the drying chamber, these demonstrate the system's effectiveness in achieving optimal drying conditions. The relative humidity figure shows a rapid initial decrease in relative humidity during the first hour of operation, followed by stabilization for most air flow rates, with the exception of the two highest flow rates. The highest air flow rate initially reduces humidity most rapidly but experiences humidity increases after 10 hours due to temperature decline, while the remaining flow rates maintain relative humidity below the critical 10% threshold throughout the entire operational period. The cumulative energy figure demonstrates a direct relationship between air flow rate and total energy transferred, with the highest flow rate transferring 39.9MJ of energy compared to 8.5MJ for the lowest flow rate at 36000 seconds. This behavior aligns with fundamental heat transfer principles where increased

mass flow rate of the cold fluid enhances thermal energy transfer. However, this energetic advantage results in accelerated consumption of stored thermal energy, thereby limiting the system's operational duration.

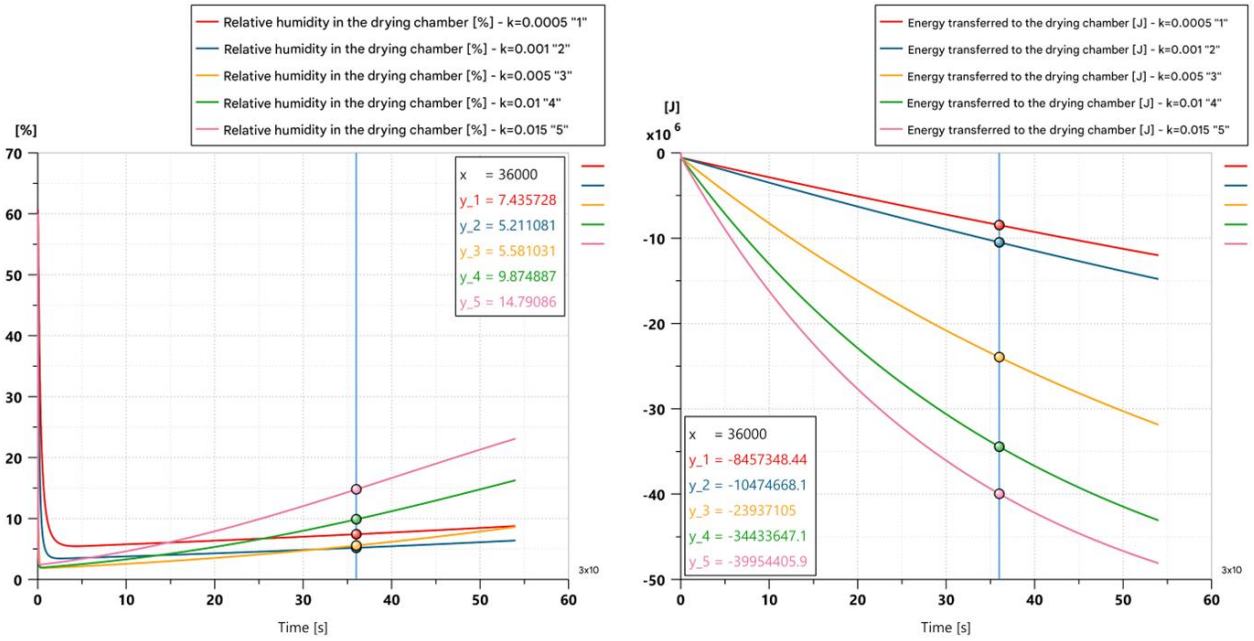

Fig. 4. Humidity control and energy transfer dynamics

Fig. 5 confirms that the air mass flow rate is maintained constant for each simulation run, as prescribed by the experimental protocol.

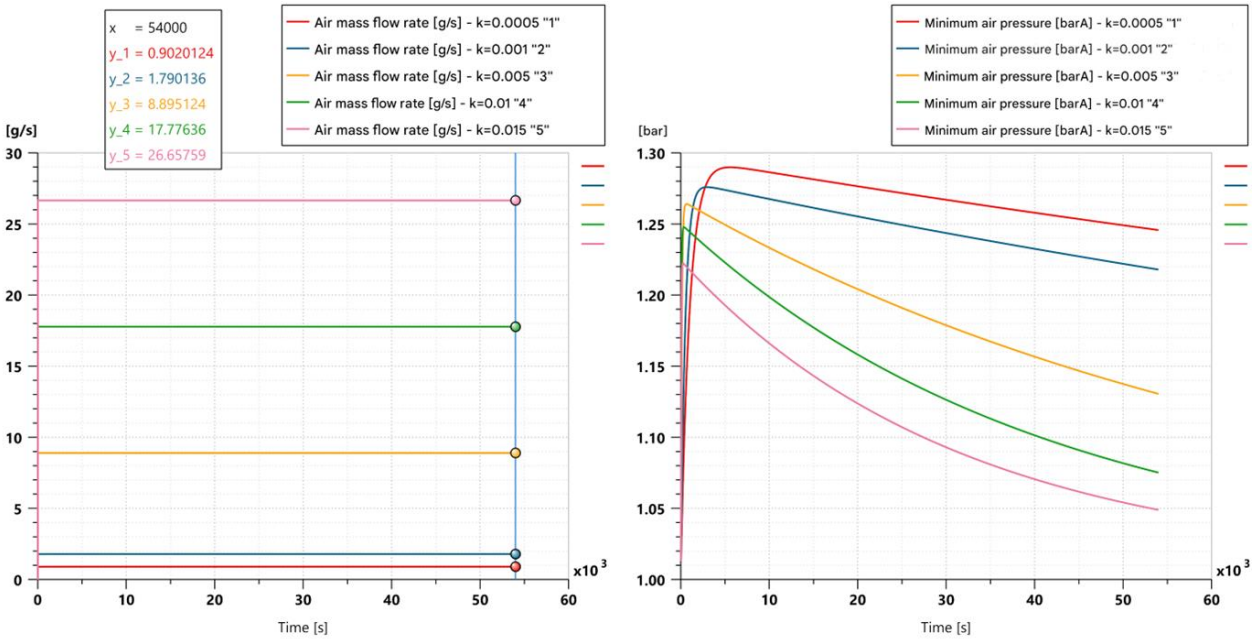

Fig. 5. Evolution of pneumatic parameters

The values are ranging from 0.9 g/s for the lowest volumetric flow rate to 26.6 g/s for the highest flow rate. The pump discharge pressure curves demonstrate minimal variation over time, with all curves remaining within a very narrow range of 1.0195 to 1.02 bar, indicating minimal head losses

in the hydraulic network and confirming the hydraulic design efficiency. The minimum air pressure figure reveals a distinct dynamic behavior, showing an initial pressure increase at system startup followed by gradual decline due to air heating and expansion, with higher air flow rates experiencing more pronounced pressure decreases, suggesting important considerations for fan selection and system design. The hydraulic characteristics of the system reveal important insights regarding flow stability and pressure dynamics. The mass flow rate of the heat transfer fluid figure shows that the mass flow rate remains approximately constant over time for all five simulated cases, with slight increases observed throughout the simulation period due to temperature variations.

The dynamic evolution of the convection coefficient and associated heat losses presented in Fig. 6 reveals critical thermodynamic behavior that warrants deeper theoretical consideration. The observed convection coefficient range (321-341 W/m²/K) aligns with established correlations for forced convection in serpentine tube configurations, though the noted instability at higher flow rates suggests transitional flow regime characteristics that merit further investigation through dimensionless analysis. The inverse relationship between airflow rate and heat loss magnitude, while consistent with Fourier's law of heat conduction, demonstrates a non-linear response that challenges conventional lumped parameter modeling approaches.

The observed thermal loss dynamics reflect complex interactions between the system's thermal inertia and the time-dependent boundary conditions. The minimal heat loss at elevated flow rates, despite the increased convective heat transfer surface activity, indicates a dominant influence of the temperature potential gradient as the primary driver of parasitic heat losses. This phenomenon suggests that conventional thermal insulation strategies may require re-evaluation when applied to systems with dynamic operational profiles.

From a system optimization perspective, the heat loss profile reveals a critical trade-off between thermal storage utilization efficiency and energy conservation.

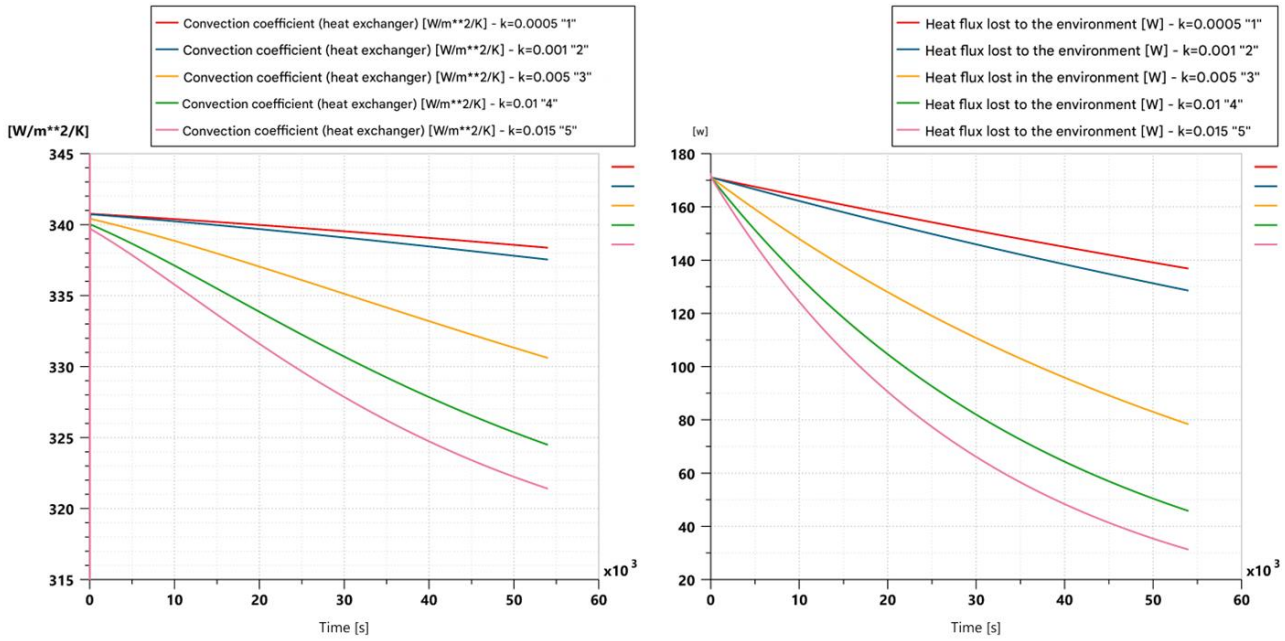

Fig. 6. Evolution of convection coefficient and heat losses

Prolonged exposure of thermal tank at high temperatures and at lower flow rates creates a significant energy loss, which cannot be fully compensated by the reduced convective losses during operational transitions. This observation has profound implications for the design of thermal storage systems in intermittent renewable energy applications.

The temporal evolution of the convection coefficient provides valuable information about the transient thermal behavior of the system, which could inform more sophisticated control algorithms. The stability of the coefficient at lower flow rates, in contrast to the increased variability at higher flow conditions, suggests potential opportunities for adaptive control strategies that could optimize the thermal extraction process while minimizing parasitic losses.
These observations highlight the need to consider second-law thermodynamics in the design of thermal energy storage systems for agricultural processing applications. The observed heat loss patterns indicate that conventional first-law efficiency values may be insufficient to capture the actual thermodynamic performance of such systems, especially during extended nighttime operation when the system operates solely on stored thermal energy.

4. Conclusions

Numerical simulation of the thermal module with water-air heat exchanger has successfully identified the optimal air flow rate for nighttime operation of the net-zero emission continuous dryer system.
The comparative analysis of 5 operational scenarios demonstrated that an air flow rate of 0.01m^3/s represents the ideal balance between sufficient thermal energy extraction from the storage system and maintenance of process parameters within critical limits for agricultural product drying. At this optimal flow rate, the drying chamber temperature remained at 49.28°C after 10 hours of operation, the relative humidity was consistently maintained below 10%, and the heat exchanger efficiency exceeded the 90% threshold throughout the entire process duration.
These results confirm the technical feasibility of continuous nighttime operation for solar drying systems through the integration of thermal storage and optimized heat exchange processes.
This research provides a scientific foundation for the design and implementation of net-zero emission agricultural drying technologies that align with European Green Deal objectives and renewable energy directives, offering a practical solution for reducing the carbon footprint of the agricultural processing sector while enhancing food security through effective post-harvest preservation.
The optimized thermal module design represents a significant advancement toward sustainable food processing systems with full operational autonomy regardless of meteorological conditions.

Acknowledgment

This work was supported by a grant of the Ministry of Research, Innovation and Digitization, CCCDI - UEFISCDI, project number PN-IV-P7-7.1-PTE-2024-0039, within PNCDI IV.

References

[1] Panwar, N. L., S. C. Kaushik, and Surendra Kothari. "Role of renewable energy sources in environmental protection: A review." *Renewable and Sustainable Energy Reviews* 15, no. 3 (April 2011): 1513-24. DOI: https://doi.org/10.1016/j.rser.2010.11.037.
[2] IPCC. “Global Warming of 1.5°C. An IPCC Special Report on the impacts of global warming of 1.5°C above pre-industrial levels.” Geneva, World Meteorological Organization, 2018. https://www.ipcc.ch/site/assets/uploads/sites/2/2022/06/SR15_Full_Report_HR.pdf.
[3] European Commission. “The European Green Deal. COM (2019) 640 final.” Brussels, European Commission, 2019. https://www.eea.europa.eu/policy-documents/com-2019-640-final.
[4] European Parliament and Council. "Directive (EU) 2018/2001 of the European Parliament and of the Council of 11 December 2018 on the promotion of the use of energy from renewable sources." Official Journal of the European Union L 328 (December 2018): 82-209. https://eur-lex.europa.eu/eli/dir/2018/2001/corrigendum/2020-09-25/oj/eng.
[5] FAO. “The State of Food and Agriculture 2021. Making agrifood systems more resilient to shocks and stresses.” Rome, Food and Agriculture Organization of the United Nations, 2021. DOI: https://doi.org/10.4060/cb4476en.
[6] Mujumdar, Arun S. *Handbook of Industrial Drying*. 4th ed. Boca Raton, CRC Press, 2014. DOI: https://doi.org/10.1201/b17208.

[7] El-Sebaii, A. A., and S. M. Shalaby. "Solar drying of agricultural products: A review." *Renewable and Sustainable Energy Reviews* 16, no. 1 (January 2012): 37-43. DOI: https://doi.org/10.1016/j.rser.2011.07.134.
[8] Sharma, Atul, V.V. Tyagi, C.R. Chen, and D. Buddhi. "Review on thermal energy storage with phase change materials and applications." *Renewable and Sustainable Energy Reviews* 13, no. 2 (February 2009): 318-45. DOI: https://doi.org/10.1016/j.rser.2007.10.005.
[9] Jay, James M., Martin J. Loessner, and David A. Golden. *Modern Food Microbiology*. 7th ed. New York, Springer, 2005. DOI: https://doi.org/10.1007/b100840.
[10] Versteeg, Henk Kaarle, and Weeratunge Malalasekera. *An Introduction to Computational Fluid Dynamics: The Finite Volume Method*. 2nd ed. Pearson Education, 2007. ISBN 9780131274983.
[11] Institutul Național de Statistică. "Anuarul Statistic al României 2023 / Romanian Statistical Yearbook 2023." Bucharest, Institutul Național de Statistică, 2023. https://insse.ro/cms/sites/default/files/field/publicatii/anuarul_statistic_al_romaniei_carte_ed_2023-en.pdf
[12] Dincer, Ibrahim. "Renewable energy and sustainable development: a crucial review." *Renewable and Sustainable Energy Reviews* 4, no. 2 (June 2000): 157-75. DOI: https://doi.org/10.1016/S1364-0321(99)00011-8.

ISSN 1454 - 8003
Proceedings of 2025 International Conference on Hydraulics and Pneumatics - HERVEX
November 19-21, Băile Govora, Romania

APPLICATIONS OF TEXTURED SURFACES TO HYDRAULIC SYSTEM COMPONENTS: A REVIEW

Geanina-Mihaela ANDRONACHE (MATEESCU)[1], Alexandru Valentin RĂDULESCU[1], Cătălin DUMITRESCU[2], Andreea Mirela TELEAȘĂ[1]

[1] Department of Machine Elements and Tribology, Faculty of Mechanical Engineering and Mechatronics, National University of Science and Technology POLITEHNICA Bucharest, Bucharest, Romania, geanina.mateescu@upb.ro

[2]The Hydraulics and Pneumatics Research, Institute INOE 2000-IHP, Bucharest, Romania, dumitrescu.ihp@fluidas.ro

Abstract: *This paper presents an analysis of how micro-textures created on the surfaces of various hydraulic components influence friction, wear, lubrication and energy efficiency. The first part describes the main causes of failure of hydraulic components, such as abrasion, corrosion, material fatigue and wear of sealing elements. Subsequently, recent results from the specialized literature on the performance of textured components are synthesized, including experimental studies and numerical models that highlight the role of micro-cavities in capturing wear particles, maintaining the lubricating film and reducing the friction coefficient.*

Keywords: *Hydraulic applications, surface texturing, tribological performance, abrasive wear, friction, stress corrosion cracking*

1. Introduction

Hydraulic systems are used to transfer energy by converting mechanical energy into hydraulic energy and then back into mechanical energy. The main reason for converting mechanical energy into fluid energy is the convenience of easily transferring it. The transmission and control of power by means of pressurized fluid is widely used in all branches of industry and mobile equipment [1].
Hydraulic systems are made up of several components, as follows: hydraulic cylinder, piston and fluid flow pipes, sealing systems and guide elements, hydraulic pump, pressure regulator, control valve, filters and storage tank [2], [3].
Hydraulic cylinders are actuator components that convert hydraulic energy into mechanical energy and generate linear motion through pressure exerted on the surface of the moving piston [4].
The piston is the component of the hydraulic cylinder composed of piston body, rod, connectors and other components. The connection between the piston and the piston rod is made depending on the working pressure, installation and operating conditions of the system. The piston has the role of separating two working chambers in a cylinder and preventing the flow of working fluid between the two chambers [5, 6].
The guide elements ensure the centring of the piston in the cylinder. They transmit lateral forces and absorb radial loads [7].
Seals prevent the flow of hydraulic fluid both between the cylinder chambers and to the outside and prevent the transfer of oil contamination from the outside to the inside of the cylinder but also contribute to increasing the service life of components. Seals are of great importance for the efficiency of hydraulic systems, because they prevent lubricant losses. If oil leaks occur, then pressure losses also occur in the hydraulic system and thus, it loses its efficiency [4, 7, 8, 9].
The hydraulic pump is the component of the system that converts mechanical energy into hydraulic energy. It is responsible for creating hydraulic pressure by pumping fluid from the reservoir into the system [10].
A directional control valve is a component of a hydraulic system used to control the distribution of power by directing hydraulic fluid, allowing it to flow in one direction only. This valve is used to start, stop, and change the direction of the flow of lubricant [2].

The pressure regulator/pressure control valve is an essential component of a hydraulic system, as it protects the hydraulic components from excessive pressure and helps the system to function optimally. The main role of this component is to limit the pressure in the system within a specified range, usually the pressure regulator is closed and opens only when the pressure in the system exceeds the maximum preset value, directing the flow of lubricant from the pump back to the reservoir [2, 10].
Filters are components of a hydraulic system that purify hydraulic fluid, being the most effective method against contamination [11].

2. Failures of hydraulic system components

The most common causes of failure of hydraulic components are abrasive wear, material fatigue and friction, but the most significant cause of damage to cylinders, pistons and piston rods can be corrosion. To prevent its occurrence, it is necessary to use corrosion-resistant materials or apply anti-corrosion coatings to the surface of these components. Faults in hydraulic cylinders can occur both from the manufacturing process and from the operating mode, since these components are used under high pressure conditions, in this case, material fatigue, corrosion and even fatigue cracking most often occur. Damaged parts of hydraulic cylinders are those that show cracks, cavities, deformations, seizing and can be corroded to varying degrees [7, 12, 13].
Piston rods are the elements that fail most often, as they are subject to high tensile and compressive stresses, but also to external factors such as temperature changes, precipitation, dust and dirt. In their work, Moreira D. et al. analysed the causes of failure of the piston rod of a hydraulic cylinder used to move a weir. The material used to make the piston rod was stainless steel. The results of the analysis showed that the crack (Fig. 1.) could have been caused by the low performance of the hydraulic component. This low performance could be due to improper heat treatment during the rod manufacturing process, which led to low material hardness, embrittlement at temperature, and stress corrosion cracking [14].

Fig. 1. Cracked surface of the piston rod, followed by component failure [14]

Sealing systems are important elements of hydraulic systems that are exposed to external factors, due to which failures such as: swelling, thermal degradation, deformation and wear can occur. Destruction of sealing systems leads to fluid leakage (loss of tightness) and even failure of the entire hydraulic system [7].

In the work of J. Bae and K.H. Chung [15] three situations of contact between seals and hydraulic cylinders were studied. For the three situations, a hydraulic seal made of a polyurethane elastomer was used as the material pair, and the counter material of the hydraulic cylinder was galvanized stainless steel with chromium. The lubricant used was ISO VG 46 under several conditions, one was a new lubricant, the second was worn for 1000 hours, and the third was the new lubricant in which 1 μm aluminium oxide particles were introduced to accelerate abrasive wear. The first situation was the study of three polyurethane rings obtained from an excavator after being used for 26, 11 and 10 months, during which they operated for 2989, 955 and 632 hours. The lubricant introduced was a new lubricant, but its change at a certain time interval could not be monitored. The hydraulic pressure at which it worked was between 0 and 22 MPa, with a sliding speed from 0 to several hundred mm/s, at a maximum stroke of the pistons of 850 mm in operation. Fig. 2. shows photographs of the polyurethane rings after operation.

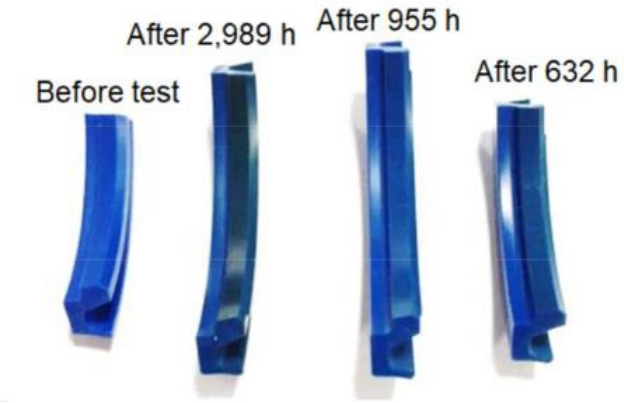

Fig. 2. O-rings before testing, after 2989, 955 and 632 hours [15]

The second set of tests was performed on a hydraulic seal test stand shown in Fig. 3. The hydraulic pressure during one cycle varied from 0 to 22 MPa. The maximum sliding speed was 180 mm/s at the mid-section of the hydraulic cylinder when the hydraulic pressure was 22 MPa. The temperature was set to 100°C. These conditions are like the harsh conditions experienced in the field. The test stroke was set to 200 mm. Four polyurethane rings were tested with a new lubricant, and the test times were 694, 726, 909, and 941 hours, which corresponded to sliding distances of 250, 261, 327, and 339 km, respectively.

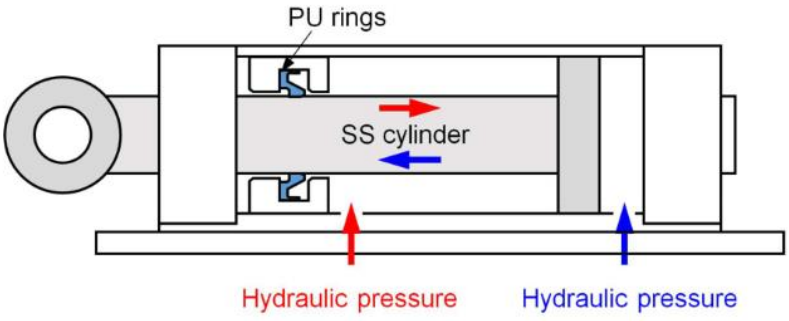

Fig. 3. Hydraulic seal tester [15]

Fig. 4. shows photographs of the specimens obtained from the polyurethane rings after 694, 726, 909 and 941 hours of testing. As can be seen from the images, all the specimens proved to be significantly discolored after testing, the causes being due to the repetitive translational motion, high pressure and high temperatures.

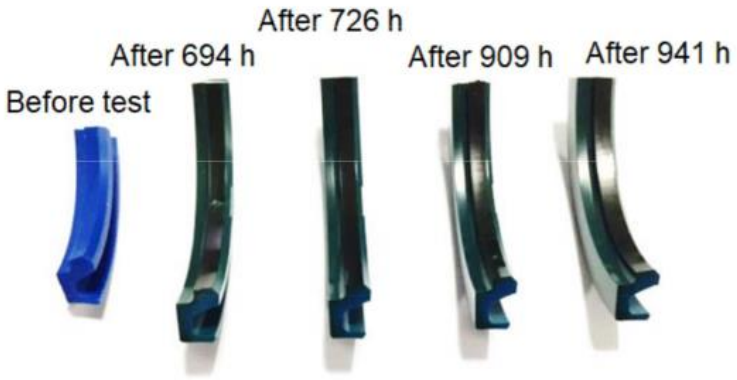

Fig. 4. Specimens after 694, 726, 909 and 941 hours of testing [15]

The third set of tests was performed using a tribometer exemplified in Fig. 5. Given that the lubrication state of a ring can vary from boundary lubrication to mixed lubrication, it is considered that the normal force and sliding speed can change the lubrication states during the test. The wear characteristics can be influenced by the interaction of particles and viscoelastic behavior under mixed or elasto-hydrodynamic lubrication conditions. The normal force was 200 N, corresponding to a contact pressure of approximately 10 MPa. This pressure was comparable to the average hydraulic pressure applied to the polyurethane rings during operation in service and during the test on the hydraulic seal tester.

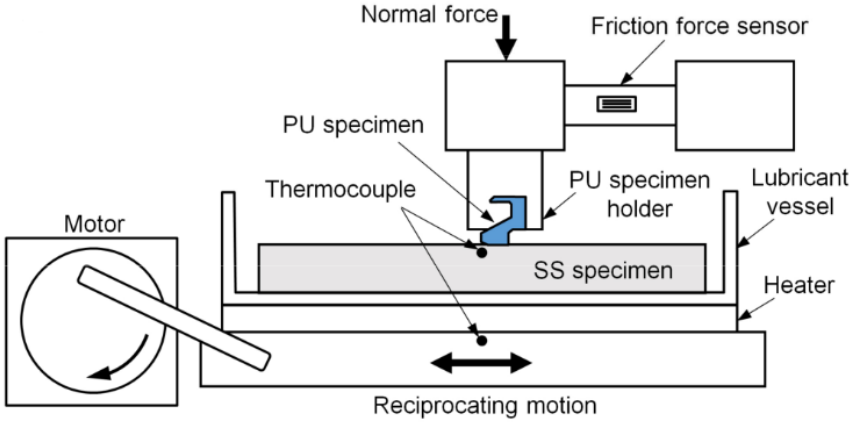

Fig. 5. Tribometer used for pin-on-disk tests [15]

Different from the polyurethane specimens obtained in the first two tests, in the case of the pin-on-plate tests, no significant discoloration was observed, probably due to the shorter testing time. The microscopic images of the sealing surfaces of the specimens for the tribometer tests, using three different lubricants, are presented in Fig. 6. The formation of scratches and grooves in the sliding direction can be clearly observed on all sealing surfaces, as seen in the high magnification images in the figure, indicating that the main wear mechanism observed in the field was reproduced using the pin-on-plate tests. In the case of the polyurethane specimens tested with lubricant B, relatively

large scratches were observed on the sealing surface. The formation of scratches on the sealing surface was highest for the specimens tested with lubricant C. The particles in lubricant B were probably generated by the hydraulic system or the environment; therefore, they were softer than alumina. In addition, the number of alumina particles in lubricant C was higher than the number of particles in lubricant B.

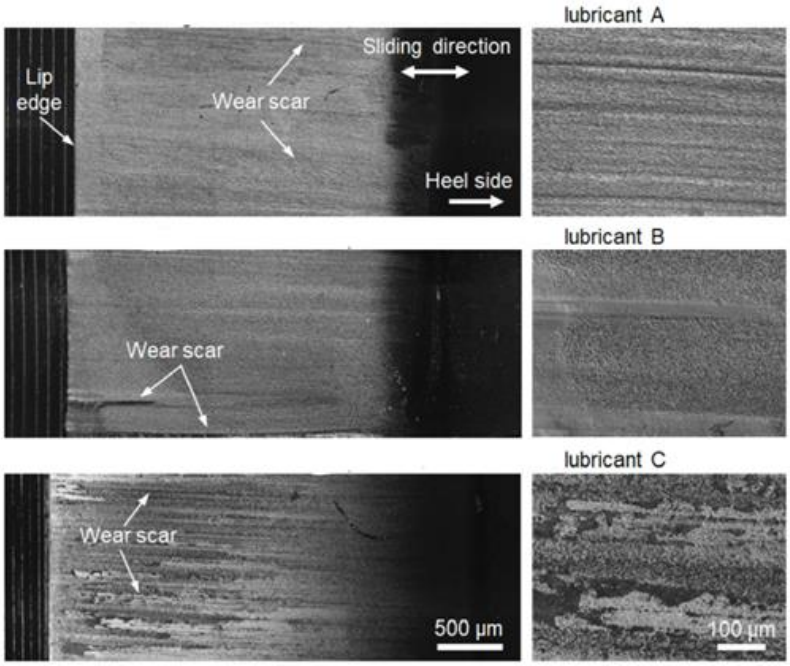

Fig. 6. Microscope images for tests performed with a tribometer [15]

The results showed that wear is mainly caused by abrasion, influenced by pressure, temperature, and lubricant contamination. Scratches, grooves, and plastic deformation were observed on the sealing surfaces under the microscope. Contaminated lubricant caused the most wear and increased the friction coefficient.

3. Applications of textured surfaces to hydraulic system components

Surface texturing consists of modifying the surface to create a micro-cavity composed of uniformly distributed asperities with a controlled geometry. Typically, these micro-cavities are created to improve the tribological properties of the systems. The situations for which micro-cavities are created are quite varied, such as dry friction sliding, hydrodynamic lubrication, elasto-hydrodynamic lubrication or even mixed lubrication [16, 17].
In recent years, research has been carried out on textured surfaces with micro-cavities of different sizes and geometries, made on hydraulic components, regarding tribological applications in the field of hydraulic installations.

A recent study [18] was conducted to improve the tribological performance of two materials found in the sealing area of hydraulic cylinders, polytetrafluoroethylene PTFE and 40# steel (AISI 1040), under fully lubricated conditions, using laser texturing technology to create micro-cavities on the surface of the steel discs. In this article, the authors aimed to optimize the parameters of the textured surface through repeated wear tests to reduce the coefficient of friction and wear between the two surfaces using anti-wear hydraulic fluid for fully lubricated components. The 40# steel discs were made with a diameter of 63 mm and a thickness of 5 mm, the material having a surface hardness of HB114, and their texturing was performed with laser technology (LST). It was

necessary to make a hole with a diameter of 10 mm and an eccentricity of 7 mm to prevent the automatic rotation of the discs during the wear tests (Fig. 7. a) and b). The upper surfaces of the discs were polished with silicon carbide paper, and subsequently the surface roughness was measured using a profilometer, resulting in a surface roughness of approximately 0.8 μm. The rings were made of polytetrafluoroethylene (Fig. 7. a) and d) with an inner diameter of 35 mm, an outer diameter of 47 mm and a thickness of 15 mm. Also, in the case of the rings, it was necessary to polish the inner surface, resulting in a surface roughness of 1.1 μm. The texturing on the contact surface of the steel discs was performed with a fiber optic laser, for different diameters (200, 250 and 300 μm) and depths (5, 15 and 25 μm) of micro-cavities distributed uniformly around the circumference of the disc at an angle of 2.5° (Fig. 7. e). Before the texturing process the steel discs were cleaned with ultrasound, and after the texturing process the surface had to be repolished.

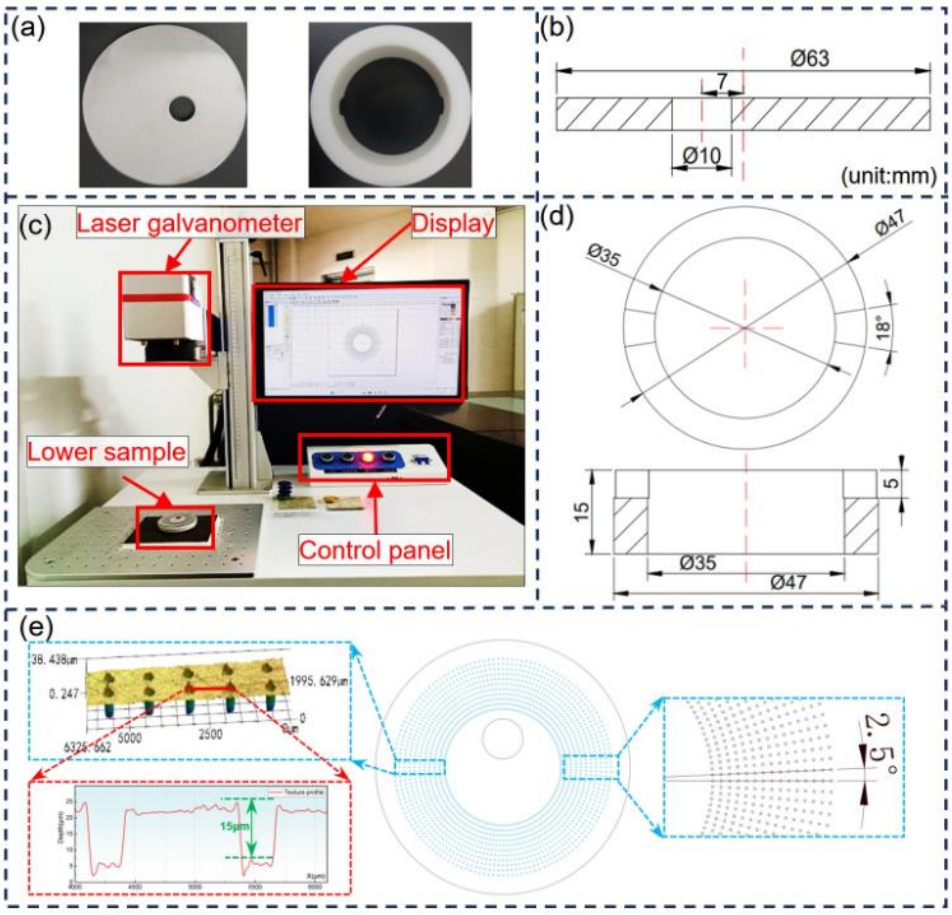

Fig. 7. Steel and PTFE components and the Laser used for surface texturing [18]

To perform tribological tests and study the sliding friction behavior of steel discs and PTFE rings, a vertical tribometer with a pin-on-disk configuration was used, shown in Fig. 8.: 1− upper device; 2− upper sample (PTFE ring); 3− lower sample (40# steel disc); 4− oil deflector; 5− lower device; 6− loading flange. Considering the operating parameters under normal working conditions applied to hydraulic cylinders, such as hydraulic system pressure less than or equal to 25 MPa and seal movement speed less than or equal to 3 m/s, the test parameters on the stand were chosen as: vertical external load of 1000 N, rotation speed of 200 rpm and test time of 2400 s, resulting in a sliding distance of 1 km. Before testing, a quantity of 25 ml of hydraulic lubricant was added to the lower device of the tribometer to completely submerge the disc. To obtain realistic results and minimize errors, each test was repeated three times, and the studied components were polished after each test.

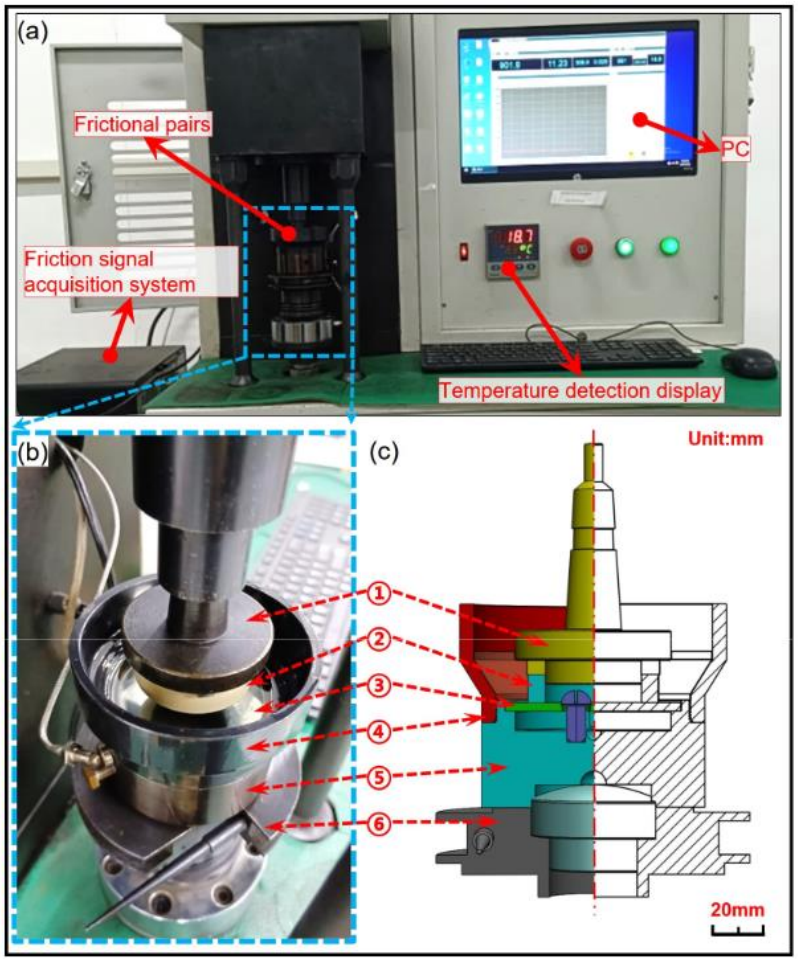

Fig. 8. Test stand - vertical tribometer [18]

The tests yielded results regarding the friction coefficient, which was significantly reduced due to the existence of micro-cavities on the surface of the discs, this result being important for improving the dynamic performance and lifespan of hydraulic cylinders. The wear losses of PTFE rings and 40# steel discs decreased by 91.8% and 30.3%, respectively, indicating that the micro-cavity parameters significantly increase wear resistance. It was concluded that this research and the results obtained are optimal for improving the tribological performance of seals, which can be used in hydraulic cylinders, and the surface texturing contributed to the capture of wear particles, preventing excessive abrasion and retaining lubricants, thus acting as small oil reservoirs and creating a hydrodynamic micro-bearing effect.

Another research on improving tribological conditions in hydraulic components that have textured surfaces is [19] where M. Gadari and M. Hajjam, analyze the effect of using a grooved rod on the friction force in a U-cup hydraulic seal, taking into account the roughness of the seal edge. U-cup rod seals (Fig. 9.) are often used in hydraulic systems because they operate under severe conditions of high temperatures and pressures and must prevent leakage from the system and the ingress of dirt from outside.

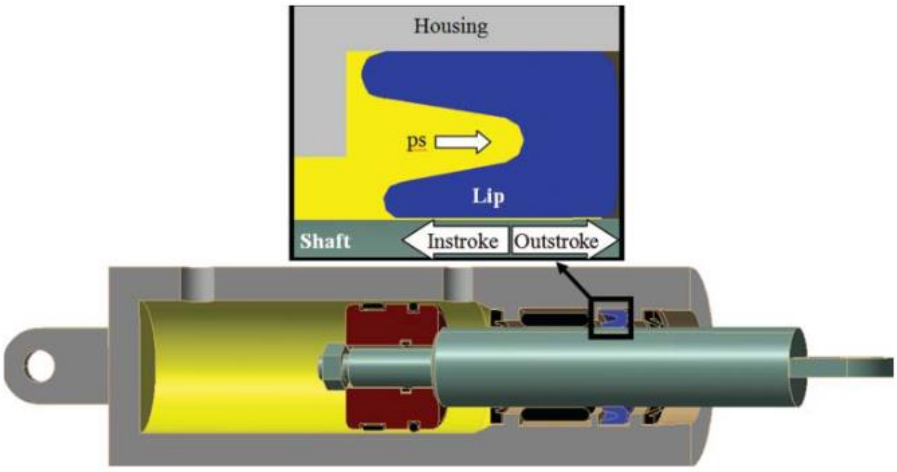

Fig. 9. Hydraulic cylinder with U-type rod seal [19]

Research has been carried out that analyzed the influence of surface roughness and different lubrication models, so starting from these, the authors of this article have developed a one-dimensional elasto-hydro-dynamic model to analyze the tribological behavior of seals. This model aims to analyze the interaction between the lubricant and the elastic deformation of the seal edge, taking into consideration the roughness of the rod and the seal edge and comparing the results obtained with the inverse hydrodynamic lubrication (IHL) model and with existing experimental data. Fig. 10. highlights the piston rod seal and the sealing area, for which it is desired to determine the hydrodynamic pressure, the distribution of the lubricant film thickness and the friction over the contact width between the two components, the structural analysis of the model where it was necessary to simulate the seal assembly and calculate the static contact pressure distribution.

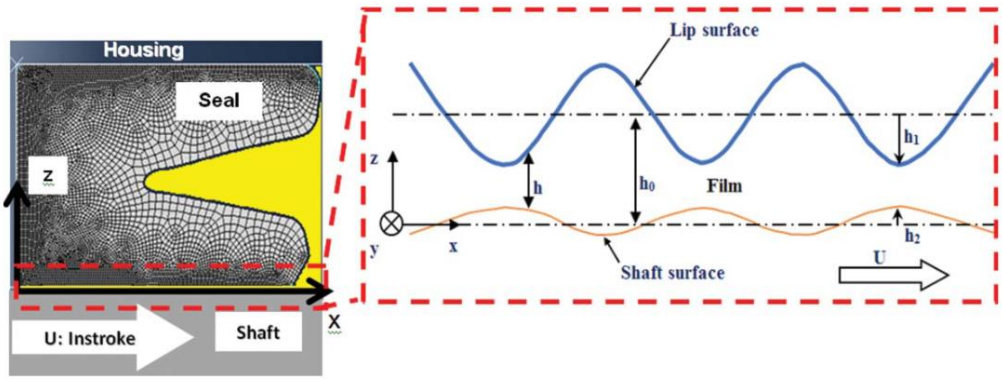

Fig. 10. U-type seal mounted on the stem [19]

Three types of grooves on the rod surface were tested and compared, shown in Fig. 11., SH#1 with rectangular grooves, SH#2 with asymmetrical grooves inclined towards the fluid pressure side and SH#3 with asymmetrical grooves inclined towards the air pressure side. It was found from the tests that the SH#3 surface with asymmetrical profile contributes to complete lubrication and significantly reduces the friction force compared to other surfaces.

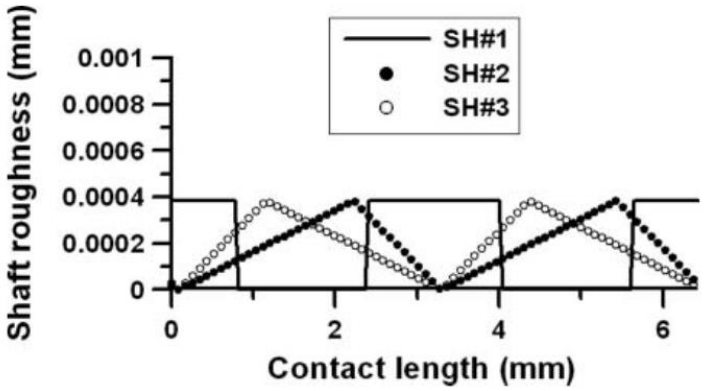

Fig. 11. Profile of the rod grooves [19]

The results of the obtained model were compared with experiments carried out by other researchers, and the difference between the numerical simulations and the experimental data was approximately 7%, thus confirming the accuracy of the model compared to the results obtained with the inverse hydrodynamic lubrication (IHL) model. It was observed that the roughness of the rod significantly influences the friction force and the power loss due to the hydrodynamic pressure generated by the rod's roughness, which increases the thickness of the lubricant film, therefore the roughness must be considered to obtain realistic results. At the same time, it was found that a greater depth of the grooves reduces the friction and power losses in the system, while a higher density can lead to increased friction.

Swash plate axial piston pumps are frequently used in hydraulic installations, as they have a simple and compact construction. These pumps have three lubrication interfaces: the piston-cylinder interface, the swash plate interface and the cylinder block-valve interface. Thus, starting from these aspects, the authors of the paper [20] investigate how the textured surface of the valve plate influences the tribological performance of the interface between the cylinder block and the valve plate in an axial piston pump. This research includes both the development of a mathematical model and numerical and experimental simulations to analyze the effect of texturing on the lubricant film and fluid leakage. The cylinder block has relative rotational movement on the valve plate, having the task of adjusting its position to take on the external load by changing the pressure area in the lubricant film. The structure of the cylinder block valve interface is shown in Fig. 12., consisting of the cylinder block, piston, valve plate and lubricant film.

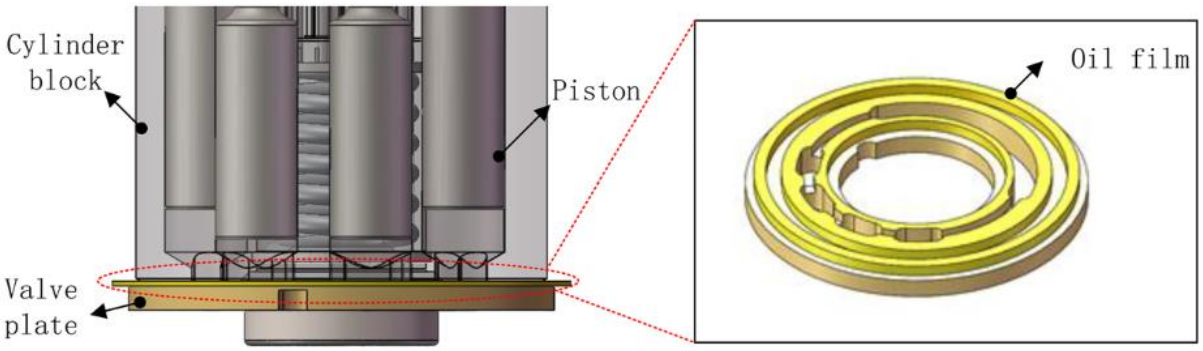

Fig. 12. Interface structure between cylinder block and valve plate [20]

In this study, the surface exploration was carried out by regularly arranging microcavities on the surface of the valve plate, as shown in Fig. 13. The parameter values used for this study are cylinder block radius of 45 mm, valve plate diameter of 88 mm, microcavity depth of 30 μm, and microcavity radius of 50, 100, 150, and 200 μm Fig. 14. To investigate the influence of microcavities on the lubrication mode, the authors considered equations for lubricant film thickness, pressure distribution, and flow leakage, and developed a mathematical model based on them.

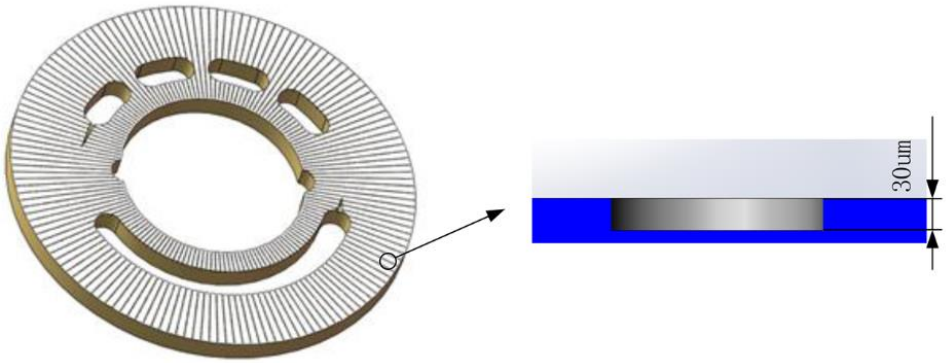

Fig. 13. Valve plate model with textured surface [20]

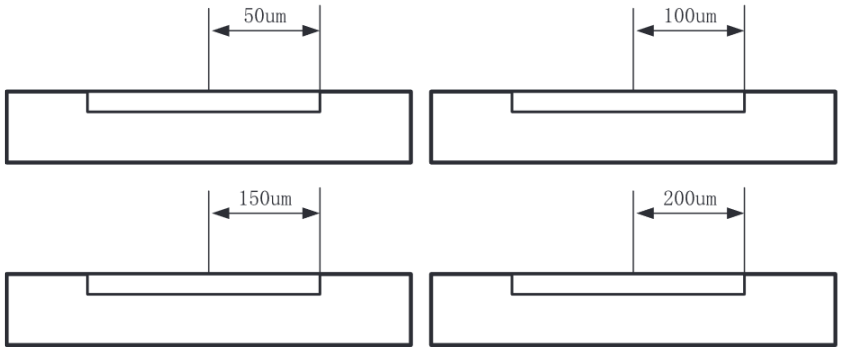

Fig. 14. Micro-cavity radii [20]

The numerical simulation part was performed for all four dimensions of the micro-cavities at a pump rotation speed of 2000 rpm, using calculation methods for pressure distribution and leakage flow. The simulation results showed that the pressure distribution is influenced by the size of the micro-cavities and increases with it. It was observed that when the radius of the micro-cavities increased from 50 μm to 100 μm, the pressure increased fourfold. Another result obtained from the numerical simulation showed that the leakage flow of the lubricant is directly proportional to the size of the micro-cavities, and the thickness of the lubricant film was influenced by the position in the interface, having lower values in the suction zone and higher values in the discharge zone. Following simulations and their analysis, it was found that micro-cavities with the smallest radius (50 μm) reduce lubricant leakage and provide good lubrication, being the optimal texturing option for this application.
For the experimental part, a test stand was created (Fig. 15.) consisting of a pump set at 2000 rpm, a hydraulic motor, a coupling and a torque sensor for measuring friction resistance, sensors for measuring pressure, lubricant film thickness and leakage flow rate.

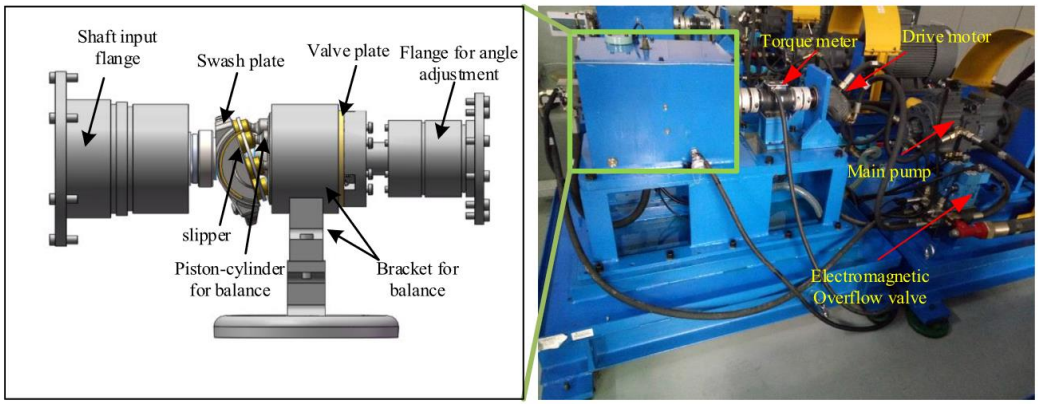

Fig. 15. Experimental test stand [20]

For testing the four micro-cavity sizes, the maximum applied pressure was between 6 and 14 MPa and a standard hydraulic oil was used. The experimental results were like simulation results, both for pressure and leakage flow. For example, the maximum pressure measured for the 100 μm micro-cavities was 9620 Pa, and in the case of leakage flow for the 50 μm texture size, the leakage was 0.0521 mm^3/s and for the 200 μm micro-cavities, the leakage flow was 0.7036 mm^3/s, which confirmed the increase in leakage flow with increasing texture size. Thus, it was concluded that texturing the valve plate significantly reduces lubricant leakage, the experimental results validating the simulation results, and the optimal texturing variant is that micro-cavities with a size of 50 μm, as it offers the best transmission efficiency, balances lubrication and reduces lubricant losses.

4. Conclusions

Hydraulic systems with textured component surfaces are part of a new and highly interesting field.
Surface texturing is a modern solution for creating tribological performance of components used in hydraulic systems.
Research in this field shows that surface texturing improves lubrication, reduces friction, and increases the service life of components and the entire system.
Studies have shown that the use of micro-textures on the surfaces of hydraulic components can significantly improve energy efficiency, lubrication performance, and system durability.

References

[1] Khayal, O. M. E. S., and S. A. Burma. Study of Failure in Hydraulic Systems (Case study of machinery used in local gold mining). Master's thesis. Nile Valley University, 2014.
[2] Khayal, O. M. E. S. "Introduction to hydraulic systems." In *Hydraulic Systems*, 2017.
[3] Khandare, Y., R. Badhe, A. Belkhode, T. Dhakne, and Dr. S. P. Jhole. "Overview of Hydraulic Power Packs: Components, Functionality, and Industrial Applications." *IJRASET Journal for Research in Applied Science and Engineering Technology* 12, no. 12 (December 2024): 1067–1072.
[4] Merkle, D., B. Schrader, and M. Thomes. *Hydraulics, Basic Level* (Textbook). Denkendorf/Germany, 2003.
[5] Skowrońska, J., J. Zaczyński, A. Kosucki, and Ł. Stawiński. "Modern Materials and Surface Modification Methods Used in the Manufacture of Hydraulic Actuators." Paper presented at the International Scientific-Technical Conference on Hydraulic and Pneumatic Drives and Control NSHP 2020, Staniszow, Poland, October 21-23, 2020. In Stryczek, J., and U. Warzyńska (eds.). *Advances in Hydraulic and Pneumatic Drives and Control* 2020 (2021): 427–439.
[6] Luo, P., J. Hu, and S. Tan. "Design and Realization of Hydraulic Cylinder." *Region - Water Conservancy* 1, no. 1 (September 2018): 27-34.
[7] Skowrońska, J., A. Kosucki, and Ł. Stawiński. "Overview of Materials Used for the Basic Elements of Hydraulic Actuators and Sealing Systems and Their Surfaces Modification Methods." *Materials* 14, no. 6 (March 2021): 1422.
[8] Trelleborg Sealing Solutions. "Hydraulic Seals – Linear, Rod seals, Piston seals". April 2007.

[9] Nikas, G. K. "Research on the Tribology of Hydraulic Reciprocating Seals." In *Tribology Research Trends*. London, Nova Science, 2008.
[10] Yuken Kogyo Co., Ltd. *Basic hydraulics and components* (Original Japanese edition Pub.JS-100-2: Jan. 2005). Tokyo, 2006.
[11] Ahmed, S. M. "Study on the Basic Components of Hydraulic Systems." *International Journal of Engineering Trends and Technology (IJETT)* 39, no. 5 (September 2016): 267–273.
[12] Kowalski, K., and T. Zloto. "Exploitation and Repair of Hydraulic Cylinders Used in Mobile Machinery." *TEKA. Commission of Motorization and Energetics in Agriculture* 14, no. 4 (2014): 53–58.
[13] Pan, Q., Y. Zeng, Y. Li, X. Jiang, and M. Huang. "Experimental investigation of friction behaviors for double-acting hydraulic actuators with different reciprocating seals." *Tribology International* 153 (January 2021): 106506.
[14] Moreira, D. C., H. C. Furtado, J. S. Buarque, B. R. Cardoso, B. Merlin, and D. D. C. Moreira. "Failure analysis of AISI 410 stainless-steel piston rod in spillway floodgate." *Engineering Failure Analysis* 97 (March 2019): 506–517.
[15] Bae, J., and K.-H. Chung. "Accelerated wear testing of polyurethane hydraulic seal." *Polymer Testing* 63 (October 2017): 110–117.
[16] Costa, H., and I. Hutchings. "Some innovative surface texturing techniques for tribological purposes." *Proceedings of the Institution of Mechanical Engineers, Part J: Journal of Engineering Tribology* 229, no. 4 (April 2015): 429–448.
[17] Grützmacher, P. G., F. J. Profito, and A. Rosenkranz. "Multi-Scale Surface Texturing in Tribology—Current Knowledge and Future Perspectives." *Lubricants* 7, no. 11 (October 2019): 95.
[18] Long, R., et al. "From Experimentation to Optimization: Surface Micro-Texturing for Low-Friction and Durable PTFE–Steel Interfaces Under Full Film Lubrication." *Polymers* 16, no. 24 (December 2024): 3505.
[19] Gadari, M. E., and M. Hajjam. "Effect of the Grooved Rod on the Friction Force of U-Cup Hydraulic Rod Seal with Rough Lip." *Tribology Transactions* 61, no. 4 (July 2018): 661–670.
[20] Lv, Q., D. Wang, S. E, H. Chen, and B. Hu. "Study on the effects of the textured surface to improve the performance of cylinder block/valve plate interfaces." *AIP Advances* 9, no. 4 (April 2019): 045128.

ISSN 1454 - 8003
Proceedings of 2025 International Conference on Hydraulics and Pneumatics - HERVEX
November 19-21, Băile Govora, Romania

CONSIDERATIONS ON IMPROVING THE EFFICIENCY OF IRRIGATION SYSTEMS BY USING OF ELECTRIC PUMPS WITH ADJUSTABLE ROTATIONAL SPEED

Teodor Costinel POPESCU[1,*], Alina Iolanda POPESCU[1], Radu CIUPERCĂ[2]

[1] National Institute of Research & Development for Optoelectronics/ INOE 2000 – Subsidiary Hydraulics and Pneumatics Research Institute / IHP, Bucharest, Romania

[2] The National Institute of Research – Development for Machines and Installations Designed for Agriculture and Food Industry – INMA Bucharest, Romania

* popescu.ihp@fluidas.ro

Abstract: *Water consumption management in modern agriculture influences crop yields and the long-term sustainability of traditional irrigation systems. These contain pumps driven by fixed-rotational speed electro motors or fixed-rotational speed heat engines, powered by gasoline or diesel. Traditional solutions, which ensure the basic supply of water for irrigation, have the following disadvantages: high energy consumption, limited adaptability, frequent wear and tear of irrigation equipment. For agricultural areas that face seasonal variations in water demand, a fixed-rotational speed pump cannot effectively regulate its power, which leads to energy waste and a reduction in the life of the irrigation equipment.*
These disadvantages can be eliminated by controlling the frequency and voltage supplied to the electric motor driving the pump. In this way, the pump rotational speed can be adjusted in real time, so that the water flow supplied corresponds to the actual needs of the irrigated area. The adjustable pump, driven by a variable frequency electric motor, reduces the energy consumption of the irrigation system in which it is integrated and allows precise irrigation programming, saving water resources.
The authors present the advantages of using adjustable pumps in agricultural irrigation systems and the schematic diagram of an experimental stand that demonstrates these advantages.

Keywords: *Water consumption management, adjustable pump, variable frequency electromotor, irrigation system*

1. Introduction

Variable rotational speed pumps (also known as inverter or variable rotational speed drives – VFD) are playing an increasingly important role in modern irrigation systems, due to the technical, economic and sustainability advantages they provide. They ensure:
- *energy efficiency*, by adjusting the rotational speed according to the actual water demand, which reduces energy consumption and eliminates the high energy losses caused by constant operation at maximum power of fixed rotational speed pumps;
- *constant and stable pressure*, which is essential for correct water distribution in the irrigation process. Variable rotational speed pumps adapt immediately to changes in flow rate (opening or closing of irrigation sectors);
- *longer equipment life*. Sudden starts and stops of pumps are reduced, which means less mechanical and hydraulic shocks on pipes, sprinklers and solenoid valves. At the same time, wear on the drive motor and pump components is significantly reduced;
- *flexibility in operation.* The same irrigation system can serve different crops, with variable flow and pressure requirements. In this way, water resources are used more efficiently during periods of low consumption (partial watering, drip irrigation, etc.);
- *reduction of operating costs*. Energy bills are lower, maintenance and repair costs are reduced, the lifespan of the entire irrigation system increases.

2. The importance of variable frequency drive of electric pumps in irrigation systems

Variable frequency drives (VFDs) provide high-performance, energy-efficient electric motor control for a wide range of industrial [1] and agricultural applications. They allow precise rotational speed control of electric pumps, easy start/stop and significant energy savings. With nominal powers from 0.75kW to 500kW, they are ideal for pumps, fans, conveyors and automation systems.

By varying the frequency of the current, the VFD performs:

- *control of the increase or decrease of the pump motor rotational speed*, respectively controlling the water flow rate supplied;
- *regulation of voltage levels*, respectively optimizing the operation of the electric motor and preventing energy waste;
- *elimination of sudden surges* at start-up by gradually increasing/decreasing the voltage, a method that allows smooth acceleration, minimizing wear and protecting pipes from pressure shocks.

2.1 Variable Frequency Drive of Electric Pumps for Agricultural Irrigation

Variable frequency drive brings the following benefits to agricultural irrigation:

- *water efficiency irrigation water*: requirements fluctuate daily and seasonally. With a VFD, the rotational speed of the electric pump, and thus the flow rate delivered, can match crop requirements, avoiding excess water waste;
- *energy savings*: instead of operating at maximum capacity, the pump consumes only the amount of electricity needed, thus reducing operating costs and extending the life of the irrigation equipment;
- *system protection:* overheating, overcurrent and voltage fluctuations can damage pumps. VFDs integrate protection functions to ensure long-term stability.

Variable frequency electric pumps are essential for irrigation water distribution systems; by combining precise control of the electric motor with dedicated pump operation, water delivery can be optimized under various field conditions.

Energy efficiency and cost reduction are required by the constant maximum rotational speed of traditional electric pumps, consuming unnecessary energy even when water demand is low. A VFD electric pump adjusts the flow rate according to *soil moisture* and *crop requirements*, significantly reducing electricity bills. For farms that rely on *solar or hybrid energy systems*, VFD electric pumps perfectly align with variable energy inputs, ensuring uninterrupted irrigation.

Variable frequency electric pumps ensure the seasonal adaptability of the irrigation system. At the beginning of the planting season, when crops require less water, the pumps operate at reduced capacity, reducing unnecessary energy consumption. During hot and dry months, the system can increase production instantly, without overloading, ensuring peak water demand.

Water demand for irrigation is not constant. It changes with the season, time of day, and crop type. A VFD-controlled electric pump can automatically respond to these variations, *providing constant flow in drip irrigation, high-volume delivery for sprinklers, or controlled pressure for greenhouse systems*. This adaptability prevents both *over-* and *under-irrigation*, protecting crops and soil health.

Constant operation at high rotational speeds causes pumps and motors to wear out faster. By operating at variable rotational speeds, a VFD-controlled electric pump reduces mechanical stress, resulting in longer equipment life and lower maintenance costs. This translates into fewer repairs, less downtime, and higher productivity during critical periods of plant growth.

The smooth start and stop of VHD electric pumps prevent water hammer in pipes, protecting valves and pipe joints. When equipped with VFDs, electric motors are started and stopped smoothly, with gradual acceleration and deceleration, protecting irrigation infrastructure. Even when multiple sectors are opening or closing, VFD-controlled electric pumps maintain a constant pressure.

Solar integration: Many modern farms combine solar energy systems with VFD pumps. The adaptability of VFDs to power fluctuations makes them ideal for off-grid or hybrid energy applications.

Voltage stability: If local grids experience frequent fluctuations, a robust VFD with integrated protection functions is essential to prevent motor damage.

2.2 Practical applications in agriculture of VHD controlled electric pumps

The main practical applications in agriculture of VFD-controlled electric pumps are:
- *drip irrigation,* which provides precise water delivery at low pressure, optimized by VFD-controlled flow;
- *greenhouse irrigation*, which provides consistent water distribution for controlled environments. Controlled microclimates benefit from precise water dosing, specific to sensitive crops;
- *small-scale farm and orchard irrigation*, where pumps must adapt to fluctuating irrigation schedules;
- *large-scale field irrigation* with high-power VFD pumps, which can support water transport over long distances with stable pressure. Large fields benefit from uniform coverage, preventing dry areas and waterlogging. By aligning irrigation to the actual needs of crops, farmers ensure that they achieve *optimal soil moisture levels*, while conserving limited water resources. Over-irrigation not only wastes water, but can also damage soil structure and plant root systems. A VFD-controlled electric pump allows for precise water delivery and maintains stable pressure in drip lines, sprinklers, or pivot irrigation systems.

The correct selection of the VFD and electric pump required for a specific agricultural irrigation application is based on a clear assessment of: the *daily water* requirement; *the irrigation method* used; the available *water source*; *the flow rate and service pressure* required by the consumers of the irrigation system; *the distance and altitude of the consumer* furthest from the water source (the most disadvantaged consumer).

For modern farmers, a variable frequency electric pump is not only a technical upgrade but also a strategic investment, improving productivity while conserving vital resources.

For solar farms, VFD-equipped electric pumps offer unparalleled compatibility with fluctuating power availability. Farms that integrate solar panels with VFD electric pumps benefit from a more consistent and efficient use of renewable energy sources. This optimization leads to substantial savings; energy consumption is reduced by 20-40% compared to fixed-rotational speed pumping systems. *The evolution of agricultural irrigation is no longer about simply moving water from one place to another. Today, it is about delivering the right amount of water, at the right time, with maximum efficiency and reliability, and variable frequency drives (VFD) and VFD pumps make this possible. By adjusting motor rotational speed and pump performance, VFD technology allows irrigation systems to operate in harmony with field requirements in real time.*

3. Demonstration stand for testing a pumping group for agricultural irrigation

The authors propose to create a test stand for a pumping group intended for agricultural irrigation, consisting of two identical centrifugal electric pumps, coupled in parallel. One of the electric pumps is *fixed*, to ensure the *constant water needs* (*at low, medium and high loads*) of the irrigation system, and the other is *adjustable*, to ensure the water effectively distributed to the plants (*at low and medium loads*), during the irrigation process.

3.1 Basic scheme of the stand

The stand, with the schematic diagram in Figure 1, works as follows:
The electric pump **1** with adjustable flow, coupled in parallel with the electric pump **2** with fixed flow, sucks water from the tank **11**, equipped with the drain valve **13**, through the common collector **9**, and discharges water into the same tank through the common collector **10**. On the discharges of the two pumps, one-way valves **4** and **7** are provided, respectively, and on-off separation valves **3** and **5**, respectively **6** and **7** are provided on the suction/discharge pipes of the pumps. The load (required pressure) of the irrigation system is simulated with the control valve **12**, operated by the **SM** servomotor. The parameters measured during the experimental tests are: the pressures on the discharges of the two pumps, measured with the pressure transducers $\mathbf{T_{P1}}$ and $\mathbf{T_{P2}}$ and the

manometers **M_1** and **M_2**; the *flow rates* provided by the two pumps, measured with the flow rate transducers **T_{Q1}** and **T_{Q2}**, respectively; *the vibrations* of the two pumps, measured with the acceleration sensors **a_1**, **a_2**, mounted on the pump housings. The electrical and control cabinet **14**, in which the control module contains a programmable logic controller and a single-board computer, ensures: power supply to the motors of the electric pumps **1** and **2**; *control* of the frequency converter of the adjustable electric pump **1**; *control* of the valve servomotor **12**; acquisition of the hydraulic parameters (pressure and flow rate) of the two electric pumps and monitoring of their vibrations.

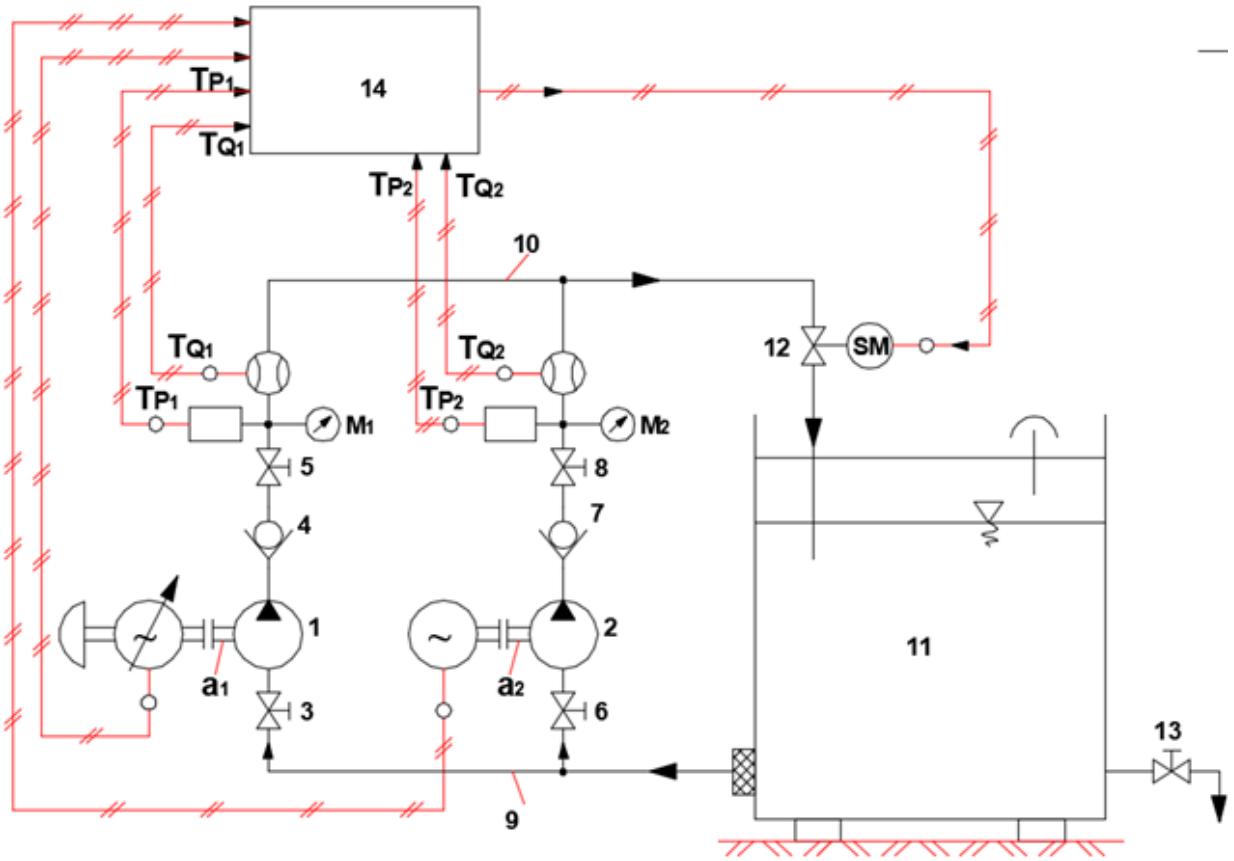

Fig. 1. Basic scheme of the stand

Minimal technical characteristics of the main components from the basic scheme of the stand are:
- for the electric pumps 1 and 2

Table 1: Flow rate Q and pumping height (according to technical data sheet of the electro pump [2])

Q (m^3/h)	0	1,5	3	6	9	12
Q (l/min)	0	25	50	100	150	200
H (m)	72	70	68	60	52	39

Suction nominal diameter *DN = 1 ¼"*; Discharge nominal diameter *DN = 1"*
Induction triphasic electrical engine for pump drive: 2 pols, 230/400 V, rotational speed n=2850 rev/min, nominal power = 4 kW, current intensity = 7A.
- for tank: volume = 1000 l; equipped with water filtration elements and filling cock /purge DN 25.
- for the variable frequency drive (variable rotational speed drive): Nominal supply voltage = 3x380...480 V - 15...10 %; Supply frequency = 50...60 Hz - 5...5 %; Engine power = 7,5 kW – normal usage; 5,5 kW – intense usage; communication port protocol Serial Modbus/RS485.

- for programmable automatic: Inputs number / Digital outputs = 24; Supply voltage = 24 V DC; Inputs module/Analog outputs = 2 pieces 2 x 4 - 8 analogue inputs, 2 x2 - 4 analogue outputs.
- for single board computer (Single Board Computer - SBC): Raspberry Pi 5/8GB; box Raspberry Pi 5 track DIN ABS; supplier 27W with USB-C for Raspberry Pi 5; battery RTC for Raspberry Pi 5; adaptor cable from Micro-HDMI to HDMI Black (A/M), 1 m; radiator case for Raspberry Pi 5 (black, with dual fan); Raspberry Pi Active Cooler; memory card SanDisk Extreme microSDXC 256GB,until at 190MB/s & 130MB/s Read/Write s A2 C10 V30 UHS-I U3.
- for pressure transducers: Measurement range = 0…10 bar; Supply voltage = 24 V DC; Current outputs = 4…20mA.
- for manometers: Measurement range = 0…10 bar; Dial diameter = 100 mm; Stainless steel case with glycerine (antivibration), radial (vertical mounting).
- for flow transducers: Measurement range = min 0,5 m³/h, max 18 m³/h; Supply voltage = 220 V AC, la 50 Hz; Maximum pressure =16 bar; Output voltage = 4…20 mA; Nominal diameter DN 25 mm; Communication protocol Modbus RTU / RS48.
- for accelerometers: supply = 1.71… 3.6 V; interface I2C (max. frequency 100KHz) and SPI (max. frequency 10MHz); automat standby function; it can be selected between ±2g/±4g/±8g/±16g.

3.2 Calculation of the collectors diameters and flow variation

For the pumping group made from two centrifugal pumps the collectors diameters and variations intervals of the flow are computed.

3.2.1 Diameters calculation

Both pumps extract water from the tank through the same suction collector and feed the tank through the same discharge collector. The collectors diameters of the pumping group formed by pumps coupled in parallel are calculated with the relation:

$$D = d \cdot \sqrt{n} \quad (1)$$

where: D = collectors diameters; d = individual pipe diameter (suction or discharge); n = number of pumps (here 2).
Suction collector: Individual pipe: 1¼" ≈ 32 mm
$D = 32 \cdot \sqrt{2} = 32 \cdot 1.41 = 45.12$ mm. **Recommended diameter**: DN50 mm (2")
It is chosen the following superior diameter: **DN50 mm (2")**, for reducing suction losses and cavitation risk.
Discharge collector: Individual pipe: 1" ≈ 25 mm
$D = 25 \cdot \sqrt{2} = 25 \cdot 1.41 = 35.25$ mm. Recommended diameter: DN 40 or even **DN 50 mm (2")**.

3.2.2 Calculation of the flow rate variation

3.2.2.1 For the pump with variable rotational speed:

In order to assure the cooling of the engine with variable rotational speed drive, minimum rotational speed value of the adjustable pump must be 1/5 from the nominal rotational speed of the electric engine. At this value the engine torque decreases at 70% from the maximum torque.

$$n_{min} = \frac{1}{5} n_n = \frac{1}{5} \cdot 2850 = 570\ rpm$$

The variation interval of the rotational speed of the adjustable pump is: *570...2850 rpm*
At centrifugal pump, load characteristic curve [3] can be exemplified with the following equation:

$$H(Q) = H_0 - kQ^2 \quad (2)$$

where: H_0 is pumping height at zero flow (closing height) and *k* is a coefficient that cumulates the geometry effect of the pump rotor and the losses effect of the intern load.
The graph of this equation of the second order is a quadratic curve, that represents the set of points from the plane of coordinates *(Q,H)*.
We use the pairs of values *(Q,H)* from the table 1, at n_0=2850 rpm we have two points on the characteristic curve of the pump: *Point 1: (Q_1=1.5 m³/h, H_1=70 m)*; *Point 2: (Q_2=12 m³/h, H_2= 39 m)*
Replacing these values in equation (2) we obtain: *$70= H_0-k\ 1.5^2$*, respectively *$39= H_0-k\ 12^2$*

Results: H_0=*70.942 m*; *k=0.218695*; Q_0=*17.95 m³/h*
Observations:

- In technical data sheet of electric pump, the value of the height (table 1) is *72 m*, very close to the value resulted from the calculation (H_0=*70.942 m*).
- $Q_{0,2850}$=*17.95 m³/h* is the theoretic flow of the pump at the zero pumping height.

The laws of similitude [3], applied to centrifugal pumps for two similar functionality regimes (the same pump at different rotational speed), mention that the flow varies direct proportional with rotational speed, the pumping height varies direct proportional with rotational speed at square, and the absorbed power by the pump varies direct proportional with rotational speed at cubic power:

$$\frac{Q}{Q_0} = \frac{n}{n_0};\ \frac{H}{H_0} = \left(\frac{n}{n_0}\right)^2;\ \frac{P}{P_0} = \left(\frac{n}{n_0}\right)^3 \quad (3)$$

When n_0 represents reference rotational speed and *n* represents the new rotational speed, maximum and minimum reports of the speed variation are:

$$s_{min} = \frac{570}{2850} = 0.2;\quad s_{max} = 1$$

Complete theoretical interval of the flow variation, corresponding to variation of the pumping height at H_0 at zero, is:
at n_{max}=*2850 rpm, Q* belongs to the interval *[0,17.95] m³/h;*
at n_{min}=*570 rpm, Q* belongs to the interval *[0,0.2 x 17.95] = [0, 3.59] m³/h.*
So, totally, adjusting rotational speed (from variable frequency drive) *570-2850 rpm* the theoretical maximum flow of the adjustable pump varies between *0-17.95 m³/h*.
At rotational speed decreasing, at the same load ends, the two points change as follows:
For ***H=70*** (point 1): *Q(n)=sx1.5*. At *n=570* results: *Q=0.2x1.5=0.30 m³/h*. At *n*=2850 results *Q=1.5 m³/h*.
For ***H=39*** (point 2): *Q(n)=sx12*. At *n=570* results: *Q=0.2x12=2.40 m³/h*. At *n*=2850 results *Q=12 m³/h*.
If are compared the same two points (*H=70 m* and *H=39 m*) at different speeds, the numeric results are:
At H=*70*, Q belongs to the interval *[0.30, 1.50] m³/h*;
At H=*39*, Q belongs to the interval *[2.40, 12.00] m³/h*.

Table 2: The pump flows at different rotational speeds for two heights (falls) (H = 70 m and H = 39 m)

n (rot/min)	s = n/n₀	Q at H = 70m (m³/h)	Q at H = 39m (m³/h)
570	0.200	0.2 x 1.5 = 0.30	0.2 x 12 = 2.40
855	0.300	0.3 x 1.5 = 0.45	0.3 x 12 = 3.60
1140	0.400	0.4 x 1.5 = 0.60	0.4 x 12 = 4.80
1425	0.500	0.5 x 1.5 = 0.75	0.5 x 12 = 6.00
1710	0.600	0.6 x 1.5 = 0.90	0.6 x 12 = 7.20
1995	0.700	0.7 x 1.5 = 1.05	0.7 x 12 = 8.40
2280	0.800	0.8 x 1.5 = 1.20	0.8 x 12 = 9.60
2565	0.900	0.9 x 1.5 = 1.35	0.9 x 12 = 10.80
2850	1.000	1.0 x 1.5 = 1.50	1.0 x 12 = 12.00

In figure 2 are presented load characteristic curves H=f(Q) of the adjustable centrifugal pump, at different rotational speeds, between the interval *570 rpm* and *2850 rpm*.
At starting: $H_0(Q)=70.492 - 0.218695\ Q^2$ (for n_0 = *2850 rpm*).
Adjusting of rotational speed: with step 10% from n_0.
For ***H=70 m*** results: $70=70.492 - 0.218695\ Q^2$. So, ***Q=1.499 m³/h****;*
For ***H=39 m*** results: $39=70.492 - 0.218695\ Q^2$. So, ***Q=11.999 m³/h****.*
Observations:

- In fig. 2 is observed how to move load characteristic curve of the pump when the rotational speed increase from the minimum value of *570 rpm*, to the maximum value of 2850 *rpm*. At minimum rotational speed H_{max}=*3m* and Q_{max}=*3.5 m³/h*, and maximum rotational speed

H_{max}=71m *and* Q_{max}=18 m^3/h. The graph was drawn for variable *s*, with step of *0.1*, in the interval *[0.2,1.0]*;

- The load characteristic curve of rotational speed *n=2850 rpm* passes through the point 1, of coordinates *(Q_1=1.5 m^3/h, H_1=70 m)* and the point 2, of coordinates *(Q_2=12 m^3/h, H_2=39 m).*

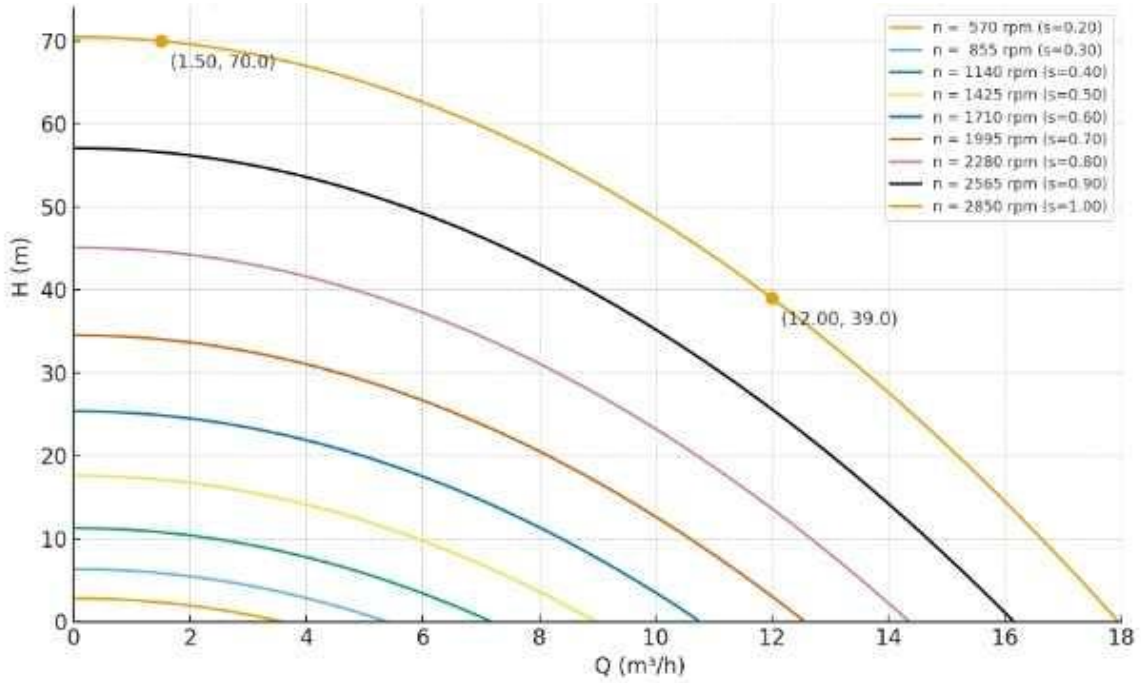

Fig. 2. Load characteristic curve H = f(Q); adjustable pump at different rotational speeds

3.2.2.2 For the pumping group made from two identical pumps coupled in parallel:

The pumping group is made from two identical pumps, coupled in parallel, one variable with drive rotational speed between *570...2850 rpm* and other fix, driven at the nominal rotational speed of *2850 rpm*.

At coupling in parallel [5], at the same pumping height H the flow rate of the two pumps Q_{total} is added:

$$Q_{total}(H,n) = Q_{fix}(H) + Q_{var}(H,n) \quad (4)$$

If the fix pump functions at the rotational speed n_0 and the variable pump at the rotational speed $n = s\ n_0$, according to the laws of similitude, at the same pumping height *H*, the following linear relation between flow rates results:

$$Q_{total}(H,n) = (1+s)\ Q_{ref}(H) \quad (5)$$

Where $Q_{ref}(H)$ is the the flow rate of a pump at the rotational speed n_0 and the pumping height (fall) *H*.

Reference data, at n_0 = *2850 rpm* are:

at *H=70 m*, each pump has $Q_{ref}(70)$=1.5 m^3/h;

at *H=39 m*, each pump has $Q_{ref}(70)$=1.5 m^3/h;

at *H=0 m*, for a single pump $Q_{0,\ 2850}$=17.95 m^3/h.

Rotational speed factor *s* varies between s_{min}=570/2850=0.2 and s_{max}=1.

Total flow rate of the pumping group, at the two falls when *s* varies between *0.2* and *1* is:

For *H = 70 m:*

Q_{total} = *(1 + s)1.5*, respectively for *s=0.2*, results $\boldsymbol{Q_{total} = 1.8 m^3/h}$, for s=1.0, results $\boldsymbol{Q_{total} = 3 m^3/h}$;

For *H = 39 m:*

Q_{total} = *(1 + s)12.0*, respectively for *s=0.2*, results $\boldsymbol{Q_{total} = 14.4 m^3/h}$, for s=1.0, results $\boldsymbol{Q_{total} = 24.0 m^3/h}$.

Variation interval of the flow rate at zero load (*H=0*) is:

$Q_{0,\,total}(s) = Q_{0,\,2850}(1+s)$, so for s from the interval *[0.2,1]*, $Q_{0,\,total}$ belongs to the interval *[1.2 x 17.95, 2 x 17.95] =* ***[21.54, 35.90]***
In table 3 are presented the key value of the pumping group at three pumping heights:

Table 3: Key values of the flow rate of the pumping group

Size Q_{total} at certain H	For s=0.2 (n=570rpm)	For s=1 (n=2850rpm)
Q_{total} la *H = 70 m* (m^3/h)	1.80	3.00
Q_{total} la *H = 39 m* (m^3/h)	14.40	24.00
Q_{total} la *H = 0* (m^3/h)	21.54	35.90

Generation of load characteristic curve of the pumping group made from fix pump driven by the rotational speed n_0*=2850 rpm* and the adjustable *pump (570...2850 rpm).*
Load curve of a single pump driven at rotational speed n_0 is:

$$H_0(Q) = 70.492 - 0.218695\,Q^2 \qquad (Q \text{ in } m^3/h).$$

General equation of a load curve of an adjustable pump is:

$$H(Q,s) = s^2 H_0 - aQ^2 \tag{6}$$

So, adjustable pump curve, with factor $s=n/n_0$ is: $H_0(Q) = s^2\ 70.492 - 0.218695\,Q^2$
For a certain fall *H* the flow rate of a pump $Q = \sqrt{(A-H)/B}$ if $(A-H)/B > 0$
In conclusion the total flow rate of the two pumps coupled in parallel is:

$$Q_{tot}(H,s) = Q_{fix}(H) + Q_{var}(H,s) \tag{7}$$

For the moment doesn't exist technical data about hydraulic network in which the pumps function (valve **12** of the load simulation from fig.1). From this reason, were overlapped three representative network load curves of form $H_{sist}(Q) = H_s + kQ^2$, for: *easy system (H_s=5m, k=0.03); medium system (H_s=10m, k=0.07); heavy system (H_s=15m, k=0.15).* The graph was drawn for variable *s*, with the step of *0.05*, in interval *[0.2,1.0]*.
At the intersection of the network curve with the load curves exist *functioning points* of group. *There* were marked on a graph few functioning points, of coordinates *(Q,H)*, respectively: ***s=1.0***, three functioning points *(27.01, 28.2); (22.02, 44.0); (16.46, 55,7);* ***s=0.8***, three functioning points *(24.69, 23.3); (19.16, 35.7); (13.77, 43,6);* ***s=0.7***, one functioning point: *(12.27, 37,6); s= 0.55*, one functioning point: *(14.47, 24.7);* ***s=0.50***, one functioning point *(18,83, 15,7);* ***s=0.40***, one functioning point *(16.23, 12.9).*

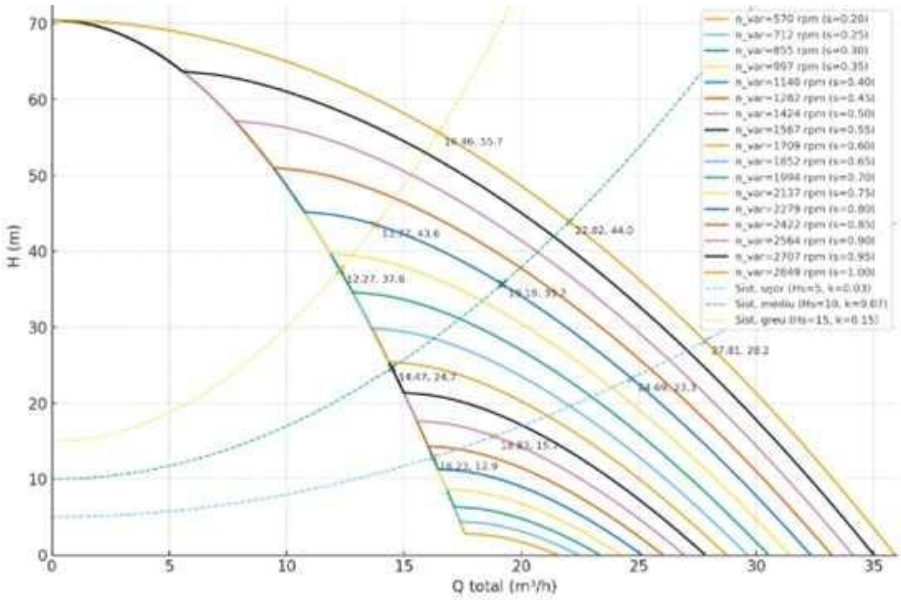

Fig. 3. Load characteristic curves H = f(Q), at different rotational speeds, overlapped over three network curve (fix pump coupled in parallel with adjustable pump)

Few values of the flow rate of the pumping group, extracting from the figure 3:
For H=0 we have Q_{tot}*=21.545 m³/h*, at *s=0.20* and Q_{tot}*=35.895 m³/h*, at *s=1.00*;
For H=39 m we have Q_{tot}*=14.400 m³/h*, at *s=0.20* and Q_{tot}*=24.00 m³/h*, at *s=1.00*;
For H=70 m we have: Q_{tot}*=1.800 m³/h*, at *s=0.20* and Q_{tot}*=3.000 m³/h*, at *s=1.00*.

Table 4: Total flows rates for different rotational speeds for three falls (H=0, H = 39 m, H = 70 m)

n_{var} (rpm)	s	Q_{tot} at H=0 (m^3/h)	Q_{tot} at H=39 (m^3/h)	Q_{tot} at H=70 (m^3/h)
570	0.200	21.54	12.00	1.50
670	0.235	22.17	12.00	1.50
770	0.270	22.80	12.00	1.50
870	0.305	23.43	12.00	1.50
970	0.340	24.06	12.00	1.50
1070	0.375	24.69	12.00	1.50
1170	0.411	25.32	12.00	1.50
1270	0.446	25.95	12.00	1.50
1370	0.481	26.58	12.00	1.50
1470	0.516	27.21	12.00	1.50
1570	0.551	27.84	12.00	1.50
1670	0.586	28.47	12.00	1.50
1770	0.621	29.10	12.00	1.50
1870	0.656	29.73	12.00	1.50
1970	0.691	30.36	12.00	1.50
2070	0.726	30.99	12.00	1.50
2170	0.761	31.62	14.92	1.50
2270	0.797	32.25	17.11	1.50
2370	0.832	32.88	18.68	1.50
2470	0.867	33.51	19.99	1.50
2570	0.902	34.14	21.15	1.50
2670	0.937	34.77	22.23	1.50
2770	0.972	35.40	23.23	1.50

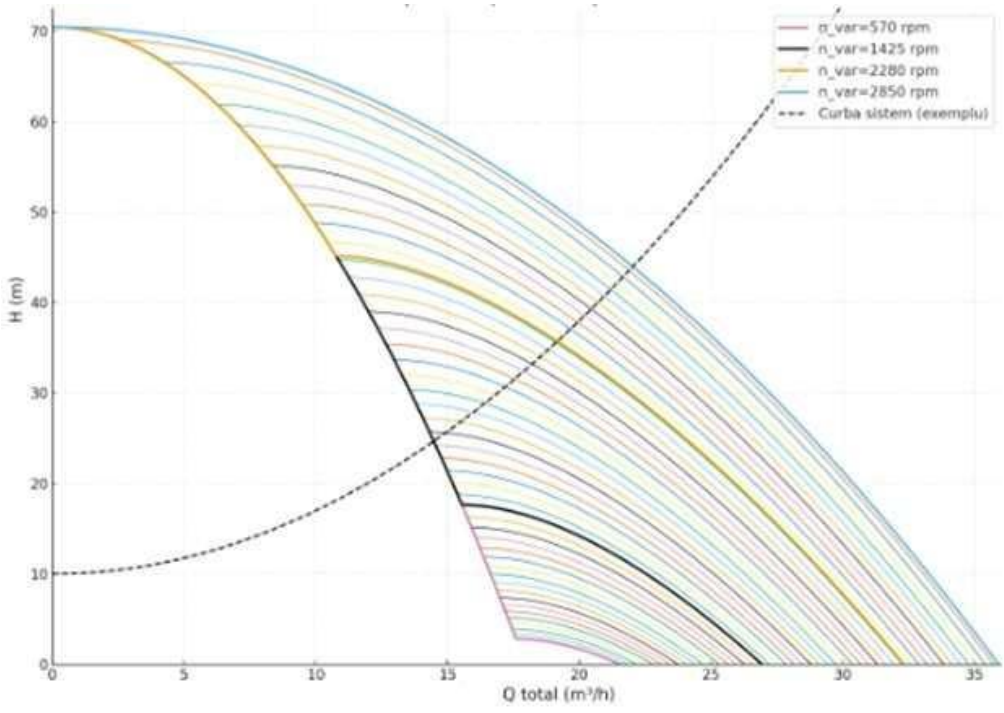

Fig. 4. Load characteristic curve H = f(Q), at different rotational speeds over a network curve (fix pump, coupled in parallel with an adjustable pump)

If rotational speed variation of the adjustable pump is made with more fine steps, for instance *100 rpm*, results the values of the flow rate from the table 4, and characteristic curves of the pumping group from the figure 4, which are overlapped only of one single network curve. In fig. 4 were mentioned load curves at four rotational speeds n_{var}, respectively: *570, 1425, 2280, 2850 rpm*.
The values tendency from table 4 is presented in linear graph from figure 5.

n_{var} (rpm)	Q_{tot} / H=0 (m^3/h)	sparkline H=0m	Q_{tot} / H=39 (m^3/h)	sparkline H=39m	Q_{tot} / H=70 (m^3/h)	sparkline H=70m
570	21.544		12.000		1.500	
670	22.174		12.000		1.500	
770	22.804		12.000		1.500	
870	23.434		12.000		1.500	
970	24.064		12.000		1.500	
1070	24.694		12.000		1.500	
1170	25.324		12.000		1.500	
1270	25.954		12.000		1.500	
1370	26.584		12.000		1.500	
1470	27.214		12.000		1.500	
1570	27.844		12.000		1.500	
1670	28.474		12.000		1.500	
1770	29.104		12.000		1.500	
1870	29.734		12.000		1.500	
1970	30.364		12.000		1.500	
2070	30.994		12.000		1.500	
2170	31.623		14.921		1.500	
2270	32.254		17.112		1.500	
2370	32.883		18.676		1.500	
2470	33.513		19.986		1.500	
2570	34.143		21.153		1.500	
2670	34.773		22.226		1.500	
2770	35.403		23.232		1.500	

Fig. 5. Sparkline graphical representation of values tendency from table 4
Sparkline's Scale: **H=0**, sparkline is scaled at maximum flow rate observed for H=0 (**35.403 m^3/h**); **H=39 m**, sparkline is scaled at maximum flow rate observed for H=39 (**23.232 m^3/h**); **H=70 m**, sparkline is almost constant (**1.50 m^3/h**) for majority steps.

4. Conclusions

- For *H=0 m*, the total flow rate increases almost continuously with a variable rotational speed of the pump, between *21.5 m^3/h (n=570 rpm)* until at *35,4 m^3/h (n=2770 rpm);*
- For *H=39 m,* the flow rate increases almost constantly *at 12 m^3/h* until at *2070 rpm* (only the fix pump covers this value). Over *2170 rpm*, the variable pump stars to contribute at the total flow rate, that reaches the value at *23.2 m^3/h*;
- For *H=70m,* the flow rate is constant, at the value of *1,5 m^3/h,* regardless of the value of the variable pump. Practically, the fix pump determines the maximum flow rate at this height of pumping;
- Variation intervals of the pumping group are:
at *H=0 m*, *21.5...35.4 m^3/h*;
at *H=39 m*, *12...23.2 m^3/h* (plateau until at *2070 rpm*, then increases);
at *H=70 m*, 1.5 m^3/h (without variation);
- The adjustment of the variable pump rotational speed brings considerable flexibility in functioning domains with small and medium falls (*H=0...39 m*), but is inefficient for load close to the maximum pressure (*H=70 m*);
- On the shown stand can be simulated different characteristic curves of irrigation installation (by varying the opening of the load valve, driven by servomotor) and these determine: load characteristics curves of the pumping group (formed by a fix pump and a variable pump);

functioning points in which pumping group works stably, at maximum yield, for constant different values of the pumping height (situated at the intersection of the two types of characteristic curves). The pumping group pressure, simulated by varying the opening of the servomotor valve in the principle scheme of the stand, represents the working pressure of the pumping group consisting of the fixed pump and the adjustable pump, coupled in parallel. This pressure, in a hypothetical plot of irrigation, served by the pumping group, consists of:

- the sum of the linear and local pressure losses on the pump discharge circuit, from the discharge collector of pumping group, to the hydrant in the plot farthest from the it;
- the pressure necessary to supply water to the hydrant, positioned at the highest height relative to the discharge collector of the group;
- working pressure at which the most disadvantaged hydrant (the farthest and the highest situated from the discharge collector source) must operate.

For example, if the pumping group supplies a hydrant, located at 200 m away from the discharge collector of the group, the sum of the local pressure losses, on a horizontal supply circuit is 1 bar, and the working pressure of the hydrant is 1 bar, the opening of the stand's servomotor valve is adjusted at a value corresponding to a pressure of 4 bar.

References

[1] Hangzhou KUVO Electronics Co., Ltd. "How variable frequency drives (VFDs) and pumps transform agricultural irrigation efficiency and sustainability?" / "Cum transformă unitățile de frecvență variabilă (VFD) și pompele eficiența și durabilitatea irigării agricole?" September 8, 2025. Accesed October 28, 2025. https://hzkuvo.com/ro/cunostinte/pompa-vfd-agricultura-irigatii/ .

[2] ***. "SPERONI 2C 25/180A - 72 mCA Centrifugal pump" / "Pompa centrifugă SPERONI 2C 25/180A - 72 mCA." *Arena Instalațiilor*. Accessed October 28, 2025. https://www.arenainstalatiilor.ro/pompa-centrifuga-speroni-2c-25-180a-72-mca-p4555 .

[3] Edgars, Repsa, and Kronbergs Eriks. "Investigation of centrifugal pump characteristics." Paper presented at 20th International Scientific Conference Engineering for Rural Development, Jelgava, Letonia, May 26-28, 2021, DOI: 10.22616/ERDev.2021.20.TF119.

[4] VSX - Vogel Software GmbH. "Speed – Affinity Laws", *Impeller Net.* Accessed October 28, 2025. https://impeller.net/encyclopedia/affinity-laws/.

[5] Georgescu, Andrei-Mugur, Sanda-Carmen Georgescu, Costin Ioan Coșoiu, Nicolae Ioan Alboiu, and Dan Hlevca. *Solved Problems in Hydraulic Machinery* / *Probleme de Mașini Hidraulice*. Bucharest, Printech Publishing House, 2014.

ISSN 1454 - 8003
Proceedings of 2025 International Conference on Hydraulics and Pneumatics - HERVEX
November 19-21, Băile Govora, Romania

USING SOFTWARE APPLICATIONS TO SIMULATE THE OPERATIONAL PERFORMANCES OF A MANIPULATOR ARM

Carmen Nicoleta DEBELEAC[1]

[1] "Dunarea de Jos" University of Galati, Engineering and Agronomy Faculty in Braila, Research Center for Mechanics of Machines and Technological Equipments, Braila, Romania

Abstract: *This study focuses on developing a virtual model of a manipulator arm, integrating both the mechanical structure and the complete driving system, comprising actuators and a power unit. The research aims to provide a general, adaptable mechanical configuration that can be used on various robot structures and has a wide range of applications. The integrated model allows for virtual simulation based on mathematical modeling and virtual instrumentation software.*

Keywords: *Virtual model, hydraulic system, manipulator arm, simulation, operational performance*

1. Introduction

The manipulator arms, often programmable structures, consisting of multiple joints and links, represent the devices that perform a lot of tasks without direct physical contact. Thus, its structural elements allow it to move in a manner similar to a human arm and terminate with an end effector (e.g., a gripper or other specialized tool) to grasp, lift, and move objects in various industries for tasks such as manufacturing, surgery, and hazardous materials handling. Research from this paper focused on analyzing the dynamic behavior of a manipulator arm (used in emergency cases) using virtual simulation to effectively highlight its specific operational characteristics and dynamic.
As is generally known, the dynamic characteristics of manipulator arm revealed by simulation on virtual models (Figure 1) consist of:

a) Torque and force analysis on each joint and link governing the manipulator arm's motion in different working scenarios for established structural integrity and design optimization.
b) Vibration and stability analysis for arm's movement under various loads and at different speeds to investigate the arm response to dynamic forces, the natural frequencies, the impact overall stability, and reveal potential working cases with excessive vibration.
c) Collision detection and avoidance for the optimization of fail-safe and damage-mitigation strategies.
d) Payload and control parameter optimization to maximize efficiency and performance while minimizing wear and tear on the hydraulic system.

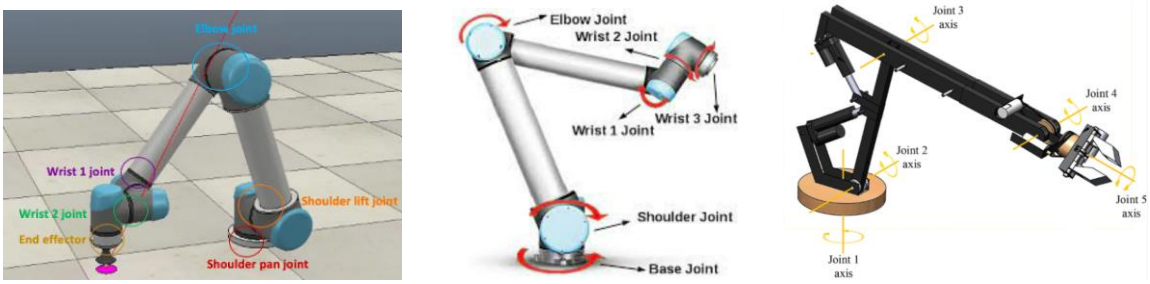

a) b) c)

Fig. 1. Examples of robotic arms with multiple degrees of freedom [1,2,3]

2. Methods and Materials

Generally, for development of a virtual model of a manipulator arm are needed followings steps:

- designing and initial analysis.
- establishing physic-mathematic model of the mechanical structure.
- developing physic-mathematic model of the hydraulic drive system (hydraulic, electric etc.).
- modeling of the ensemble system.
- processing and analysis data.

The virtual modeling process for a manipulator arm begins with structural design using Computer-Aided Design (CAD) techniques [4,5]. This stage is foundational, creating a precise 3D digital representation of the arm's components before any physical prototyping or advanced analysis occurs. In Figure 2 All the main parts of the manipulator were designed using aluminum material (cod 6061 in Inventor Software libraries).

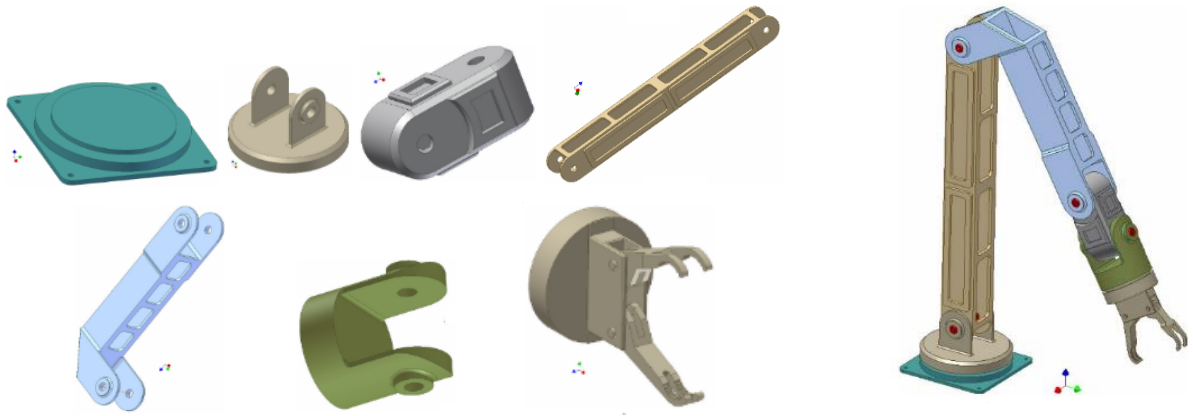

a) b)

Fig. 2. Design of manipulator arm [6]:
a) individual parts; b) assemble.

The position and orientation of a manipulator's end-effector are determined by its kinematics model (forward or inverse kinematics) useful to obtain a set of geometric transformations that describes the relationship between joint parameters and the end-effector's pose without considering forces, torques, or other dynamic factors (e.g., mass and inertia) [7]. In Figure 3 is described the specific configuration of the kinematic model of the manipulator arm's structure with 6 DOF showing the arrangement of its links and joints. The numerical symbols used have the next signification: (0) support; (1) rotational platform; (2) main arm; (3) handler; (4) coupler; (5) prehensile port-device.

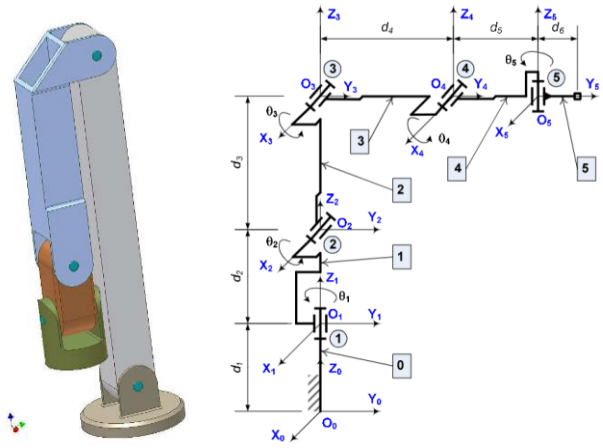

Fig. 3. Kinematics model of the manipulator arm with 6 DOF (six rotations) [6]

The forward kinematics of the manipulator arm can be solved by Eq.(1) that describes the transformation matrix between the frame O_0 and frame O_5.

$$T_5^0 = T_1^0 T_2^1 T_3^2 T_4^3 T_5^4 . \quad (1)$$

Therefore, the position and orientation transformation matrix between O_0 and O_5 can be determined using the Denavit–Hartenberg (D-H) parameter [8]. Knowing the workspace of a manipulator is a very important aspect and is represented by the total volume swept by the end effector as the manipulator executes all possible movements [9]. The applications or specialized tools (e.g., WSRender, Robotics System Toolbox – Matlab, Space Dream Robotic Arm, WorkSpace etc.) provide functions like robot kinematics and joint limits, collision detection, workspace generation, analysis and visualization of workspace data (Figure 4) useful for design engineers in their activities.

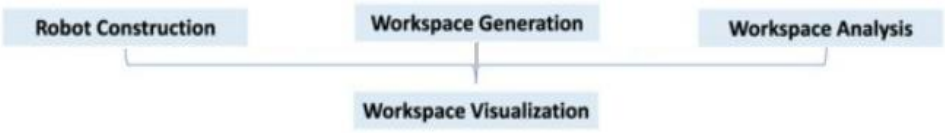

Fig. 4. Base configuration of the software architectures

For example, the linkage between the model performed in Autodesk - Inventor 9© and WorkSpace 5© was possible by exporting the Inventor part to a SAT file, which is a standard format for sharing 3D models between different CAD systems [10]. Once exported, the SAT file could be imported into WorkSpace 5©, creating a new, non-linked model in that program for working space generation of the manipulator arm (as can be seen in Figure 5).

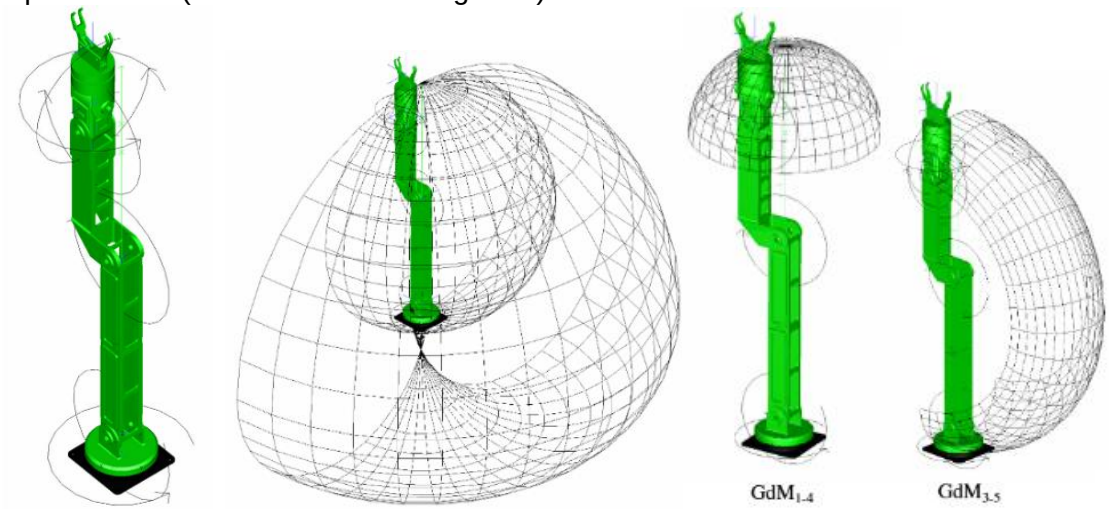

a) b) c)

Fig. 5. Working space of the manipulator arm [6]:
a) SAT model; b) working space for the first three DOF; c) working spaces for other DOF (1-4, 3-5).

3. Simulation Results

The manipulator arm's mechanical configuration was developed using MATLAB's SimMechanics (Figure 6a) for direct angular input testing, while the hydraulic system, including the actuators and a classical power unit, was modeled in MATLAB's SimScape (Figure 6b). Finally, a complete diagram of a manipulator arm, including its power unit, was created using MATLAB and SimScape. Thus, the diagram, shown in Figure 7, illustrates the manipulator's components, while a specific part of the diagram, the power unit, uses a classical configuration developed through mathematical computations in the software.

The virtual manipulator arm model was tested in three steps: first, the mechanical structure was tested with direct angular inputs; second, the hydraulic driving system was tested both for individual actuators and then for the entire system working together; and third, the complete model was tested by having the hydraulic actuators directly drive the mechanical parts according to manual angular references.

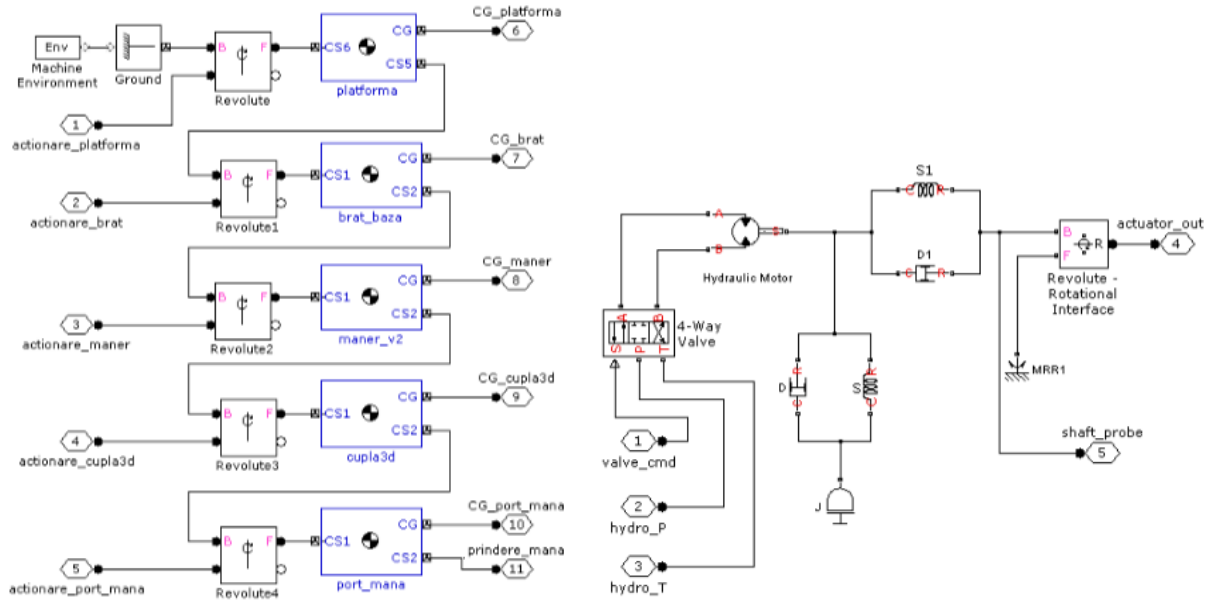

a) b)

Fig. 6. Configuration of the virtual subsystems of the manipulator arm [11]:
a) mechanical configuration in MATLAB - SimMechanics; b) hydraulic system in MATLAB - SimScape.

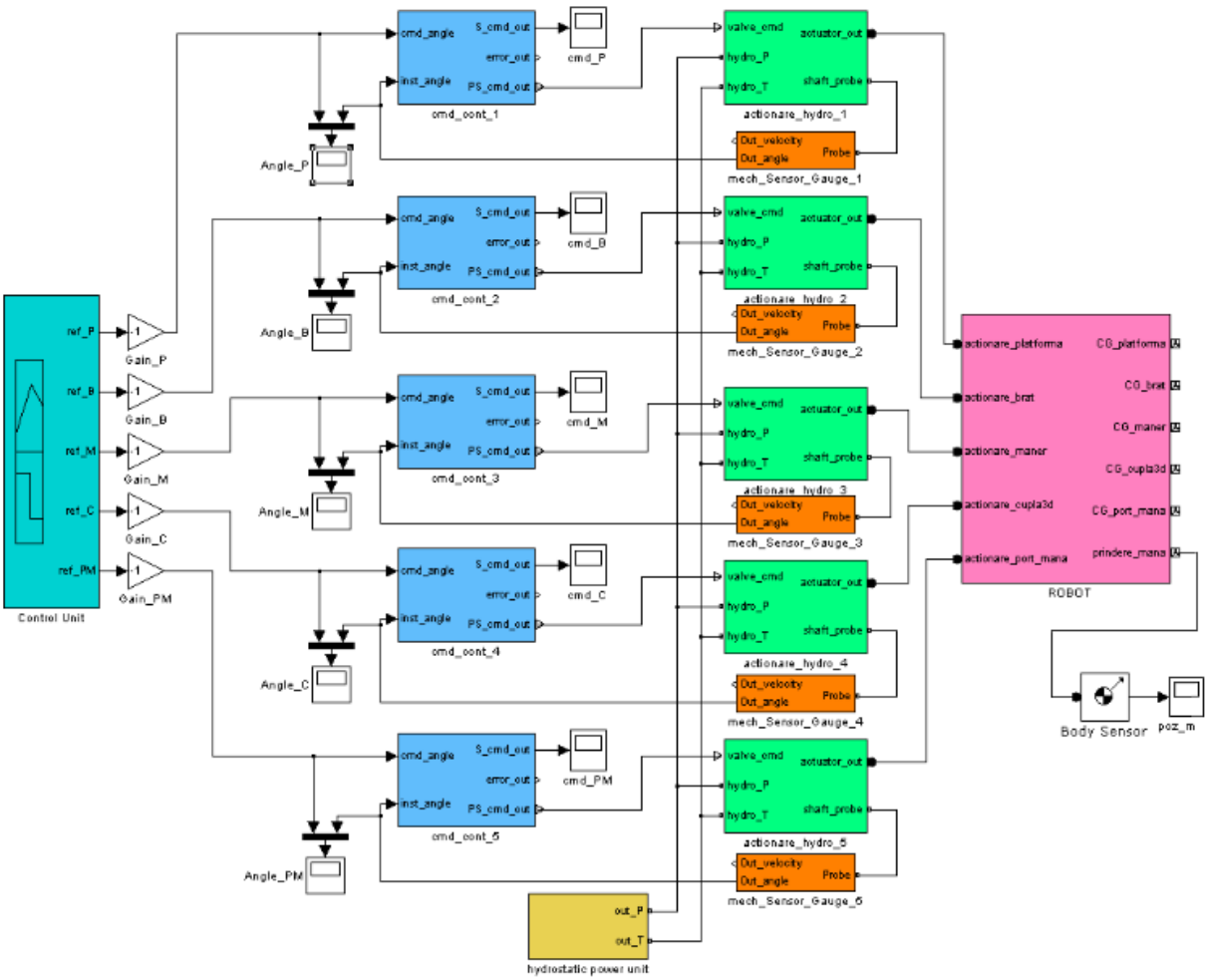

Fig. 7. General virtual model of the manipulator arm [11]

The results obtained from simulation process were depicted in Figure 8.

a)

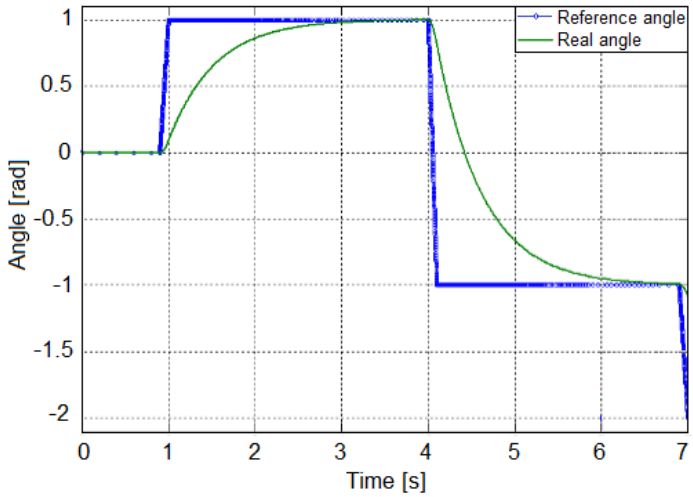

b)

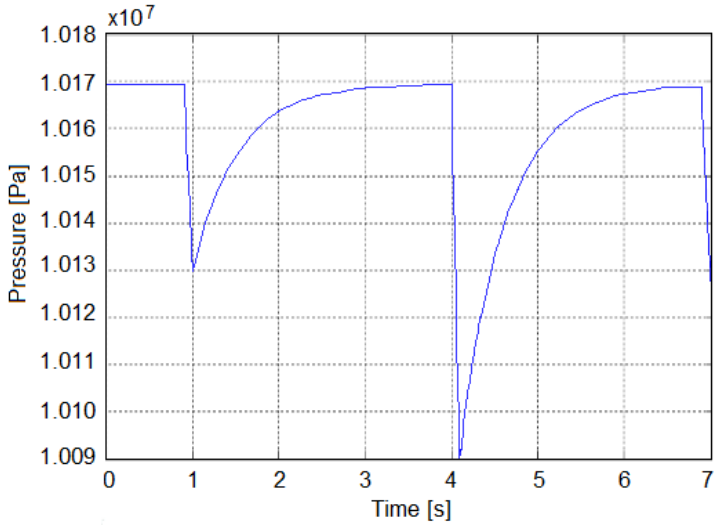

c)

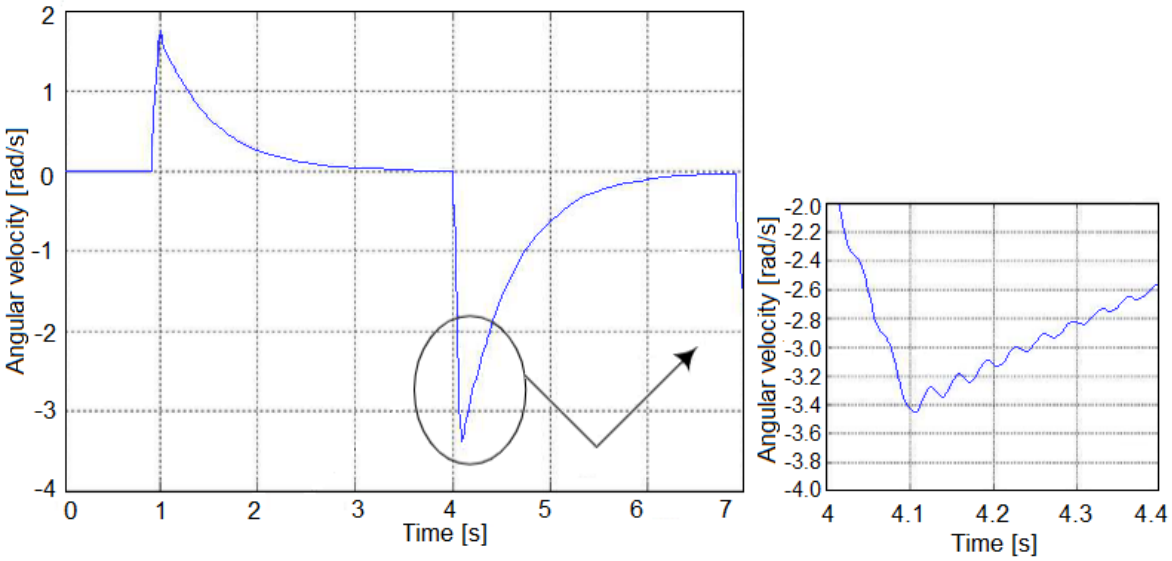

Fig. 8. The response of hydraulic system at input signal:
a) angular displacement (thin line); b) total pressure in driving system;
c) speed of the actuator shaft (with detail)

The results obtained in Figure 8 describe a simulation of a manipulator arm's motion, analyzing the resulting actuator displacement, system pressure, and shaft velocity. Thus, in Figure 8a two diagrams are represented to compare the desired reference movement (thick line) with the actual displacement of the actuator (thin line). The graph given in Figure 8b shows how the pressure changed within the system over the working cycle, based on the input requirements. The graph given in Figure 8c depicts the behavior of the velocity at the actuator shaft that demonstrates the dynamic effects on the system (consisting of rigidity and damping) with high-frequency oscillations caused by energy transferring back and forth between the system's kinetic energy and the elastic potential energy stored in its rigid components. As energy is dissipated, the magnitude of the oscillations in the velocity graph decreases. In the simulation, this effect is visible as the peaks of the velocity graph diminish over the duration of the movement. The ultimate effect is to bring the velocity to zero as the system settles into its final position.

4. Conclusions

In this paper the design and behavior of working operation of a manipulator arm is discussed on an illustrative example based on serial arm with 6 DOF consisting in six rotations. The system has been simulated in MATLAB/Simulink environment, and it was determined that the desired control was achieved. The simulation shows how mechanical rigidity affects the oscillations in the velocity diagram and how damping influences the magnitude of these oscillations. It is important to note that the operational characteristics are not determined solely by kinematic conditions, but also by dynamic factors such as the overall system inertia. Overall, the performance of manipulator characteristics was put into evidence using dedicated application software available in the mechanical engineering field.

References

[1] Liu, Wenxing, Hanlin Niu, Muhammad Nasiruddin Mahyuddin, Guido Herrmann, and Joaquin Carrasco. "A Model-free Deep Reinforcement Learning Approach for Robotic Manipulators Path Planning". Paper presented at the 21st International Conference on Control, Automation and Systems (ICCAS 2021), Jeju, Korea, October 12-15, 2021.

[2] Topalidou-Kyniazopoulou, Angeliki. "Motion Planning Strategy for a 6-DOFs Robotic Arm in a Controlled Environment". Master thesis. Universität Bonn, August 2017.

[3] Fahim, S.R., Y. Sarker, and S.K. Sarker. “Modeling and development of a five DoF vision based remote operated robotic arm with transmission control protocol.” *SN Applied Sciences 2* (2020):1263.

[4] Emmanuel Chukwudi Agbaraji, Hyacinth Chibueze Inyiama, and Ifeyinwa Obiora-Dimson. "Joint Torque and Motion Computational Analysis for Robotic Manipulator Arm Design." *Journal of Engineering and Applied Sciences,* 12 (2018):1-9.

[5] Sharkawy, Abdel-Nasser, and Panagiotis N. Koustoumpardis. "Dynamics and Computed-Torque Control of a 2-DOF manipulator: Mathematical Analysis". *International Journal of Advanced Science and Technology* 28, no. 12 (2019): 201-212.

[6] Naidin, G., S. Năstac, and C. Debeleac. "Workspace Drawing from a Manipulator Arm with 6 DOF". *Journal of Industrial Design and Engineering Graphics - JIDEG* 6, no. 1 (2011): 37-40.

[7] Bagheri, Mostafa, Arash Ajoudani, Jinoh Lee, Darwin G. Caldwell, and Nikos G. Tsagarakis. ”Kinematic Analysis and Design Considerations for Optimal Base Frame Arrangement of Humanoid Shoulders”. IEEE International Conference on Robotics and Automation (ICRA), Seattle, WA, USA, May 25-30, 2015.

[8] Elsamanty, M., E.M. Faidallah, Y.H. Hossameldin, S.A. Rabbo, S.A. Maged, H. Yang, and K. Guo. ”Workspace Analysis and Path Planning of a Novel Robot Configuration with a 9-DOF Serial-Parallel Hybrid Manipulator (SPHM)”. *Applied Sciences 13* (2023): 2088.

[9] Ceccarelli, Marco. "Challenges for Workspace Analysis of Manipulators". *Journal of the Indian Institute of Science* 104 (2024): 611–621.

[10] Huo, Z., M. Yuan, S. Zhang, and X. Zhang. "Observer-Based Adaptive Robust Force Control of a Robotic Manipulator Integrated with External Force/Torque Sensor". *Actuators* 14, no. 3 (2025):116.

[11] Naidin, G., S. Năstac, and C. Debeleac. "Computational Dynamics of a Manipulator Arm for Emergency Cases Interventions". Paper presented at The Annual Symposium of the Institute of Solid Mechanics SISOM 2011 and Session of the Commission of Acoustics, Bucharest, Romania, May 25-26, 2011.

ISSN 1454 - 8003
Proceedings of 2025 International Conference on Hydraulics and Pneumatics - HERVEX
November 19-21, Băile Govora, Romania

LOW-COST VIBRATION MONITORING SYSTEM FOR GEAR-TYPE HYDRAULIC PUMPS TO SUPPORT PREDICTIVE MAINTENANCE

Daniel-Vasile BANYAI[1], Ioan-Lucian MARCU[1], Andreea-Larisa PUGNA[1]

[1] Technical University of Cluj-Napoca, Daniel.Banyai@termo.utcluj.ro

Abstract: *Gear-type hydraulic pumps are widely used in industrial hydraulic systems due to their simplicity, durability, and low cost. However, their reliable operation can be jeopardized by cumulative wear and faults if not monitored. This paper presents the development of a low-cost vibration monitoring system tailored for gear pumps, aimed at enabling predictive maintenance on these commonly used but often unmonitored components. The proposed system is built around an Arduino microcontroller and basic vibration sensors, offering real-time measurement and logging of pump vibration signals. We discuss the motivation for monitoring gear pump health, the challenges of employing high-end vibration analysis equipment on low-cost pumps, and the design of our cost-effective solution. The system captures vibration data from a pump, performs on-board processing for fault indicators, and logs or transmits the data for analysis. Fundamental vibration analysis principles for fault detection in rotating machinery are reviewed, and case references to similar low-cost implementations are provided. Initial tests on a laboratory gear pump setup show that the system can successfully measure characteristic vibration signatures, laying the groundwork for early fault detection. The results suggest that even a simple, inexpensive setup can support predictive maintenance by identifying abnormal vibration patterns indicative of developing issues.*

Keywords: *Gear pump, predictive maintenance, vibration analysis, low-cost sensor, Arduino, condition monitoring*

1. Introduction

Hydraulic gear pumps are among the most ubiquitous pump types in industrial applications, valued for their simple and robust design (see Figure 1). They are used extensively in agriculture, construction, manufacturing, and other sectors where reliable high-pressure fluid power is required. Gear pumps are also highly cost-effective compared to more complex pump types, making them a popular choice for a wide range of equipment [1].

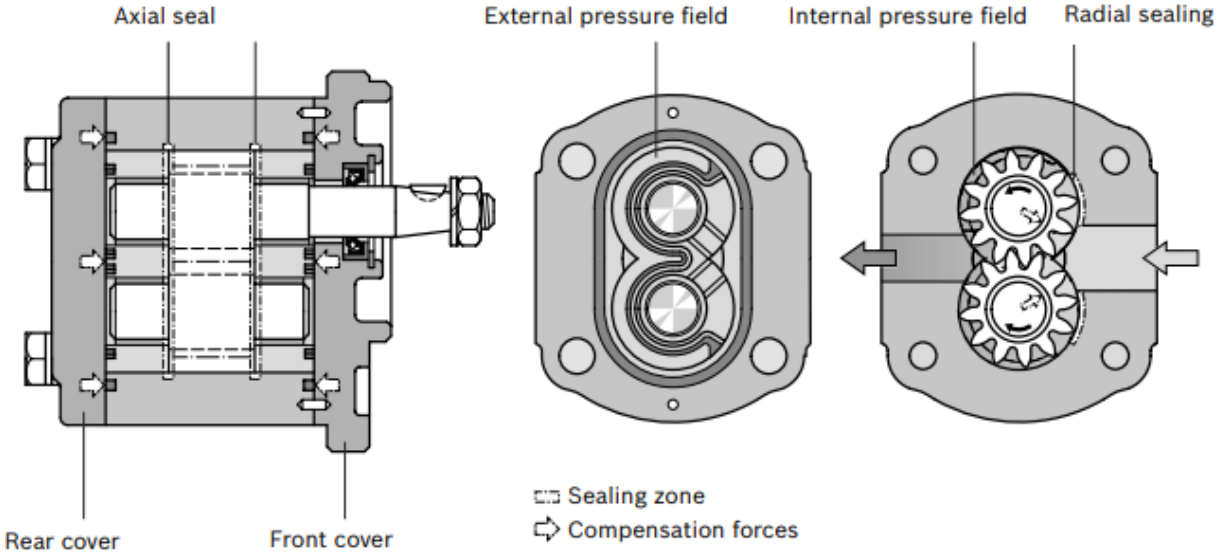

Fig. 1. External gear pump

Despite their reliability, these pumps do experience wear and performance degradation over time. Internal issues such as gear tooth pitting, cracking, excessive clearances, or bearing wear can lead to imbalance and elevated vibration levels. In other words, a failing gear pump often “carries the signature” of its faults in its vibration pattern. Without proper monitoring, such faults may progress to catastrophic failure in critical systems, potentially compromising the entire machine.
Vibration in rotating machinery originates from multiple sources (see figure 2). Mechanical vibrations are generated by internal moving components and interactions; for example, the meshing of gear teeth in a pump causes periodic excitation. Imperfections in gear geometry (such as profile errors, surface roughness or misalignment) and internal clearances lead to dynamic forces that induce vibration. In gear pumps, the precision class of gears and any tooth-profile corrections strongly influence these mechanical noise/vibration levels. Hydraulic vibrations, on the other hand, are caused by fluid pulsations and pressure fluctuations. Pump phenomena like fluid cavity collapse (cavitation), pressure ripple at gear tooth passing, and flow turbulence all generate oscillating forces in the fluid. Consequently, a gear pump’s vibration signal is a combination of structural (mechanical) and fluid-induced components. Monitoring these vibrations can reveal the pump’s condition—a deviation in vibration characteristics often indicates developing faults such as gear wear, imbalance, bearing damage, or cavitation issues.

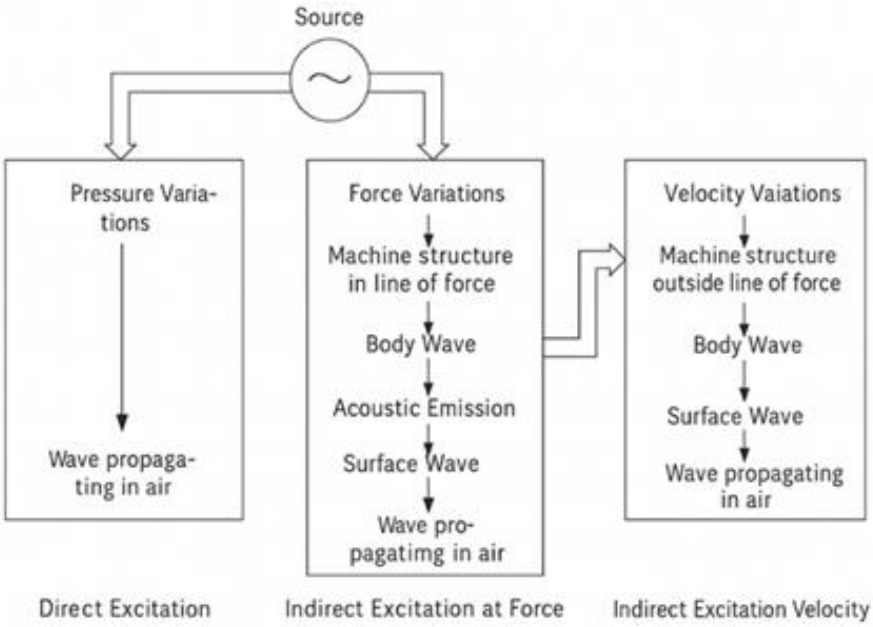

Fig. 2. Vibrations sources in rotating machinery

Maintenance strategies in industry have evolved from reactive fixes and periodic servicing toward predictive maintenance approaches. Unlike reactive maintenance (“run-to-failure”) which incurs unplanned downtime, and preventive maintenance which replaces components on a fixed schedule (sometimes unnecessarily), predictive maintenance aims to intervene only when needed, based on actual condition indicators.
For pumps in particular, vibration-based condition monitoring is a cornerstone of predictive maintenance programs. Pumps are critical assets in many facilities and are therefore often monitored routinely for any sign of trouble. Predictive maintenance through vibration analysis can reduce unplanned downtime, improve safety, and extend the lifespan of equipment. Studies have shown that collecting and analysing pump vibration data allows maintenance personnel to predict deterioration and take action before a failure occurs. This proactive approach prevents sudden breakdowns and enables scheduled repairs, thereby increasing productivity and reducing total maintenance costs [2].

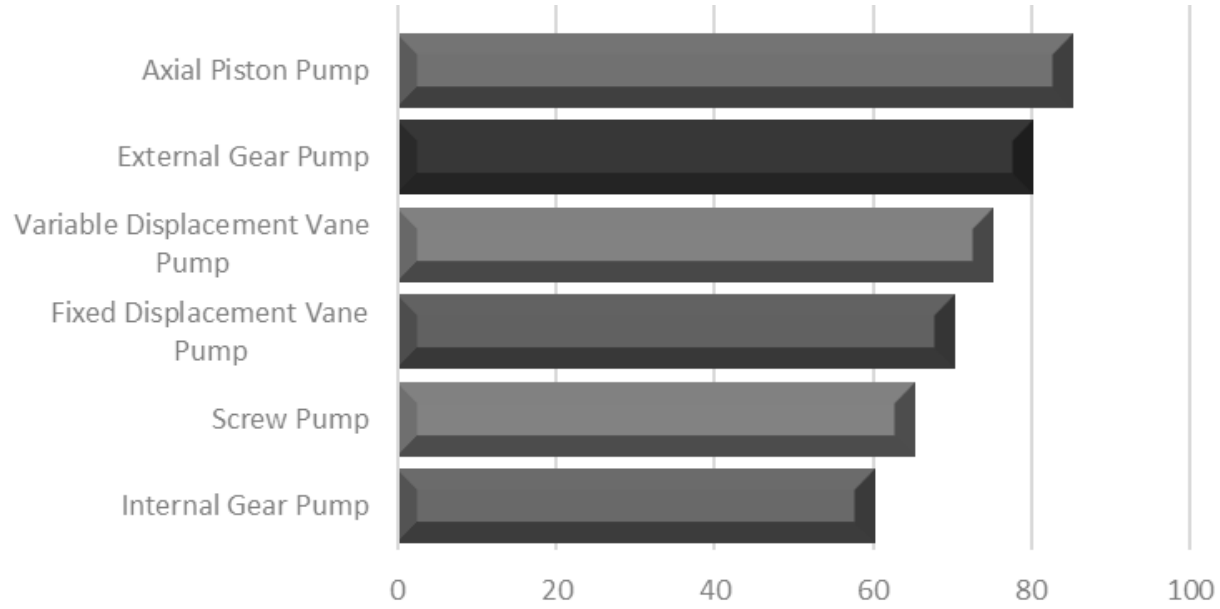

Fig. 3. Noise levels in hydrostatic machines

However, implementing advanced vibration monitoring on every gear pump is not straightforward. High-end vibration analysis equipment, such as industrial grade online monitoring systems or portable analyzers, can be prohibitively expensive relative to the cost of a small gear pump. Many complex and feature-rich predictive monitoring systems exist, but they often carry high costs that are justified only for expensive or mission-critical applications [3]. For example, a professional portable vibration data collector can cost on the order of thousands of dollars, and permanent wired vibration monitoring installations for large equipment can run into hundreds of thousands of dollars [4] (see figure 4). Such an investment is difficult to justify for a gear pump that itself may be worth only a few hundred dollars. As a result, gear pumps in the field are commonly left uninstrumented, or checked only periodically (e.g. during scheduled maintenance) with handheld devices. This creates a cost–benefit mismatch: the lack of continuous monitoring means small faults in gear pumps can go unnoticed until they cause a bigger problem, yet equipping each pump with a top-tier monitoring system would be economically inefficient.

Fig. 4. a) Industrial multichannel vibrations monitoring system. b) Portable vibrations analyzer [4]

The above considerations motivate the development of a low-cost vibration monitoring system specifically for gear-type hydraulic pumps. The goal is to bridge the gap between doing nothing (or only sporadic checks) and deploying costly instrumentation. By leveraging inexpensive microcontrollers and sensors, along with modern connectivity, one can implement a simple condition monitoring solution that provides valuable insight into pump health at a fraction of the cost of industrial systems. Indeed, the rapid advancement of affordable sensors and IoT devices has opened opportunities for “budget” condition monitoring that keeps equipment running efficiently without large capital expense [5]. In this paper, we present a compact vibration monitoring system built around an Arduino-based platform and basic accelerometer sensors, intended for continuous or periodic monitoring of gear pump vibrations. We emphasize simplicity and cost-effectiveness: the hardware uses low-cost, off-the-shelf components and the analysis methods are tailored to the limited processing capabilities of microcontrollers. The system supports predictive maintenance strategies by providing data to detect abnormal vibration trends or frequency signatures indicative of developing faults.
The paper is organized as follows. Section 2 provides background on vibration analysis for predictive maintenance, including the relevance of vibration monitoring for gear pumps and the scientific principles used to detect faults. Section 3 describes the design and implementation of the proposed low-cost monitoring system, covering the hardware components, sensor integration, and data acquisition/software approach. In Section 4, we discuss example results and observations from a case study deployment on a gear pump, and we compare our approach with similar low-cost systems reported in the literature. Section 5 outlines potential enhancements, such as integration with edge computing or remote monitoring, and Section 6 concludes the paper with final remarks on the effectiveness and future prospects of the system.

2. Background: Vibration Analysis for Predictive Maintenance

2.1 Vibration Monitoring of Gear Pumps

Vibration analysis is one of the most powerful techniques for condition monitoring of rotating machinery, including gear-type pumps. Therefore, by measuring and analyzing vibrations, one can infer the condition of the pump’s internal components. Gear pumps normally operate at rotational speeds on the order of a few hundred to a few thousand RPM (e.g. 1500–3000 RPM for typical small pumps). This rotation, combined with the meshing of the gear teeth, produces distinct vibration components: the fundamental running frequency (pump shaft speed) and the gear mesh frequency (the product of number of gear teeth and shaft speed), along with their harmonics. In a healthy gear pump, these vibration components remain relatively stable in amplitude. But as faults develop, new frequencies or amplitude changes often occur. For instance, imbalance due to wear will increase the 1x running speed vibration, a cracked or missing tooth will introduce impacts at the rotation frequency (often appearing as sidebands around the gear mesh frequency in the spectrum), and a deteriorating bearing will generate high-frequency vibration content. A study by Osman et al. observed that even a small notch on a gear tooth significantly altered the vibration spectrum of a gear pump, confirming that early fault detection is possible by spectrum analysis of the vibration signal [5]. Given that gear pumps have relatively low inherent vibration (thanks to their simple mechanism and usually stable flow), any abnormal vibration is a strong indicator of a problem. In safety-critical applications, continuous monitoring of pump vibrations is thus highly desirable to avoid sudden failures.

2.2 Predictive Maintenance and Fault Detection

In predictive maintenance, the aim is to continuously track machine condition and schedule repairs just in time before a failure. Vibration monitoring plays an essential role in this strategy by providing real-time insight into machine health. For pumps, ISO standards such as ISO 10816 provide guidance on acceptable vibration levels for machine condition, and exceeding those levels can trigger maintenance actions. More importantly, trending the vibration data over time allows

maintenance teams to identify subtle increases or pattern changes that signal a developing fault. As noted in Section 1, pumps have many potential failure modes (imbalance, misalignment, cavitation, bearing failure, etc.), and most of these modes have well-known vibration signatures. For example, misalignment often causes strong vibration at twice the running frequency (2x RPM), while a rolling element bearing with a spalled race will generate specific high-frequency vibration frequencies (the bearing fault frequencies) and a rise in overall high-frequency vibration. Cavitation in a pump (due to low inlet pressure or high vapor content in the fluid) produces broadband vibration and noise, often in a higher frequency range, and sometimes a distinctive sound; accelerometer measurements can detect this as a high-frequency vibration component. By setting up vibration sensors on a pump and analyzing the data, maintenance engineers can catch such issues early. As the Wilcoxon technical notes highlight [6], developing faults will appear as rising vibration levels or emerging spectral components over time, even if overall levels remain below alarm thresholds. Thus, continuous or regular monitoring combined with trend analysis is recommended for effective fault detection in pumps. The benefits are significant: early fault detection through vibration analysis allows repairs to be planned at convenient times, avoids secondary damage (since issues are fixed before catastrophic failure), and extends the equipment's life by preventing operation under fault conditions. In summary, vibration-based predictive maintenance offers minimal downtime, improved reliability, and cost savings compared to run-to-failure approaches.

2.3 Vibration Analysis Principles

The scientific principle behind vibration-based fault detection is that mechanical defects alter the dynamic forces in a machine, which in turn alters the measured vibration signal. To extract meaningful information from raw vibration data, signal processing techniques are used. A typical vibration monitoring process begins with an accelerometer or similar sensor mounted on the pump (usually on the bearing housing or pump casing) that converts the physical vibration into an electrical signal. This signal is a time-domain waveform representing acceleration (or velocity) vs. time. An example waveform might show periodic oscillations at the pump's rotation frequency and gear mesh frequency. To identify specific fault-related components, the time waveform is often transformed into the frequency domain using the Fast Fourier Transform (FFT). The FFT converts the vibration signal into a spectrum of amplitude vs. frequency. This allows clear identification of frequency peaks corresponding to different mechanical sources: e.g. a peak at the gear mesh frequency (GMF) indicates the meshing action of the gears, sideband patterns around the GMF can indicate gear tooth damage, and broadband high-frequency content can indicate turbulence or cavitation. Figure 5 conceptually illustrates this process of going from sensor to spectrum. By analyzing the frequency spectrum, maintenance teams can pinpoint issues such as misalignment, bearing wear, imbalance, gear defects, or looseness. For instance, a strong increase in vibration at a frequency matching a bearing's ball-pass frequency outer race (BPFO) would strongly suggest an outer race defect in that bearing. In addition to spectral analysis, time-domain features like root-mean-square (RMS) amplitude, crest factor, or kurtosis are also useful. A sudden increase in overall RMS vibration level often accompanies faults (and is often used in simple vibration threshold alarms), while changes in statistical features like crest factor can indicate the presence of impacts or spikes in the vibration (potentially from cracked gear teeth or bearing defects). More advanced analysis can involve time-frequency techniques (like wavelet transforms or envelope analysis for bearing faults) to detect transient or modulated signals. These techniques, however, typically require more processing power.

It is worth noting that effective vibration monitoring requires proper selection and mounting of the sensor. Gear pump vibrations span a range of frequencies – typically from a few Hz (for low-speed pumps) up to several kHz. Most pump vibration energy is found in a mid-frequency range (for example, 7.5 Hz to 5000 Hz for common pump and motor issues, covering 450 to 300,000 cycles per minute). An accelerometer chosen for a gear pump should have sufficient bandwidth to capture frequencies up to at least the gear mesh frequency and its harmonics, as well as any higher-frequency fault signatures (like those from bearings or cavitation). For our low-cost system, we use

readily available MEMS accelerometers, which typically have usable frequency ranges up to a few kHz, and we mount them securely on the pump casing near the bearing location to get a clear vibration reading. With these fundamentals, we proceed to designing a practical monitoring system within the constraints of low-cost hardware.

3. Low-Cost Vibration Monitoring System Design

3.1 Hardware Components

The proposed monitoring system is built around an Arduino microcontroller board as the core data acquisition unit. In our implementation, we use an Arduino Uno (ATmega328P-based) board for its simplicity, wide availability, and sufficient analog input capability (figure 5).

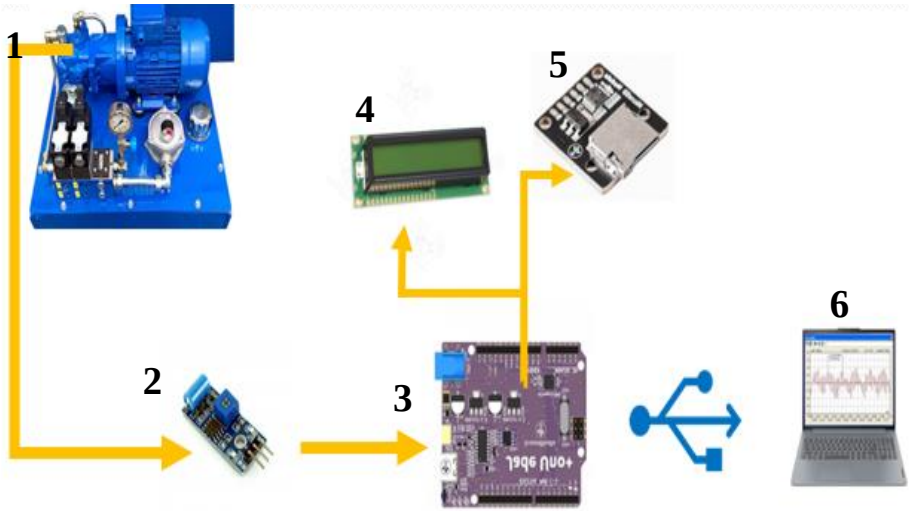

Fig. 5. Block diagram of low-cost gear pump vibration monitoring system

The choice of Arduino provides a low-power, low-cost embedded platform with multiple analog input channels and digital communication interfaces for connecting sensors and modules.
The primary sensor used for vibration measurement is a low-cost vibration sensor module based on a piezoelectric accelerometer. There are several options in this category: one can use a piezoelectric disk or an SW-420 knock sensor module (which detects vibrations via a spring-mass triggering a comparator) or a small MEMS accelerometer (such as the Analog Devices ADXL335 or ADXL345). For better fidelity of vibration measurement, we opted for a MEMS accelerometer (ADXL345) which can provide analog or digital readings of acceleration on one or more axes. The sensor is mounted firmly on the gear pump's casing to capture its vibrations. In our design, a single-axis measurement (vertical or radial direction on the pump body) is typically sufficient to detect most faults, though the system could be expanded to tri-axial sensing if needed.
Besides the accelerometer, the system integrates a few ancillary components to support data logging and user interaction, all of which are inexpensive modules compatible with Arduino. A microSD card module is included to log vibration data locally. This allows the Arduino to record time-stamped vibration readings (either raw or processed) to a file for offline analysis. We also incorporate a basic 16x2 character LCD with an I2C interface for real-time display of readings or status messages. This local display is useful for on-site personnel to observe vibration levels (e.g., the current RMS vibration or peak value) without needing a computer. A few push-buttons and indicator LEDs can be added for user control (such as starting or stopping data logging, or indicating alarm conditions when vibration exceeds a threshold).
The sensor and Arduino assembly are powered by a standard 5 V DC supply; a DC barrel connector and a simple on/off toggle switch are included in the hardware design for convenience.
Figure 5 below shows a block diagram of the system hardware configuration. The accelerometer(2)

sensor (2), attached to the pump (1), connects to the Arduino's (3) analog input (in our case, using analog pin A0). The Arduino reads the sensor's voltage output, which corresponds to the vibration acceleration. The Arduino also interfaces with the microSD card module (5) over an SPI bus (using digital pins 10–13 for CS, MOSI, MISO, SCK respectively, as per the standard Arduino SD library), and with the I2C LCD (4) using the I2C pins (A4/A5 on an Uno, which serve as SDA/SCL).
Power supply and basic controls are omitted for simplicity. In addition, the Arduino's USB connection can be used to stream live data to a computer for real-time analysis or calibration.
The total hardware cost of the components is on the order of tens of dollars (the Arduino board ~$20, accelerometer sensor module $5–$15, SD card module $5, and LCD module $5, plus miscellaneous connectors), making this an economically attractive solution.

3.2 Data Acquisition and Processing

The Arduino-based system samples the vibration sensor signal and processes it to extract useful indicators of pump health. Given the hardware limitations (the Arduino Uno has a 10-bit ADC and runs at 16 MHz), we prioritize simple time-domain processing and decimation of data for logging, rather than performing heavy real-time spectral analysis on the microcontroller. In our setup (see figure 6 and 7), the Arduino continuously reads the analog voltage from the accelerometer at a fixed sampling interval. The sampling rate can be adjusted depending on the expected frequency content of interest – for example, to capture up to around 1 kHz vibration signals, a sampling rate of 2–2.5 kHz (i.e., a read interval of ~0.4 ms) would be chosen to satisfy Nyquist sampling criteria. In practice, using the Arduino's analogRead() in a loop, we achieved sampling rates on the order of a few kHz, which is sufficient to capture gear mesh vibration (typically a few hundred Hz for small pumps) and lower-frequency fault vibrations. If higher frequency resolution is needed (e.g., for detecting early bearing fault frequencies in the 5–10 kHz range), a faster microcontroller or an external ADC might be required. An alternative is to use an ESP32 or similar 32-bit microcontroller, which can sample at tens of kHz and also provide more processing power; indeed, some researchers have demonstrated pump monitoring with an ESP32 at 100 kHz sampling, but here we focus on the Arduino Uno class for cost and simplicity.
The raw vibration readings (in ADC counts corresponding to accelerometer output) are processed in the Arduino firmware to derive basic metrics. One such metric is the RMS vibration level over a given period. The Arduino can compute a running RMS by squaring each sample, accumulating over e.g. 100 ms, then taking the square root of the average. This RMS value gives an indication of overall vibration severity. In our implementation, we compute the average vibration level and display it on the LCD in real time (updated, say, every 0.1 s). Another useful metric is the peak amplitude observed – the Arduino tracks the maximum and minimum values in a moving window, which can capture any sudden jolts or impacts (for instance, if a gear tooth chip causes a transient spike). These simple computed features require minimal processing and memory. The system can be configured with a preset alarm threshold: if the RMS or peak vibration exceeds a certain value (determined based on baseline healthy operation), the Arduino can trigger an alarm indicator (e.g., light an LED or send a notification via serial). In the code, we included a conditional check that if the vibration value rises above a threshold (e.g. a value corresponding to an acceleration of a certain g-level), the system could log an event or activate a visual alert.
For data logging, the Arduino writes timestamped samples or summary statistics to the microSD card. Given the limited storage of the Arduino's RAM, we write data to the SD card in text (CSV) format periodically (for example, writing one line per second containing timestamp, RMS, and peak values). This yields reasonably small log files while still preserving the essential trend information. Alternatively, the raw time-series data can be logged for a short duration if a detailed spectral analysis is to be done offline on a PC. We successfully used the Arduino's serial output in conjunction with a PC software (the Arduino IDE's serial plotter and Microsoft Excel's Data Streamer plugin) to visualize the vibration waveform in real time (see figure 7 [10]).
This approach turns the Arduino into a basic data acquisition (DAQ) device streaming data to a computer, where more advanced processing (like FFT) can be performed with ease.

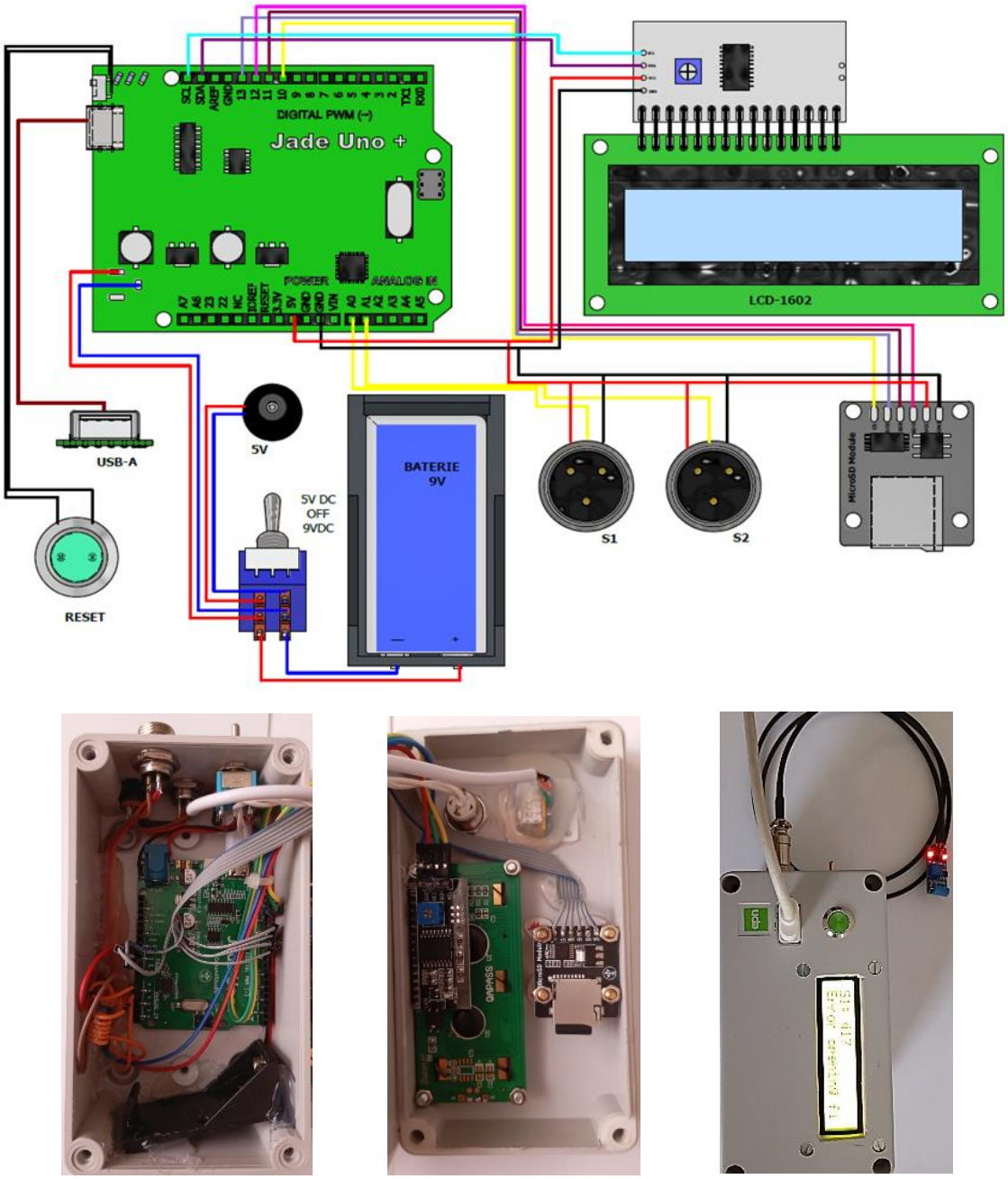

Fig. 6. Experimental setup of low-cost gear pump vibration monitoring system

3.3 System Communication and Integration

Although the core system can function in a stand-alone manner (logging data to SD and displaying values), integration with broader maintenance systems or remote monitoring is often desirable. We have designed the system with flexibility to add communication modules. For instance, the Arduino can be paired with a low-cost Bluetooth or Wi-Fi module (such as the ESP8266 or an HC-05 Bluetooth module) to transmit data wirelessly. This would enable the vibration data to be sent to a central server or to maintenance staff smartphones in real time. In an industrial IoT context, one could use an ESP32 board in place of the Arduino Uno; the ESP32 offers built-in Wi-Fi and Bluetooth, higher sampling capability, and more computing power, all while still being low-cost.
In fact, Brito et al. [7] developed an advanced pump monitoring node using an ESP32-S3 microcontroller that could sample at 100 kHz and perform edge computing for anomaly detection.

Their results showed that even with low-cost hardware, complex models could run on the edge device to detect pump faults with high accuracy. Our system can be seen as a simpler step in that direction: at minimum, it provides the data acquisition foundation upon which more sophisticated analysis (potentially using edge or cloud computing) could be layered. For example, the Arduino could stream vibration data to a Raspberry Pi or an edge gateway that performs machine learning-based anomaly detection (like a one-class classifier to recognize deviations from normal vibration patterns). This modular approach keeps the sensor node inexpensive, while offloading heavier computations to a more capable device if needed.
In summary, the hardware and software design emphasizes simplicity, reliability, and cost-efficiency. All components are easily obtainable and require minimal configuration. This makes the solution attractive for deployment in large numbers across an operation that has many gear pumps, an important consideration since the predictive maintenance benefit increases when coverage of many assets is achieved. We next present some example usage and validation of the system's performance, as well as discuss related implementations to put our work in context.

4. Case Study and Discussion

To evaluate the effectiveness of the proposed monitoring system, we implemented a prototype on a test gear pump setup in a laboratory environment. The gear pump used for testing is a small external gear pump (displacement ~5 cc/rev) driven by an electric motor at approximately 1500 RPM (25 Hz). The vibration sensor module (a piezoelectric accelerometer with sensitivity ~100 mV/g) was attached to the pump housing near the drive-end bearing. The Arduino Uno sampled the accelerometer signal at ~2 kHz and computed the instantaneous vibration level continuously.
Despite the simplicity of on-board processing, the system is quite effective in capturing the key signatures needed for predictive maintenance. The analog measurements can distinguish normal operation from abnormal because faults generally cause a noticeable change in either amplitude or pattern of the vibrations. During our bench tests, a healthy gear pump produced a steady vibration level (with minor fluctuations corresponding to the gear mesh frequency), whereas when we introduced a fault (such as partially loosening the pump mounting to mimic misalignment or adding a small mass to a gear to mimic imbalance), the measured RMS vibration level increased significantly and the waveform showed distinct irregularities. These changes were readily recorded by the Arduino system, confirming that even our low-cost sensor could detect them. In one scenario, a slight bend in the pump's drive shaft led to roughly a 2x increase in the peak vibration reading at 1x rotational frequency, an indication of misalignment, which our system captured and flagged as exceeding the normal threshold. While a high-end analyzer could provide a detailed frequency spectrum to diagnose the issue, our simple system still fulfilled the basic function of fault detection by noticing the deviation from baseline. This demonstrates that a low-cost approach can be viable for condition-based maintenance of gear pumps, especially in settings where only a binary indication of "normal vs abnormal" is needed to prompt a closer inspection.
Even without performing detailed spectral analysis on board, the system clearly captured the changes in vibration due to the faults. Under baseline (healthy) conditions, the pump's vibration signal was relatively steady (see figure 8). When the imbalance fault was introduced, the overall vibration level increased, the Arduino measured values around and the peak readings increased accordingly, often exceeding the preset threshold value (we had set an arbitrary threshold corresponding to 400 Arduino units, for this test). The LCD display on the prototype showed real-time values, and one could see the numbers jump when the imbalance was present. This aligns with expectations, as an imbalance adds a strong rotational frequency component. In the misalignment case, the increase was slightly less dramatic but still noticeable: RMS rose by ~50%, and an interesting variation of the rotation frequency could be seen when we later examined the data in Excel (using a Fourier analysis on the logged data). The Arduino's recorded data file showed a periodic fluctuation a hallmark of misalignment. These findings confirm that the low-cost system can detect changes in the pump's vibration signature that are symptomatic of developing faults.

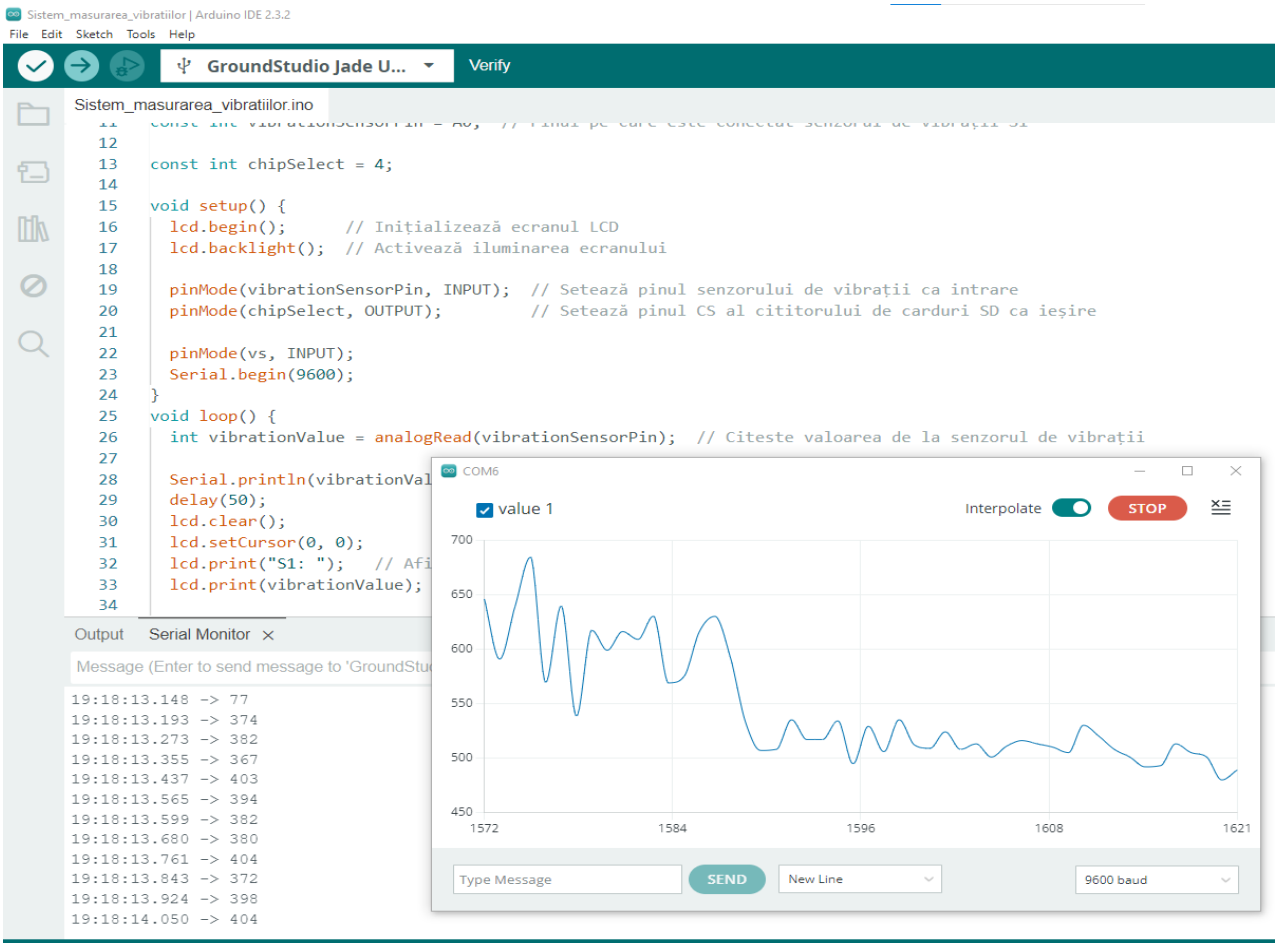

Fig. 7. Arduino code and experimental measurements

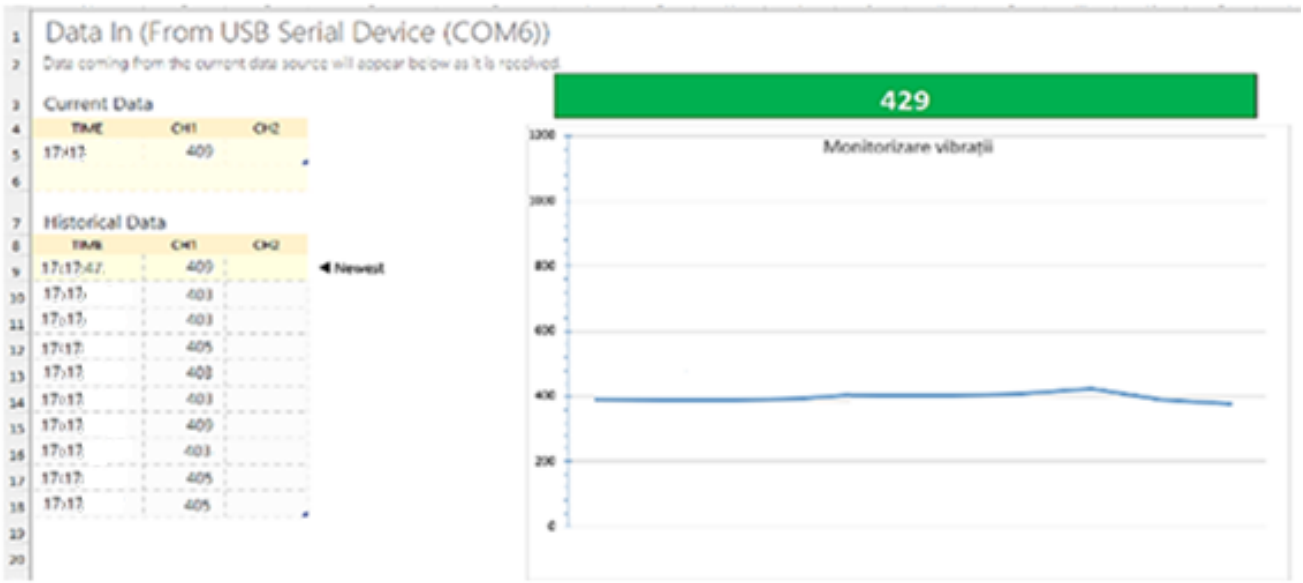

Fig. 8. New pump – baseline condition for pump vibration

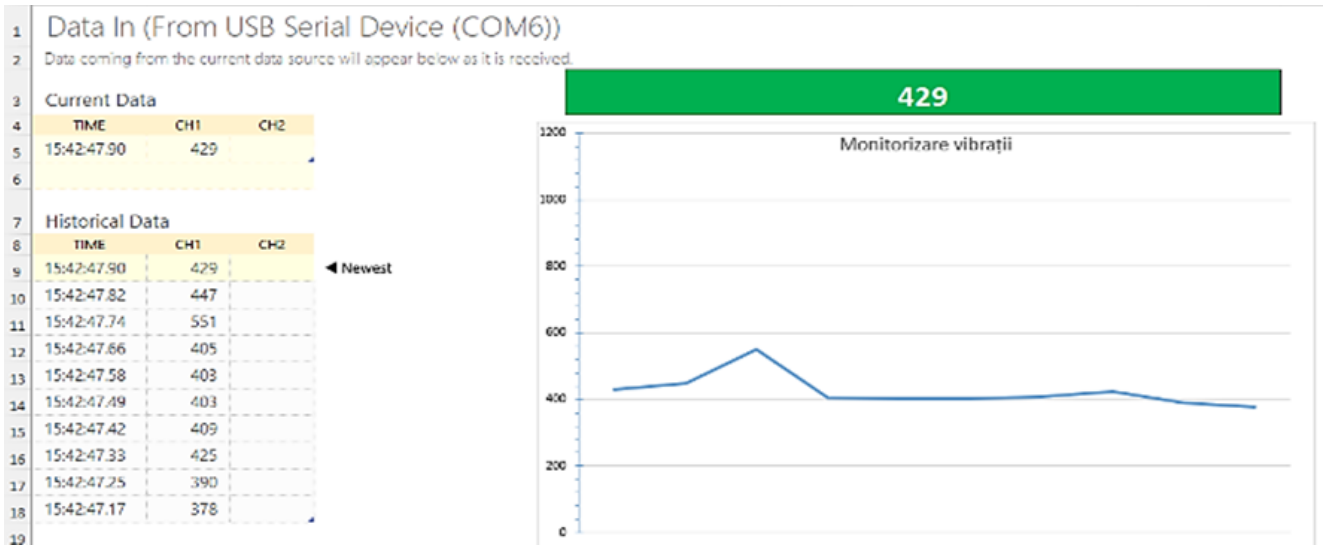

Fig. 9. Fault pump

It is instructive to compare our approach with other similar low-cost monitoring solutions reported. In a recent study, Abidin et al. [8] deployed an Arduino Mega 2560 microcontroller with an ADXL345 accelerometer to monitor water pump vibrations for anomaly detectionpertanika.upm.edu.my.

Their system, much like ours, aimed to provide continuous vibration data at low cost. They demonstrated that even using the Arduino's limited ADC and processing, the device could successfully capture vibration patterns and detect anomalies in a pump's operation. Another work by Brito et al. (mentioned earlier) took a more advanced route: they created an IoT sensor node using an ESP32 and implemented local spectral analysis and unsupervised machine learning models for fault detection. Impressively, their low-cost hardware combined with tailored algorithms achieved near-perfect classification of pump faults in a controlled test bench (100% precision/recall in many configurations).

These examples from literature reinforce the notion that inexpensive hardware, when used thoughtfully, can indeed support effective predictive maintenance. Our system sits on the simpler end of this spectrum, focusing on straightforward time-domain detection, but it can be seen as a building block toward more complex implementations. We have prioritized ease of deployment and user-friendliness; for instance, maintenance technicians can simply install the Arduino and sensor on a pump, and immediately start seeing vibration readings and receive alerts if something is off, without needing specialized training in vibration analysis.

One practical consideration in real-world use is the environmental durability of the sensor node. Industrial environments can be harsh (temperature extremes, moisture, electromagnetic noise). The Arduino and modules should be enclosed in a suitable enclosure (preferably IP65 or better if near fluids) and the sensor firmly glued or bolted to the pump. The power draw of the Arduino and sensor is only a few tens of milliamps, so it can be powered continuously from the machine's power supply or even a battery for a portable setup.

Table 1 provides a qualitative comparison of our low-cost system with a typical high-end vibration monitoring system in the context of gear pump maintenance. While the high-end system offers comprehensive spectral analysis, higher accuracy, and integration with plant monitoring software, it comes at a high cost and complexity. Our Arduino-based system offers the core functionality needed to flag potential issues, at a tiny fraction of the cost, though with limitations in frequency range and analysis detail.

Table 1: Qualitative comparison of the low-cost system with a typical high-end vibration monitoring system

Feature	High-End System	Low-Cost Arduino System
Hardware Cost	$10,000s per unit	$100 (approx.)
Frequency Range	Wide (up to 10–20 kHz or more)	Moderate (reliable up to ~1–2 kHz)
Analysis Capability	Full FFT, advanced diagnostics on device	Basic time-domain analysis on device; deeper analysis offloaded
Output	Detailed spectra, automated fault diagnosis	Overall vibration level, simple alarms
Connectivity	Often integrated with plant network/cloud	Option for add-on (e.g. Wi-Fi, SD card logging)
Deployment	Needs skilled setup & calibration	Simple installation, user-friendly
Use Case	Critical or high-value machinery	Wide deployment on many standard pumps

As seen above, each approach has its place. Not every pump justifies an expensive system [9], especially gear pumps which are generally low-cost components used in large numbers. Our system is meant to fill that niche: it can be deployed on numerous pumps as a “front line” monitoring tool. If it indicates abnormal behavior on a pump, maintenance staff can then follow up with a detailed inspection or bring in a portable analyzer to diagnose the precise fault. This hybrid strategy yields a good cost-benefit balance.

5. Conclusions and Future Work

In this paper, we have presented the development of a low-cost vibration monitoring system for gear-type hydraulic pumps, aimed at facilitating predictive maintenance in industrial settings. The motivation for this work stems from the high prevalence of gear pumps in industry and their vulnerability to wear related failures if left unmonitored. While advanced vibration analysis solutions exist, their cost and complexity often outweigh the value of the pumps in question, leading to a gap in practical condition monitoring for these components. Our proposed solution addresses this gap by leveraging inexpensive hardware, an Arduino microcontroller and basic vibration sensors, to continuously measure and log pump vibration data. The system, although simple, is capable of detecting changes in vibration signatures that indicate common faults such as imbalance, misalignment, or gear damage. By providing real-time feedback and alerts on pump health, it supports maintenance teams in shifting from reactive to predictive strategies, thereby reducing unplanned downtime and extending the service life of equipment.
The prototype implementation demonstrated that even with a 10-bit ADC and limited processing power, the Arduino-based monitor could successfully capture the telltale signs of induced faults on a gear pump. In practice, this means that maintenance personnel can deploy these monitors on multiple pumps and receive early warnings of abnormal vibrations, enabling them to schedule repairs or part replacements before a pump fails in service. The low cost per unit (on the order of tens of dollars) makes it economically feasible to monitor many pumps in parallel, which is a significant advantage for facilities with dozens of similar pumps. Furthermore, the design’s modularity allows integration with higher-level systems: the vibration data can be fed into edge computing devices or cloud platforms for advanced analysis (e.g., machine learning-based anomaly detection) if desired. As an example, recent research has shown that sophisticated anomaly detection algorithms running on IoT hardware can achieve very high fault classification

accuracy for pumps. In the future, our system could incorporate such algorithms once an anomaly is flagged, essentially creating a two-tier monitoring approach, a simple threshold-based detection on the microcontroller, followed by a more detailed analysis on an edge device when needed.
There are several avenues for future work and improvements to this system. First, calibrating the vibration sensor readings to standard units (e.g., mm/s or g) and correlating them with ISO vibration severity levels would make the output more interpretable for maintenance engineers. This would involve a one-time calibration using a known vibration source or comparing with a reference instrument. Second, adding multi-axis sensing and perhaps a second sensor on a different pump location could help in diagnosing the nature of a fault (for instance, comparing axial vs radial vibration could indicate misalignment vs imbalance). Third, implementing basic frequency analysis on the device is conceivable, for example, using an Arduino compatible FFT library to compute a low-resolution spectrum. This could allow the system to recognize specific frequency spikes (like gear mesh frequency) and associate them with certain faults. While the current Arduino Uno might be limited for this, switching to an Arduino Nano 33 BLE Sense or an ESP32 (both of which have more CPU power and even built-in IMUs) could enable edge processing of vibration data, including machine learning classification (TinyML models). This opens the door to an intelligent edge monitoring node that not only detects increased vibration but can classify the likely fault type (as imbalance, bearing, etc.) using trained models, all in real time on the pump.
Another future enhancement is improving the user interface and connectivity. We plan to implement a Bluetooth Low Energy (BLE) link so that a technician can wirelessly retrieve data on a tablet or smartphone from the pump-mounted Arduino unit. This would simplify data collection from multiple pumps without needing to physically access each one's SD card. In a plant-wide scenario, a mesh network of such wireless vibration sensors could feed into a central dashboard, offering a comprehensive overview of all gear pumps' condition. This aligns well with Industry 4.0 initiatives where legacy equipment (like simple gear pumps) can be retrofitted with smart sensors to become part of the IoT ecosystem for maintenance.
Finally, field validation of the system in an actual industrial environment would be an important step. Our lab tests are promising, but long-term deployment under real operating conditions would provide insight into reliability (e.g., sensor attachment durability, noise handling, etc.). We envision running a pilot program where a handful of pumps in a hydraulic power unit or manufacturing line are instrumented with the system, and the vibration trends are monitored over several months. Success would be measured by whether the system can catch anomalies that correspond to known wear (for example, detecting a slowly increasing vibration that leads to a scheduled bearing replacement, as opposed to an unexpected failure). We will also gather user feedback from maintenance technicians to refine the alert thresholds and output format (perhaps integrating with existing maintenance software).
In conclusion, the research and development presented here shows that a predictive maintenance approach for gear pumps is achievable with minimal investment, using accessible technology. By focusing on the core requirement, detecting abnormal vibration behavior, our low-cost monitoring system enables a broader adoption of predictive maintenance practices even for smaller, cost-sensitive components like gear-type hydraulic pumps. This contributes to improved overall equipment effectiveness in industrial operations, reducing downtime and maintenance costs. Future integrations with edge computing and IoT networking will further enhance the capabilities, making the system a valuable part of modern smart maintenance toolkits.

Acknowledgments

The paper and testing were made possible by the Laboratory of Master's degree program Reliability and Maintenance of Mechanical Systems within the Faculty of Automotive, Mechatronics and Mechanical Engineering at the Technical University of Cluj-Napoca.

References

[1] Hyspeco. *The Main Uses for Different Types of Hydraulic Pumps*. Hyspeco Blog, August 9, 2024.

[2] Epson Sensing Device. *What are Vibration Sensors? – Pump Vibration Measurement*. Technical Column, Epson Device, 2023.
[3] Hydraulic Institute. *Condition Monitoring on a Budget*. Pump Systems Matter Newsletter, June 15, 2021.
[4] Knower Network. *Recommended Vibration Analysis Tools and Technology for Predictive Maintenance*. KnowerNetwork.com, October 20, 2025.
[5] Osman, A.H., Mohamed H. Gobran, and Farouk F. Mahmoud. “Vibration Signature of Normal and Notched Tooth Gear Pump.” *European Scientific Journal* 15, no. 15 (May 2019): 64–75.
[6] Wilcoxon Sensing Technologies. *Pump Monitoring: 3 Warning Signs Your Vibration Signal Is Corrupted*. Wilcoxon Technical Blog, 2023.
[7] Brito, Sérgio Duarte, Gonçalo José Azinheira, Jorge Filipe Semião, Nelson Manuel Sousa, and Salvador Pérez Litrán. “Non-Intrusive Low-Cost IoT-Based Hardware System for Sustainable Predictive Maintenance of Industrial Pump Systems.” *Electronics* 14, no. 14 (2025): 2913.
[8] Mohd, Azahar, Khairil Anas Md Rezali, Sharafiz Abdul Rahim, Mohammad Yazdi Harmin, Abdul Murad Zainal Abidin, and Mohamad Fikri Mohamad Yunus. “Effective Vibration-Based Anomaly Detection in Water Pump Operation Using Arduino Microcontroller.” *Pertanika Journal of Science and Technology* 33, no. 2 (March 2025): 725–744.
[9] Liao, J., J. Zheng, and Z. Chen. “Research on the Fault Diagnosis Method of an Internal Gear Pump Based on a Convolutional Auto-Encoder and PSO-LSSVM.” *Sensors* 22, no. 24 (2022): 9841.
[10] Zudor, S. A. *Hydraulic pump monitoring system for predictive maintenance*. Master degree work on Reliability and maintenance of mechanical systems, 2024.

ISSN 1454 - 8003
Proceedings of 2025 International Conference on Hydraulics and Pneumatics - HERVEX
November 19-21, Băile Govora, Romania

FLOW SPIKE ATTENUATION FOR ELECTROHYDRAULIC UNIT WITH MIXED ANALOG AND DIGITAL CONTROL

Marian BLEJAN[1], Robert BLEJAN[1], Carmen-Anca SAFTA[2], Alexandru IONESCU[3]

[1] National Institute of Research & Development for Optoelectronics/ INOE 2000 – Subsidiary Hydraulics and Pneumatics Research Institute / IHP, Bucharest, Romania

[2] National University of Science and Technology POLITEHNICA Bucharest, Romania

[3] The National Institute of Research – Development for Machines and Installations Designed for Agriculture and Food Industry – INMA Bucharest, Romania

blejan.ihp@fluidas.ro, robertblejan@yahoo.com, carmen.safta@upb.ro, alex.alex12alx@gmail.com

Abstract *Recent advances in digital hydraulics, direct-drive hydraulics (DDH), and pump-controlled architectures have opened new possibilities for energy-efficient solutions. In this work, we present a hybrid approach for converting electrical energy into hydraulic energy with superior efficiency. The method combines Digital Flow Control (DFC) — through valve switching with predefined flow rates—with induction motor speed regulation via a frequency converter. Simulation results confirm the benefits of this strategy, showing reduced hydraulic shocks and highly flexible flow control.*

Keywords: *Asynchronous motor, digital hydraulics, DDH, electrohydraulic, mixed actuation, MATLAB/Simulink*

1. Introduction

Variable-flow hydraulic power units are traditionally based on variable-displacement pumps driven by constant-speed motors. While widely used, these systems face challenges such as structural complexity, reduced reliability, high costs, and the need for specialized adjustments. Recent research proposes several strategies to improve efficiency and flexibility in electrohydraulic systems, including digital pumps with multi-valve switching [1], fast-switching valves for discrete flow control [2], induction motors with frequency converters [3], and hybrid control methods [4–7].
Digital hydraulics has evolved to meet modern industrial demands, prioritizing energy efficiency in drive systems [1, 9–12]. A notable milestone was achieved in 1984 with the development of a 1.5 MW hydrostatic wind-turbine transmission using a Digital Displacement (DD) ring-cam pump and two DD generator drive motors [8]. These advancements highlight the potential of combining digital control concepts with conventional hydraulics to achieve superior performance.
Digital hydraulics is defined as a system that controls fluid flow using modulated, discrete digital signals to achieve active and intelligent output control [13]. It offers key advantages such as improved energy efficiency, linearity, control flexibility, robustness, and reduced sensitivity to oil contamination [14]. Digital hydraulic technology is generally categorized into three types:
(i) **Parallel digital hydraulics** – components connected in parallel;
(ii) (ii) **High-speed switching hydraulics** – on/off valves controlled by PWM signals;
(iii) (iii) **Stepping digital hydraulics** – stepping motors driven by discrete digital signals [1, 13].
New hydraulic devices based on digital hydraulics are increasingly replacing conventional components. For example, the Digital Flow Control Unit (DFCU) is a parallel valve assembly with a full response time of only 2 ms [13–15]. In addition to pulse-based modulation techniques—such as PWM, PCM, and PFC—for discrete flow control via parallel on/off valves, digital hydraulics employs intelligent algorithms (e.g., reinforcement learning) to improve motion accuracy and energy efficiency [12, 16–22].
Digital Displacement Pumps and Motors (DDPMs) represent another major innovation, replacing traditional displacement machines. This technology uses high-speed digital on/off valves to control

the displacement of cam-piston pumps and motors [22]. Reported efficiencies reach 97% at full displacement and 80% at 20% displacement [22].
Direct-Driven Hydraulics (DDH) offers an efficient solution for flow regulation in hydraulic systems. This technology leverages advancements in permanent magnet synchronous motors (PMSMs), enabling precise speed control and supporting hydrostatic transmission architectures where pump flow is continuously modulated by motor speed. DDH systems stand out for their high energy efficiency, superior dynamic response, broad applicability, and seamless integration with PLCs [23–26].
This paper presents a hybrid control strategy that segments the flow range of a hydraulic power unit using digital switching of fixed-displacement pumps. Within each segment, flow is continuously regulated by adjusting the induction motor speed. This approach ensures proportional flow control while reducing mechanical complexity and minimizing hydraulic shocks.

2. Control actuation strategy

This paper continues to analyse the two methods proposed in paper [27] for generating flow proportional to a given command in a hydraulic power unit. Both approaches segment the flow range using digital switching of fixed-displacement pumps, while proportionality within each segment is achieved by varying the induction motor speed, based on direct-drive principles. The motor operates between 50% and 100% of its nominal speed, ensuring optimal efficiency and torque characteristics (93–100% of nominal torque, see Fig. 1).

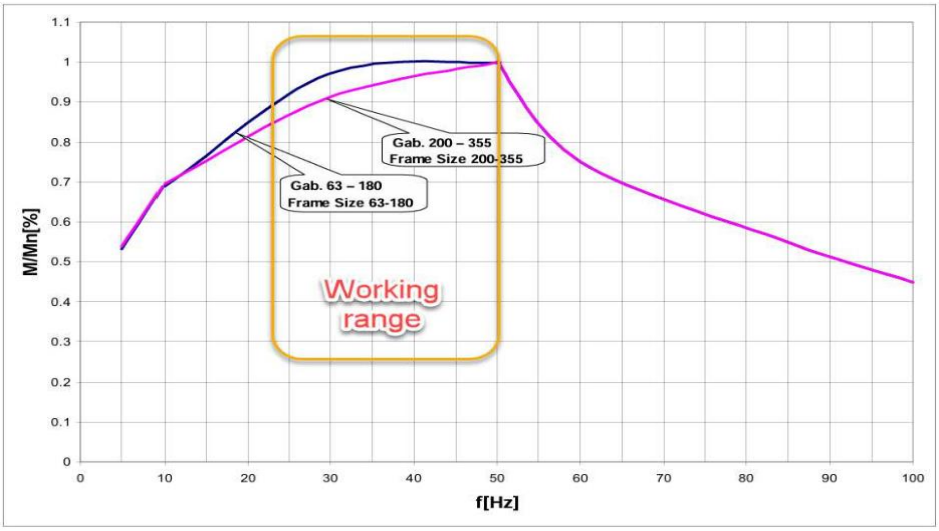

Fig. 1. Load capacity graph with frequency converter (data from UMEB – General-purpose three-phase induction motors catalogue) [27]

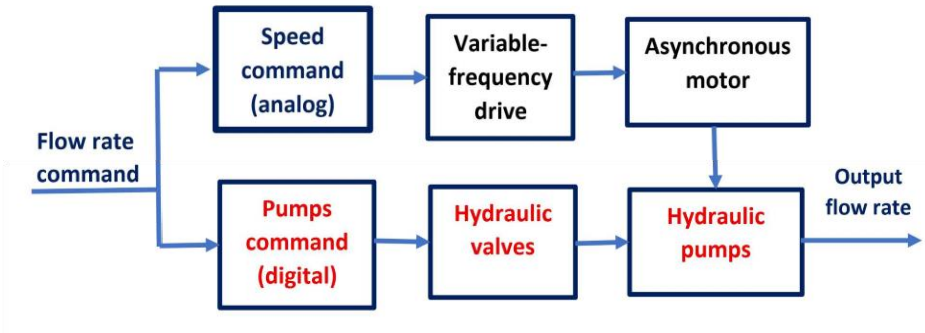

Fig. 2. Block diagram of the electro-hydraulic unit with mixed control [27]

To reduce the amplitude of hydraulic shocks, a hydraulic inductance is proposed to be connected in series with the load of the hydraulic unit.
The bloc diagram of the two proposed control methods for hydraulic drive systems is presented in Figure 2, highlighting the integration between electronic and hydraulic components for optimized performance. Thus, the coarse flow adjustment is performed through digital control, while the fine adjustment is achieved by varying the rotational speed of the electric motor by DDH control [27].
So, by employing *N* fixed-displacement pumps, with displacements arranged in a geometric progression of ratio 2 and driven by an asynchronous motor operating within a speed range from half the nominal speed to the nominal speed, a continuous flow regulation range from $V_g \cdot \frac{n}{2}$ to $V_g \cdot n \cdot (2^N - 1)$ can be achieved.
Here, V_g denotes the smallest displacement among the fixed pumps, and n represents the nominal rotational speed of the electric motor.
Thus, the flow range is divided into $2 \cdot (2^N - 1)$ equal intervals. For each interval, the two control signals required for the mixed control of the flow rate will be computed: the digital control of the active/inactive hydraulic pumps and the analog control of the asynchronous motor speed [27].
In Figures 3 and 4 are given the algorithms of the control in the C language implementations for both methods of the control for computing the digital and analog control signals based on the desired flow rate value. The case of using four hydraulic pumps is presented, where represents the flow control input, defined over the range [1, 30]. The values of *p0*, *p1*, *p2* and *p3* represent the hydraulic pumps control, where a value of 0 indicates an inactive pump and a value non-zero indicates an active pump. The value of *n* is asynchronous motor speed.

```
//C language implementation

float u;//desired flow rate in the range [1,30) float n;//
motor speed in percent [50%,100%] int
p0,p1,p2,p3;//pumps control

// analog control

// asynchronous motor speed

n= ((u>=1)&&(u<2))?( 50*u):

    ((u>=2)&&(u<4))?( 50*u/2):

    ((u>=4)&&(u<8))?( 50*u/4):

    ((u>=8)&&(u<16))?( 50*u/8):

    ((u>=16)&&(u<30))?( 50*u/15);

//digital control

//hydraulic pumps control
p0=((u>=1)&&(u<2))||(u>=16)&&(u<30));
p1=((u>=2)&&(u<4))||(u>=16)&&(u<30));
p2=((u>=4)&&(u<8))||(u>=16)&&(u<30));
p3=((u>=8)&&(u<16))||(u>=16)&&(u<30));
```

Fig. 3. Algorithm for Method 1

```
// C language implementation

#include <math.h>

float u;//desired flow rate in the range [1,30) float n;//
motor speed in percent [50%,100%] int
p0,p1,p2,p3;//pumps control

// analog control

// asynchronous motor speed

n= (u<16)?( 50*u/floor(u)):(50*u/15);

//digital control

// hydraulic pumps control p0=(floor(u)&1);
p1=((floor(u)&2)>>1); p2=((floor(u)&4)>>2);
p3=((floor(u)&8)>>3);
(u>=16)?(p0=p1=p2=p3=1):(1);
```

Fig. 4. Algorithm for Method 2

3. Flow spike attenuation

Spike reduction will be achieved by implementing a hydraulic inductance in series with the output of the hydraulic unit.
Hydraulic inductance or hydraulic inertance is the resistance to changes in fluid flow rate, analogous to electrical inductance. It is caused by the inertia of the fluid and is quantified by the mass of the fluid in motion and the geometry of the passageway. Just as an electrical inductor resists changes in current, a hydraulic inductor resists changes in fluid flow, requiring a pressure difference to accelerate the fluid.

In fluid mechanics [28], **inertance** is a measure of the pressure difference in a fluid required to cause a unit change in the rate of change of volumetric flowrate with time. The base SI units of inertance are (kg m^{-4}) or (Pa s^2 m^{-3}) and the usual symbol is *I*. The inertance of a pipe is given by:

$$I = \frac{\rho \ell}{A} \tag{1}$$

where: ρ (kg/m^3) the density of the fluid, ℓ (m) is the length of the pipe, A (m^2) is the cross-sectional area of the pipe.

The pressure difference is related to the change in flowrate by the equation:

$$\Delta p = I\dot{Q} = I\frac{\mathrm{d}Q}{\mathrm{d}t} \tag{2}$$

where: Δp (Pa) is the pressure of the fluid, Q (m^3/s) is the volumetric flowrate.
This equation assumes constant density, that the acceleration is uniform, and that the flow is fully developed "plug flow". This precludes sharp bends, water hammer, and so on.
To some, it may appear counterintuitive that an increase in cross-sectional surface of a pipe reduces the inertance of the pipe. However, for the same mass flowrate, a lower cross-sectional area implies a higher fluid velocity and therefore a higher pressure difference to accelerate the fluid.

4. Numerical simulation and results.

Numerical simulations of the proposed algorithms were carried out in MATLAB using Simulink and the Simscape library, which enables modeling of hydraulic drive systems. The simulation scheme of the hydraulic unit is shown in Figure 5. For dynamic behavior, Simscape models were applied; according to MATLAB documentation, these models neglect fluid inertia and spool loading. The electric motor was represented as a first-order system with the transfer function:

$$H(s) = \frac{1}{0.0002s+1} \tag{3}$$

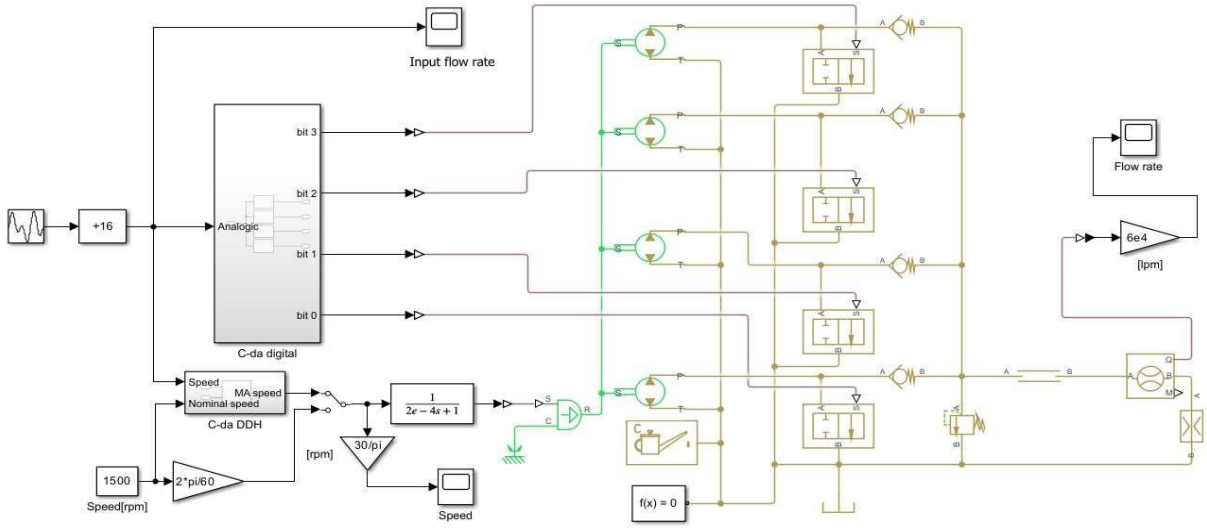

Fig. 5. MATLAB/Simulink/Simscape simulation diagram of the hydraulic unit [27]

The scheme includes a 'C-da digital' block that receives the flow command from a generator and generates control signals for the distributors activating or deactivating four fixed-displacement pumps. The algorithm for 'C-da digital,' implemented in MATLAB/Simulink, is shown in Figure 3 for Method 1 and Figure 4 for Method 2 [27].

The pumps used in the simulation have displacements in geometric progression: 2, 4, 8, and 16 cm³/rev. Driven by an asynchronous motor at a nominal speed of 1500 rpm, their nominal flow rates are 3, 6, 12, and 24 L/min. The minimum flow is achieved by operating the smallest pump at half speed (≈1.5 L/min), while the maximum flow results from all pumps running at nominal speed, respectively: $(2cm^3 + 4cm^3 + 8cm^3 + 16cm^3) \cdot 1500rpm = 45$ L/min [27].

To generate the speed command for the hydraulic pumps, the flow range is divided into 30 equal intervals of 1.5 L/min. For each interval, a control configuration for active and inactive pumps is determined according to the selected method. Additionally, a linear ramp command for motor speed is applied within each interval to ensure smooth variation of total flow. These commands are computed by the 'C-da digital' and 'C-da DDH' blocks (Figure 5). Continuous flow adjustment from 1.5 to 45 L/min is achieved using two methods, each with specific advantages and limitations, assuming a quasi-static variation of the flow command (Figure 6). Method 1 operates the 2 cm³/rev, 4 cm³/rev, 8 cm³/rev, and 16cm³/rev pumps successively, with a linear increase in speed from 750 rpm to 1500 rpm. Finally, all the pumps are operated simultaneously, also with a linear speed increase from 750 rpm to 1500 rpm (see Figures 7 and 8) [27].

Method 2 activates pumps based on the binary representation of numbers from 1 to 15. Within each interval, speed varies from 750 rpm to a value that ensures a linear, continuous increase in flow according to the command. In the upper half of the range, pump control follows the same logic as Method 1 (Figures 11 and 12). The motor speed command is computed by the 'C-da DDH' block, using the input flow command and the algorithm shown in Figure 4.

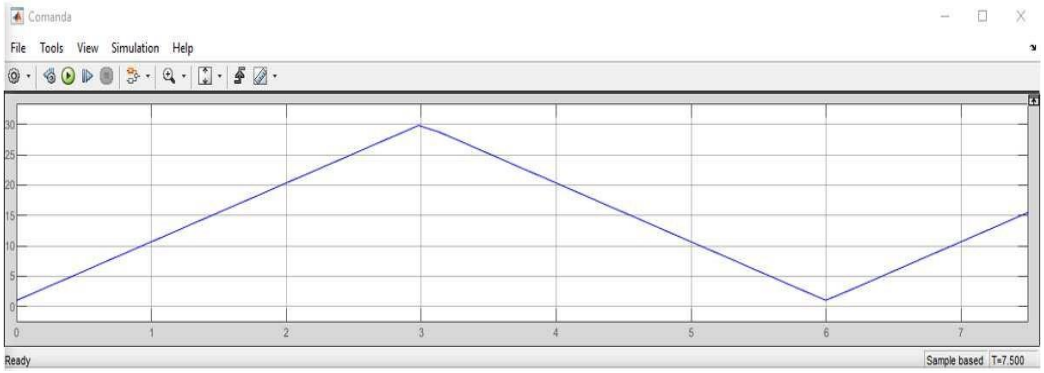

Fig. 6. Flow command: time (s) on the *X*-axis, desired flow on the *Y*-axis [27]

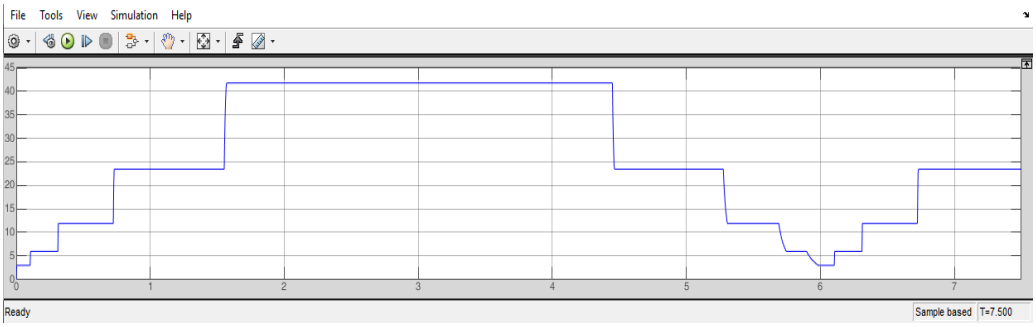

Fig. 7. Flow with digital control, Method 1 [27]

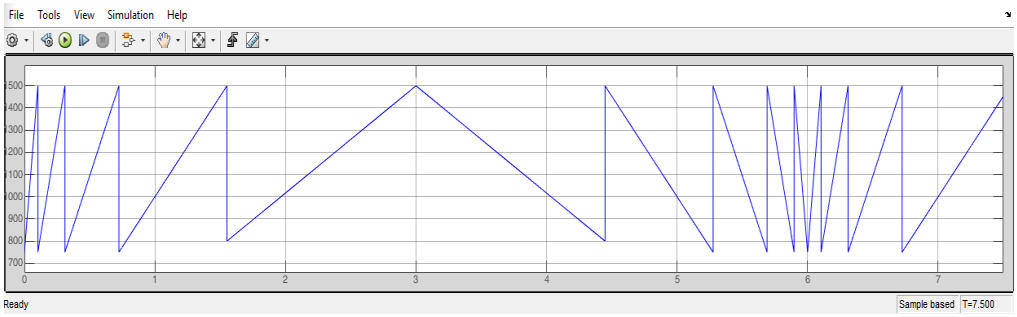

Fig. 8. Motor speed control, Method 1 [27]

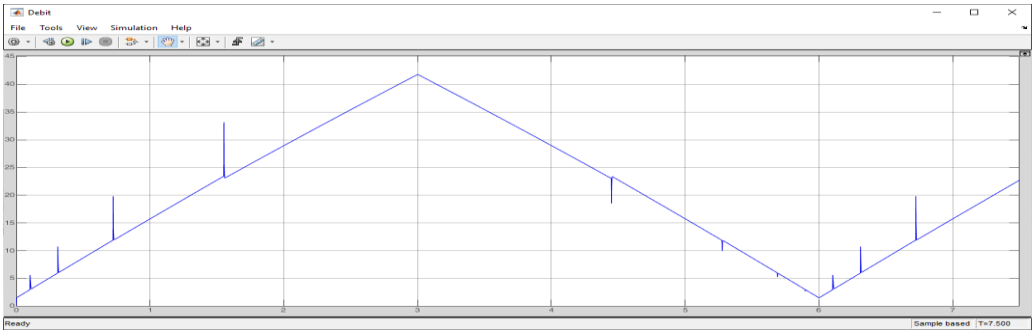

Fig. 9. Flow delivered by the hydraulic unit, Method 1 [27]

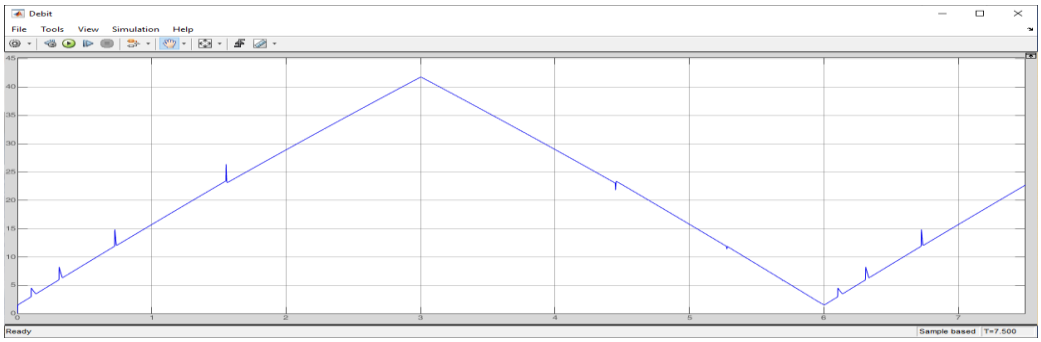

Fig. 10. Output flow with spike reduction, Method 1

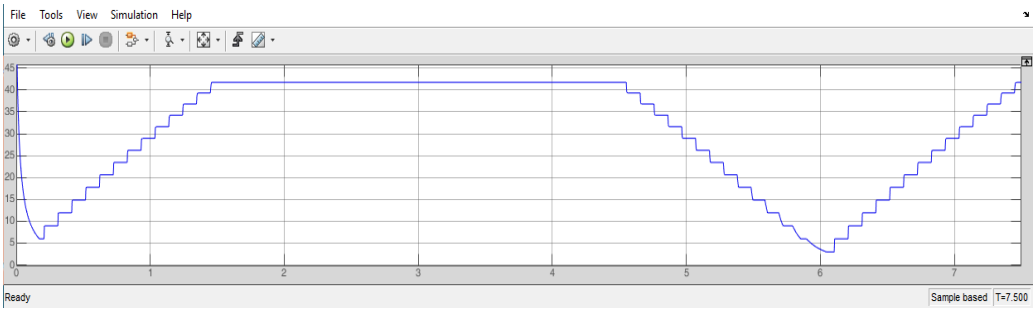

Fig. 11. Flow with digital control, Method 2 [27]

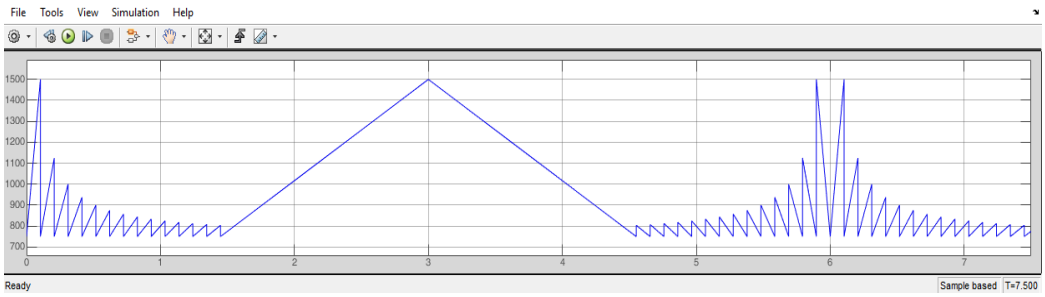

Fig. 12. Motor speed control, Method 2 [27]

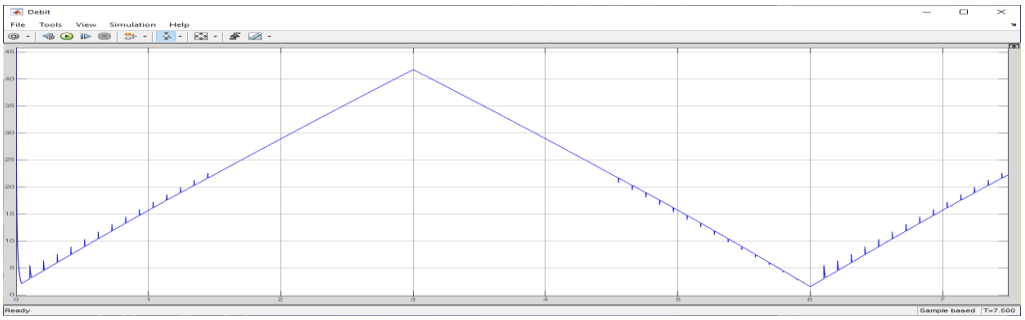

Fig. 13. Flow delivered by the hydraulic unit, Method 2 [27]

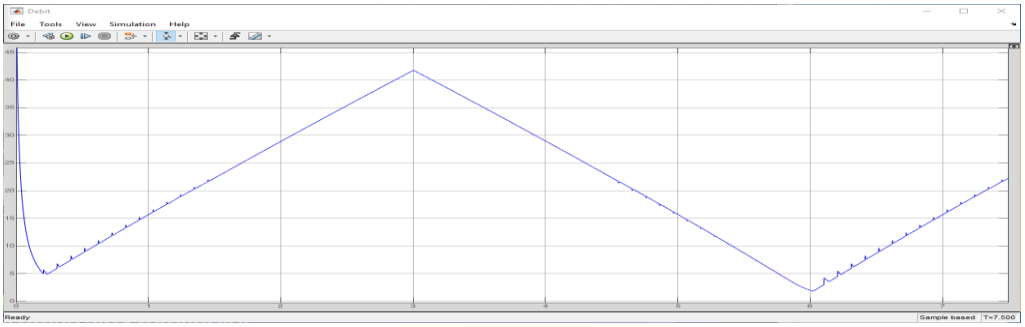

Fig. 14. Output flow with spike reduction, Method 2

In figures above, time (in seconds) is plotted along *x*-axis, and flow rate (in L/min) along *y*-axis.
When applying to both commands, digital and analog, simultaneously, the time variation of the delivered flow is shown on Fig. 9 and Fig. 13. Thus, Method 1 uses four pump switching events across the flow range (Fig. 9), while Method 2 requires fifteen switching events. (Fig. 13).
Regarding motor speed control: in Method 1, motor speed varies between 50% and 100% for each pump configuration.
In Method 2, motor speed for a given pump configuration varies within 50% and $\frac{x}{[x]} \cdot 50\%$, where *x* is the desired flow rate, ranging from 1 to 15.
The hydraulic inductance was implemented using a circular pipe 3 m in length and 4 mm in diameter. The results obtained using the hydraulic inductance to filter flow spikes are shown in Fig. 10 for Method 1 and in Fig. 14 for Method 2.
Depending on the application of the electro-hydraulic unit, Method 1 or Method 2 can be chosen: the first method provides fewer pump switching but larger hydraulic shocks, whereas the second method involves more frequent switching with lower-amplitude shocks.
Regarding the selection of the hydraulic unit control method based on the application: Method 1, which generates significant amplitude shocks, is suitable for driving high-inertia loads, as load's inertia helps dampen the spikes – for example, hydraulic traction system for locomotives. Method 2 is more appropriate for low-inertia loads, such as hydraulic positioning systems or servomotors.

4. Conclusions

This paper is the development of paper [27] regarding the reducing amplitude of hydraulic shocks generated by the dynamic behavior of a controlled hydraulic drive system.
Two solutions for generating hydraulic flow proportional to a commanded input are proposed, combining digital and direct-drive hydraulics. Mathematical models were developed and validated through numerical simulations to assess performance, including:

- operating flow range (Q…30Q, i.e., 3.33%–100%);
- magnitude of shocks from pump switching;
- methods to reduce shock amplitude using hydraulic inertance.

To further reduce hydraulic shocks, a series hydraulic inductance was introduced.
Algorithms were designed to convert flow commands into pump activation signals and motor speed control, implemented via a dedicated software application. Future work will include dynamic analysis and experimental validation under static and dynamic conditions.

Acknowledgments

This work was carried out through the Core Program within the National Research Development and Innovation Plan 2022-2027, carried out with the support of MCID, project no. PN 23 05.

References

[1] Linjama, M. “Digital Fluid Power – State of the art.” Paper presented at the Twelfth Scandinavian International Conference on Fluid Power, Tampere, Finland, May 18-20, 2011.
[2] Rahmfeld, R., and M. Ivantysynova. “Energy saving hydraulic actuators for mobile machines.” Paper presented at the he 1st Bratislavian Fluid Power Symposium, Casta-Pila, Slovakia, June 2–3, 1998.
[3] Tammisto, H., and T. Linjama. “Pump-Controlled Differential Cylinder Using Digital Flow Control Unit.” Paper presented at the ASME/BATH 2014 Symposium on Fluid Power and Motion Control, Bath, United Kingdom, September 10–12, 2014.
[4] Johnson, D. F. R. *Electrohydraulic Control Systems*. Springer, 2018.
[5] Watton, J. *Fundamentals of Fluid Power Control*. Cambridge University Press, 2009.
[6] Ehsan, Md., W. H. S. Rampen, and Stephen Salter. “Modeling of Digital-Displacement Pump-Motors and Their Application as Hydraulic Drives for Nonuniform Loads.” *Journal of Dynamic Systems Measurement and Control* 122, no. 1 (2000): 210-215.
[7] Padovani, D., M. Rundo, P. Fresia, and G. Altare. “Energy analysis of a hybrid electro-hydraulic system for efficient mobile hydraulics.” *Journal of Physics: Conference Series* 2648 (2023): 012051.
[8] Rampen, Win, Daniil Dumnov, Jamie Taylor, Henry Dodson, John Hutcheson, and Niall Caldwell. “A Digital Displacement Hydrostatic Wind-turbine Transmission.” *International Journal of Fluid Power* 22, no. 1 (2021): 87–112. doi: 10.13052/ijfp1439-9776.2213.
[9] Li, W., Z. Zhang, T. Liu, H. Cao, T. Ni, and Y. Wang. “Analysis of and Experimental Research on a Hydraulic Traction System Based on a Digital Hydraulic Transformer.” *Sensors* 22, no. 10 (2022): 3624. https:// doi.org/10.3390/s22103624.
[10] Huova, M., A. Aalto, M. Linjama, K. Huhtala, T. Lantela, and M. Pietola. “Digital hydraulic multi-pressure actuator – the concept, simulation study and first experimental results.” *International Journal of Fluid Power* 18, no. 3 (2017): 141-152, DOI: 10.1080/14399776.2017.1302775.
[11] Ganziuc, A., N. Vasiliu, R. Pulhalschi, and S. Feher. “Using digital electrohydraulic servovalves in fluid control systems.” *U.P.B. Sci. Bull., Series D* 75, no. 4 (2013): 229-238.
[12] Pedersen, N. H., P. Johansen, L. Schmidt, R. Scheidl, and T. O. Andersen. “Control and Performance Analysis of a Digital Direct Hydraulic Cylinder Drive.” *International Journal of Fluid Power* 20, no. 3 (2020): 295–322. doi: 10.13052/ijfp1439-9776.2032.
[13] Zhang, Q., X. Kong, B. Yu, K. Ba, Z. Jin, and Y. Kang. “Review and Development Trend of Digital Hydraulic Technology.” *Appl. Sci.* 10, no. 2 (2020): 579. doi:10.3390/app10020579.
[14] Pan, M., and A. Plummer. “Digital switched hydraulics.” *Frontiers of Mechanical Engineering* 13, no. 2 (2018): 225–231. https://doi.org/10.1007/s11465-018-0509-7.
[15] Elsaed, E., and M. Linjama. “A Review of Pilot-operated Hydraulic Valves – Development, Challenges, and a Comparative Study.” *International Journal of Fluid Power* 24, no. 4 (2023): 683–724.

[16] Donkov, V. H., T. Ol. Andersen, M. Linjama, and M. K. Ebbesen. “Digital Hydraulic Technology for Linear Actuation: A State of the Art Review.” *International Journal of Fluid Power* 21, no. 2 (2020): 263–304. https://doi.org/10.13052/ijfp1439-9776.2125.
[17] Sciatti, F., P. Tamburrano, E. Distaso, and R. Amirante. “Digital Hydraulic Technology: Applications, Challenges, and Future Direction.” *Journal of Physics: Conference Series* 2648 (2023): 012053.
[18] Kogler, H. “Digital Hydraulic Transformer Concepts for Energy-Efficient Motion Control.” *Actuators* 14, no. 2 (2025): 54. https://doi.org/10.3390/act14020054.
[19] Pedersen, N. H., P. Johansen, and T. O. Andersen. “Challenges with Respect to Control of Digital Displacement Hydraulic Units.” *Modeling, Identification and Control* 39, no. 2 (2018): 91-105. https://doi.org/10.4173/mic.2018.2.4.
[20] Schmidt, L., M. Groenkjaer, H. C. Pedersen, and T.O. Andersen. “Position Control of an Over-Actuated Direct Hydraulic Cylinder Drive.” *Control Engineering Practice* 64 (2017): 1–14.
[21] Ozalp, A. F., R. Polat, C. Cetinkaya, and M. H. Cetin. “Investigation of a Digital Hydraulic Valve Operated by Servo Motors.” *Eng. Technol. Appl. Sci. Res.* 11, no. 6 (2021): 7957–7963.
[22] Darnet, J., and É. Bideaux. “State-of-the-art of Variable Displacement Technologies for Radial Piston Hydraulic Machines”. Paper presented at the Bath/ASME Symposium on Fluid Power and Motion Control (FPMC) 2022, Bath, United Kingdom, September 14–16, 2022.
[23] Zhang, S., A. Wu, and F. Dai. “Active Disturbance Rejection Control for Double-Pump Direct-Driven Hydraulics.” *Proceedings* 64, no. 1 (2020): 14. doi:10.3390/IeCAT2020-08497.
[24] Zakharov, V., and T. Minav. “Influence of Hydraulics on Electric Drive Operational Characteristics in Pump-Controlled Actuators.” *Actuators* 10, no. 12 (2021): 321. https://doi.org/10.3390/act1012032.
[25] Ketelsen, S., D. Padovani, T. O. Andersen, M. K. Ebbesen, and L. Schmidt. “Classification and Review of Pump-Controlled Differential Cylinder Drives.” *Energies* 12, no. 7 (2019): 1293. doi:10.3390/en12071293.
[26] Bonato, C., T. A. Minav, P. Sainio, and M. Pietola. “Position control of direct driven hydraulic drive.” Paper presented at the 8th Ph.D Symposium on Fluid Power FPNI2014, Lappeenranta, Finland, June 11-13, 2014.
[27] Blejan, Robert, Marian Blejan, and Carmen-Anca Safta. “Electro-hydraulic Unit with Mixed Control.” Paper presented at the ATEE 2025 IEEE Conference, Bucharest, Romania, October 9-11, 2025, https://atee.upb.ro/atee2025/.
[28] Massey, B.S. *Mechanics of Fluids.* Chapman & Hall, 1989.

ISSN 1454 - 8003
Proceedings of 2025 International Conference on Hydraulics and Pneumatics - HERVEX
November 19-21, Băile Govora, Romania

MECHATRONIC ENGINEERING – SCIENTIFIC SUPPORT FOR THE EFFICIENCY AND COMPETITIVITY OF INTELLIGENT INDUSTRY (4.0)

Florentina BADEA[1], Sorin Ionuț BADEA[1], Cristian Radu BADEA[1], Despina Paula DUMINICĂ[2]

[1] National Institute of Research Development in Mechatronics and Measurement Technique – INCDMTM Bucharest, florentina.badea@incdmtm.ro

[2] National University of Science and Technology Politehnica Bucharest, despina.duminica@gmail.com

Abstract: *The scientific paper deals with the role and support of Mechatronic Engineering and the competitivity of Intelligent Industry (4.0), presenting the generative developments of the new field and highlighting scientific and technological advances and innovative concepts. The scientific work also responds to the paradigm challenge of the European strategy to create and develop new scientific concepts and new intelligent multi-applied systems in new industrial and engineering value chains for the efficiency of products eco-innovation. Moreover, mechatronic engineering and respectively complex mechatronic products and systems are used in smart networks, with embedded sensors, with processing and actuation, made to take data and interact, the physical world with the virtual world, supporting in real time, performance assurance and applications in industry, economy and society.*
Also, the scientific paper concretely presents the adaptability of the new complex mechatronic concept, the realization of ultra-precise complex mechatronic systems of intelligent 3D control, in the industrial and laboratory metrological process, the realization of ultra-precise complex mechatronic systems of multi-application 3D remote control and remote monitoring in industrial and laboratory processes, the realization of Data and IT&C systems, necessary for the integration of the physical system with the virtual system, etc.
The 3D mechatronic systems, realize the functions of 3D remote control and remote monitoring within intelligent industrial processes.

Keywords: *Mechatronic engineering, competitivity of intelligent industry (4.0), European strategy paradigm, new scientific concepts, intelligent systems, new industrial value chains*

1. Introduction

The paper addresses the “challenge of the European strategy paradigm to create and develop new scientific concepts and new intelligent systems replicated in new industrial value chains,” which requires focusing, combining, and fusing various competencies and innovative solutions — especially new mechatronic technologies — and integrating them into advanced high-tech IT&C solutions and competencies for the efficiency and eco-innovation of products and systems, significantly more advanced and intelligent [6,7].
Moreover, complex mechatronic systems, are highly intelligent systems used in smart networks with embedded sensors, processing, and actuation elements. These are designed and built to collect data and interact — the physical world with the virtual world — aiming to support, in real time, guaranteed performance and safety in both standard and critical applications in industry, economy, and society.
In these mechatronic systems, they integrate and generate the overall behavior of mechatronic elements, including computing, control/remote control, detection/remote detection, and smart network components. These can be deeply integrated and assembled, and their actions can be secure and interoperable [1].
Therefore, it is emphasized that complex mechatronic systems are multi-applicative, adaptive, and future-ready, acting as driving factors for the sustainable development of many industrial, economic, and societal sectors (such as aerospace, energy and environment, construction, transportation, defense, healthcare, agriculture, etc.) [2,3].

2. Adaptability of the New Complex Mechatronic Concept

The adaptability of the new complex concept involves the flexible adaptation of intelligent system architectures, expressed through complex structures of specialized sensors and actuators placed on static and/or mobile physical work systems and equipment. These transmit information to smart 4G devices that process, store, and forward data to monitoring / remote monitoring entities or centers for command and/or database integration.
Thus, mechatronic systems will be designed, structured, and architected into specialized intelligent modules assembled into dedicated configurations that serve multiple applications and add value to all components/devices within the general system.
By using smart 4G devices, real-time remote monitoring, diagnostics, and interventions are enabled for all static and mobile systems and equipment.
These multi-applicative and adaptive mechatronic systems will take the form of “black box” entities, innovatively integrating hardware circuits and software for data capture, modeling, and communication to/from the “command center.”
The architecture of adaptive multiplicative mechatronic devices/systems will be modular, allowing the integration of additional smart “add-on” other devices dedicated to specific or specialized activities.
The types of data captured by these smart devices will be processed, normalized, and standardized by the parent mechatronic adaptive multiplicative system/device into formats that ensure interoperability with the real-time monitoring platform.
Between mechatronic adaptive multiplicative systems/devices and the command center, communication will occur via a secure information exchange protocol. This will record and display real-time data. The command center, operated via a WEB platform, will be able to issue real-time alerts and ON/OFF commands that will be sequentially transmitted to the parent systems/devices and then to the targeted smart devices.
This complex mechatronic concept can be applied in many industrial environments, such as:

- Real-time remote monitoring and control of the quality and operation of automotive electronic and control systems
- Real-time remote monitoring and control of parameters in complex thermochemical treatment installations under controlled atmosphere
- Real-time remote monitoring and control of hydraulic oil quality in agricultural machinery actuation systems
- Real-time monitoring and control of CO_2 and other exhaust emissions in the automotive industry
- Real-time remote monitoring and control of electronic and control systems for vehicle stability
- etc.

3. Overview of Ultra-Precise Complex Mechatronic Systems for Intelligent 3D Control in Industrial and Laboratory Metrology

Through the new complex concept of Integrative Intelligent Mechatronics, the architectural concept was created for new solutions involving ultra-precise complex mechatronic systems for intelligent and integrated control in the automotive industry, specifically for cast and machined automotive parts.
Integrative Intelligent Mechatronics technology is considered an advanced technology with rapid, efficient, and competitive effects, offering top-tier performance in the improvement, modernization, and development of products, processes, product systems and intelligent systems. It creates new solutions for industry, new connections, new interfaces, and total integrations, similar to human anatomy and functions, aligned with the needs of modern society.
In the architecture of integrative intelligent mechatronic technology, a substantial role is played by the software of the intelligent sensors integrated into the system. This includes informational modules

for preprocessing, signal conditioning, feature extraction, defect detection, recalibration, and reconfiguration, such as:

- Initial preprocessing phase: Converts the signal into an engineering unit
- Calibration process: May include signal linearization using a simple lookup table approach with coefficients stored in the sensor's electronic datasheet
- Alternative linearization technique: Involves summing the reciprocal characteristic of the sensor with the signal
- Additional calibration functions: Include eliminating polarization effects of the sensors
- Calibrated signals: Pass through a signal conditioning software module to extract a series of features that characterize the data
- Feature extraction: Derives hidden information from the sensor's "signal history," useful both as output data and as part of defect detection strategies
- Main derived features: Serve as components for self-diagnosis and defect detection
- Sensor management communication: Uses error code sets based on electronic mechanisms

Figure 1 illustrates the block diagram of the intelligent mechatronic system for integrated measurement and control, highlighting the main functional modules and their interconnections.

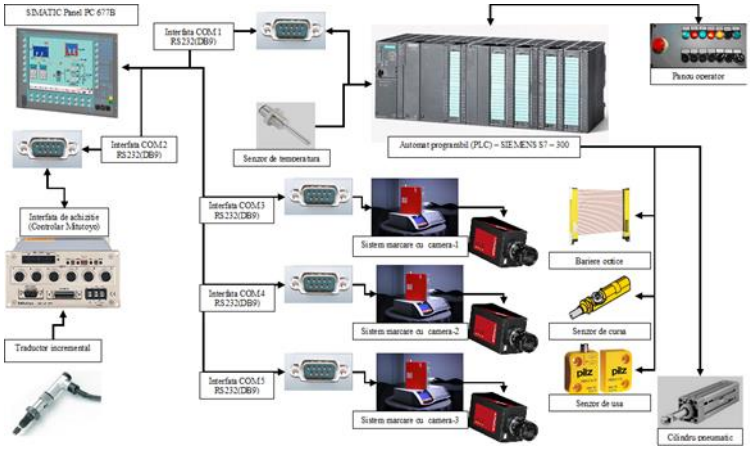

Fig. 1. Block diagram of the intelligent mechatronic system for integrated measurement and control

Legend:

1 – PC with visualization application;
2 – Optical safety barrier;
3 – Measurement station 1;
4 – Measurement station 2;
5 – Measurement station 3;
6 – Signal tower;
7 – Programmable logic controller (PLC);
8 – Sensor interface;
9 – Control panel

Fig. 2 Intelligent complex mechatronic system for measurement and control of automotive parts

4. Presentation Of Ultra-Precise Mechatronic Systems for Intelligent 3D Remote Control and Monitoring

The new complex mechatronic concept has been implemented in the construction of mechatronic systems for intelligent 3D remote control, aiming to fulfill several functions specific to the new concept, such as ultra-precise 3D remote control adapted to the appropriate environment (laboratory/industrial metrology), remote data transmission and transfer and remote monitoring of the intelligent control process via a command center (for ultra-precise 3D control), with information transfer via Internet and Intranet [4,5].
Below is the concept of a multi-application ultra-precise mechatronic system for intelligent 3D remote control and monitoring in laboratory or industrial metrology (Figure 3).
The ultra-precise mechatronic system is designed to perform displacement control functions along X, Y, Z axes and measurement (control) functions based on the system and data from the "ultra-precise 3D probe" integrated into the system.

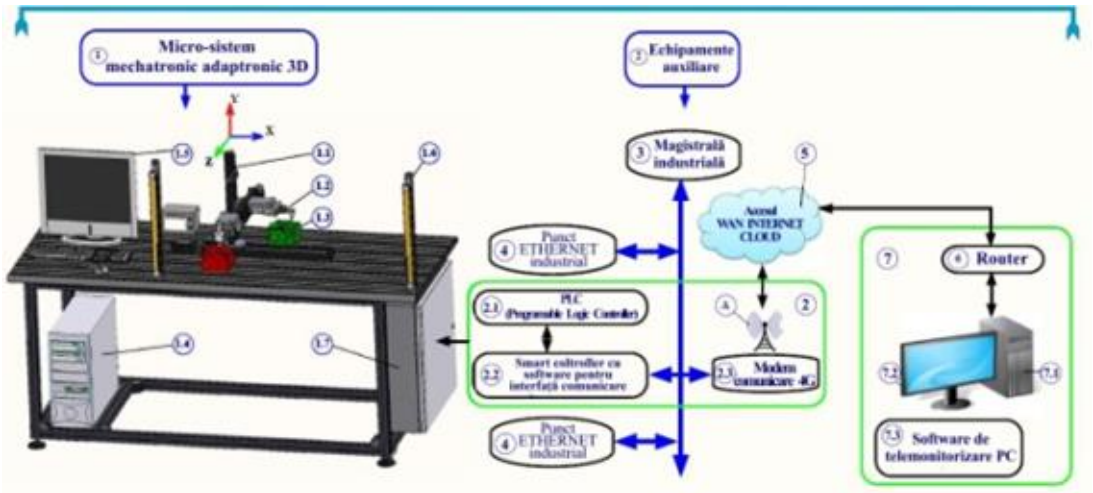

Fig. 3. Ultra-Precise Mechatronic System for Multi-Application Intelligent 3D Remote Control and Monitoring

1. 3D Mechatronic System:
1.1 Ultra-precise 3D measurement/control robot (x=300mm; y=200mm; z=250mm; accuracy: 0.1–1nm);
1.2 Ultra-precise 3D probe (fidelity 0.1 nm);
1.3 Part to be measured/controlled;
1.4 Local PC unit;
1.5 Visualization monitor and local user interface;
1.6 Laser safety barrier
1.7 Unit with control, actuation, and telecom systems;

2. Auxiliary Equipment:
2.1 PLC (Programmable Logic Controller);
2.2 Smart controller with communication interface software;
2.3 4G communication modem;
3. Industrial bus;
4. Industrial ETHERNET point;
5. WAN INTERNET CLOUD access;
6. Router
7. Control center
7.2 Monitor PC
7.3 Remote monitoring software

In 3D displacement mode, the mechatronic system can be operated both locally using pre-installed software on a PC with display and control interface, and remotely through position modeling and emulation. In 3D control mode, "position–probing information packets" are formed into "vector packets" for complex mathematical processing, either locally or remotely.
Switching between the two operating modes can occur at any time, and measurement points (3D control) can be stored for automatic operation in the PLC's memory.
All these complex functions are achieved by functionally testing and integrating multiple intelligent subsystems.

The general block diagram of the ultra-precise mechatronic system also presents the mechatronic & cybernetic component structure for functional illustration:

- **On the local PC unit (1.4)**, data from the 3D mechatronic system is collected and transmitted to the SMART TELECONTROL system. The data provided by SMART TELECONTROL is packaged, compressed, and protected via a VPN system with a private key. After establishing bidirectional communication with the telemonitoring system, the data is sent and validated. Once unpacked, the collected information is inserted into a database where the components of the mechatronic microsystem are analyzed.

Additionally, the positions of the telemetry system are stored in the same database and replicated on the telemonitoring screen using software. Based on the received data, the software generates a high-fidelity 3D image. Where data is insufficient, interpolation from previous data is used to ensure smooth rendering. Upon request, the session and generated image can be saved for future use and analysis. The mechatronic microsystem can be controlled in real time using the TELECONTROL software.

- **Connections and interconnections** between subsystem modules and system architecture components vary depending on their type. The 3D mechatronic system and ultra-precise 3D probe (nanometric precision) may be equipped with intelligent data transmission interfaces such as serial, parallel, CAN, PROFIBUS, SSI, INTERBUS, ETHERNET, DEVICENET, and other specialized types.
- **The 3D mechatronic system (1)**
- **The Programmable Logic Controller (PLC) (2.1)** is a digital computer used for automating cyber-mixmechatronic processes. It stores the specific control program for the 3D microsystem (X, Y, Z axes or control robot) and synchronously receives data from the 3D probe.

This controller is designed for multiple inputs and outputs, operates across extended temperature ranges, and withstands vibrations from machine kinematics and accidental impacts. The control program is typically protected by a backup or stored in non-volatile memory. The PLC operates in “real time,” meaning outputs must respond to inputs within a limited time frame to avoid unintended operations and undesirable outcomes.

- **The intelligent telecontrol module (2.2)** can be implemented using either a RISC architecture microcontroller or FPGA and connects the PLC to the 4G telecom modem via RS232 protocol.
- **Various public or private networks are used for 4G access (2.3)**. A range of compatible modems support RS232 data protocols. Event-driven or cyclic data processing is performed using specialized telecontrol protocols, allowing operators to manage the process efficiently. One or more advanced software platforms are used for remote connection via modern GPRS technologies or the global WAN Internet network, commonly used in other mechatronic automation equipment.
- **At the Telecontrol Center (7)**, Internet access is provided via a router with VPN functionality for initial data security. A second security layer may be implemented using a proprietary encryption algorithm and specific firewall configuration on the PC operating system (Windows or Linux). Programming a network application requires a Real-Time Operating System (RTOS), which supports multitasking, resource allocation, and memory constraints for Blackfin process programming.
- **The software application (7.3)** is a web-based telecontrolling desktop tool with two components: a PHP web service and a telecontrol front-end software with real-time emulation capability. The PHP service integrates the telemetry database backend and returns results to the front-end in a specific telecontrol format. To minimize real-time data transfer, only measurement-mode data is requested. Upon receiving data, the front-end software generates a real-time emulated virtual model of the 3D cyber-mixmechatronic system.
- The structural component of testing, evaluation, and validation aims to configure the final system to meet initial requirements and specifications.

To achieve this, the following aspects are detailed:

- Determining criteria for testing, evaluation, and validation of the 3D mechatronic system
- Describing categories of tests and evaluations involved
- Planning testing and evaluation during system development

- Preparing the mechatronic system for testing and evaluation.

5. Presentation Of Data And IT&C Systems Required For Integrating The Physical And Virtual Systems In A 3D mechatronic Intelligent System For Industrial And Laboratory Metrology

5.1. Intelligent Architectures Of The Physical And Virtual Systems (Figures 4 And 5)

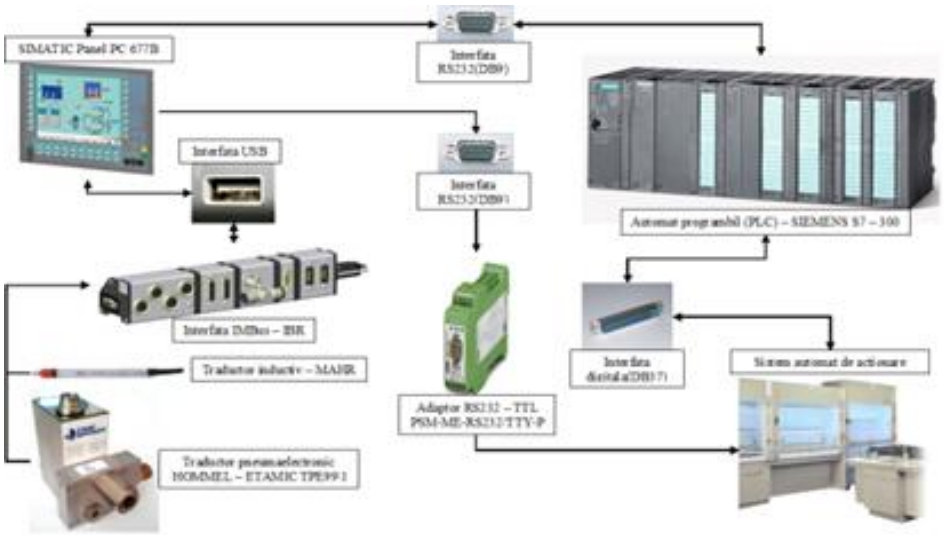

Fig. 4. Intelligent Architecture of the Physical System

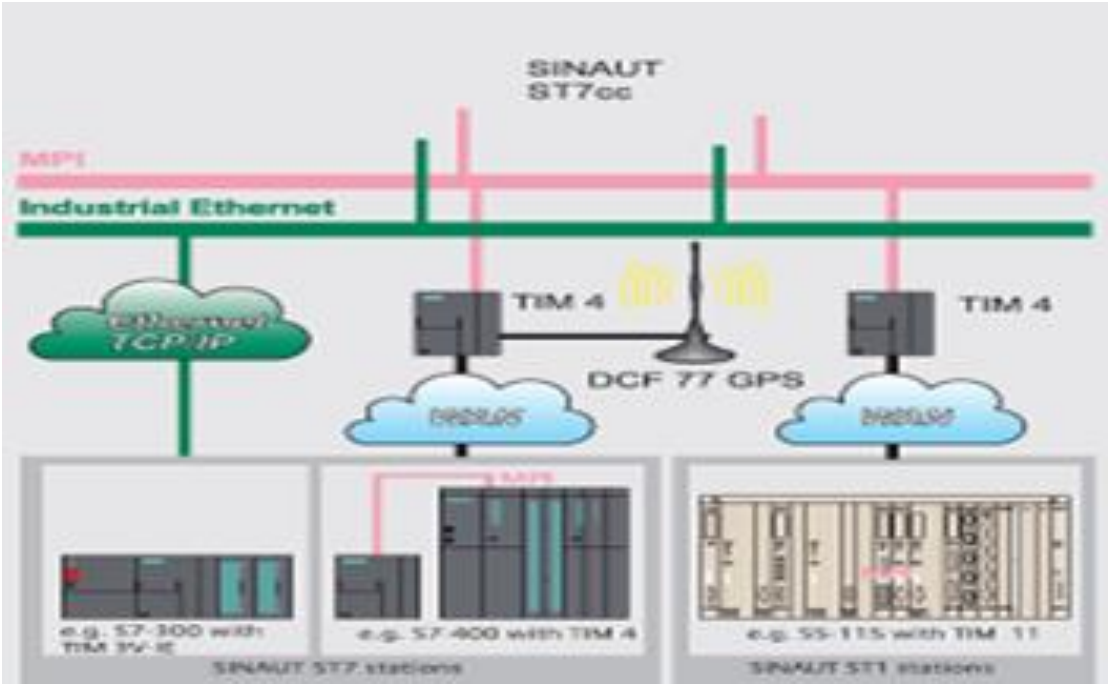

Fig. 5. Intelligent Architecture of the Virtual System

Within these figures, an industrial computer, a programmable logic controller, a signal adapter, an interface for acquiring electrical signals, a marking system equipped with a camera, and pneumatic-electronic and inductive transducers were employed. In the figure, the automatic actuation system transmits to the programmable logic controller, in digital format, the moment when the measurement should be performed as well as its current state (errors, measurement status, operating status). Once

the programmable logic controller receives the measurement command, it forwards it to the industrial computer, which—through the acquisition interface—carries out the measurements, processes them, displays the results, and transmits them back to the automatic actuation system via a communication adapter.
- The PC computer has the function of measuring, with the aid of transducers, 18 dimensions and verifying whether the measured values fall within predefined ranges. The visualization of the measured data is achieved by displaying the value of each measured dimension and by coloring these values in green or red;
- The use of the programmable logic controller was required by the communication of the automatic actuation system, through which the communication between the industrial computer and the controller was carried out;
- By using the adapter, the results concerning the inspected part are transmitted to the automatic control system;
- In the figure, the measurement system acquires data from the transducers through the acquisition interface—in this case, a Mitutoyo controller—and the data are processed and stored by the industrial computer;
- Depending on the measurement results, the part is marked using a marking system equipped with a camera for verifying the execution of the operation;
- This dimensional control system is equipped with a programmable logic controller that manages the temperature sensors, optical barriers, travel sensors for the actuation system, the actuation system itself, and door presence sensors, while also enabling interaction between the user and the dimensional control system through the operator panel;
- The optical barriers and door sensors are used to ensure user protection in accordance with the standards imposed by the client;

5.2. Data Acquisition

In this case, it is considered that the control equipment is located at a distance from the controlled process. The actuating elements receive command signals through the communication network, while the data acquired from the process by the transducers are directed to the controller also via the network. Due to this topology, additional delays occur as a result of data transfer. These network delays can be classified according to the direction of data transfer as sensor–controller delays and controller–process delays, both being present on the forward path as well as on the feedback path. For ease of analysis, the delay times can be grouped into a single time constant, referred to as the ‘control delay.’ Both types of network-induced delays may be either shorter or longer than the sampling period T.
In the first case, the process can be conducted under optimal conditions (assuming that no packets are lost).
In the second case, major discontinuities in the control process occur, which may lead to unsatisfactory developments and to the loss of process stability.
Based on the experiments carried out, the following stages are proposed:
- Evaluation of the dynamic characteristics of the controlled process, including the actuating elements and the transducers (the fixed part of the control elements)
- Selection of the sampling period in compliance with stability and performance requirements
- Testing of the network to be used in the control and/or monitoring process, taking into account the average delay times and the probability of error (packet loss).
If these delay times are much smaller than the required sampling period, the process can be controlled by incorporating a delay block into the fixed part of the regulation elements. If the delay times become comparable to the sampling period, it is recommended to use a structure that employs a Smith predictor;
The delays consist of at least the following parts:
●● Waiting time – this is a delay in which a source (the controller) must wait for the availability of the network before sending the data packets;
●● Sampling time – this is a delay caused by the insertion of the data packet into the network;

●● Propagation time – this is a delay caused by the transmission of the data packet through the physical network. The propagation time depends on the signal transmission speed and the distance between the source and the destination;
●● These three types are fundamental delays that occur in a local network. When data packets are transmitted over the network, additional delays may arise, such as the waiting time at a switch or router, and the propagation time between network nodes. Delays also depend on other factors, such as the maximum bandwidth length and the size of the data packets;
●● Based on the experiments conducted, three distinct cases of remote process control have been identified:

●●● Case 1: Predictive control for time-delay systems.

●●● Case 2: Adaptive predictive control using a delay calculated a posteriori: based on the experimental values of the delays, an average value was computed, which is then used in the control algorithm.

●●● Case 3: Adaptive predictive control using a variable delay estimated a priori: based on the experimental values of the delays, the delay time was estimated for the next sampling period.

5.3. Telemonitoring And Teleservice Software On A Pc Platform (Fig. 6)

The software application is written in Visual C++. The PC running the application uses a modem configured as a client. This modem connects to the PC RS232 serial interface. The modem configured as a server connects to the mechatronic equipment being monitored, also using an RS232 connection.
The initial screen of the software application is shown in Figure 6. Indicator 1 represents the state of the digital inputs Ixx at the bit level. Indicator 3 represents the current values of the digital outputs Qxx. Validation controls 2 (checkboxes) provide a convenient means for the user to set or reset the desired value for output Qxx. Button 4 is pressed to establish the connection between the application and the monitored equipment. Field 8 represents the list of commands that can be sent to the monitored equipment. Field 7 is optional. The start address 6 is filled in with a numeric value in the range 0–7, specifying the address of the first selected I/O module. Edit control 5 is filled in with the number of numeric values to be issued or for which the actual value retrieved from the monitored cyber-mechatronic equipment is requested.

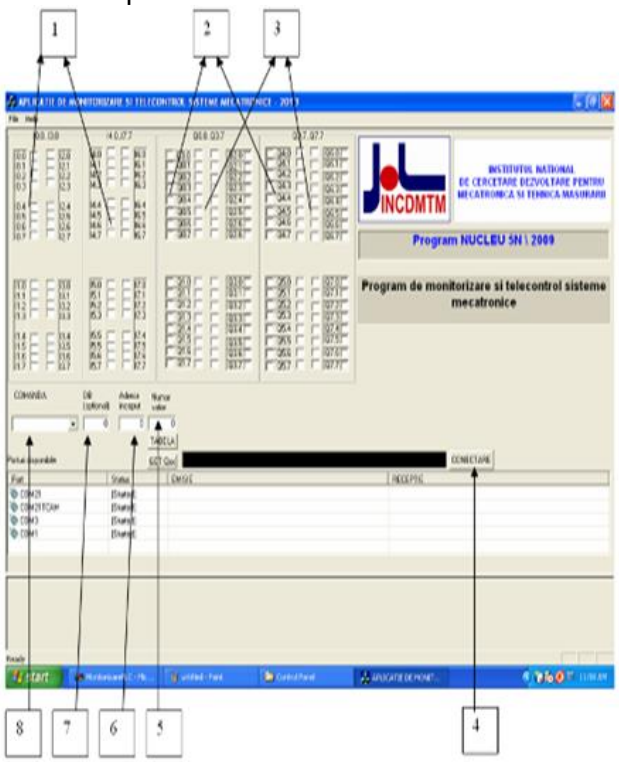

Fig. 6. Telemonitoring and Teleservice Software on a PC Platform

For reading the digital outputs, the user selects the command ‘bord’ from list 8 and enters the start address in editor 6 as well as the number of bytes in editor 5. The message is then sent to the monitored equipment (Figure 7). The response received is displayed through indicators of type 1.

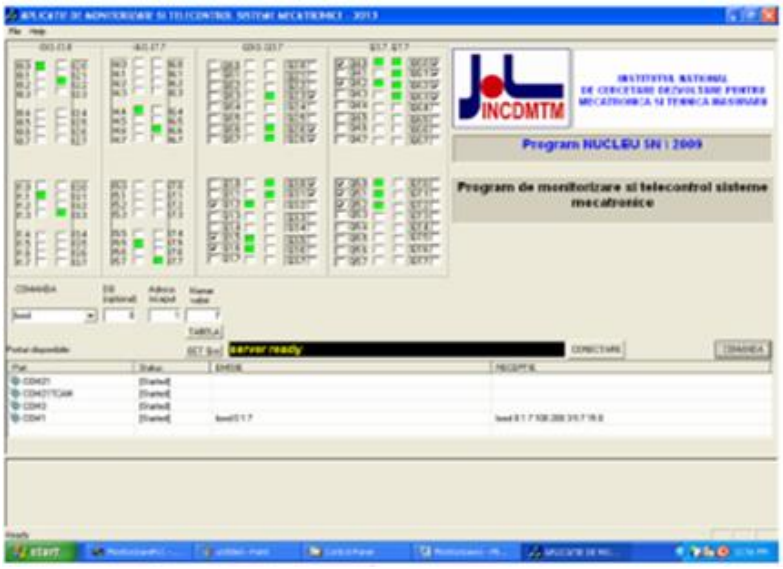

Fig. 7. Displaying the Message to the Monitored Equipment

For writing the digital outputs, the user selects the command ‘bowr’ from list 8 and enters the start address in editor 6 as well as the number of bytes in editor 5. Then, button 9 (table) is pressed. An editable table 11 appears. The number of columns is equal to the number of output bytes whose values will be transmitted to the monitored equipment. In each column of the table, the operator can enter numerical values between 0 and 255.
The assembled numerical values of each output byte are placed in the corresponding field. The command message is sent to the monitored system (Figure 8). The response received is displayed through indicators of type 1.

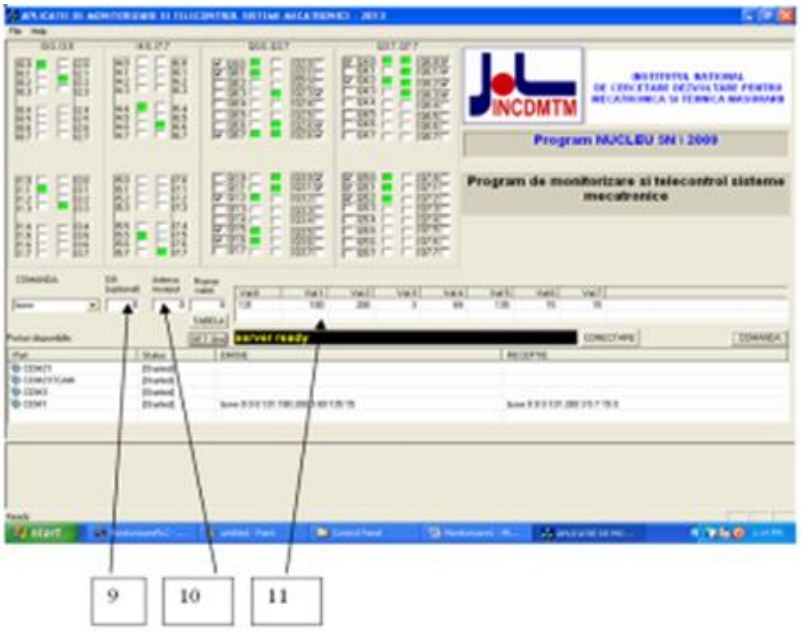

Fig. 8. Sending the Message to the Monitored Equipment

6. Conclusions

The purpose of this scientific work is to present the new mechatronic ultraprecise concept for intelligent 3D multi-application remote control and remote monitoring,' used in the construction of mechatronic ultraprecise systems for intelligent 3D remote control intended for laboratory metrological processes and/or industrial processes in the automotive, aerospace, hydronic and pneutronic, medical and biomedical industries, etc.
The 3D mechatronic system is designed to perform 3D telecontrol and telemonitoring functions within intelligent metrological and/or industrial processes, through ultraprecise X, Y, Z displacement signals and information, as well as the measuring/control probe in 3D, based on the preinstalled PC program and the command software for modeling and remote positioning. In this way, the 'position–probing information packets' are structured into 'vector packets' for complex mathematical processing, which can be carried out both locally and remotely.
The 3D mechatronic system is based on intelligent architectures of specialized sensors and actuators, as well as specialized static and mobile work modules, which transmit information to intelligent 4G mechatronic units. These units process, store, and transmit the data to monitoring–command entities or databases, through the cybernetic and integronic system – the physical (mechatronic) system fused with the virtual system (Internet, Intranet).

References

[1] Phatak, Sujit S., D.J. McCune, and George Saikalis. "Cyber Physical System: A Virtual CPU Based Mechatronic Simulation." *IFAC Proceedings Volumes* 43, no. 18 (2010): 405-410. https://doi.org/10.3182/20100913-3-US-2015.00077.

[2] Zhou, K., Ye Cen, J. Wan, B. Liu, and L. Liang. "Advanced Control Technologies in Cyber-physical System." Paper presented at the 5th International Conference on Intelligent Human-Machine Systems and Cybernetics (IHMSC 2013), Hangzhou, China, August 26-27, 2013. doi: 10.1109/IHMSC.2013.284.

[3] Gheorghe, Gh. *Intelligent Systems Adaptronics* / *Adaptronica Sistemelor Inteligente*. Bucharest, AGIR Publishing House, 2014. ISBN: 978-973-720-509-4.

[4] Gheorghe, Gh. *Mechatronics & Cyber–Mechatronics Systems* / *Mecatronica & Sistemele Cyber – Mecatronice*. Bucharest, CEFIN Publishing House, 2015. ISBN 978-606-8261-22-5.

[5] Voicu, Adrian, Gheorghe I. Gheorghe, and Liliana Laura Bădiță. "Studies and research on the measurement and 3D integrated control of complex components from automotive industry by laser scanning." Paper presented at the 12th International Conference of Numerical Analysis and Applied Mathematics ICNAAM 2014, Rodhos, Greece, September 22-28, 2014.

[6] Lincaru, Cristina, Florentina Badea, Speranta Pirciog, Adriana Grigorescu, Sorin Ionut Badea, and Cristian Radu Badea. "An Overview About Mechanics Developments and Achievements in the Context of Industry 4.0." Paper presented at the International Conference on Reliable Systems Engineering (ICoRSE) – 2023, Bucharest, Romania, September 7-8, 2023. *Lecture Notes in Networks and Systems* 762 (2023): 17-41. DOI: 10.1007/978-3-031-40628-7_2.

[7] Badea, Florentina, Gabriela Tudose, Cristina Lincaru, Speranta Pirciog, Sorin Ionut Badea, and Cristian Radu Badea. "Neighbor-Joining Analysis of Mechanics and the Industry 4.0 Domains." Paper presented at the International Conference on Reliable Systems Engineering (ICoRSE) – 2023, Bucharest, Romania, September 7-8, 2023. *Lecture Notes in Networks and Systems* 762 (2023): 42 - 55. DOI: 10.1007/978-3-031-40628-7_3.

ISSN 1454 - 8003
Proceedings of 2025 International Conference on Hydraulics and Pneumatics - HERVEX
November 19-21, Băile Govora, Romania

FUNDAMENTAL CONCEPTS OF DIGITAL HYDRAULICS - DIGITAL FLOW CONTROL UNIT (DFCU)

Ahmed Zubair JAN[1], Krzysztof KĘDZIA[1]

[1] Wroclaw University of Science and Technology, Faculty of Mechanical Engineering, Department of Technical Systems Operation and Maintenance, ahmed.jan@pwr.edu.pl, krzysztof.kedzia@pwr.edu.pl

Abstract: *Classic hydrostatic systems, based on continuous control using proportional or servo-valves, are characterized by high precision but also significant energy losses, mainly related to flow throttling. Digital hydraulics represents an alternative concept for controlling hydrostatic systems, replacing continuous modulation with discrete, binary states of hydraulic valves (ON/OFF type). This approach is, in many cases, associated with improving the system's energy efficiency, increasing system reliability, and lowering its construction costs. The core of digital hydraulic systems is the Digital Flow Control Unit (DFCU). This article presents the basic operational features of the DFCU and compares its key characteristics with traditional analog solutions. Key engineering challenges, such as pressure pulsations and shock loads identified during experimental research, are also discussed.*

Keywords: *Digital Hydraulics, DFCU, discrete control, energy efficiency, ON/OFF control, hydrostatic systems*

1. Introduction- The Digital Hydraulics Paradigm

Classic hydraulic systems use continuously variable components (e.g., variable displacement pumps, proportional valves) for precise control of force and speed. Despite their precision, systems based on throttling control are primarily characterized by relatively low energy efficiency. Energy is lost in the form of heat during flow throttling, which is an inherent feature of continuous regulation [6]. Digital Fluid Power (DFP) represents a proposed paradigm shift. Instead of smooth modulation, DFP utilizes discrete control based on the binary states of "on/off" (ON/OFF) type valves. This concept can be compared to the digital revolution brought about by electronics, where analog signals were replaced by digital ones, leading to an increase in the efficiency and reliability of control systems [5]. The key advantages of digital hydraulics compared to classic "analog" hydraulics (Table 1) are:

- Higher energy efficiency: Elimination of throttling losses by operating components only in fully open or fully closed states.
- Greater reliability and fault tolerance: Digital systems often use multiple parallel, simpler components. The failure of one element does not stop the entire system's operation, but only degrades its operating parameters (e.g., resolution).
- Contamination resistance: Simple ON/OFF valves are much less sensitive to oil contamination than the precise spools of proportional or servo-valves [12].
- Lower system construction costs: The use of standard, mass-produced components (e.g., gear pumps, 2/2 valves) instead of complex and consequently expensive axial-piston units or proportional valves.

Table 1: Comparison: Digital vs. Analog Hydraulics [7]

Feature	Classic Hydraulics	Digital Hydraulics
Signal Type	(with proportional valves)	Discrete (On/Off)
Energy Losses	Continuous (Proportional)	Minimal
Fault Tolerance	High due to throttling	High – redundant components
Precision	Low – susceptible to minor failures	Depends on valve resolution
Contamination Sensitivity	Very High	Low

2. Digital Flow Control Unit (DFCU)

2.1 Principle of Operation

A Digital Flow Control Unit (DFCU) is, by definition, a device that performs the regulation of hydraulic flow rate in a discrete (stepped) manner. Instead of a single element with continuous regulation, the DFCU consists of multiple parallel-connected switching elements (valves) (Fig. 1). The total flow rate at the output of the DFCU (Q_{total}) is the arithmetic sum of the flow rates of all units that are currently in the "ON" state (are active). By digitally controlling the appropriate combinations of valves, the required, stepped output flow characteristic can be achieved [11], [12].

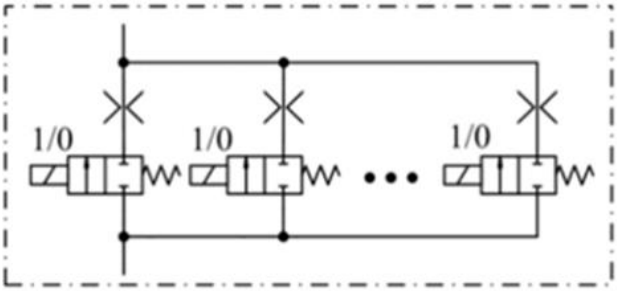

Fig. 1. Schematic diagram of a DFCU based on parallel switching valves [7]

2.2 Architecture and Encoding

The DFCU architecture can be implemented in two main ways, both consistent with the digital concept:

- Valve-based DFCU: Consists of a bank of parallel ON/OFF valves, where each valve has a specific (usually different) flow capacity (e.g., Q, 2Q, 4Q, 8Q).
- Pump-based DFCU: The architecture that forms the basis of the research in co-author Ahmed Jan's doctoral dissertation. In this setup, a single variable displacement pump is replaced by a set of several fixed displacement pumps (e.g., gear pumps). These pumps are typically mounted on a common shaft, driven by a single motor. Each pump is connected to a simple ON/OFF valve (e.g., 2/2), which decides whether the flow from that pump is directed to the working circuit or pressure-free to the tank.

Regardless of the architecture, the method of flow "encoding" is key. Binary encoding is most commonly used, where the capacities of successive units (valves or pumps) are selected in a 1:2:4:8:... ratio.

For a system with N units (e.g., 4 pumps with displacements of 2, 4, 8, and 16 cm³/rev), the number of discrete, non-zero flow levels is (2^N - 1). For N=4, this yields 15 different flow levels. As shown in Fig. 2, the greater the number of units (the more bits), the higher the system's resolution, and the

more the "stepped" digital characteristic approaches the ideally smooth characteristic of a proportional valve.

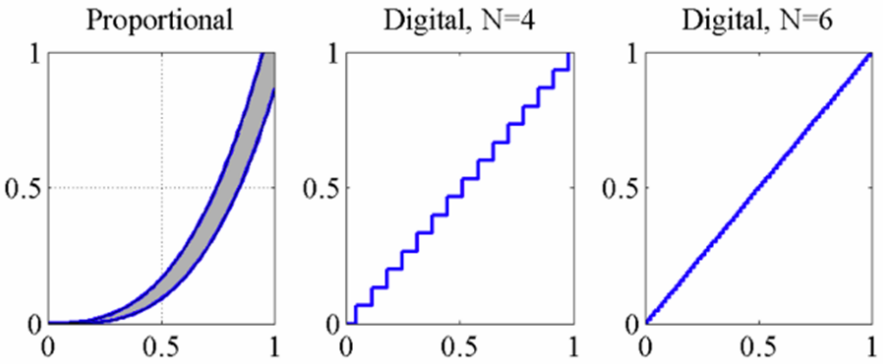

Fig. 2. Comparison of the flow characteristic of a proportional valve (left) with the stepped characteristic of a DFCU for N=4 (middle) and N=6 (right) [7]

3. Key Advantages and Challenges of DFCU

The application of the DFCU concept, whether in the form of valves or pumps, brings benefits, but also specific engineering challenges.

3.1. Advantages

- Relatively High Energy Efficiency: Compared to throttling control, this is the primary advantage of DFCU. By eliminating throttling control, the main source of losses in classic hydrostatic systems is removed. The pumps either operate at optimal efficiency, delivering fluid to the system, or they operate with minimal load caused by flow resistance through the pipeline (flow directed freely to the tank), thereby minimizing energy consumption.
- Low Costs and High Reliability: As mentioned, DFCU is based on standard, mass-produced components (gear pumps, ON/OFF valves). They are significantly cheaper and more resistant to harsh operating conditions (e.g., contamination) than precision axial-piston units or proportional valves.
- Modularity and Fault Tolerance: The failure of a single pump or valve in an *N*=4 DFCU system does not cause the machine to stop. The system can continue to operate with limited (but often sufficient to complete the task) performance.

3.2. Challenges: Dynamic Characteristics

The main engineering challenge and the trade-off for higher efficiency is the different dynamic characteristic of the DFCU system [7]. The discrete (stepped) nature of the control inevitably generates undesirable dynamic phenomena in the system. Experimental research conducted as part of the doctoral dissertation (Fig. 3, Fig. 4, Fig. 5) clearly demonstrated the existence of these phenomena, which were not visible in simplified simulation models:

- Pressure and Torque Pulsations: Even in a steady state, the "noisy" torque profile (Fig. 3) is a physical signature of DFCU operation. It results from the summation of flow pulsations from multiple gear pumps and pressure fluctuations.

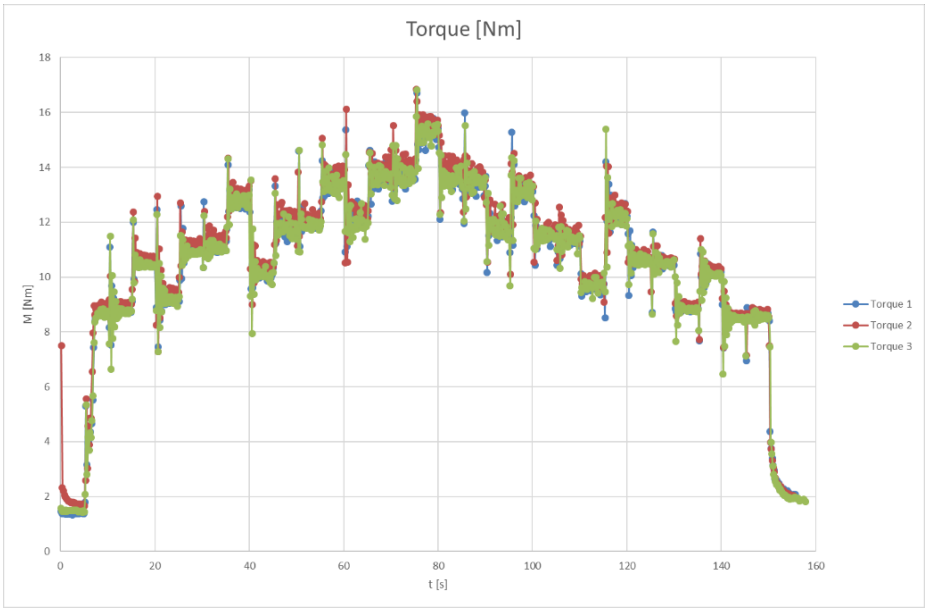

Fig. 3. Torque of 1st experimental test [7]

- Shock Loads (Hydraulic Shocks): At the moment of switching (engaging or disengaging) subsequent units to the common pressure line, hydraulic and mechanical shocks are generated. Experimental research in intermittent operation scenarios (Fig. 4 and Fig. 5) revealed the occurrence of sharp, short-term torque peaks, multiply exceeding the nominal value. The amplitude of these shock loads intensifies with the increase in operating pressure.

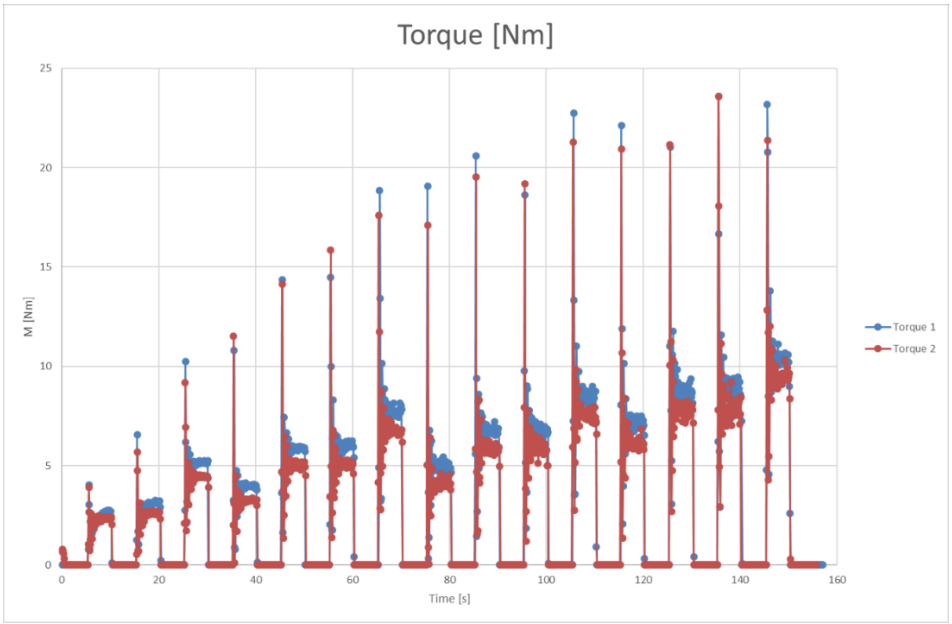

Fig. 4. Torque of 2nd experimental tests 1,2 MPa [7]

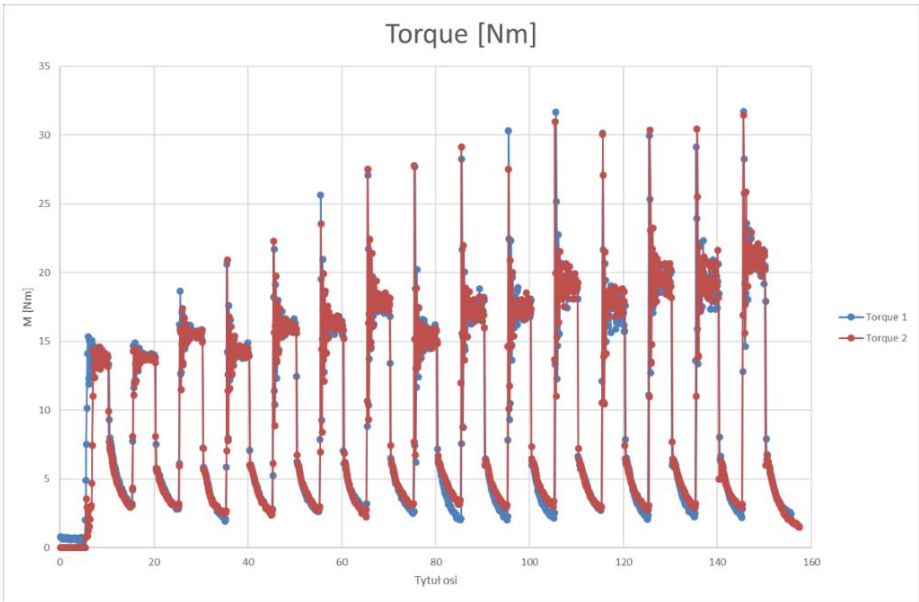

Fig. 5. Torque of 2nd experimental tests 6 MPa [7]

Managing these dynamics – ensuring operational stability, low noise levels, and the fatigue life of components – is a key aspect of designing and implementing DFCU systems.

4. Conclusion

The Digital Flow Control Unit (DFCU) is an interesting element of modern digital hydraulics, offering significant benefits in terms of energy efficiency, system construction costs, and increased reliability compared to classic analog systems. Both architectures based on valve manifolds and on sets of fixed displacement pumps appear to be an interesting alternative, allowing for the replacement of classic throttling regulation with effective discrete control.
Simulation and experimental research have confirmed that these systems can approximate the kinematic characteristics of classic drive systems with high fidelity. At the same time, this research has revealed that the main engineering challenge remains managing the inherent features of DFCU: pressure pulsations and shock loads arising during valve switching. Further work on advanced control strategies that minimize these adverse phenomena is key to fully harnessing the potential of DFCU technology.

References

[1] Zhang, Qiwei, Xiangdong Kong, Bin Yu, Kaixian Ba, Zhengguo Jin, and Yan Kang. “Review and development trend of digital hydraulic technology.” *Applied Sciences* 10, no. 2 (2020): 579.
[2] Linjama, M. “Digital Fluid Power – State of the Art.” Paper presented at the Twelfth Scandinavian International Conference on Fluid Power (SICFP’11), Tampere, Finland, May 18-20, 2011.
[3] Linjama, M., A. Laamanen, and M. Vilenius. "Is it Time for Digital Hydraulics?” Paper presented at the 8th Scandinavian International Conference on Fluid Power (SICFP’03), Tampere, Finland, May 7 - 9, 2003.
[4] Lu, W. *Review of the digital hydraulics technologies*. Master Thesis. Polytechnic University of Turin, 2020.
[5] Wang, H., Z. Chen, J. Huang, L. Quan, and B. Zhao. “Development of high speed on–off valves and their applications.” *Chinese Journal of Mechanical Engineering* 35 (2022): 67.
[6] Linjama, M. “On the numerical solution of steady-state equations of digital hydraulic valve-actuator.” Paper presented at the Eight Workshop on Digital Fluid Power, Tampere, Finland, May 24-25, 2016.
[7] Jan, A. Z. *Method of efficient utilization of digital hydraulic concept in multisource hydrostatic drive systems*. PhD. Dissertation. Wrocław University of Science and Technology, 2025.
[8] Jan, A. Z., and K. Kędzia. “Method of effective use of the concept of digital hydraulics in multi-source hydrostatic drive systems.” Paper presented at the International Scientific-Technical Conference on

Hydraulic and Pneumatic Drives and Controls NSHP 2025, Kazalnica, Poland, October 8-10, 2025. In Stryczek, Jarosław, Urszula Warzyńska, and Michał Banaś (eds.). *Lecture Notes in Mechanical Engineering - Advances in Hydraulic and Pneumatic Drives and Control, Centrifugal Pumps, Valves, and Seals 2025* (Cham: Springer, 2026): 23–34.

[9] Jan, A. Z., K. Kędzia, and D. Prostański. “A new approach in hydrostatic drives: "digital" pumps.” Paper presented at the International Scientific-Technical Conference on Hydraulic and Pneumatic Drives and Controls NSHP 2023, Piechowice, Poland, October 11-13, 2023. In Stryczek, Jarosław, and Urszula Warzyńska (eds.). *Lecture Notes in Mechanical Engineering - Advances in Hydraulic and Pneumatic Drives and Control 2023* (Cham: Springer, 2024): 58-70.

[10] Jan, A. Z., P. Śliwiński, and K. Kędzia. “Digital hydraulics circuit based on PWM function for controlling hydraulic actuator position.” Paper presented at the 26th International Conference on Hydraulics and Pneumatics HERVEX 2022, Băile Govora, Romania, November 9-10, 2022.

[11] Huova, M., M. Linjama, and K. Huhtala. “Energy Efficiency of Digital Hydraulic Valve Control Systems*”* Paper presented at the SAE 2013 Commercial Vehicle Engineering Congress (COMVEC), Rosemont, Illinois, USA, October 1-3, 2013 (SAE Technical Paper 2013-01-2347).

[12] Ding, R., and M. Cheng. *Independent Metering Electro-Hydraulic Control System*. Ed. 1. Springer Singapore, 2024. doi:10.1007/978-981-99-6372-0.

ISSN 1454 - 8003
Proceedings of 2025 International Conference on Hydraulics and Pneumatics - HERVEX
November 19-21, Băile Govora, Romania

NUMERICAL MODEL FOR HYDRAULIC SERVO-VALVES

Fănel Dorel ȘCHEAUA[1]

[1] "Dunarea de Jos" University of Galati, fanel.scheaua@ugal.ro

Abstract: *Hydraulic actuation systems remain essential in applications requiring high force density, robust operation and precise motion control. Recent advancements in electro-hydraulic architectures, intelligent sensing and energy-efficient components have significantly improved performance, reliability and sustainability. This study presents a coupled electro–mechanical–hydraulic model of a servo-valve in order to analyze its dynamic behavior under varying operating conditions. The model integrates electrical control signals, mechanical armature motion, and hydraulic flow to capture the system's transient response accurately. A numerical approach is employed to simulate key performance metrics, allowing evaluation of system stability during operation. The frequency analysis performed was intended to evaluate the dynamic response of the servo-valve at different excitation frequencies. The obtained results for the coupled electro–mechanical–hydraulic servo-valve model provide insight into the system's frequency response. The numerical results from the Bode analysis confirm the accuracy of the coupled model and its suitability for predicting real-world servo-valve performance. The results demonstrate that the coupled model provides a robust framework for design optimization, control strategy development and fault analysis in precision hydraulic applications.*

Keywords: *Fluid power, hydraulic actuation, servo valves, numerical model*

1. Introduction

Hydraulic actuation systems play a central role in industrial equipment, heavy machinery, aerospace structures and robotic systems where the key requirements include high power, reduced weight ratio, smooth motion control and reliability under harsh operating conditions.
Despite the emergence of high-power electric drives, hydraulics remains unmatched in many high-load applications due to the compressibility characteristics of fluids, high stiffness levels and the ability to generate large forces with compact actuators.
The last decade has seen significant innovation in hydraulic power control, particularly through electro-hydraulic interfaces, intelligent sensors and advanced control electronics, while all of this are allowing the improved efficiency, closed-loop accuracy and reduced environmental impact.
This paper investigates current trends in the design and optimization of hydraulic actuation systems, discussing both theoretical and practical aspects. Among all circuit elements servo-valves are critical components in precision hydraulic systems, translating electrical control signals into precise mechanical motion and hydraulic flow. Their performance depends on the complex interactions between electrical, mechanical, and hydraulic subsystems. Modeling the coupled electro–mechanical–hydraulic dynamics of servovalves provides a deeper understanding of their transient behavior, enabling improved design, control, and reliability in high-performance applications such as aerospace, robotics, and industrial automation.

2. Main principles of Fluid Power

Hydraulic actuation is based on transmitting power via pressurized fluid, while according to Pascal's principle, pressure value applied to a confined fluid is distributed uniformly.
The resulting force is given by 0, 0:

$$F = p \cdot A$$

where
F – output force,
p – system pressure,
A – piston surface area.
This fundamental relationship is central to the design of cylinders, motors and valves.
Regarding the system architecture a classical hydraulic actuation system includes a power source (pump, electric motor), a fluid reservoir, control valves (which can be directional, pressure, proportional, servo), actuators (linear or rotary), filtration and cooling subsystems, sensors for pressure, temperature and position.
Modern architectures integrate digital control, compact power units and modular valve manifolds 0, 0, 0.

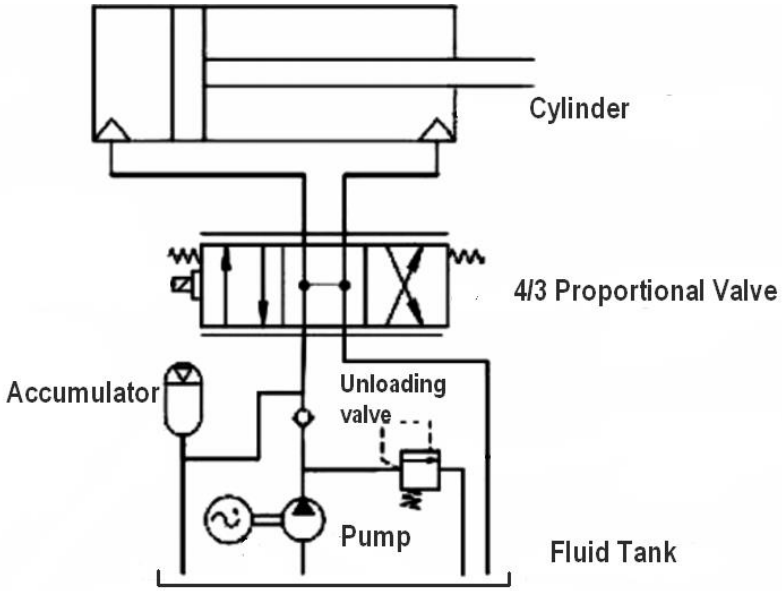

Fig. 1. Hydraulic circuit schematically representation

The physical and mathematical model for a hydraulic drive system includes fluid dynamic equations, cylinder mechanical equations, control valve modelling, linearization and transfer function.
Hydraulic valves are mechanical or electro-hydraulic elements that regulate or limit the pressure within the hydraulic and control circuits of hydraulic control, control and drive systems.

3. Hydraulic servo-valve numerical model

Typically, a hydraulic valve can be modeled on three levels represented by an electrical-mechanical model for servo-valves, a mechanical-hydraulic model for proportional valves and servo-valves and the fully nonlinear electro-mechanical-hydraulic model that is used in advanced control and precise simulations.
The electrical-mechanical model for servo valves includes the dynamics of the spool and the moving armature, since the spool produces electromagnetic force, then the armature that moves the valve element, as well as other assembly elements represented by an elastic spring-type element that provides damping and mechanical resistance.
The mechanical-hydraulic model for proportional valves and servo-valves has the ability to connect the spool position with the flow through the orifices, which means the variation of the orifice section that determines the volumetric flow rate, then the pressure differences that influence the flow rate and the return force of the spool.

The fully nonlinear electro-mechanical-hydraulic model combines electromechanical dynamics with fluid dynamics, including nonlinear effects.
The stages of modeling hydraulic valves represented by servo valves and proportional valves used in automation, industrial hydraulics and simulations of the operation of these components are presented.
The flow rate model through orifice (nonlinear model) for a proportional opening valve can be described as follows 0, 0:

$$Q = C_d A(x)\sqrt{\frac{2}{\rho}(p_1 - p_2)} \tag{1}$$

where:
$A(x)$ – nonlinear function of drawer position;
C_d - discharge coefficient;
ρ - fluid density.
The pressure model in actuator chambers can be described as 0, 0:

$$\begin{aligned} p_1 &= \frac{\beta}{V_1}(Q_1 - A_1\dot{y}) \\ p_2 &= \frac{\beta}{V_2}(Q_2 - A_2\dot{y}) \end{aligned} \tag{2}$$

where:
y - cylinder rod position;
β - compressibility modulus;
Q_1, Q_2 - the circulated flow rates through the valve.

For a numerical analysis the servo-valve is represented using a coupled electro–mechanical–hydraulic model that captures the essential dynamic behavior of the device.
The electrical subsystem describes the current through the coil using a first-order differential equation based on the coil resistance and inductance.
The resulting current produces an electromagnetic force proportional to Kii, which drives the spool in the mechanical subsystem.
The spool motion is modeled as a second-order system including inertia, viscous damping, and optionally stiffness.
The hydraulic subsystem relates the spool displacement to the flow through the orifice, which follows a nonlinear square-root law with respect to the pressure drop. Around a chosen operating point, the flow equation is linearized, leading to the sensitivity coefficients *Gx* and *Gp* that describe the small variations in spool position and pressure which are able to affect the fluid flow.
When combined, these three subsystems form a transfer function from input voltage to output flow that exhibits distinct electrical and mechanical poles and captures the dominant bandwidth limitations of the servo-valve.
The main parameters included in the numerical analysis are presented in table 1.

Table 1: Model parameters used for numerical analysis

Symbol	Description	Value	Units	Physical Role in the Model
L	Coil inductance	0.001	H	Governs current dynamics; part of the electrical pole *(L s + R)*
R	Coil resistance	2	Ω	Defines electrical response speed; sets pole at −R/L
m	Spool mass	0.01	kg	Mechanical inertia; part of 2nd-order mechanical dynamics
b	Mechanical damping	1	N·s/m	Controls resonance damping; affects stability and bandwidth
K_i	Force–current coefficient	0.1	N/A	Converts coil current into force acting on the spool
Cd	Discharge coefficient	0.7	—	Describes turbulent flow efficiency through the orifice
w	Orifice width	1×10^{-4}	m	Geometric parameter of the valve slot
ρ	Fluid density	850	kg/m³	Affects flow rate value
x_0	Spool displacement at operating point	1×10^{-4}	m	Linearization point for flow derivative
Δp_0	Pressure drop at operating point	5×10^{6}	Pa	Sets steady-state flow and G_x,
G_x	∂Q/∂x (flow sensitivity to displacement)	0.00759	m³/(s·m)	Main flow gain; scales system magnitude
G_p	∂Q/∂Δp (flow sensitivity to pressure)	7.59×10^{-14}	m³/(s·Pa)	Determines hydraulic feedback strength
β	Bulk modulus of hydraulic fluid	$1.5–2\times10^{9}$	Pa	Determines pressure dynamics (dp/dt)

4. Results and discussion

The purpose of the present model was to analyze the dynamic behavior of the servo-valve and identify the factors that limit the frequency band and the stability of the hydraulic system.
By separating and coupling the electrical, mechanical and hydraulic subsystems, the model allows the evaluation of the influence of each component on the frequency response and on the sensitivity of the flow to voltage, position and pressure variations.
The linearized model was used in order to obtain Bode diagram plots and to determine the pole-zero structure, highlighting dominant poles, operating regimes and the effect of pressure on local gains.

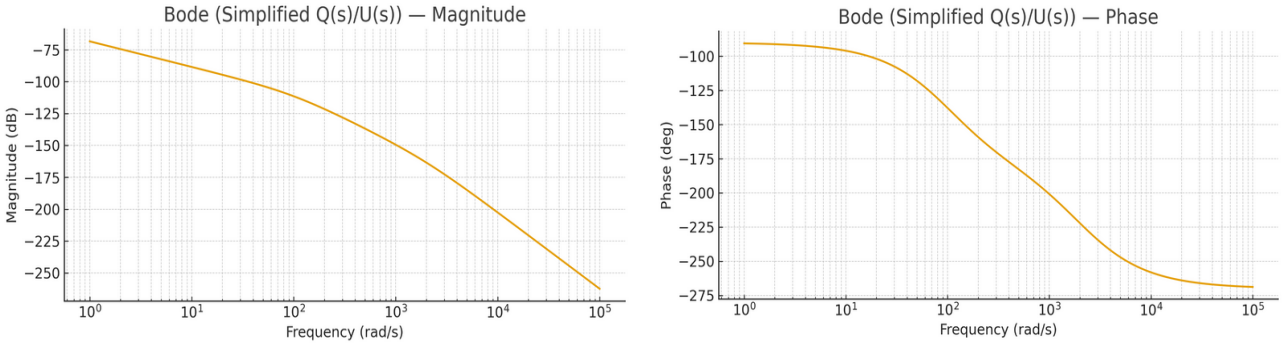

a) Bode diagrams for magnitude and phase –simplified model

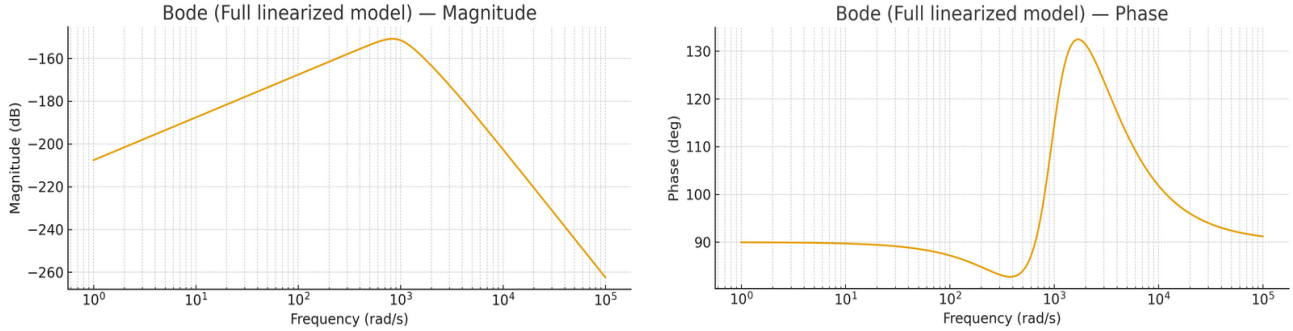

b) Bode diagrams for full linearized model

Fig. 2. The obtained results from the servo-valve model numerical analysis

The objective was to obtain a simplified but representative tool that allows the prediction of servo-valve performances and to support the design and optimization of hydraulic actuator systems.
The Bode diagrams obtained from the simplified transfer function highlight the dominant dynamic contributions of the electrical circuit and spool mechanics. The magnitude plot shows a clear low-frequency gain followed by two characteristic roll-off regions associated with the coil electrical pole and the second-order mechanical subsystem, while the phase curve confirms the corresponding phase lag accumulation.
In contrast, the Bode plots of the full linearized model exhibit an extended low-frequency dynamics due to hydraulic compressibility and flow-pressure coupling. This is reflected by an additional pole at low frequencies and a slight modification of the high-frequency slope, making the full model more representative of real servo-valve behavior.
The schematic diagram summarizes the coupling between electrical, mechanical, and hydraulic domains and visually supports the structure captured in the mathematical model.
The complete model, which includes hydraulic pressure dynamics and fluid compressibility, produces an additional low-frequency pole. This makes the phase curve more negative at very low frequencies and slightly reduces the system gain. However, the dominant bandwidth is still determined by the mechanical subsystem, with the hydraulic and electrical subsystems contributing secondary effects.
Overall, the results confirm that the servo-valve behaves like a cascaded mechanical–electrical system with strong low-frequency gain, limited bandwidth, and smooth roll-off.
The model captures the essential dynamic behavior and provides a more accurate representation of the low-frequency hydraulic effects.

5. Conclusions

The coupled electro–mechanical–hydraulic model for servo-valves provides a comprehensive framework for analyzing and predicting system behavior by integrating the electrical control, mechanical actuation, and hydraulic response.
The model captures the dynamic interactions between the electrical input, mechanical armature motion and hydraulic fluid flow, enabling more accurate predictions of valve response under varying load conditions.
It allows assessment of transient behavior such as overshoot, settling time and bandwidth, which are critical for precision control applications.
Coupled modelling criteria helps in optimizing parameters like armature mass, spring stiffness, damping, and spool geometry to achieve desired performance, minimize overshoot and enhance stability.
Integrating the multi-domain interactions makes it easier to detect and analyze anomalies, such as spurious oscillations due to mechanical resonance or hydraulic delay.
It provides a foundation for advanced control strategies, such as PID tuning, feedforward compensation, or adaptive control, improving system responsiveness and robustness.

In essence, the coupled electro–mechanical–hydraulic approach provides a holistic understanding of servo-valve behavior, which is essential for high-precision hydraulic control applications in aerospace, robotics and industrial automation, while the approach emphasizes the importance of multi-domain modelling in order to accurately capture real-world performance, enabling better design, control and reliability.

References

[1] Axinti, S., and F. D. Scheaua. *Introduction to Industrial Hydraulics* / *Introducere în hidraulica industrială*. Galati, Galati University Press, 2015.
[2] Axinti, G., and A. S. Axinti. *Hydraulic and pneumatic drives* / *Acţionări hidraulice şi pneumatice*. Vol I-V. Chişinău, Tehnica-Info Publishing House, 2008-2012.
[3] Scheaua, F. D. “Functional description of a hydraulic throttle valve operating inside a hydraulic circuit.” *Hidraulica Magazine*, no. 1 (March 2016): 47-50.
[4] Scheaua, F. D. “Theoretical aspects regarding the pressure safety valves operation within a hydraulic circuit.” *Hidraulica Magazine*, no. 1 (March 2018): 65-70.
[5] Merritt, H. E. *Hydraulic Control Systems*. Wiley, 1991.
[6] Watton, J. *Fundamentals of Fluid Power Control.* Cambridge University Press, 2009.
[7] Esposito, A. *Fluid Power with Applications*. Pearson, 2012.
[8] Edge, K. A. “The control of fluid power systems — responding to the challenge.” *Proceedings of the Institution of Mechanical Engineers, Part I: Journal of Systems and Control Engineering* 216, no. 6 (2002): 355–368.
[9] Manring, N. D. *Hydraulic Control Systems*. Wiley, 2020.

ISSN 1454 - 8003
Proceedings of 2025 International Conference on Hydraulics and Pneumatics - HERVEX
November 19-21, Băile Govora, Romania

DESIGN CRITERIA AND COMBUSTION ANALYSIS FOR A 10 KW TLUD REACTOR

Gabriela MATACHE[1], Ioan PAVEL[1], Andrei-Ionel PĂTRUȚ[2], Elena SORICĂ[3]

[1] National Institute of Research & Development for Optoelectronics/ INOE 2000 – Subsidiary Hydraulics and Pneumatics Research Institute / IHP, Bucharest, Romania; fluidas@fluidas.ro

[2] S.C. CALORIS GROUP S.R.L. Bucharest, Romania; andrei.patrut@ymail.com

[3] National Institute of Research-Development for Machines and Installations Designed to Agriculture and Food Industry INMA Bucharest, Romania

Abstract: *This paper presents the theoretical background and the main design elements for Top-Lit Up Draft (TLUD) burners, aimed at producing cleaner thermal energy from biomass and reducing emissions associated with incomplete combustion. The key stages of biomass conversion (drying, pyrolysis, oxidation) are described, together with the conditions for complete combustion and the role of stoichiometric air and excess air in controlling CO and particulate emissions. Draft (chimney effect) and flue-gas analysis are discussed as optimization tools for safe operation and higher overall efficiency. The applied section proposes a sizing algorithm for a 10 kW TLUD reactor operating in batch mode for about 3.5 h, starting from a specific reactor power of ~300 kW/m² and a standardized diameter of 0.20 m. For pellets, an initial fuel charge of ~9.42 kg and a gasified biomass rate of ~2.67 kg/h are estimated, corresponding to an available energy of ~160 MJ. The air supply is split into primary (≈70%) and secondary (≈30%) streams, with indicative flows of about 18 m³/h and 8 m³/h, respectively, to support complete combustion of the produced gas. Overall, TLUD technology is highlighted as an efficient, low-emission option for biomass-based heating applications, including the co-production of biochar.*

Keywords: *TLUD (Top-Lit UpDraft), biomass micro-gasification, reactor sizing; low emissions (CO, PM)*

1. Introduction

The adverse impacts of biomass use for energy production mainly stem from incomplete combustion and the release of CO_2 and particulate matter (PM) into the atmosphere, which contribute to global temperature rise and aggravated climate change. Climate change mitigation and the conservation of forest resources have been major drivers behind many improved-combustion system projects. From an energy perspective, direct burning of woody fuels to generate heat often exhibits significant inefficiencies and should be replaced with modernized combustion systems with higher efficiency and lower pollution.

In many developing countries, traditional open fires are still used for cooking, often with energy efficiencies below 10%. This can be substantially improved by using enhanced combustion devices, thereby reducing firewood consumption and, implicitly, uncontrolled deforestation. Top-Lit UpDraft (TLUD) burners belong to this category of improved systems because they enable staged combustion and finer control of combustion air [1].

Combustion is the reaction of a fuel with oxygen from the air that releases heat. This process is used daily in households for heating and cooking and in industry to generate heat or steam. Combustion accounts for roughly 85% of the world's energy use and is vital to modern life.

In the current context—where emissions reduction, higher energy efficiency, and sustainable biomass utilization are pursued simultaneously—TLUD systems are of particular interest because they can provide low-emission thermal energy and, at the same time, produce biochar with potential for carbon storage. The aim of this paper is to present the sizing elements for a 10 kW TLUD reactor, starting from combustion principles and natural-draft flow fundamentals, and to illustrate the relationship between design parameters and the energetic and environmental performance of the system.

2. Combustion Mechanism

To convert solid biomass into useful thermal energy, it must undergo combustion. Although many different combustion systems are available, the fundamental principle of biomass combustion is essentially the same in each case. There are three main stages of the combustion process, as shown in studies by specialists from the University of Arkansas and the United States Department of Agriculture.

Main stages of the combustion process

1. **Drying** — All biomass contains moisture, which must be removed before combustion can proceed. The heat for drying is supplied by radiation from the flame and heat stored in the combustion chamber. No chemical decomposition occurs in this stage—only phase change from liquid water to vapor.
2. **Pyrolysis** — When the temperature of dried biomass reaches approximately 200–350°C, volatile compounds are released. Pyrolysis products include carbon monoxide (CO), carbon dioxide (CO_2), methane (CH_4) and heavier compounds (tar) that may condense upon cooling. These gases mix with oxygen and burn, producing a yellow flame. The remaining solid, after volatiles have been released, is char (biochar). Oxygen must be supplied to sustain the gas-phase combustion.
3. **Oxidation** — At around 800°C, fixed carbon oxidizes (burns). Oxygen is required both in the fuel bed and above it, where CO can further oxidize to CO_2. Adequate residence time in the combustion zone supports complete burnout. In practice, all stages may occur simultaneously in different zones of the combustion chamber.

Combustion is considered complete when the fuel's chemical energy is extracted to the greatest extent and conversion to CO_2 and H_2O is maximized. Achieving as complete a combustion as possible improves fuel utilization and reduces pollutant emissions. Sufficient air must be present, while excess air should be controlled to avoid increased losses with flue gases [2].

Air Requirement for Complete Combustion

Complete combustion occurs when fuel and air are mixed for a sufficient time under adequate turbulence and temperature. Biomass can be approximated chemically as CH_2O. As an example, consider the combustion of 30 kg of biomass. For complete combustion, approximately 32 kg of oxygen are required, along with about 105.3 kg of nitrogen from the air (air contains roughly 21% oxygen and 79% nitrogen by volume). The total required air mass is therefore about 32 + 105.3 = 137.3 kg, i.e., approximately 4.58 kg of air per 1 kg of perfectly dry biomass (0% moisture).

Besides heat, this reaction produces about 18 kg of water vapor, 44 kg of CO_2 (a greenhouse gas), and 105.3 kg of nitrogen. Exact values depend on the actual biomass composition (carbon, hydrogen, oxygen content and moisture), which is why detailed burner design often uses elemental analysis.

Stoichiometric combustion represents the theoretical optimal fuel–air ratio. In practice, it cannot be perfectly achieved due to imperfect mixing, cold zones, and limited residence time. Therefore, additional air—known as excess air—is supplied.

Typical excess-air levels for combustion systems range from 5% to 50%, depending on fuel and system configuration. For TLUD burners, an excess air ratio corresponding to approximately 40–50% can help achieve stable operation with low CO and PM, particularly when the produced gas is burned in a well-mixed burner (e.g., FLOX-type) [3].

Combustion Efficiency

Combustion efficiency depends on how completely the fuel burns and how much of its chemical energy is converted into useful heat. While 100% efficiency is theoretically possible, it cannot be reached in practice due to heat losses (through walls, flue gases, radiation, and convection) and localized incomplete combustion.

Typical combustion-efficiency values are:

- Open fireplace: 10–30%;
- Conventional space heater/stove: 50–80%;
- Commercial gas boiler: 70–82%;

- Residential gas boiler: 70–82%;
- Oil- burner heating system: 73–85%;
- Induced- draft furnace: 74–80%;
- Gas-burner boiler: 75–85%;
- Condensing furnace (gas or oil): 85–93%.

Combustion is a chemical reaction that involves various substances (mainly C, H, and O) and oxygen, producing light and heat as forms of energy. The luminous energy appears in the form of a flame, but most of the energy is released as thermal energy. In the design of biomass burners, including TLUD systems, the emphasis is on increasing the overall thermal efficiency of the system (combustion + heat transfer) and on reducing pollutant emissions.

Complete vs. Incomplete Combustion

Complete combustion occurs when a controlled excess of oxygen is available. Under near-ideal conditions, the fuel mainly produces CO_2 and H_2O, with very low CO and volatile organic compounds Incomplete combustion occurs when oxygen is insufficient or mixing is non-uniform. In that case, products may include CO along with CO_2, water vapor, and sometimes unburned carbon particles (soot). Incomplete combustion causes energy losses and negative impacts on the environment and health.

Although flame color can sometimes indicate the presence of certain species, the main goal in TLUD operation is to minimize incomplete combustion and maximize both energy efficiency and biochar quality [4].

Draft (Chimney Effect)

Draft refers to the gas flow through the combustion system, from air intake to flue-gas exhaust through the chimney. After combustion, hot gases leave the combustion chamber, pass heat exchangers, and exit through the stack.

Depending on the design of the combustion system, draft can be:

- **natural**, in which combustion air is drawn in due to the density difference between the hot gases and the outside air;
- **mechanical**, when air is pushed or pulled through the system by a fan;
- **combined**, when both the natural draft effect and assist fans are used.

The flow rate of gases from the combustion chamber must be carefully controlled to ensure that all flue gases are removed from the combustion zone at the correct velocity. Insufficient draft leads to a buildup of toxic gases (CO) and potentially explosive gases, such as hydrogen–air mixtures, which may form in the combustion chamber or be vented indoors, creating health hazards.

By contrast, excessive draft can cause unwanted turbulence in the system, preventing complete combustion (the flame is “pulled” out of its optimal zone) and increasing heat losses through the flue gases. High draft is also undesirable because it tends to mechanically overstress the combustion chamber and the heat exchanger.

In TLUD reactor design, chimney height, the indoor–outdoor temperature difference, and pressure losses along the flow path are critical parameters for achieving sufficient natural draft, especially in fan-less configurations.

Combustion Analysis and Key Indicators

Combustion analysis involves monitoring the gases leaving the system after combustion (flue gases) in order to improve the overall process. It is important to monitor flue-gas composition for three main reasons:

- **Environmental concerns** — regular flue-gas testing ensures compliance with environmental standards imposed by national and European legislation.
- **Maintenance and safety** — high concentrations of toxic gases or soot may indicate that equipment maintenance is required (e.g., cleaning heat exchangers, adjusting the burner) to reduce toxic compounds and deposits.
- **Energy efficiency** — the presence of compounds such as carbon monoxide (CO) or high levels of residual oxygen indicates that the combustion process could operate more efficiently, saving fuel and reducing costs.

Combustion analysis typically includes measuring:

- volumetric concentrations of O_2, CO, and CO_2;
- flue-gas temperature**;**
- chimney pressure or draft**.**

When oxygen (O_2) is found in the flue-gas exhaust at high levels, it usually means that more air than necessary has been supplied (high excess air), which increases heat losses. When too little oxygen is supplied to the burner, carbon monoxide (CO)—a highly toxic gas—forms in the flue gases, and combustion efficiency decreases [5].

An optimal operating regime for a TLUD gasifier is one in which excess air is sufficient to keep CO below the limits imposed by regulations, but not so high that it significantly penalizes thermal efficiency.

Sizing Elements for TLUD Stoves with Biochar Co-Production

When carbon storage in biochar is desired, sizing calculations determine the reactor diameter and height for a target biochar yield. Biochar composition is useful because it enables calculation of stoichiometric air demand and the regulated (actual) air flow.

Sizing is based on thermodynamics and natural-draft flow principles. Air for gasification is kept below stoichiometric demand to maintain a gasification regime (not direct full combustion of biomass). The total air is split into **primary** and **secondary** flows in typical ratios (e.g., 9:1 or 7:3), depending on geometry and application goals [6].

The reactor diameter (D) is selected so that the maximum gas velocity is on the order of 1 m/s, to avoid entrainment of ash and to ensure a stable flame.

Chimney height (H) can be estimated to provide sufficient natural draft, using:

$$q = CA\sqrt{2gH\frac{T_i - T_e}{T_e}} \tag{1}$$

where:

- (q) = flue-gas flow rate (m^3/s),
- (A) = chimney cross-section (m^2),
- (C) = discharge coefficient (–),
- (g) = gravitational acceleration (m/s^2),
- (H) = chimney height (m),
- (T_i) = average gas temperature in the chimney (K),
- (T_e) = outdoor temperature (K).

Reactor height is set according to the fuel-bed height and the required volume for combustion and post-combustion so that the pyrolysis front advances steadily and produced gases are completely oxidized.

3. General Initial Data on TLUD Gasifiers

Operating principle

A functional scheme of a TLUD gasifier with an integrated burner is typically used. The micro-gasification process is supplied with air either by a variable-speed fan or, in some configurations, by natural draft only. In certain designs, the burner is separated from the reactor. The produced gas (producer gas) has a relatively low heating value, and efficient combustion is supported by specialized burners (e.g., FLOX-type) that provide intense mixing [7].

Biomass is loaded into the reactor and rests on a grate through which gasification air flows upward. Ignition starts from the top of the fuel bed (top-lit).

In most cases, thermal energy is obtained by burning the hot producer gas generated during pyrolysis. The gas mixes with preheated combustion air introduced through ports near the top of the reactor. With strong turbulence, the mixture burns at the reactor outlet at temperatures typically around 900–1000°C.

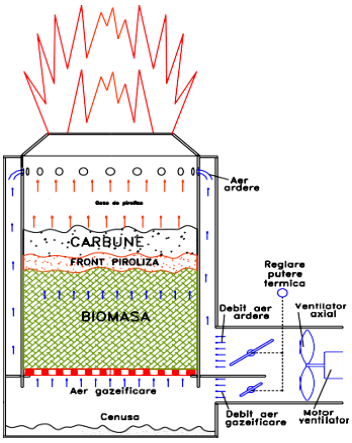

Fig. 1. Functional scheme of a TLUD gasifier with a coupled burner [8]

Output power is controlled by adjusting the gasification air flow (D_{ag}) and the combustion air flow (D_{ard}), either via mechanically linked dampers or by fan speed control. TLUD systems are fixed-bed and operate in batch mode, requiring reloading after the fuel is consumed.
Micro-gasification proceeds at relatively low intensity, with specific hourly fuel consumption of about 80–150 kg biomass/m²·h, leading to reactor specific powers of 250–350 kW/m². The slow process keeps the superficial gas velocity very low ($v_{sup} \leq 0.06$ m/s), which reduces ash entrainment and can yield very low PM2.5 concentrations at the burner outlet (reported values on the order of ≤ 5 mg/MJ_{bm}), significantly below many regulatory limits.
Because producer gas and combustion air can be mixed very effectively, at an optimal excess-air ratio of roughly 1.4–1.5, CO in flue gases can be kept very low (reported as <2% or about 0.8 g/MJ_{bm}), depending on conditions and measurement basis. These features make TLUD thermal generators among the least polluting solid-fuel heat-production options.
Figure 2 compares CO and PM emissions for different combustion technologies; TLUD gasifiers typically show substantially lower values than many conventional systems and can fall below common limit values (e.g., sources such as drtlud.com documentation) [9].

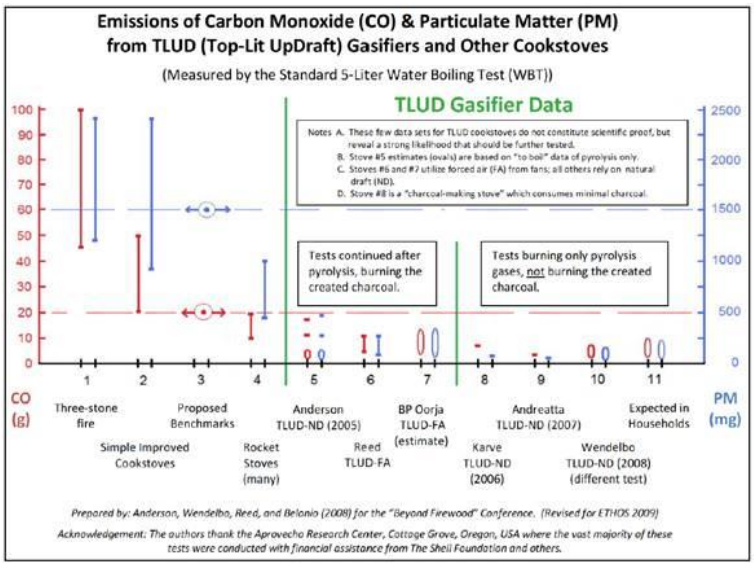

Fig 2. Comparison of CO and PM emissions from different combustion technologies and systems

Gasification stages (drying, pyrolysis, oxidation, reduction) occur simultaneously in different zones of the reactor.

- **Drying** is required because biomass moisture content typically ranges from 5% to 55%. Above 100°C, water is removed as vapor without chemical decomposition.
- **Pyrolysis** occurs roughly between 150–700°C and is the thermal decomposition of biomass in the absence of oxygen.
- **Oxidation** takes place with the help of air introduced into the oxidation zone. Air contains oxygen, water vapor, and inert gases (nitrogen, argon), of which only oxygen actively participates in combustion. Oxidation occurs at 700–2000°C.
- **Reduction** occurs at about 800–1000°C in oxygen-depleted conditions and includes reactions (e.g., Boudouard, water-gas) that generate syngas/producer gas.

Combustible gas components typically include CO (15–30%), H_2 (10–20%), and CH_4 (2–4%), while non-combustible components include N_2 (45–60%), H_2O (6–8%), and CO_2 (5–15%). Exact composition depends on biomass type, temperature, and air–fuel ratio [10].

4. Sizing calculation for a 10 kW TLUD Reactor

Consider a TLUD gasifier with a nominal thermal output of about 10 kW and a batch operating time of 3.5 h.
If the reactor specific power is approximately 300 kW/m², then the required reactor cross-section is: A ≈10/300=0.033 m ².
Choose a standardized reactor diameter of D = 0.20 m, giving:

$$S_r = \frac{\pi \cdot D_r^2}{4} = \frac{\pi \cdot 0.2^2}{4} = \frac{0.19625}{4} = 0.0314\ m^2.$$

Sizing algorithm for the 10 kW reactor:

- **Reactor diameter: D = 0.20 m**
- **Reactor cross-diameter: S_r = 0.0314 m²**
- Biomass bed height (fuel charge height)**:** $H_{rbm} = 0.5\ m$ Assume pellet bulk density: 600 kg/m³ (pellets).

The required initial fuel mass (derived below): $M_{bm0} = 600\ \cdot 0.0157 = 9.42\ kg$.
Biomass volume : $V_{rbm} = H_{rbm} . S_r = 0.5 \cdot 0.0314 = 0.0157\ m^3$
Initial mass in the reactor: $M_{bm0} = 600\ \cdot 0.0157 = 9.42\ kg$
Specific hourly gasified biomass consumption is taken as 85 kg/m²·h; therefore, for the chosen cross-section:

$$C_{hbmg} = 85 \cdot 0.0314 = 2.669\ kg/h$$

Operating time: $T_f = \frac{9.42}{2.669} = 3.53\ h$
Energy in the gasified biomass:

$$E_{bmg} = M_{bmo} \cdot P_{Cibm} = 9.42 \cdot 17 = 160.14\ MJ$$

Average thermal power in the hot gases:

$$P_g = \frac{E_{bmg}}{T_f\ \cdot 3.6} \cdot \eta_{gTLUD} = \frac{160.14\ \cdot\ 0.93}{3.53\ \cdot 3.6} = 11.719\ kWth$$

Useful thermal power at the burner, considering producer-gas combustion efficiency ($\eta_{burn} = 0.95$) and insulation efficiency $\eta_{insul} = 0.96$, will be:

$$P_{burn} = P_g \cdot \eta_{burn} \cdot \eta_{insul} = 11.719 \cdot\ 0.95\ \cdot 0.96 = 10.68\ kWth$$

This is close to the 10 kW target, with a small margin to accommodate additional losses and fuel-quality variations.

Combustion Air Requirement

The combustion-air demand is estimated for complete combustion with a chosen excess-air level. Indicative values are:

- **Theoretical air :** ~6.5 m^3 air/kg biomass
  Actual air (with excess):~9-10 m^3 air/kg

For M_{bmo}≈ 9.42 kg, the total actual air volume is:

$V_{air,tot}$ ≈9.7 · 9.42 ≈ 91m^3aer

Average air flow rate:

$$\dot{V}_{air,med} = \frac{V_{air,tot}}{t_f} \approx \frac{91}{3.5} \approx 26\ \frac{m^3}{h}$$

This is split between primary and secondary air in an approximate 70%/30% ratio:

- Primary air ≈ 18 m³/h
- Secondary air ≈ 8 m³/h

Such a split supports complete combustion of the produced gas while keeping CO low, as typically reported for TLUD technology [11,12].

Figure 3 shows the theoretical temperature evolution in the combustion chamber of the 10 kW TLUD burner, with an autonomy of 3.5 h. The following can be observed:

- **Start-up phase (0–30 min):** a rapid temperature rise to approximately 700°C, as the pyrolysis front forms and producer gas begins to be generated in sufficient quantities.
- **Stable operating phase (30–150 min):** the temperature remains around 720°C, with small fluctuations, characteristic of a quasi-steady regime.
- **Shut-down phase (150–210 min):** a gradual temperature decrease toward 100°C, as the biomass is depleted and the process transitions from gasification to biochar cooling.

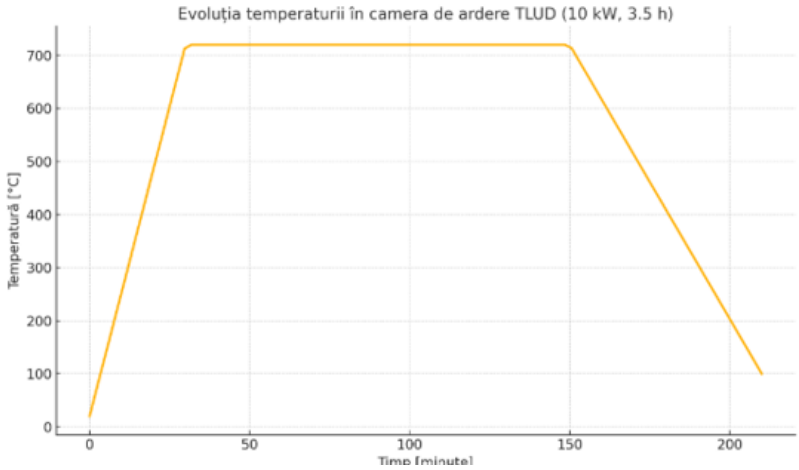

Fig. 3. Theoretical temperature evolution in the combustion chamber of a 10 kW TLUD

Figure 4 shows the evolution of oxygen concentration and airflow rate in the TLUD system. The oxygen concentration in the flue gases changes as follows:

- it decreases from 21% (atmospheric air) to approximately 16% during the complete-combustion phase;
- it stabilizes during the optimal operating phase (30–150 min), indicating efficient combustion;
- it increases again toward the end, signaling fuel depletion and a higher relative share of unused air.

The total supplied airflow rate:

- increases gradually to about 25–26 m³/h to sustain stable combustion;
- remains nearly constant in steady operation, ensuring complete combustion;
- decreases gradually during the shut-down phase to avoid excessive cooling of the combustion zone and to limit cold-air infiltration into the chimney.

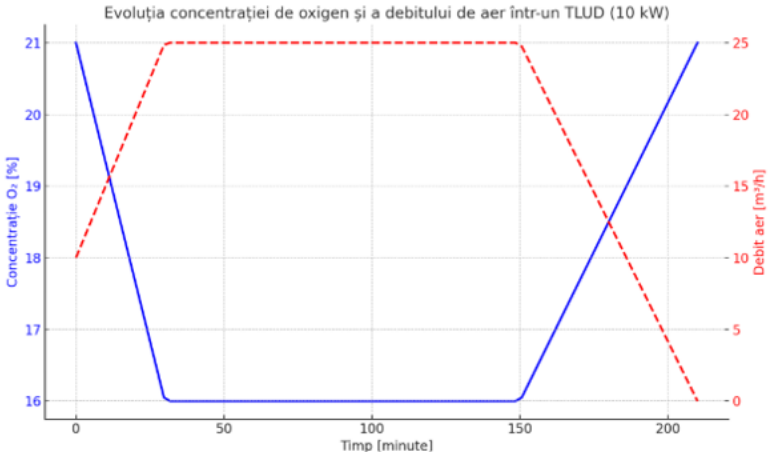

Fig. 4. Evolution of oxygen concentration and air flow in a TLUD system

5. Conclusions

The most important benefit offered by a TLUD-based hot-air generator is that it delivers relatively "clean" thermal energy compared with most other biomass-combustion methods. The equipment is simple and reliable and allows the use of a wide variety of chipped biomass dried to below 20% moisture, while also providing an environmental protection solution by keeping PM and CO emissions below the limits required by regulations.

The sizing calculations presented for a TLUD reactor of approximately 10 kW indicate:

- a cross-sectional area of about 0.0314 m² (diameter 0.20 m),
- a biomass bed (fuel charge) height of about 0.5 m,
- an hourly biomass consumption of approximately 2.7 kg/h,
- an operating time of about 3.5 h in batch mode,
- a useful thermal output at the burner of approximately 11–12 kW, depending on the system's actual efficiencies.

According to the scientific literature, the TLUD gasification process features a slow advance of the pyrolysis front, with a specific hourly biomass consumption of 80–150 kg/m²·h, which leads to relatively low reactor-specific power of 250–350 kW/m². The slow process keeps the superficial gas velocity in the reactor at very low values ($v \leq 0.06$ m/s) and prevents the entrainment of free ash particles larger than $PM_{2.5}$, achieving values of up to 5 mg/MJ_{bm} at the burner outlet; this is at least five times lower than the current standards required for solid-fuel heat generators.

From an energy-policy perspective, better organization of the agricultural sector is needed to increase bioenergy production in Romania. Such organization involves:

- coordination and information exchange based on examples of implemented projects;
- establishing a dedicated biomass information point;
- implementing pilot projects;
- creating functional markets and a biomass trading platform.

A comprehensive bioenergy strategy is required for Romania to clarify aspects related to markets, target groups, and priority technologies (including TLUD micro-gasifiers for rural applications). The strategy must set clear objectives and coordinate individual actions so that national and EU targets can be achieved.

In addition, legislative and organizational measures need to be adopted to reduce pollution, greenhouse-gas emissions, and dependence on crude-oil imports, which are increasingly expensive and uncertain, as oil is on a path toward depletion. One solution is to use biomass resources to produce solid biofuels (firewood, pellets, and wood chips), liquid biofuels (ethanol, biodiesel, and crude vegetable oil), and gaseous biofuels (biogas, TLUD producer gas).

It is also necessary to resume and intensify research on the cultivation and industrialization of energy crops (for example, sweet sorghum, rapeseed, and other fast-growing species, including aquatic

plants), as well as to develop robust micro-gasification technologies that can efficiently valorize these resources while simultaneously producing biochar with a role in carbon sequestration.

Acknowledgments

This work was supported by a grant of the Ministry of Research, Innovation and Digitization, CCCDI - UEFISCDI, project number PN-IV-P7-7.1-PTE-2024-0035, within PNCDI IV.

References

[1] Anderson, P.S., T.B. Reed, and P.W. Wever. “Micro-gasification: What it is and why it works.” *Boiling Point*, no. 53 (2007): 35–37.
[2] Anderson, P.S., and J.S. Schoner. “Origins, History, and Future of TLUD Micro-gasification and Cookstove Advancement.” Technical report, v. 2.0, February 2016. https://woodgas.com/wp-content/uploads/2022/01/TLUD-History-V2-17FEB2016.pdf.
[3] Anderson, P.S. “Micro-gasification Terminology: An Instructional Summary of MG.” November 2013. https://www.bioenergy.org.nz/documents/resource/Factsheet-MG-terms-definitions-2013-11-14.pdf.
[4] Anderson, P.S, and Paal Wendelbo. “Construction Plans for the “PP-Plus” TLUD Gasifier Cookstove”, v. 1, Revision Date 2009-01-21.
[5] Anderson, P.S. “Construction Plans for the “Champion-2008” TLUD Gasifier Cookstove (including operational instructions)”, v. 1.1, Revision Date 2009-03-11. http://www.bioenergylists.org/files/Construction%20Plans%202009-03-11.pdf.
[6] Bhusal, Pitamber, Bhakta Bahadur Ale, and Ramesh Man Singh. “Performance Evaluation of Domestic Rice Husk Gasifier Stove (Belonio Type) and Study on Modification of Design for using Different Biomass.” Paper presented at the Third IOE Graduate Conference, Kathmandu, Nepal, October 2015.
[7] Ahmad, Riaz, Zhou Yuguang, P. Raman, Zhang Yixiang, Zhang Zongxi, Crispin Pemberton-Pigott, Jianbin Guo, and Dong Renjie. “Performance analysis of a top lit updraft (TLUD) gasifier stove, operated with respect to fuel characteristics of multiple types of biomass feedstock.” Paper presented at the 2016 ASABE Annual International Meeting, Orlando, Florida, USA, July 17-20, 2016.
[8] Murad, E., E. Maican, S. Șt. Biriş, and V. Vlăduţ. “Heating greenhouses with TLUD biomass energy modules.” *Balkan Agricultural Engineering Review* 16 (2011): 21-27.
[9] Andreatta, Dale. “A Report on Some Experiments with the Top-Lit Up Draft (TLUD) Stove.” Paper presented at the 2007 ETHOS Conference, Kirkland, Washington, USA, January 26-28, 2007.
[10] Birzer, C., P. Medwell, J. Wilkey, T. West, M. Higgins, G. MacFarlane, and Matthew Read. “An analysis of combustion from a top-lit up-draft (TLUD) cookstove.” *Journal of Humanitarian Engineering* 2, no. 1 (2013): 1-7. https://doi.org/10.36479/jhe.v2i1.11.
[11] Drumea, P., E. Murad, S. Anghel, and M. Bratu. “Motor-pump for irrigation, supplied on gas produced by gasification of vegetal waste.” Paper presented at the International Conference on ENERGY and ENVIRONMENT “CIEM 2003”, Bucharest, Romania, October 29-31, 2003.
[12] Drumea, P., G. Matache, and I. Pavel. “The importance of the byproduct biochar achieved in the process of obtaining energy from biomass.” Paper presented at the 4th International Conference of Thermal Equipment, Renewable Energy and Rural Development TE-RE-RD 2015, Posada Vidraru, Romania, June 4–6, 2015.

ISSN 1454 - 8003
Proceedings of 2025 International Conference on Hydraulics and Pneumatics - HERVEX
November 19-21, Băile Govora, Romania

MARKET FEASIBILITY ON THE CONSTRUCTION OF A MODERN VERTICAL WIND TUNNEL FOR SKYDIVING

Alin Matei POPILIAN[1], Andrei HORHOGEA[2], Dragos MICA[3]

[1] Technical University of Cluj-Napoca, Faculty of Industrial Engineering, Robotics, and Production Management, Specialization Robotics, matei.popilian@outlook.com

[2] Brind Solution SRL, Andrei.horhogea@gmail.com

[3] Technical University of Cluj-Napoca, Faculty of Auto vehicles, Mechatronics, and Mechanics, Specialization Mechatronics, micadragos05@gmail.com

Abstract: *This study evaluates the technical and economic feasibility of developing a large-scale recirculating indoor vertical wind tunnel (4.2-5.2m flight chamber, up to ~300 km/h wind speed) in Romania to serve both civilian users and military freefall training. The information is combined into a multi-segment demand assessment (domestic leisure, inbound tourism, sport skydivers, corporate groups, and military units) with a techno-economic model of capital costs, operating costs, and risks associated. Civilian total addressable demand is estimated at 50,000-100,000 flight sessions/year nationally, with a realistic serviceable share of ~40,000 sessions in Year 1, ramping to almost 100,000 sessions by Year 5 under base-case assumptions. The reference technical configuration is a ~2 MW recirculating tunnel with total CAPEX of ~€9 million and steady-state OPEX of ~€0.6 million/year, yielding projected revenues of ~€2-2.5 million/year at maturity and an approximate internal rate of return of approximately 15-18% with a payback period between 5 and 6 years. Sensitivity analyses highlight utilization and electricity prices as key value drivers, while qualitative risk assessment underscores the importance of early military and corporate block-booking, advanced energy-efficient tunnel design, and robust acoustic and community-acceptance measures. Overall, the project is found to be technically feasible and financially attractive in the capital region, with competitive potential as a regional training and tourism hub for Eastern Europe.*

Keywords: *Vertical wind tunnel, feasibility study, techno-economic analysis, military and civilian training*

1. Introduction

Indoor recirculating vertical wind tunnels have evolved from niche entertainment attractions into multi-purpose testbeds for sports, training, and applied research.[1,2] They enable safe simulation of freefall conditions for skydivers and military personnel, while also serving as high-throughput leisure facilities and platforms for aerodynamic experiments and human-factors studies.[1] In Western Europe and North America, such tunnels are now part of a mature industry with standardized technical solutions, as shown in figure 1., diversified business models, and established user communities.[2,3,4] By contrast, Eastern Europe remains significantly underserved, with limited access to large-scale, high-performance facilities capable of supporting both civilian and professional training requirements.

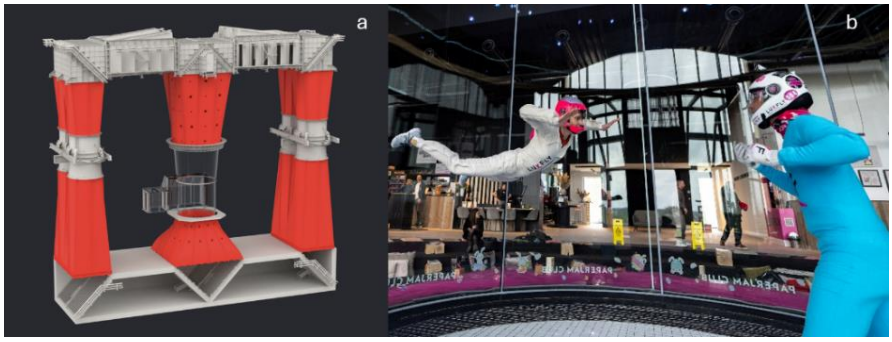

Fig. 1. a. Example of Vertical Wind Tunnel Design [4]; **Fig. 1. b.** LuxFly, Belgium [4]

Romania is a particularly relevant case within this regional context. The country combines a growing middle class and rising tourism [5] with an expanding defense and security sector that increasingly relies on advanced training capabilities. At present, Romanian skydivers, indoor skydiving athletes, and military freefall units must either rely on a small number of regional facilities abroad or operate without access to a domestic large diameter recirculating vertical wind tunnel. A prior attempt to integrate a wind tunnel into an entertainment resort near Bucharest named the Freelo Project, shown in Figure 2. Was attempted and illustrates both the perceived market potential and the execution challenges; the project was announced with an investment of about EUR 8 million [6] but the project was never realized. This situation creates both a capability gap for professional users and a missed economic opportunity in terms of domestic spending, tourism capture, and technology development. A large-scale recirculating vertical wind tunnel could address these shortcomings if it can be shown to be technically and financially feasible under local conditions.

Fig. 2. Freelo project proposed design [6]

The development of such infrastructure is capital intensive however and is highly sensitive to utilization rates, energy costs, and location decisions. Vertical wind tunnels require multi-megawatt drive systems, large building volumes, and specialized civil and MEP(Mechanical, Electrical, and Plumbing engineering), which together generate high up-front investment and long-term operational commitments.[2,7,8] In parallel, demand for tunnel time is fragmented across multiple segments-leisure customers, sport skydivers, corporate groups, and military users-with different willingness to pay, seasonality patterns, and booking behaviors.[1-3] In emerging markets like Romania, where historical data on indoor skydiving are limited, conventional rule-of-thumb approaches to feasibility assessment are insufficient. A structured techno-economic and locational analysis is needed to quantify market potential, to define realistic operating scenarios, and to identify the conditions under which such a project can be developed sustainably.
This study addresses that need by evaluating the opportunity to develop a large-scale indoor vertical wind tunnel in Romania, with a focus on serving both civilian and military users. First, the potential demand is assessed by segment, combining national demographic and income indicators with benchmarks from established tunnel markets and scenario-based assumptions on adoption rates.[2-5] Secondly, a comparative location analysis is conducted across major Romanian urban centers, considering population and tourism density, energy and land availability, proximity to military units, and regulatory or incentive frameworks. Third, a detailed techno-economic model of

the proposed facility is built, including capital expenditures, operating costs, pricing strategies, and cash-flow projections under base-case and sensitivity scenarios, drawing on international cost and performance benchmarks for the proposed tunnels. [2,7,8]
Beyond quantifying feasibility, the study aims to clarify the strategic positioning of a Romanian vertical wind tunnel within the wider Eastern European context. Technical design choices (e.g., tunnel size, configuration, energy-efficiency measures) and business model options (e.g., civilian retail vs. contracted military training blocks, regional team camps) are examined in terms of their influence on both risk and return.[1,2,7-10] The results highlight key value drivers—particularly utilization and electricity prices, and outline the conditions under which Romania could host a competitive regional hub for vertical freefall training and indoor skydiving.

2. Methodology

The study follows a techno-economic methodology, designed to evaluate feasibility and potential of a project based mainly on technical factors, and economic factors. Firstly, different types of indoor wind tunnels were analyzed based off already existing, active wind tunnels. Data was broken down into type of tunnel, chamber diameter, max air speed, power consumption, typical capex costs, and typical build times. The ratio of approximate capital expenditure (CAPEX) cost to chamber diameter, max air speed, and power was then done to compare the existing options.
Secondly, a further analysis of CAPEX was estimated including other costs other than just the tunnel. Wind-tunnel equipment, building and civil works, electrical and HVAC systems, fit-out and ancillary systems, engineering and project management, and contingency were all considered. Benchmark data for recirculating tunnels indicate that most projects in this size range require total investments of roughly EUR 6-10 million, depending on specification and local construction costs. [2,7] Operating expenditure (OPEX) was estimated, and structured into energy, staffing, maintenance, rent or land cost, insurance, marketing, and general administration. The model projects a 10-year profit and loss (P&L), cash flow, and key financial indicators (NPV, IRR, payback) under base-case, conservative, and optimistic utilization scenarios. Sensitivity analyses were then run on the most uncertain and impactful variables-primarily utilization, average price per minute, electricity tariffs, and CAPEX variance-to assess robustness, using industrial electricity prices around EUR 0.14/kWh as representative for Romanian medium non-household consumers.[11] Finally, qualitative risk identification and mitigation strategies were integrated with the quantitative results. This included analysis of demand risk (under-utilization), energy price volatility, construction and schedule risk, financing and interest rate risk, regulatory and community-acceptance risk (noise, traffic), and operational risk (safety incidents, equipment downtime).[1,2,7-10,11] Mitigation concepts such as early memorandum-of-understanding (MoU) blocks with military and corporate clients, energy-efficient tunnel design, phased investment options, and conservative leverage assumptions were considered in interpreting the model outputs and deriving location-specific recommendations.

3. Analysis of existing tunnel types

The design of vertical wind tunnels for skydiving is driven primarily by requirements on flow uniformity, turbulence intensity, acoustic emissions, and operating cost. Existing facilities can be broadly categorized along three axes: openair shown in Figure 3 versus closed recirculating flow tunnels as shown in Figure 1, portable versus fixed installations, and small versus large test-section diameter. Each configuration imposes constraints on achievable flow quality and on the economic feasibility of intensive training or competitive use.

Fig. 3. Example of open-air wind tunnel [12]

3.1 Open-air versus closed-circuit vertical wind tunnels

Open-air (open-jet, non-recirculating) wind tunnels accelerate ambient air through a contraction and eject the jet to the surroundings after the test section. This configuration is structurally simpler and generally involves lower initial capital cost, as it avoids complex flow-conditioning loops. However, for skydiving applications, open-air tunnels exhibit several limitations. The jet is directly influenced by ambient conditions, leading to variations in density, temperature, and crossflow, which in turn affect air speed stability and perceived flight quality. Energy efficiency is also significantly lower, because the full volumetric flow must be continuously accelerated from rest. Closed-circuit recirculating tunnels route the flow through a return loop that may include turning vanes, diffusers, and heat exchangers. In vertical tunnels for skydiving, this configuration enables stringent control of airspeed and temperature, as the working fluid is reused and conditioned continuously. Recirculating designs achieve higher energy efficiency for a given free-stream velocity, particularly at the high volumetric flow rates required for human flight. The enclosed flow path also reduces external noise emissions and permits installation in urban environments. The main disadvantages are higher construction cost, increased structural complexity, and the need for precise aerodynamic design of corners and diffusers to minimize secondary flows and turbulence.

3.2 Portable versus fixed installations

Portable wind tunnels are realized as modular or containerized systems, using open-jet or partially ducted configurations. Their primary advantage is rapid deployment for temporary events, demonstrations, or short-term training programs. Structural elements, fan assemblies, and support systems are designed for transportability, which constrains achievable test-section diameter, maximum air speed, and overall stiffness. As a result, portable tunnels usually provide shorter flight columns, higher turbulence levels, and reduced throughput of flyers compared with permanent facilities. Fixed (non-portable) installations are integrated into purpose-built buildings or large industrial halls. These tunnels can employ full recirculating layouts with substantial flow-conditioning sections, vibration isolation, and large-diameter test sections. Fixed facilities allow optimization of structural dynamics, acoustic treatment, and safety systems, and can support continuous, high-volume operation. The trade-off is the requirement for significant capital investment, building permits, and constraints related to site selection and long-term occupancy.

3.3 Large-scale (4.3–5.2 m) recirculating vertical wind tunnels

Large-scale recirculating vertical wind tunnels with test-section diameters in the range of approximately 4.3–5.2 m represent the upper tier of current skydiving infrastructure. At these diameters, the flow can accommodate multiple flyers simultaneously, realistic skydiving

configurations, and advanced coaching scenarios while maintaining adequate wall clearance and safety margins. However, the cost of these facilities is considerable. A comparison between already existing facilities is illustrated in Figure 4.

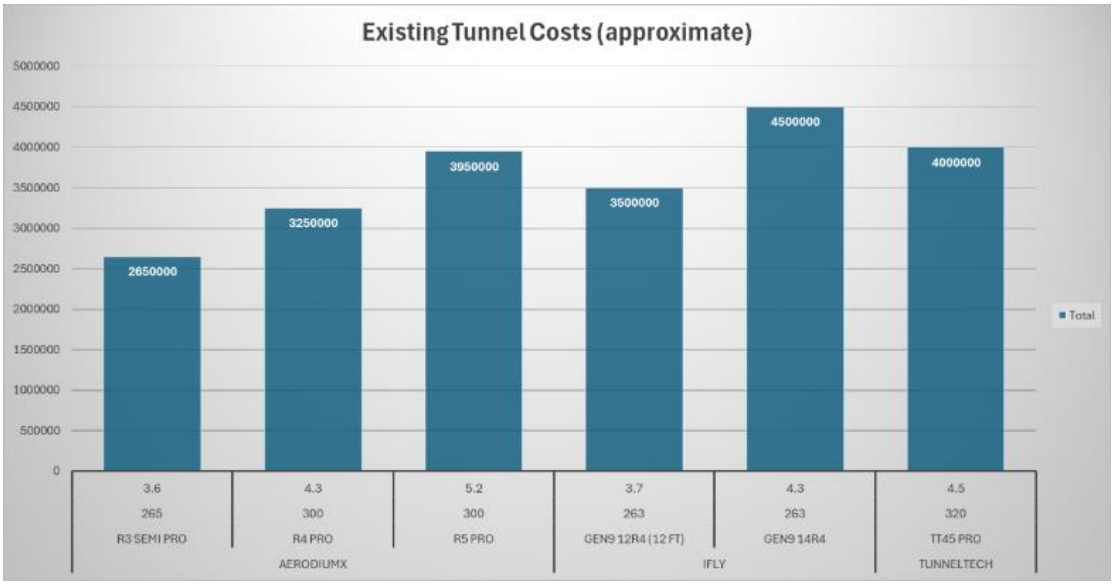

Fig. 4. Cost comparison between different existing manufacturers[4,12-14]

Nevertheless, for this study the choice of tunnel to be studied economically will be that will have a diameter of 5.2m, similar to the R5 Pro tunnel from AERODIUMX [12] shown in Figure 4 above.

4. Techno-Economic Evaluation and Sensitivity Analysis

The tunnel chosen for the Romanian market is therefore a 5.2m wind tunnel with a maximum air speed of around 300 km/h. This configuration offers highest amount of flexibility and allows for both general commercial uses, professional and possibly military training. This configuration is consistent with existing training-grade tunnels providing airspeed control from roughly 180 km/h for first-time flyers up to nearly 300 km/h for advanced maneuvers.[8] The CAPEX estimate, based on already existing data, is on the order of EUR 8-10 million, with EUR 9.5 million adopted in the base-case model.[2,6,7] Approximately EUR 4 million is allocated to tunnel equipment (fans, motors, VFDs, airflow ducts, flight chamber, control systems), about EUR 2.0 million to building and civil works (foundation, structure, cladding, interior fit-out), around EUR 0.8 million to electrical and HVAC systems (high-voltage connection, transformers, ventilation, cooling), roughly EUR 0.7 million to soft costs (design, engineering, project management, permitting), and about EUR 1.0 million to contingency to cover price volatility and scope changes.[2,7] These figures lie within the EUR 6-10 million range reported for most recirculating “PRO” tunnel projects.[2,7]
Operating expenditure is dominated by energy and staffing. Under realistic operating profiles (not full power continuously), annual energy costs are estimated in the EUR 150,000-200,000 range. This is consistent with an average effective power draw of several hundred kilowatts over the day, combined with Romanian industrial electricity tariffs around EUR 0.14/kWh and allowing for demand charges and ancillary fees.[8,11] Staffing a 7-day-per-week operation with instructors, front-office, technical, and management personnel requires roughly 15-20 full-time equivalents, corresponding to approximately EUR 200,000-250,000 per year in payroll. Additional OPEX items include maintenance and consumables (~EUR 50,000/year), rent or property tax (for owned land and building), insurance (~EUR 30,000/year), and marketing and administrative overheads (~EUR 50,000/year). In aggregate, steady-state annual OPEX for the base-case utilization is of the order of EUR 0.5-0.7 million, in line with cost structures reported for comparable facilities. [2,3,7,8]

On the revenue side, the estimated revenue per flight minute in the fifth year, including the time taken in between sessions, Is around EUR 9.5. This calculation considered a mix of packages including basic 2 session packages, packages with 4 sessions, and “pro” packages with 10 sessions included as shown in Figure 5 below.

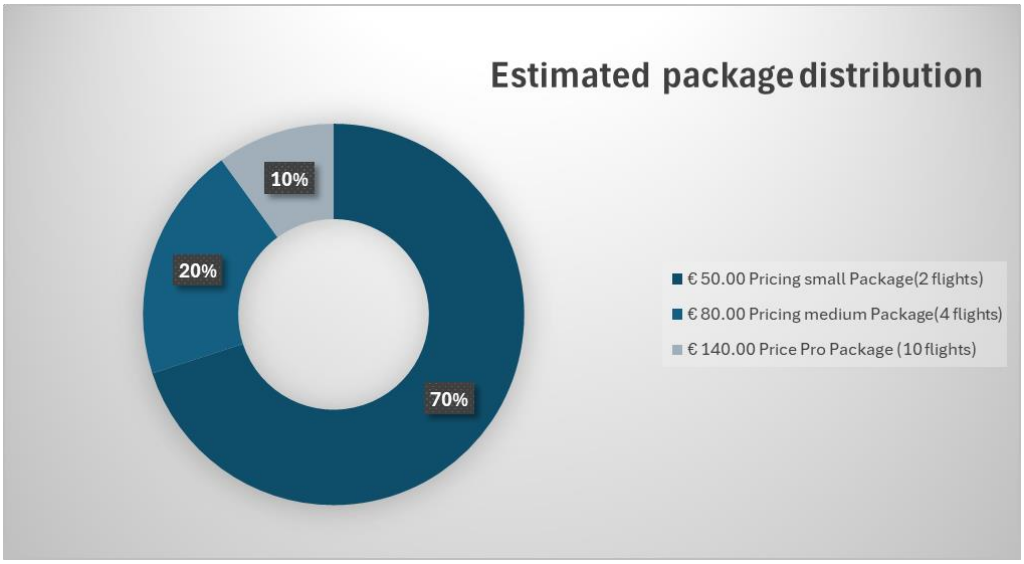

Fig. 5. Package pricing and distribution

This is just below international pricing, where first-time packages in Europe and North America typically range from about USD 60-100 (or EUR 50-90) for two to four minutes of flight, with substantially lower effective rates for bulk sport time.[3] Under the base-case utilization trajectory (ramping toward almost 100,000 sessions by year 5). This target ramp up is illustrated in figure 6 b.

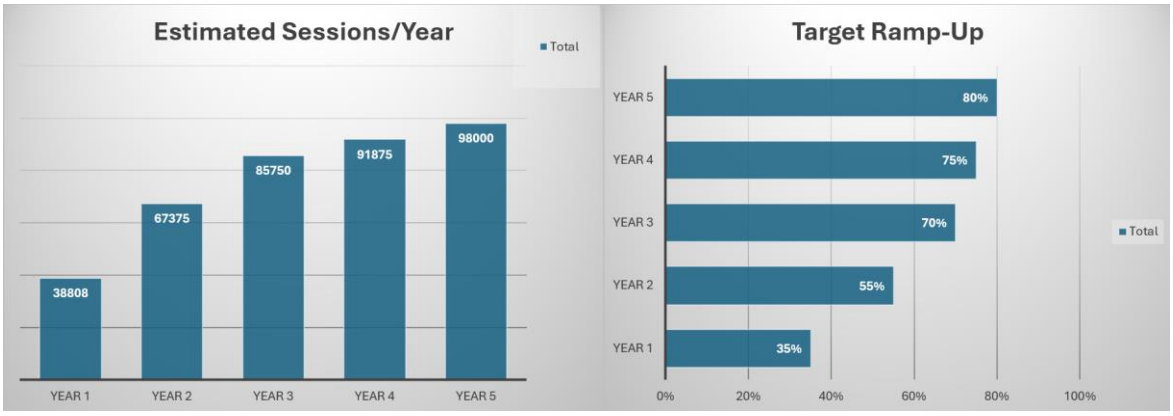

Fig. 6.a. Estimated sessions per year, **Fig. 6.b.** Target Ramp-up capacity

annual revenues at maturity are projected to be just over EUR 2 million euros per year. The calculation of revenue took into consideration estimated work hours of 14 hours per day, 330 days per year, average wind tunnel time of 1.5 minutes, time between sessions of 1 minute in the first year, dropping to 0.9 min after the first year and the Capacity utilization (rate) which is shown in Figure 4 b. The theoretical maximum revenue was also calculated considering the same data with 100% utilization. The projected revenue is compared to the theoretical maximum revenue and is shown below in Figure 5 below.

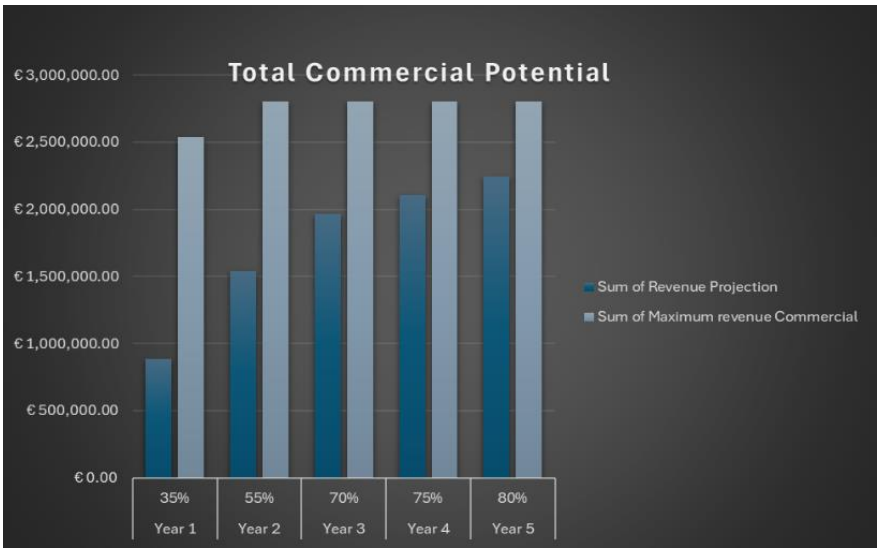

Fig. 7. Revenue projected compared against theoretical maximum revenue

combined with the OPEX structure described above, yields positive EBITDA margins and supports coverage of financing costs and depreciation.

Financial results indicate that the project can achieve an internal rate of return (IRR) on equity in the approximate range of 15-18% and a payback period of 5-6 years after opening, assuming a 10-year analysis horizon plus terminal value and a moderate leverage structure. Sensitivity analyses show that utilization and electricity prices are the dominant value drivers. A sustained shortfall in demand (e.g., 20-30% below base-case) materially reduces IRR and lengthens payback, while favorable utilization—supported by strong marketing and institutional contracts—can push IRR above 20%. Similarly, significant increases in electricity tariffs compress margins unless partially offset by dynamic power management, energy-efficient design measures, or long-term fixed-price supply contracts. [7,8,11] CAPEX overruns are also impactful but can be mitigated through staged contracting, robust contingencies, and potential access to local or EU development incentives.

Overall, the techno-economic evaluation confirms that a well-executed large-scale tunnel in Bucharest is financially viable under realistic assumptions but also exposes the project's dependence on high operational reliability, strong sales and partnership capability, and proactive management of energy and financing risks. These findings inform both the recommended configuration and the strategic risk-mitigation measures discussed with potential investors and stakeholders.

5. Conclusions

This research assessed the feasibility of developing a large-scale recirculating vertical wind tunnel in Romania by integrating multi-segment demand analysis with a detailed techno-economic model. The results indicate that Romania's combined civilian, tourism, and military markets can sustain a high-performance tunnel, provided the facility is developed in a major metropolitan area with strong transport connectivity and supported by professional marketing and institutional partnerships. From a financial perspective, a reference facility with approximately 2 MW installed power, a 4.2–5.2 m flight chamber, and CAPEX of about EUR 9 million can achieve revenues of EUR 2–3 million per year at maturity and generate mid-teens IRR with a 5–6-year payback period, assuming base-case utilization and current cost structures. However, the project's attractiveness is sensitive to utilization levels and electricity tariffs, underscoring the need for conservative planning, robust pre-sales (including military and corporate block bookings), and energy-efficient technical design. Beyond the narrow financial metrics, a Romanian vertical wind tunnel could deliver broader strategic benefits: retention of training expenditure currently spent abroad, development of a domestic indoor skydiving ecosystem, enhancement of military training capabilities, and creation of

a flagship leisure and tourism asset with regional reach in Eastern Europe. To realize this potential, early stakeholder engagement, careful integration into the surrounding urban and regulatory environment, and disciplined project execution will be critical. Future work may extend this analysis by incorporating more granular behavioral data for Romanian consumers, exploring alternative financing and ownership structures, and evaluating the role of public-private partnerships or EU-level funding in de-risking such high-impact recreational and training infrastructure.

Acknowledgments

This study was conducted with the support of AIMA Innovations and BRIND Solution.

References

[1] Urbanová, Kateřina. 'Free Falling Like 007.” Accessed October 29 2025. https://aero-space.eu/2022/09/13/free-falling-like-007-effective-and-safe-training-for-not-only-military-users/.
[2] Indoor Skydiving Source.
“Effective and Safe Training for (Not Only) Military Users.” September 13, 2022. Accessed November 4 2025. https://indoorskydivingsource.com/articles/build-an-indoor-skydiving-facility/.
[3] Indoor Skydiving Source.
“How Much Is Indoor Skydiving? iFLY Prices and More.” October 22, 2022. Accessed October 30 2025 https://indoorskydivingsource.com/articles/indoor-skydiving-prices-the-cost-of-flight/.
[4] TTE GmbH. *Tunneltech website*, Accessed November 2 2025, https://tunneltech.eu/en-ro/
[5] TravelMole.
“Romania international tourist arrivals up 5.5% in the first half of 2025.” August 21, 2025. Accessed October 29, 2025. https://www.travelmole.com/news/romania-tourism-first-half-2025/.
[6] ***. “Surfing in Bucharest? An Entertainment Resort of EUR 8 M Offers This as of Next Year.”
The Romania Journal, September 27, 2015. Accessed November 2 2025. https://www.romaniajournal.ro/business/surfing-in-bucharest-an-entertainment-resort-of-eur-8-m-offers-this-as-of-next-year/.
[7] Aerodium. “How Much Does It Cost to Start an Indoor Skydiving Business?”
Aerodium Technology, FAQ page. Accessed November 1, 2025. https://aerodium.technology/faq/how-much-does-it-cost-to-start-an-indoor-skydiving-business/.
[8] Danfoss. “2 MW of Power for a Freefall Skydiving Experience under Safe Control.”
Case story, December 23, 2015. Accessed October 27 2025. https://www.danfoss.com/en/service-and-support/case-stories/dds/2-mw-of-power-for-a-freefall-skydiving-experience-under-safe-control/.
[9] Ministry of Defence Republic of Serbia. Serbian Armed Forces.
“63rd Parachute Brigade Members Receive Wind Tunnel Training.” News release, September 12, 2023. Accessed October 10 2025. https://www.mod.gov.rs/eng/20473/obuka-pripadnika-63-padobranske-brigade-u-vazdusnom-tunelu20473.
[10] United States Navy.
“Wind Tunnel Training: Key to Expeditionary and Special Warfare Readiness.” *Navy.mil* News Story, August 2, 2023. Accessed October 10 2025. https://www.navy.mil/Press-Office/News-Stories/Article/3480542/wind-tunnel-training-key-to-expeditionary-and-special-warfare-readiness/.
[11] ***. “Romania - Electricity Prices: Non-household, Medium Size Consumers.”
TradingEconomics. citing Eurostat, December 2024 data. Accessed October 26 2025. https://tradingeconomics.com/romania/electricity-prices-non-household-medium-size-consumers-eurostat-data.html.
[12] Aerodium Website. “The best vertical wind tunnels.” *Aerodium Technologies*. Accessed November 4, 2025. https://aerodium.technology./
[13] iFLY tunnel systems. iFLY Gen-8-12R2-12R4-Spec-Sheet. Accessed November 4, 2025. https://iflysales.com/wp-content/uploads/2022/03/Gen-8-12R2-12R4-Spec-Sheet.pdf.
[14] iFLY tunnel systems. iFLY Gen-9-14R4-Spec-Sheet. Accessed November 5, 2025. https://iflysales.com/wp-content/uploads/2022/03/Gen-9-14R4-Spec-Sheet.pdf.

ISSN 1454 - 8003
Proceedings of 2025 International Conference on Hydraulics and Pneumatics - HERVEX
November 19-21, Băile Govora, Romania

EVALUATION OF BIOSYNTHETIC BLENDS BASED ON POLYOL ESTERS (POE) FOR ENVIRONMENTALLY FRIENDLY HYDRAULIC APPLICATIONS

Adriana Mariana BORȘ[1], Ștefan Mihai ȘEFU[1], Lăcrimioara ȘENILĂ[2], Liliana DUMITRESCU[1], Iulian DUMITRU[3]

[1] National Institute of Research & Development for Optoelectronics/ INOE 2000 – Subsidiary Hydraulics and Pneumatics Research Institute / IHP, Bucharest, Romania, bors.ihp@fluidas.ro

[2] National Institute of Research & Development for Optoelectronics/ INOE 2000 – Subsidiary Research Institute for Analytical Instrumentation ICIA, Cluj-Napoca, Romania, lacri.senila@icia.ro;

[3] National Institute of Research – Development for Machines and Installations Designed for Agriculture and Food Industry – INMA Bucharest, Romania, dumitru.iulian2016@gmail.com

Abstract: *Increasing sustainability requirements in the lubricants sector have driven the shift from mineral bases to environmentally friendly bio-synthetic and ester bases. Ecological hydraulic oils must combine high biodegradability (>70%), oxidative stability and compatibility with elastomers and modern hydraulic systems (piston pumps, gear pumps). In the context of the transition to green and sustainable lubricants, blends of polyolesters (POE) with bio-derived esters such as TMP-esters, PE-esters, glycerol carbonate, modified phospholipids and epoxidized acylglycerides represent a promising direction for hydraulic applications with high requirements for stability, antiwear protection (AW) and EP performance. The need to reduce the ecological impact of hydraulic lubricants has led to the development of bio-synthetic bases (modified natural esters, polyol esters, glycerol carbonate, epoxidized lecithin, etc.), capable of combining high biodegradability with the tribological performance of synthetic POE (polyol ester) bases.*

Keywords: *Polyol esters (POE), modified lecithin (GPL), bio-derived esters (TMP), anti-wear protection (AW) and extreme pressure (EP) performance*

1. Introduction

The hydraulic fluids used to drive piston pumps have characteristics that enable them to work under technical conditions such as high pressures, thermal fluctuations, friction and wear stresses, demulsification requirements, compatibility with seals, etc.).
Formulations must meet requirements for viscosity, thermal stability, oxidation stability, pressure resistance, as well as foaming and demulsification properties – all of which are relevant conditions for hydraulic pumps.
Blends with polyol esters can offer:

- biodegradability and potential for reduced environmental impact;
- stability at extreme temperatures, due to the chemical structure of polyol esters (R-COO-R');
- resistance to hydrolysis, important in wet or high temperature hydraulic applications;
- good compatibility with internal materials (seal ring, gaskets, metals), depending on the esters used and the control of auxiliary properties.

2. Methods and Materials

Possibility to adjust properties through mixtures – combining different esters or esters with synthetic/mineral oils.

- the presence of the ester functional group (-COO-), confers a distinct polarity, significantly influencing the physical and chemical properties of the mixtures; (R is an acid radical and R' is an alcohol radical);
- esters can be classified into various categories:

• diesters (containing two ester groups);
• polyol esters (derived from alcohols with more than two hydroxyl groups);
• complex esters (which may also include other functional groups in their structure).

This structural diversity allows for fine-tuning of the properties of esters to meet the specific requirements of different lubrication applications [1], esters play a dual role being used as:

• base oils - which provide superior performance in applications with extreme temperatures or high loads;

• additives, being added in small quantities to optimize lubricant formulations based on mineral or synthetic oils (lubrication, antifoam, thermal stability) [2];

- esters are included in Group V, according to the American Petroleum Institute (API) which includes all base oils that do not fall into Groups I-IV classified according to the content of saturated groups and sulfur, as well as the viscosity index.

This classification helps to compare esters with other types of base oils in terms of manufacturing process, properties and typical applications [3].

Comparative analysis of esters with base oils from other API groups highlights their specific advantages, namely:

- superior thermal and oxidative stability (absence of hydrogen atoms in the beta position relative to the ester group e.g. neopolyol esters or Secondary Polyol Ester™ (SPE));

- contribute to extending the service life of the lubricant and reducing the formation of harmful deposits;

- have the ability to maintain performance at temperatures up to 220°C [4];

- low volatility - reduction of oil losses through evaporation [5];
- good solubility (e.g. polyalphaolefins (PAO)) - reduced deposit formation; keeping oxidation products in suspension, uniform distribution of additives;
- compatibility with other base oils and seals [6];
- adhesion to metal surfaces, (due to their polarity) - molecular film that lubricates, and protects against oxidation and corrosion under high pressure or extreme temperatures [7];
- biodegradability (ester derivatives) - reduce the impact on the environment in case of leakage [8], [9];
- can act as friction modifiers, (esters of dicarboxylic acids) reduce friction coefficients and wear under moderate load conditions;
- resistance to oxidative processes (e.g. polyol esters and polyalphaolefins (PAO)) [10];
- viscosity index and reduce the pour point of oils [11],
- hydrodynamic films stable at high temperatures and high shear rates [12].

Table 1: Comparative analysis with base oils from API groups

Property	Group I	Group II	Group III	Group IV (PAO)	Group V (Esters)
Saturated Solutions	<90%	≥90%	≥90%	Synthetic	Synthetic/Other
Sulfur	>0.03%	≤0.03%	≤0.03%	0%	Variable
Viscosity Index	80-120	80-120	>120	>120	Variable, good
Thermal Stability	Low	Average	High	Excellent	Superior
Oxidative Stability	Low	Average	High	Excellent	Good/Excellent
Biodegradability	Low	Low	Low	Low	Variable, good
Cost	Low	Average	Medium-High	High	Very high
Additive Solubility	Good	Good	Good	Limited	Good/Excellent
Seal Compatibility	Good	Good	Good	shrinkage	Swelling

- Group I contains less refined, lower cost, lower performance base oils containing more sulfur and aromatic groups [13];

- Group II contains slightly improved oils, but are not recommended for high performance applications [14];
- Group III includes high purity oils, sometimes considered synthetic, although they are derived from crude oil [15];
- Group IV (PAO) offers excellent stability at extreme temperatures, but has limited additive solubility, risk of seal shrinkage, and limited wear properties [16];
- Group V includes esters, polyglycols and silicones, offering superior thermal and oxidative stability, excellent lubricity and often biodegradability, have higher costs and possible seal compatibility issues [17];

➢ fire safety (synthetic esters) -Alpha-Tech® technology developed by Pakelo-combines ester bases with Group IV (PAO) bases, are advanced formulations for high performance [18];
➢ improve tribological properties (pentaerythritol esters + commercial oils) [19];

The literature indicates that the use of polyol esters (POE) in hydraulic oils offers advantages such as good thermal and oxidative stability, compatibility with a wide range of materials, and biodegradability. Although polyol esters are highly efficient and versatile, research is continuously aimed at finding solutions that combine performance with sustainability and low cost.

❖ Performance Improvement: researchers are looking for fluids with superior lubrication properties and stability at extreme temperatures to increase the life of hydraulic systems and their operating efficiency.
❖ Sustainability: there is a growing interest in biodegradable hydraulic fluids and products from renewable resources to reduce environmental impact.
❖ Costs: reducing production and maintenance costs by using economically competitive substitutes to be viable.

Table 2: Formulations of polyol ester mixtures, suitable or adaptable for gear pumps or piston pumps

Brevet / document	Formulations / important components	Properties/tests (temperature, viscosity, etc.)	Rating: Suitable for gear/piston pumps
EP 3172294 B1 / US9850444B2 („Unsaturated polyol esters used in hydraulic fluid applications”)	Unsaturated polyol esters. Polyols + unsaturated fatty acids are used	Use in hydraulic applications is mentioned, including pumps (gear, valves, piston). Requires oxidation stability, seal compatibility, wide operating temperatures.	Very promising. If the fluids meet the required viscosity and seal compatibility, they can be used in both gear and piston pumps.
Patent U.S. 6,361,711 („Flame retardant hydraulic oil containing a synthetic ester formed by reaction of a polyol … mixture of acids including oleic acid and isostearic acid”)	Polyols such as neopentyl glycol, glycerin, trimethylolpropane reacted with a combination of acids (oleic, isostearic, etc.).	Kinematic viscosity at 40 °C is specified between ~40-80 cSt; high flash point (≈ 290 °C). Good thermal stability. Oxidation resistance and flame-retardant properties.	Could be good for gear/piston pumps, especially where temperature and fire safety are important. However, the viscosity needs to be appropriate for the system.
U.S. Hydraulic fluids (UniChema Chemie B.V.) Pat. nr. 6,693,064	Fluid based almost entirely on mixed esters of polyols; short chain fatty acids (C5-C12) + long chain acids (C16-C22). Recommended polyol: Trimethylolpropane.	Emphasis is placed on low temperature properties: rheological stability after prolonged exposure to −30 °C; maximum permissible viscosity 7000 mm²/s (≈ cSt) in certain tests.	For gear or piston pumps in cold/high load environments, it could be suitable; but need to check the pour point and whether the fluid does not become too viscous at start-up.

Brevet / document	Formulations / important components	Properties/tests (temperature, viscosity, etc.)	Rating: Suitable for gear/piston pumps
US8299004B2 („Hydraulic fluid and hydraulic system")	Blend containing base oil (mineral or synthetic), polyol esters, polyalcohol's, plus other additives (viscosity index, modulators).	Fluid with high bulk modulus, viscosity index ≥ 110, pour point ≤ −25 °C; good compatibility is proposed.	Very suitable for high pressure pumps, especially piston pumps – where compressibility modulus, volumetric losses and low temperature control are critical.

To classify POE, POE/GC, POE/LPG, POE/AG-E, POE/TMP-E mixtures in wear areas (wet, high temperatures, intense loads), we must look at the hydrolytic, oxidative stability and lubricant film resistance.

❖ POE = polyol-ester — synthetic ester (base for lubricating oils) obtained by esterification of a polyol (e.g.: TMP, pentaerythritol, neopentyl glycol, etc.) with fatty acids:

- have good thermo-oxidative stability, high viscosity index and miscibility with hydrocarbons, which is why they are frequently used as oils for various systems and as technical lubricants.

❖ POE/TMP-E = trimethylolpropane (TMP) ester:

- form oils with good lubricating properties, hydraulic stability and good viscosity index;
- are used for industrial lubricants and fluids resistant to high temperatures;

❖ POE/GC- derivative based on glycerol carbonate / glycerol esters:

- give esters with eco-friendly characteristics (good biodegradability, polarity);
- tends to be more polar, with good ability to dissolve/transport moisture, useful in applications where miscibility and compatibility with polar fluids matter;

❖ POE/GPL-glycerol based on polyols or polyglycerol:

- glycerin esters (glycerol/polyglycerol) offer good lubricating properties, low pour point and stability;

❖ POE/AG-E- indicates an adipic ester or "alkyl-glycerol ester":

- provides lower viscosity, good low temperature lubricity and chemical stability;
- can be used where low temperature flow and compatibility with certain systems are required (e.g. specialized applications).

Disadvantages and limitations of ester-based lubricants

❖ The high cost is significant; polyol esters are among the most expensive base oils, [20,21];
❖ Compatibility with sealing materials (e.g. polar esters can cause swelling [22,23].

Therefore the mixture is balanced with an API Group IV base (PAO), which has the opposite tendency (contraction), to maintain both flexibility and the original dimensions of the seals).

Formulations for hydraulic systems (mobile / industrial systems, anti-wear)

POE/TMP-E (TMP-ester) 85–92% — TMP ester base oil, blend with good viscosity index, thermo-oxidative stability and tribological properties suitable for high-pressure pumps and valves.
Additives: AW/EP (5–7%), antioxidant (phenolic + amine = 1–3%), corrosion inhibitor (0.5–1%), anti-foaming agent (0.2–0.5%), pour point depressant (0.1–1%).
Viscosity: ISO VG32–46 for mobile applications; VG46–100 for industrial systems at higher temperatures.
Hygroscopicity control: POEs are polar and absorb moisture;

Formulations for lubrication processes (high temperature lubrication)

❖ POE/GC or POE/GPL (60-90%) - more polar variants for good adhesion to surfaces and ability to work at high temperatures without volatility, good lubrication of metal surfaces and resistance to oxidation in thermal processes;

❖ Additives: EP/AW as needed (3-8%), antioxidants (1-3%), thermal anti-oxidation and film stabilizers (0.5-2%).
❖ Viscosity: depending on the application- thinner (VG22-46) for spraying; thicker (VG68-150) for press/transport films.
AW = Anti-Wear
EP = Extreme Pressure - are protective additives that reduce wear on metal surfaces in contact, but act differently:
AW → forms a thin protective layer at moderate temperatures (~100-150°C).
EP → reacts chemically at higher temperatures/forces (~>180°C), forming more resistant protective compounds.

Table 3: Formulations, percentages and target properties

Application	Composition (wt%) - key components	Viscosity, 40°C (mm²/s / cSt)	Pour point (°C)	VI (index)	Quick Notes
1.Hydraulic (mobile / industrial anti-wear systems)	POE/TMP-E (base) 90 AW/EP Additive 5 (ZDDP or alternative P-free) 3 Antioxidant 1.5 Antifoam 0.3 Corrosion inhibitor 0.2	32 cSt — ISO VG32)	≤ −30°C	≥ 120	Typical formulation for ISO VG32. Adjust base to VG46/VG68 for higher temperatures. Tests: ASTM D445 (visc.), D97 (pour), D664/D2896 (TAN), bench pump (Eaton/Vickers).
2.Process lubricant (film, high temperature, transport)	POE/GPL or POE/GC (base) 80 EP/AW 6–8 Thermal antioxidant 2 Tackifier/viscosifier 8 Antifoam 0.5	~68(50–100 cSt; (adjustable)	≤ −20°C	110–140	More tacky/tacky film options: Increase tackifier. Prioritize thermal stability and low volatility. Tests: film life, TAPPI/tribology, D2272/D892.
3.PU-Polyester polyol (reactive) (for PU/isocyanate formula)	Polyester polyol (AG-E/ TMP-E)100 (main polyol component; reactive) — note: full PU formulation includes isocyanate, catalysts, surfactant, blowing agent	(reactive polyols) 500 – 5000mPa·s (viscosity at 25–40°C; depends on MW)	depends on polymer; typically −20→ 10°C	VI — not a common criterion for polyols; indicative 80–120	This is a reactive polyol (OH number & functionality are key parameters — e.g. OH 20–140 mg KOH/g, functionality 2–4+). Do not use non-reactive POE oil in place of a polyester polyol. Tests: OH titration, GPC, rheology, cure times and final mechanical properties.
4.PU-POE as additive / plasticizer (optional)	Polyester polyol (main) 92–95 POE (lubricant/plasticizer, non-reactive) 5–8 catalyst/surfactant/foam control	Varies (may increase fluidity; depends on quantity)	May reduce pour point	VI — not relevant	Used only as a flexibility/plasticizer modifier; ≤ 5–8% recommended to avoid compromising the crosslinked network. Mechanical tests required.

Viscosity - 40°C (cSt) — influences hydraulic film lubrication and pumpability;
Pour point - ensures starting/operation at low temperatures; esters can be influenced by added additives but also by their dilution.
TAN (acid number) - indicator of degradation/hydrolysis and corrosivity; for polyol esters ≦0.2 mg KOH/g.
VI (viscosity index) - for POE/TMP the viscosity and number of OH-(hydroxyl) groups matter.
Recommended tests
ASTM D445 — viscosity at 40°C and 100°C → calculate VI (ASTM D2270)
ASTM D97 — pour point
ASTM D664 / D2896 — acid number (TAN).
Compatibility tests with elastomers / gaskets / paints.
Test bench (hydraulic): pumps, valves, filters; monitoring TAN, particles, change of properties after 500–1000 hours.

Table 4: Commercial examples of AW/EP additives used in polyol esters (POE) and synthetic fluids

Chemical type	Common name / commercial example	Main function	POE compatibility notes
Zinc dialkyldithiophosphate (ZDDP)	Lubrizol 1097, Infineum C9460, Afton HiTEC 327	AW + secondary antioxidant	Very effective, but contains zinc and phosphorus → sometimes prohibited in environmentally friendly applications or systems with sensitive catalysts. Good POE compatibility.
Tricresyl phosphate (TCP)	Durad 125, Kronitex TCP	EP (arylate phosphate)	Very effective EP, good thermal stability, but limited toxicologically → used in turbine oils or closed industrial applications.
Trialkyl phosphates (e.g. tributyl phosphate, TBP)	TBP, TEP (triethyl phosphate)	Moderate EP, medium temperature lubrication	Good ester compatibility; good solubility.
Sulfurized esters / olefins	Sulfax 95, Paraflex 410S, Anglamol 99	EP (sulfurized)	Good high load performance; good POE compatibility; can darken the oil colour (slightly brown).
Phosphite esters / acid phosphates	Lubrizol LZ-9370, BASF Irgalube 353	AW/EP + antioxidant	Very good ester compatibility; used in metal-free (ashless) formulations.
Boron esters / amine phosphates	HiTEC 346, Lubrizol 1098	AW, anti-friction, oxidative stabilizer	Good POE compatibility; more expensive, used in premium products.
Ashless dithiocarbamates (MoDTC, Zn-free)	HiTEC 4313, Infineum P6000	AW + friction modifier	Effective, but watch out for oxidation stability.
Organomolybdenum compounds (MoDTC / MoDTP)	Molyvan 855, Molyvan L	Anti-friction + EP	POE compatible; provides friction reduction at high loads.

- AW/EP additives compatible with ester bases (POE/TMP-E) for biodegradable synthetic hydraulic oils.

Table 5: Classic system – high performance, economical (ZDDP + antioxidant)

Component	Trade name (example)	Function	Typical dosage	Remarks
AW/main antioxidant	Afton HiTEC 327 (ZDDP, 50 % active)	Anti-wear + secondary antioxidant	4–6 % (≈ 2–3 % active)	Good compatibility with POE, excellent protection in valve/piston pumps. Not ashless
Phenolic antioxidant	Irganox L57 (BASF) or Naugard 445	Primary antioxidant	0.5–1.0 %	Stables oxidation and oil color.
Amine antioxidant	Irganox L06, Naugard Q	Secondary antioxidant	0.5–1.0 %	Synergy with ZDDP; extends life

*ZDDP = Zinc Dialkyl Dithiophosphate, is a classic anti-wear (AW) additive and secondary antioxidant used in mineral and synthetic oils, compatible with most synthetic esters, including: POE/TMP-E, POE/GC, POE/GPL or POE/AG-E
- robust, highly thermally stable formula, suitable for heavy industrial systems, stable TAN (acid number) < 0.2 mg KOH/g after 1000 h test - indicator of degradation/hydrolysis and corrosivity.

Table 6: Ashless system (without zinc/metallic phosphorus) — biodegradable and environmentally friendly

Component	Trade name (example)	Function	Typical dosage	Remarks
Main AW/EP	BASF Irgalube 353 (phosphite ester)	AW + EP, secondary antioxidant	1.0–2.0 %	Metal-free; excellent ester compatibility. Reduces wear in pipes /axial pumps.
Auxiliary EP	Anglamol 99 (sulfurized ester, Afton)	EP (high pressure)	2.0–4.0 %	Good high-load protection; slightly colouring.
Phenolic antioxidant	Irganox L135	Primary	0.5 %	Increases oxidative stability.

- environmentally acceptable lubricant (EAL) hydraulic oil compliant with ISO 15380
Total additives: ~5–6 %; Viscosity VG 46, VI ≈ 150, pour point ≤ –30° C, TAN < 0.2.

Table 7: Premium anti-friction system / "long-life" formula for "long-drain" oils/ equipment with very long cycles

Component	Trade name (example)	Function	Typical dosage	Remarks
Main AW	HiTEC 346 (borate ester)	Anti-wear + oxidative stabilizer	1.5–2.5 %	Metal-free; good synergy with POE/TMP.
Friction modifier	Molyvan 855 (organomolybdenum)	Anti-friction + EP	0.3–0.8 %	Reduces friction at high loads.
Amine antioxidant	Irganox L06	Antioxidant	0.5 %	High thermal stability.

- 30–40% reduced friction coefficient vs. ZDDP; POE compatible; ashless.

Table 8: "Food-grade / incidental contact" system - for hydraulic applications in food areas (bottling, packaging)

Component	Trade name (example)	Function	Typical dosage	Remarks
AW	Addition RC 9300 FG (Lanxess) – NSF H1 approved phosphate ester	AW	1.0–1.5 %	POE compatible, biodegradable
Antioxidant	Irganox L57 FG	Antioxidant	0.5–0.8 %	Food-grade, oxidation stable
Antifoam	DC 200 (10 cSt)	Silicone antifoam	0.05–0.1 %	NSF H1 approved

Table 9: Comparative table

System	Tip AW/EP	Ashless	Biodegradable	Recommended area
Classic (ZDDP)	ZDDP	x	partially	General industrial
Ecological	Phosphite + Sulfurized ester	✓	✓	Biodegradable hydraulic
Premium	Borate + MoDTC	✓	✓	Heavy duty, long-life applications
Food Grade	Phosphate ester FG	✓	✓	Food industry

Table 10: Compatible AW/EP additives for POE/GC, POE/GPL, POE/AG-E and POE/TMP-E ester bases for biodegradable synthetic hydraulic oils

#	Manufacturer / Trade Name	Chemical type & role AW/EP	Ester base compatibility	Important Notes
1	Irgalube353 (BASF)	Phosphite/phosphate ester (AW + EP without metals)	Good for synthetic ester bases, zinc-free variants	Recommended for biodegradable formulations, saturated ester bases.
2	Molyvan855 (Afton)	Organomolybdenum (antifriction + EP)	Compatible with synthetic esters if added in low concentrations	Used for heavy duty applications, high loads; check protective film.
3	Additin RC9300 FG (Lanxess)	Phosphate ester AW, food grade formulation	Suitable for biodegradable synthetic ester bases	Ideal if system has food/incidental contact requirements.
4	Functional Industrial Additives – AW/EP Package (Functional Products Inc.)	Ashless system S/P/N, industrial AW/EP package	Compatible with synthetic bases and ester polyols, including biodegradable	Useful for “eco” hydraulic formulations on esters.
5	Hordaphos145 (Clariant)	Multifunctional phosphate ester AW/EP	Can be used for synthetic fluids and ester bases (e.g. TMP trioleate)	Check exact compatibility with ester base (solubility, stability)

If the ester base is POE/GC, POE/GPL or POE/AG-E, it is best to choose metal-free additives (e.g. zinc), with a good anti-wear and EP profile, thus preserving the biodegradable character and compatibility.

Table 11: Comparison of ZDDP with ashless AW/EP for synthetic ester bases (POE/GC, POE/GPL, POE/AG-E, POE/TMP-E) used in biodegradable hydraulic oils

Additive / Type	Chemistry / Function	Compatibility with ester bases	Typical dosage (%)	Advantages	Disadvantages / notes
ZDDP	Zinc dialkyl dithiophosphate (AW + antioxidant)	POE/GC, POE/GPL, POE/AG-E, POE/TMP-E – compatible	2–6% concentrate (~1–3% active)	Efficient AW/EP, secondary antioxidant, industrially tested	Contains metals (Zn, P) → not ashless, may affect biodegradability or sensitive systems
Irgalube 353	Phosphite/phosphate ester, AW + EP ashless	Compatible with all ester bases above	1–2%	Metal-free, biodegradable, elastomer compatible, environmentally friendly	Can be more expensive than ZDDP
Hordaphos 145	Multifunctional phosphorus ester AW/EP	Good compatibility with synthetic esters (POE/GC, POE/GPL, POE/AG-E, POE/TMP-E)	1–3%	Ashless, EP/AW performance, good thermostability	Check solubility depending on ester base and process temperature
Boron ester (ex. HiTEC 346)	Borate esters AW/EP	Compatible with ester bases including POE/TMP-E	1–2.5%	Ashless, anti-friction, high load performance	Higher cost, dosage must be optimized for stability
Molyvan 855 / MoDTC	Organomolybdenum, anti-friction + EP	Compatible with synthetic ester bases	0.3–0.8%	Reduces friction coefficient, synergy with AW ashless	Not a primary AW; used as a complement to EP/AW
Additin RC 9300 FG	Phosphate ester AW, food-grade	Compatible with POE/GC, POE/GPL, POE/AG-E, POE/TMP-E	1–1.5%	Food-grade, biodegradable, ashless	Moderate EP capacity; more suitable for medium loads

ZDDP= Zinc dialkyl dithiophosphate, is a classic anti-wear additive (AW) and secondary antioxidant used in mineral and synthetic oils, compatible with most of the targeted synthetic esters; industry standard, effective and inexpensive, robust formula, very thermally stable, suitable for heavy industrial systems, good for systems without environmental restrictions.

Organomolybdenum (MoDTC, Molyvan) → added for friction reduction and EP performance.

Ashless additives - preferred in biodegradable, environmentally friendly or food-grade formulations.

Lecithin-based blends as lubricants/hydraulic fluids/other similar applications. Main characteristics, advantages and limitations depending on source. Lecithin is a plant derivative such as soybean, rapeseed, cottonseed, etc.; is a natural mixture of phospholipids/ phosphatides (e.g. phosphatidylcholine, phosphatidylethanolamine, phosphatidylinositol) + lipid components, natural oils, sometimes carbohydrates in unpurified lecithin; is used as a natural lubricant/ lubricant additive in an oil-in-water emulsion environment.

Table 12: Characteristics of lecithin-based mixtures (patents and articles)

Characteristic	How is it defined/measured	What values / ranges appear in the sources
Proportion/ concentration of lecithin in fluid	expressed as % by weight (wt%) or volume; minimum/maximum specified	For example, WO2005075612A1 states: vegetable lecithin (soybean lecithin, castor etc.) between approx. 0.1-20% wt of fluid, preferably 1-5% wt for good effects without destabilization.
Types of lecithin/ structural nature	vegetable source, specific phospholipid content, purity level, “hydrogenated” lecithin, etc.	Soy lecithin, mixed vegetable lecithin (without much purification) + residual oils. There are patents that include hydrogenated lecithin for improved friction properties and stability.
Water compatibility/ dispersibility/ emulsion stability	how well lecithin + water/aqueous medium (if aqueous fluid/emulsion) mixes, stability to separation/sedimentation	WO2005075612A1 discusses the formation of a stable dispersion, high pressure homogenization, filtration for large particles, maintaining the dispersion.
Lubrication/ anti-wear properties/ film strength	friction tests (e.g. Falex test), comparisons with reference fluids, measurement of wear under load, torque, feather degradation, etc.	In WO2005075612A1, “Formulation A” (with soy lecithin) “exhibited superior torque reduction” over reference fluids and ~25% lower wear in a Falex test at 5000 lb load / 30 minutes.
Corrodibility/ chemical compatibility	effect on metals, acidity/ pH, tan (acid neutralization number)/acid formation, oxidation stability, etc.	Patent WO2005075612A1 mentions the addition of corrosion inhibitors, chelators (e.g. EDTA), stabilizers. The pH is also controlled (e.g. formulations with pH ~8.8).
Physical properties: viscosity, freezing/ freezing point, low temperature fluidity	although not much concrete data was found in the source, it is often the subject of testing	In the patents we have encountered fewer concrete values for the viscosity of lecithin fluids; but the fact that lecithin has natural lipid components means that the fluids can be more viscous or more sensitive at low temperatures, if they are not modified. For example, tests with “modified soybean lecithin” show that solutions of 1% modified lecithin have a friction coefficient of < 0.1 in the “4-ball” test in water, and good performance after aging at 120 °C.

Advantages and limitations given by the specialized literature

• Lecithin is a natural/biodegradable compound, environmentally friendly;
• good lubricity (friction/wear resistance) for aqueous solutions or emulsions, comparable or even better than some synthetic reference fluids in certain tests;
• reduces torque and wear in mechanical applications under load compared to aqueous fluids without lecithin.

Dispersion/Emulsion Stability

• Natural lecithin contains components that can degrade or separate over time, especially at high temperatures, pH variations. Homogenization, filtration, and sometimes stabilizers are required.
• Low Temperature Properties: Natural lipid/ oil components in lecithin can solidify, increase pour point, affect start-up fluidity if the proportion of lecithin is high.
• Corrosion and Compatibility with Metals/ Materials: Lecithin contains phospholipid groups that can be sensitive to oxidation, can produce acids, or can degrade some components if inhibitors are not added.

• Cost/ Purity/ Processing: High quality/ modified lecithin can be more expensive; requires additional processing if modified (e.g. hydrogenation, chemical modifications) to improve performance.

Table 13: Characteristics of lecithin-based blends and polyol esters—formulations specifically developed for hydraulic applications (gear pumps and piston pumps)

Technical criterion	Lecithin-based blends	Polyol Ester Fluids (e.g. TMP, PE)	Technical Notes
Chemical origin	Natural (vegetable phospholipids from soybeans, rapeseed, etc.)	Synthetic (polyol esters – trimethylolpropane, pentaerythritol + fatty acids)	Lecithin = complex mixture; esters = defined compounds
Polar structure/ lubricant	Highly polar (phosphatidic ends + fatty chains)	Moderately polar (esters, no ionic charges)	High polarity helps adhesion to metal surfaces
Lubricating properties (anti-wear, friction)	Very good at concentrations of 1–10% in aqueous fluids (coef. of friction 0.06–0.09 in Falex test)	Excellent in undiluted oils; coef. friction 0.05–0.08 (in 4-ball, FZG, Denison HF-0)	Lecithin is good in aqueous media; polyol esters dominate in pure oils
Oxidative / thermal stability	Limited (phospholipids degrade >120 °C, requires antioxidants)	Very good (up to 180–200 °C, depends on the fatty acid used)	Lecithin requires oxidation inhibitors, otherwise it polymerizes
Compatibility with elastomers (NBR, FKM, EPDM)	Variable (natural lecithin can swell NBR; compatible with EPDM)	Good with most industrial elastomers	Polyol esters are formulated to meet Denison HF-0 / HF-1
Biodegradability/ toxicity	Excellent (>95%)	Very good (80–98 %)	Both are environmentally friendly; lecithin has the natural advantage
Viscosity index (VI)	Variable, low-medium (if diluted with water)	High (150–190 in EP3172294B1)	Polyol esters provide stable viscosity-temperature curves
Pour point/ low temperatures	Limited (lecithin solidifies at <0 °C without solvents)	Very good (-45 °C...-60 °C, depending on the acid)	Polyol esters remain fluid in cold weather
Stability in water/ emulsions	Very good (lecithin is a natural emulsifier)	Limited (esters hydrolyze slowly in water)	Lecithin is superior for aqueous fluids.
Corrosivity (pH, TAN)	Slightly acidic (pH 6–7.5), requires corrosion inhibitors	Neutral/ stable (TAN < 0.05 mg KOH/g after 1000 h)	Lecithin must be buffered (TEA, NaOH).
Storage stability (oxidation, separation)	May phase separate after months; requires agitation	Very stable, up to 3–5 years storage	Polyol esters are more chemically uniform
Applicability in gear pumps	Good for bio-fluid prototypes; low efficiency at high loads	Excellent - film stability and superior anti-wear	Lecithin can be used as an additive, not as a main fluid
Applicability in axial/ radial piston pumps	Limited — thermally/oxidatively unstable	Excellent - meets Denison HF-0 / FZG tests > 12	Polyol esters remain the industry standard.
Cost/ availability	Very cheap (vegetable sources)	Medium-high (controlled synthesis)	Lecithin wins on cost, but loses on industrial performance

• ***Lecithin*** is excellent as a naturally biodegradable additive or as a base for low viscosity fluids, but does not provide the thermal stability and mechanical performance required by high pressure hydraulic systems.

• ***Polyol esters*** remain the standard in professional applications (Denison HF-0, Vickers 35VQ25, etc.) due to their balance between lubricity, stability and compatibility.

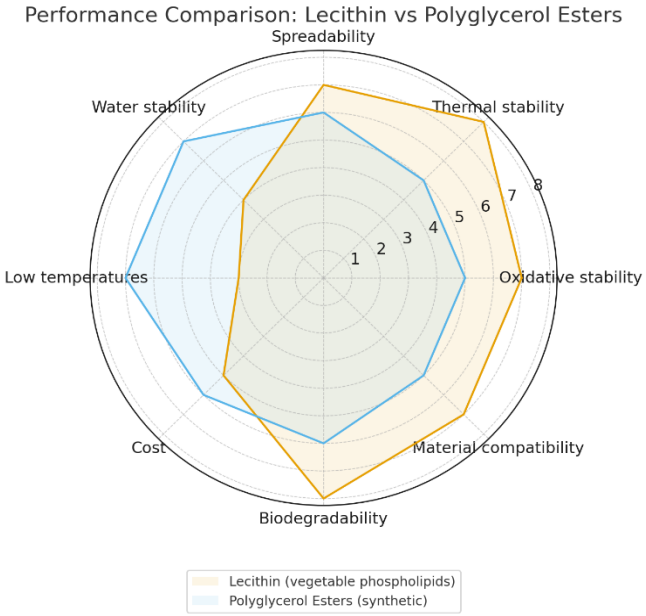

Fig. 1. Comparative radar chart Lecithin (vegetable phospholipids) vs. Polyglicerol Esters (synthetic)

The radar chart clearly shows the advantages and limitations of the two types of fluids:

- **Polyol esters** dominate in thermal and oxidative stability and low temperature behaviour;
- **Lecithin** excels in biodegradability, cost and compatibility with low viscosity fluids.

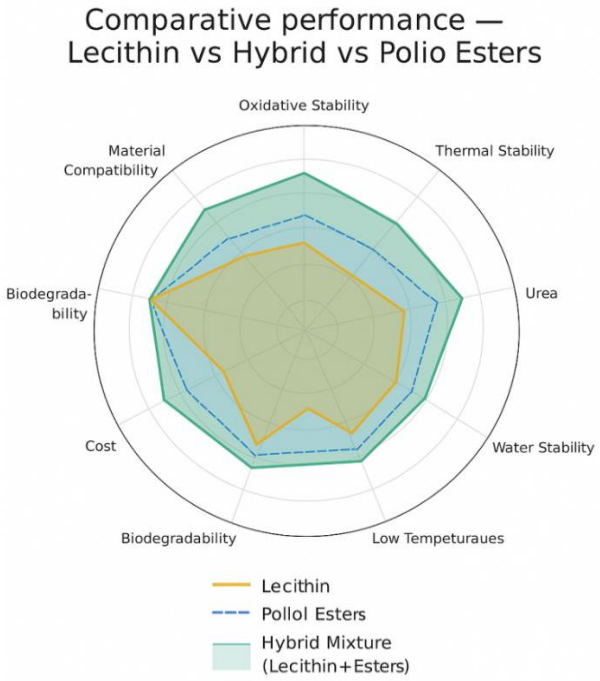

Fig. 2. Radar chart, with the hybrid profile of the lecithin and polyol ester blend

The hybrid combines the advantages of both compounds, thus preserving the biodegradability and low cost of lecithin, and gaining in thermal stability and lubrication characteristics belonging to polyol esters.
An optimized formulation for a hybrid lecithin + polyol ester hydraulic fluid, for a balance of biodegradability and performance (suitable for gear pumps and, with caution, for piston pumps).

Proportions expressed in % by mass (wt%):

• base oil - polyol ester (POE/TMP/PE): 55.0%;
(provides stable lubricating film at high temperatures and pressures; maintains anti-wear protection)
• modified vegetable lecithin (hydrogenated or agricultural grade soy lecithin): 3.0%;
(lubricant/polar agent, improves friction and reduces wear, moderate emulsifier, good adsorption on metal);
• neutral vegetable ester (C12–C18 methyl esters or biodegradable carboxyl groups): 10.0%;
(low cost, improved biodegradability);
• ashless polymethacrylate (PMA) viscosity improver: 2.0%;
(maintains viscosity at high temperatures)
• phenolic antioxidant: 0.15–0.30%;
• amine antioxidant (optional, added in small doses for long-term protection): 0.05–0.15%;
(or a commercial blend of phenolic/amine antioxidants)
• antiwear/anti-scratch (eco-friendly option: borate ester/ashless and P-free antiwear): 0.25–0.40%; (if phosphorus/sulfur is accepted: ZDDP 0.08–0.15% provides excellent protection; but reduces biodegradability)
• corrosion inhibitor (amine carboxylate or organic neutralizer): 0.20%;
• antifoam (siloxane or polymeric, very low ppm): 0.02–0.05%;
• nonionic stabilizer/emulsifier (alkyl polyglucoside or alcohol ethoxylate): 0.2–0.5%;
(stabilizes lecithin dispersion and prevents phase separation)
• pour point depressant (PPD) (polymethacrylate): 0.10–0.30%;
• biocides (only if aqueous phase or bacterial risk): 0.05–0.15%;
(used with caution; according to environmental regulations)
• adjustment up to 100% with addition of polyalphaolefins (PAO) ≈ 27–29% (fine adjustment).
(or more ester to achieve desired viscosity).

Table 14: Dosage of components in a mixture with 55% POE

Component	Dosage (wt%)	Table for 25 L (~23.75 kg)	Remarks
POE blend (polyol ester, main base)	55.00%	13.06 kg (≈ 13 062 g)	POE with properties for ISO VG ≈46
biodegradable esters (C12–C18 methyl esters)	10.00%	2.38 kg (≈ 2 375 g)	reduces cost, improves biodegradability
modified vegetable lecithin	3.00%	0.71 kg (≈ 712 g)	hydrogenated soybean lecithin/farm grade
borate ester (antiwear, ashless)	0.50%	0.12 kg (≈ 119 g)	borated glycerol ester / trialkyl borate
MoDTC (molybdenum-based modifier - optional)	0.15%	0.04 kg (≈ 36 g)	verifies Mo acceptability in application
polymethacrylate (PMA) viscosity improver, ashless)	2.00%	0.47 kg (≈ 475 g)	polymethacrylate, ashless
Antioxidant (phenolic, ashless)	0.20%	0.05 kg (≈ 48 g)	phenolic or commercial ashless blend
amine antioxidant (optional, low dose)	0.10%	0.02 kg (≈ 24 g)	optional, low dose
antifoam (siloxane or polymeric)	0.03%	0.01 kg (≈ 7 g)	ppm low
Non-ionic emulsifier/stabilizer (APG/ethoxylate)	0.35%	0.08 kg (≈ 83 g)	stabilizes lecithin in the mixture

Component	Dosage (wt%)	Table for 25 L (~23.75 kg)	Remarks
corrosion inhibitor (amine carboxylate, ashless)	0.20%	0.05 kg (≈ 48 g)	metal protection
pour point depressant (PPD, ashless)	0.10%	0.02 kg (≈ 24 g)	if necessary
biocide (if aqueous phase/microbiological risk)	0.05%	0.01 kg (≈ 12 g)	use only if necessary
polyalphaolefins (PAO)/POE adjuster (for viscosity reach)	28.32%	6.73 kg (≈ 6 726 g)	fill up to 100%
Total	**100.00%**	**23.75 kg**	**25 L ≈ 23.75 kg** (assuming 0.95 kg/L)

For a high percentage of lecithin added to the polyol ester (POE) composition, a percentage of ≥ 70% lecithin derivative (modified lecithin) was tested and the additives were adjusted for a total composition of 6.85% with a weight of 1.63 Kg.

Table 15: Dosage of components in a mixture with 70% lecithin derivatives

Component	wt%	Mass (kg)	Mass (g)
Lecithin derivative	70.00	16.625	16 625 g
Polyol esters (POE) blend	15.00	3.5625	3 562.5 g
Biodegradable esters (C12–C18 methyl esters)	8.00	1.9000	1 900 g
Borate ester	2.00	0.4750	475 g
Viscosity improver (PMA)	3.00	0.7125	712.5 g
Phenolic antioxidant	0.50	0.1188	118.8 g
Corrosion inhibitor (amine carboxylate, ashless)	0.70	0.1663	166.3 g
MoDTC (molybdenum-based modifier - optional)	0.15	0.0356	35.6 g
Non-ionic emulsifier / stabilizer (APG / ethoxylate)	0.25	0.0594	59.4 g
Antifoam (siloxane or polymeric)	0.03	0.0071	7.1 g
Pour point depressant, ashless	0.07	0.0166	16.6 g
Biocide (if aqueous phase / microbiological risk)	0.05	0.0119	11.9 g
Total additives	6.85	1.6269	1 626.9 g
Total - composition	**100.00**	**23.7500**	**23 750 g**

Required equipment (pilot / laboratory)

• Mixing tank (~50 L) with mechanical stirrer (controllable motor, 200–2000 rpm);
• High shear mixer (propeller or rotor-stator) for lecithin dispersion (optional high-pressure homogenizer);
• Thermostatic baths / controlled heating (in the temperature range of 25-90 °C);
• Thermometer/PT100 probe or pressure gauge;
• Pump and final filter (5 µm cartridge; for sensitive applications 1-3 µm);
• Analytical balance / platform (cap. ≥ 25 kg) ±1 g;
• Container for pre-dissolution mixture;
• Equipment: goggles, nitrile gloves, gown, ventilation/ hood;
• QC equipment: viscometer (ASTM D445), pour point (D97), flash point (D92) determination device, TAN (acidity) determination kit < 0.05 mg KOH/g, demulsifier (D1401), ball device (D4172).

5.1. Technical observations observed when using a high percentage of lecithin:

- Viscosity and rheological behavior: the lecithin derivative added at 70% produces a much more polar, viscous fluid with a strong change in temperature response. The viscosity at 40°C

is slightly higher than that of ISO VG 46 – measurements were made according to ASTM D445.

- Oxidative/thermal stability and risk of hydrolysis: phospholipids tend to degrade at high temperatures, therefore requiring antioxidants in sufficient doses. TAN (Total Acid Number) and PDSC (Pressure Differential Scanning Calorimetry - Oxidation Induction Time) were monitored.

Table 16: *TAN (mg KOH/g)* **-** range for each mixture type

System	TAN	Observations
POE 100%	0.03 – 0.05	Fully reacted synthetic esters → very low TAN
POE/GC (70–90% POE)	0.05 – 0.12	GC introduces –OH groups → slight increase over time
POE/LPG (70–90%)	0.08 – 0.15	Residual LPG contains phosphates → TAN increases slowly
POE/AG-E (modified acylglycerides)	0.1 – 0.25	Sensitive to hydrolysis; TAN increases
POE/TMP-E 80–90%	0.03 – 0.07	Most stable bio-ester → lowest TAN after POE

Table 17: *PDSC* **-** typical measured values for each type of mixture

System	PDSC	Remarks
POE 100%	45–70 min at 200°C	Very good performance
POE/GC	35–55 min	GC has more reactive bonds
POE/GPL	25–45 min	GPL = oxidation sensitivity
POE/AG-E	20–40 min	AG-E = lowest oxidative stability
POE/TMP-E	50–80 min	Similar to POE → best bioester in oxidation

- Sealing compatibility: elastomers may undergo changes (swelling, stretching) in the presence of phospholipid compounds, ASTM D471 tests are required on NBR (Nitrile Butadiene Rubber), HNBR (Hydrogenated Nitrile Butadiene Rubber) or FKM (fluoroelastomer).
- Separation/sedimentation: lecithin derivatives may tend to agglomerate or separate over time, therefore emulsifier is added and the mixture must be homogenized.
- Microbiological risk: lecithin requires the addition of biocides.
- Filterability: common filters (1–5 μm), require monitoring – particle agglomerations may occur.

For a mixture based on derived lecithin (GPL) in a proportion of 70%, so a ratio GPL 70% : POE 30%, additives are needed to reduce some technical problems regarding filterability, viscosity and oxidizability.

• *GPL* = purified lecithin fraction (phospholipids, phosphatidylcholine predominantly), contains traces of free acids and phosphate groups; these influence TAN and PDSC (a rapid indicator of susceptibility to oxidative initiation).

Table 18: TAN and PDSC for POE/LPG mixture 30:70

Condition	TAN (mg KOH/g)	Interpretation / Comment	PDSC- (min)	Remarks
Fresh sample (fresh, neat)	0.10 – 0.18 (mean value: 0.12)	Initial TAN moderate; indicates small residual amounts of free fatty acids / phosphates from	25 – 40 (mean value: 35 min)	Relatively low OIT compared to pure POE → LPG is sensitive to oxidative initiation.

Condition	TAN (mg KOH/g)	Interpretation / Comment	PDSC- (min)	Remarks
		LPG. Acceptable for unimproved formulations.		
After accelerated oxidation (e.g. ROFT 300 min / typical condition)	0.40 – 1.20 (mean value: ~0.65)	TAN increases significantly - formation of oxidized acids; monitoring required.	10 – 25 (mean value: ~15 min)	Dramatically reduced OIT after aging → product oxidized rapidly without effective antioxidants.
Freshness + antioxidant package (e.g. 0.2% tocopherol + 0.3% boron ester)	0.06 – 0.12 (mean value: 0.08)	Threshold of concern ≈ 0.5–1.0 mg KOH/g.	45 – 70 (mean value: ~60 min)	Significant increase in OIT; efficient ashless package increases stability.
After stabilization (300 min) with antioxidant package	0.12 – 0.40 (mean value: ~0.20)	Antioxidants reduce the acidity initially formed and stabilize the product.	25 – 50 (mean value: ~35 min)	OIT is reduced but remains at acceptable operating values if the package is properly optimized.

Note: The average values are within the reference values recommended by the specialized literature. The ranges reflect the variability of the LPG sample (purity, free acid content), the efficiency of the antioxidants and the exact conditions of the oxidative test.
If: TAN exceeds the range of 0.5–1.0 mg KOH/g, it is necessary:
- optimize the amount of antioxidant, reduce the percentage of LPG% or stabilize by moderate neutralization.
✓ PDSC ≥ 30–40 min (under laboratory conditions); if <25 min → requires antioxidants.
✓ after adding antioxidants (tocopherol 0.2%) + boron ester 0.25-0.3%: PDSC ≥ 45–60 min for critical applications.
✓ TAN = 0.12 mg KOH/g and PDSC = 35 min, sample ok for tribological testing,
- after addition of a secondary antioxidant (phosphite), PDSC increases at 60 min and TAN decreases to 0.08 mg KOH/g, antioxidant activity increases and the GPL formula is less polar and the formula has proven stable.
Comparative evaluation of POE blends with bio-derived compounds (G1–G5) and identification of optimal solutions for use in piston pumps and gear pumps.

Table 19: Sample composition

Code	Base	Composition (% mass)
G0	POE (reference)	100
G1	POE + Glycerol Carbonate	90:10
G2	POE + TMP-Ester (C8–C10)	90:10
G3	POE + PE-Ester (C8–C10)	80:20
G4	POE + modified Acyl-glycerides	80:20
G5	POE + Glycerophospholipids	80:20

All samples were tested according to international standards:

Table 20: The tests applied and their scopes

Test	Standard	Parameter	Scope
ASTM D445	Viscosity (40°C, 100°C)	Rheological stability	Viscosity Index Evaluation
ASTM D4172	4-ball wear	Wear resistance	Anti-wear Effect Determination
ASTM D2783	EP (weld load)	Extreme Pressure	Welding Load Determination

DIN 51354 (FZG)	Stage failure	Progressive load	Gear Load Capacity
ROFT	Oxidation stability	Oxidation time (min)	Thermal and Oxidative Durability
ASTM D471	Elastomer compatibility	Volume change/hardness	Gasket Compatibility Evaluation

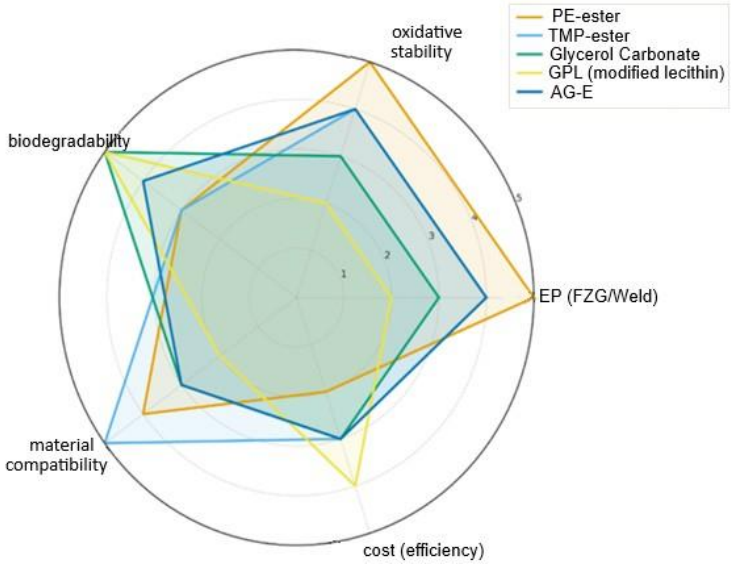

Fig. 3. Radar chart - Relative performance of POE compounds

Remarks:
G5 (POE + LPG) exhibits the best overall performance, due to its excellent compatibility with elastomeric materials and high oxidative stability.
The combination of POE + GPL + TMP (ternary) can provide a new generation bio-synthetic base, with performance >95% of the level of top synthetic esters and biodegradability >85%.

A complete, application-specific analysis that correlates the POE blend composition with the mechanical, tribological and environmental requirements of each pump type.

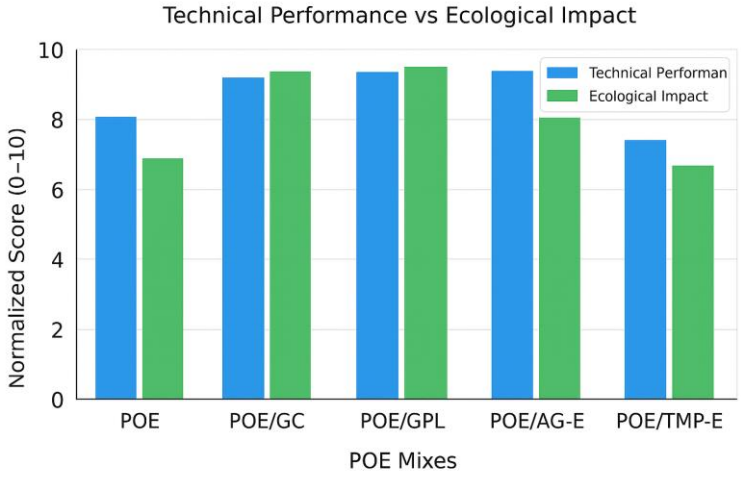

Fig. 4. Comparative graph between "Technical Performance" and "Environmental Impact" for various POE mixtures

From Figure 4, the following is clearly observed:

POE/GPL offers the best balance between performance and sustainability,
POE/TMP-E excels technically, but has a higher ecological impact,
POE/GC maintains an excellent environmental profile with solid performance.

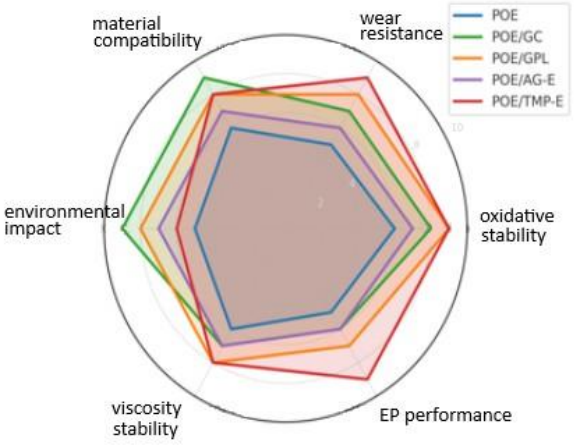

Fig. 5. Gear pumps - Performance vs Environmental impact

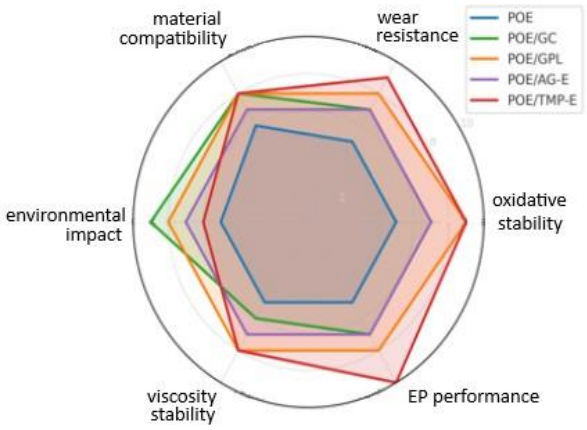

Fig. 6. Piston Pumps - Performance vs. Environmental Impact

From figures 5 and 6 the following can be observed:
1. Glycerophospholipids (GPL) offer the best biodegradability.
2. Bio-synthetic blends (especially POE/GC and POE/TMP-E) can completely replace mineral oils in critical industrial applications
3. Bio-derived TMP esters provide excellent EP resistance, making them ideal for piston pumps and high-pressure systems.

In literature and patents, the concentrations above 30% lecithin derivatives have been explored mainly in the context of aqueous hydraulic fluids or emulsified biodegradable oils, not in pure ester-based lubricants.
British Patent GB2408748A (Hydraulic Fluids) - fluids containing up to approximately 30–40% modified lecithins (natural, hydrogenated or partially acylated lecithin) in a mixture with water and vegetable oils were tested.
The results showed that above the 30% threshold, physical stability problems arise, such as phase separation, increased viscosity, and a tendency to persistent emulsion, which reduce compatibility with high-pressure hydraulic systems.
Other similar research, including Chinese and Korean studies on "modified soy lecithin-based lubricants" confirmed that at concentrations of 35–50% unhydrogenated or slightly modified lecithin, the mixture becomes thermally and chemically unstable, with accelerated oxidation and deposits.
By comparison, boronated or acylated lecithin variants (such as those described in articles about "boron-containing soy lecithin esters") tolerated somewhat higher concentrations, up to 40%, without immediate separation, but with notable tribological losses. These sources indicate that the practical limit for POE + lecithin-derived fluids is around 25–30% by weight, beyond which problems of stability, filterability and compatibility with elastomers arise, especially in gear or piston pumps. Therefore, purified lecithin derivative based on phospholipids, predominantly phosphatidylcholine and additives based on boron esters and tocopherol-type antioxidants, showed that the percentage tested at >70% in a hydraulic fluid demonstrated EP / FZG performance comparable to that of POE used in critical applications (piston pumps, gears).

- *EP performance* describes the resistance of the lubricant to extreme loads, where the fluid film can break down and metal-on-metal friction becomes unavoidable. They are evaluated in particular by: ASTM D2783 which measures:

• *Load-Wear Index (LWI)* – the progressive resistance to increasing load and Weld Load (WL) – the load at which the balls weld (absolute EP limit)

• *FZG Performance* – DIN 51354 / ISO 14635-1, measures: Load Stage (Score 1–12) – shows the level of the stage at which scoring wear occurs, indicates the protection of gears under continuous load.

Table 19: EP/ FZG performances for the main mixtures

Lubricant system	ASTM D2783 LWI (kgf)	ASTM D2783 Weld Load (kgf)	FZG Scoring Stage	Remarks
POE 100% (standard)	35–45	160–180	8–9	Good in general applications; limitations at extreme loads.
POE + LPG derivative 30:70	55–70	200–220	9–10	LPG increases EP through high polarity and reactive film.
POE + LPG 20:80	65–85	220–240	10–11	Excellent EP level, very stable adsorption film.
POE + AG-E (epoxidized acylglycerides)	50–65	200–230	9–10	Epoxides increase EP and reactivity at hot spots.
POE + TMP-E (bio-synthetic)	40–55	180–210	8–9	Moderate EP but very good oxidative stability.
POE + GC (glycerol carbonate)	45–60	180–200	8–9	Rigid EP film but limited by excessive wetting.

Table 20: Recommendations for industrial applications (depending on EP/FZG)

Working environment	Recommended system	Justification
Heavy wear / extreme pressures	POE/GPL 20:80	highest FZG score (10–11), Weld Load 220–240 kgf
High temperatures (over 110 °C)	POE/TMP-E	excellent EP + oxidation
Wet environment / risk of hydrolysis	POE/GC	stable to hydrolysis, sufficient EP
Piston pumps	POE/GPL > POE/AG-E	high EP requirement + polar film
Gear pumps	Simple POE / POE+GC	lower loading, moderate EP requirements

- POE/GPL (modified glycerophospholipids) – the best performing
GPL gives a strongly adsorbed film, rich in phosphate, phosphonate, carbonyl groups
Excellent compatibility with piston pumps or high pressure pumps.
- POE/AG-E (acylglyceride epoxide), increased reactivity, anti-scoring action.
High EP, but less stable at 120–140 °C than LPG.
- POE/TMP-E (trimethylolpropane esters)
Moderate EP, but has an advantage for oxidation → for high temperature pumps, FZG 8–9 is sufficient.
- POE/GC (glycerol carbonate)
good EP film, but excessive wetting can reduce the thickness of the hydrodynamic film.
FZG 8–9 is suitable for gear pumps, but less so for piston pumps.

Table 21: Technical observations on the mixtures used

Lubricant system	Detailed remarks
POE 100% (standard)	Basic EP performance (ASTM D2783 LWI: 35–45 kgf, Weld Load: 160–180 kgf, FZG: 8–9). Good for general applications, but can fail at very high loads. This is the benchmark.
POE + LPG derivative 30:70	Blending with derived LPG significantly increases EP properties: LWI reaches 55–70 kgf, Weld Load 200–220 kgf, FZG 9–10. This is due to the high polarity and ability to form a reactive protective film.
POE + LPG 20:80	The EP level is very high: LWI 65–85 kgf, Weld Load 220–240 kgf, FZG 10–11. The adsorption film is extremely stable, making it suitable for very high loads and high temperatures.
POE + AG-E (epoxidized acyl glycerides)	LWI 50–65 kgf, Weld Load 200–230 kgf, FZG 9–10. Added epoxies enhance wear resistance and reactive film formation in hot areas, making it effective for demanding conditions.
POE + TMP-E (bio-synthetic)	LWI 40–55 kgf, Weld Load 180–210 kgf, FZG 8–9. EP properties are moderate, but oxidative stability is very good, making it suitable for applications where high temperature durability and resistance to degradation are important.
POE + GC (glycerol carbonate)	LWI 45–60 kgf, Weld Load 180–200 kgf, FZG 8–9. The EP film is stiff, which protects the parts, but excessive wetting can limit performance in some systems

Weld Load (WL) – the load at which the balls weld (absolute EP limit)

Load-Wear Index (LWI) – progressive resistance to increasing

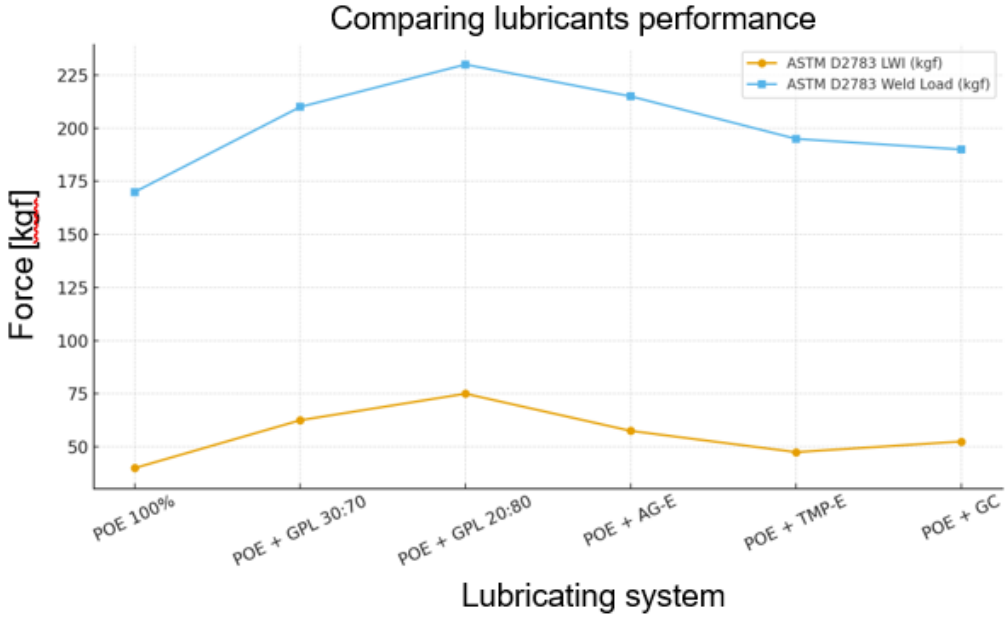

Fig. 7. Performance behaviour of polyol ester lubricants with different additives

From figure 7 it can be seen that:
• POE + GPL 20:80 has the highest values, indicating superior EP performance.
• POE 100% has the lowest values, being the standard reference lubricant.
• The rest of the systems fall between these extremes, with AG-E and GPL 30:70 near the top.

Other observations:
• LPG (modified lecithin) has been shown to have EP performance comparable to POE when tested at >70% in a hydraulic fluid.

• EP performance describes the lubricant's resistance to extreme loads, where the fluid film can break down and metal-on-metal friction becomes unavoidable.
• Excellent compatibility with piston pumps or high-pressure pumps.
• Blends with derived LPG offer the best EP performance.
• Epoxies (AG-E) provide a balance between wear resistance and thermal durability.
• Bio-synthetics (TMP-E) are excellent for oxidative stability, even if EP is moderate.
• Glycerol carbonate can be useful where film stiffness is beneficial, but wetting must be monitored.

3. Conclusions

The formulations involving polyol esters exhibited superior thermal and oxidative stability when subjected to accelerated aging tests. Comparative analysis revealed that biodegradable blends maintained functional integrity over a broader temperature range compared to traditional mineral oils. Further tests demonstrated that these blends performed admirably under heavy load conditions, showcasing reduced wear and tear on hydraulic components. The inclusion/ incorporating biodegradable esters leads to reduced ecological footprint, minimizing the risk of contamination in the event of fluid leaks, which is a benefit for the environment. To ensure optimal pump performance under operational stress conditions, the impact of temperature and pressure variations on the viscosity index of polyol ester blends was investigated.
In conclusion, the integration of polyol esters in hydraulic fluids not only aligns with sustainability goals but also addresses performance challenges in demanding applications.
The promising results advocate for continued exploration and potential standardization of these environmentally-friendly alternatives in hydraulic systems.
As a perspective of this work, further research is required to address the following aspects:
• Long-term field studies to evaluate the real-world performance of these bio-based hydraulic fluids in various applications.
• Investigating the economic feasibility of producing polyol esters on a larger scale to ensure accessibility to end users.
• Exploring the potential of hybrid formulations that leverage the strengths of both synthetic and bio-based oils.

Acknowledgments

This work was supported by a grant of the Ministry of Research, Innovation and Digitization, CCCDI - UEFISCDI, project number PN-IV-P7-7.1-PTE-2024-0618, within PNCDI IV.

References

[1] Rozga, Pawel, Abderrahmane Beroual, Piotr Przybylek, Maciej Jaroszewski, and Konrad Strzelecki. “A Review on Synthetic Ester Liquids for Transformer Applications.” *Energies* 13, no. 23 (2020): 6429. doi:10.3390/en13236429.
[2] Housel, Tyler. "Synthetic Esters: Engineered to Perform". *Lubricants*, no. 12 (2022) Zschimmer & Schwarz.com.
https://zslubes.com/wp-content/uploads/2022/12/ZS_Lubricants_Whitepaper_LTR_Syn_Esters_20220913.pdf
[3] Gryglewicz, Stanisław, Maciej Stankiewicz, F.A. Oko, and I. Surawska. “Esters of dicarboxylic acids as additives for lubricating oils.” *Tribology International* 39 (2006): 560—564.
[4] Reading, Tina. “Lubricants in the age of electric vehicles, a new road.” *Lube Magazine*, September 2025, https://www.lube-media.com/wp-content/uploads/DE01-Electric-vehicles-WEB-ONLY-Article-Sept25b.pdf.
[5] Brown, Stuart F. “Base Oil Groups: Manufacture, Properties and Performance.” *Tribology and Lubrication Technology. Additives to Transform Lubricant Technologies*, no. 71(4) (April 2015): 32-35.
[6] Lanxess. “Using Esters in PAO-Based Automotive Lubricants.” 2024, Synton® High Viscosity PAO Base Fluids. Accessed October 9, 2025. https://lanxess.com/en/products-and-brands/brands/synton.
[7] Housel, Tyler. "Synthetic Esters: Mother Nature’s Second Choice", November 19, 2020. Accessed September 17, 2025.

https://zslubes.com/documents-pdf/Lexolube%C2%AE%20NBS/Synthetic%20Esters-%20Mother%20Nature%E2%80%99s%20Second%20Choice.pdf.

[8] Juwita, Miratna, Muhammad Faizal, Muhammad Said, Juni Prianto, R. Arie Hartawan, and Nabila Aprianti. "Synthesis of Crude Palm Oil-Based Polyol Ester as Biolubricant." *Jurnal Penerapan Teknologi dan Pembelajaran. Rekayasa* 19, no. 2 (2021): 62-74.

[9] Greaves, Martin, Jeff DiMaio, Michelle DiMaio, Zach Hunt, and Ben Bergmann. “Exploring the functionality of oxygen-rich Secondary Polyol Ester™ base oils.” *Lube Magazine*, no. 183, October 2024. https://www.lube-media.com/wp-content/uploads/Lube-Tech-154-Exploring-the-functionality-of-oxygen-rich-Secondary-Polyol-Ester%E2%84%A2-base-oils.pdf.

[10] Chorus. “Synthetic Base Oils of PAGs, PAOs, Esters, and Silicone oils, What are their differences?” April 16, 2024. Accessed September 23, 2025. https://www.cnlubricantadditive.com/info/synthetic-base-oils-of-pags-paos-esters-and-94765404.html.

[11] Noria Corporation “Base Oil Groups Explained.” *Machinery Lubrication*. Accessed September 11, 2025. https://www.machinerylubrication.com/Read/29113/base-oil-groups-.

[12] Koteswara Rao, B., Abbaraju Bala, Chebattina Kodanda Rama Rao, Vadapalli Srinivas, Mysore Sridhar Srikar, Sanduru Bhanuteja, Challa Bandhavi, Kseniia Iurevna Usanova, and Anil Kumar Saxena. “Physicochemical and corrosion properties of polyol ester-commercial motorbike oil blends.” *Cogent Engineering* 11, no. 1 (2024): 2390690. https://doi.org/10.1080/23311916.2024.2390690.

[13] Pakelo Lubricants. “API Standard - Technical Classification. From Group I to Group V.” August 30, 2021. Accessed September 30, 2025. https://pakelo.com/en/magazine/oil-tech-academy/oil-trends/base-oils-classification

[14] “TestOil.” *Eurofins TestOil.* Accessed October 27, 2025. https://testoil.com/did-you-know/api-base-oil-classification-explained-by-eurofins-testoil.

[15] ***. “Synthetic Based Oils and Groups.” *ProPioneer Engineering*. Accessed October 29, 2025. https://www.propioneer.co/understainding-sythetic-oil.

[16] Twin Specialties. “A Guide to Base Oil Groups.” *Industrial Lubricants*. January 20, 2021, Accessed October 7, 2025 https://www.twinoils.com/news/a-guide-to-base-oil-groups/.

[17] AmsOil. “Are all Synthetic Oil Groups the Same? Group III vs IV vs V.” *The inside track*. February 6, 2018, Accessed October 27, 2025. https://blog.amsoil.com/are-all-synthetic-oil-groups-the-same-group-iii-vs-iv-vs-v/.

[18] Sullivan, William T., and Halou Oumar-Mahamat. “Lubricating fluids with enhanced energy efficiency and durability.” Patent US2005059563A1, 2005-03-17. https://eureka.patsnap.com/topic-patents-gear-oil.

[19] Kotturu, Chandra Mouli VV, Vadapalli Srinivas, Vemullaplli Vandana, Chebattina Kodanda Rama Rao, and Seetha Rama Rao. “Investigation of tribological properties and engine performance of polyol ester–based bio-lubricant: Commercial motorbike engine oil blends.” *Proceedings of the Institution of Mechanical Engineers Part D Journal of Automobile Engineering* 234, no. 5 (2019): 1304-1317.

[20] Greaves, Martin, Jeff DiMaio, Zach Hunt, Ben Bergmann, and Michelle DiMaio. “Secondary Polyol Ester Technology: A Novel Base Oil Family for Developing Bio-Lubricants.” *Lubes’n’Greases Magazine* no. 30 (5) (May 2024): 21-25. https://www.lubesngreases.com/magazine/30_5/secondary-polyol-ester-technology-a-novel-base-oil-family-for-developing-bio-lubricants/.

[21] Greaves, Martin, Zach Hunt, and Jeffrey DiMaio. “Novel hybrid esters: Base oils designed for sustainability.” *Lube-Tech* No. 144. https://www.lube-media.com/wp-content/uploads/Lube-Tech-144-Novel-hybrid-esters-Base-oils-designed-for-sustainability.pdf.

[22] Penrite Oil. “Esters in Oils.” *Penrite Technical Bulletin*. October 2015. Accessed October 23, 2025. https://penriteoil.com.au/assets/tech_pdfs/Esters%20and%20Engine%20Oils%20-%20October%202015.pdf.

[23] Stolz, Hermann Josef, Wilhelm Huber, Martina Mennicken-Meuthen, and Denise Weber. “Sealing compatibility of ester base oils.” *Lube-Tech* no. 138. https://www.lube-media.com/wp-content/uploads/Lube-Tech-138-Sealing-compatibility-of-ester-base-oils.pdf.

ISSN 1454 - 8003
Proceedings of 2025 International Conference on Hydraulics and Pneumatics - HERVEX
November 19-21, Băile Govora, Romania

EVALUATING A VIBRATORY DRUM ROLLER'S PERFORMANCE AT ADJUSTABLE SETTINGS

Carmen Nicoleta DEBELEAC[1]

[1] "Dunarea de Jos" University of Galati, Engineering and Agronomy Faculty in Braila, Research Center for Mechanics of Machines and Technological Equipments, Braila, Romania

Abstract: *This study focuses on the development of a virtual model of a vibratory drum to perform a dynamic analysis of the behavior at adjustable settings of the static moment values in the two mounting configurations. The movement of the roller-ground system was studied on the 2DOF model in terms of the stability of the movement and the impact force transmitted to the soil when varying the frequency and amplitude of the vibrations.*

Keywords: *Vibratory roller, virtual model, simulation, operational performance, adjustable settings*

1. Introduction

The compaction process can be carried out in two operating cases, with vibrations and oscillations (when force is cyclically applied to the ground as the drum rotates), for dynamic and static compaction (when the weight of the machine itself provides a constant and vertical force). In vibratory compaction, one or two rotating eccentric masses create a force that generates the vertical motion needed to provide the high energy for soil densification. The eccentric masses are mounted on the shaft so that as the motor operates, these generate vibrations that are transferred to the machine drum assembly and into the soil, respectively. The eccentric weights are positioned in the compactor drum to generate different compaction effects by changing the working regime in terms of amplitude, frequency and force transmitted to the ground. To create vibrations, the weights are aligned in the same direction to result in a strong vertical force. To create oscillations, these weights are placed 180° out of phase to cancel the force in the vertical direction and create a horizontal, rocking movement that generates shear forces without impact (in which case, even if the compaction effect is deep, the structure of the material of which the layer is made will not be damaged). In compactor drums, the eccentric assembly is mounted inside the steel drum, supported by bearings and driven by a hydraulic or mechanical system. Some compactors allow adjustment of the eccentric masses or the position of the drive shaft to modify the frequency and force of vibrations, correlating the working regime according to different types of soil and applications.

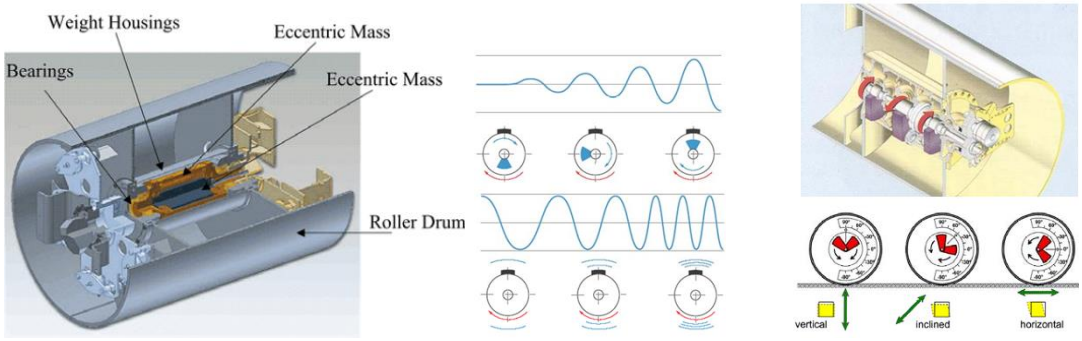

a) b)

Fig. 1. Schematization of vibratory drum compactor:
a) Ammann model [1]; b) Bomag model [2].

Of particular interest in the knowledge of the dynamic behavior of the compactor drum motion during the compaction process. This is influenced by three mechanical characteristics that will be presented below:
a) the inertial characteristics of the drum, which highlight the influence of the inertia phenomenon because of the mass distribution during the work process.
b) the kinetic characteristics of the drum, which characterize its motion from a dynamic point of view, influencing the work process by transforming the state of motion.
c) the dynamic characteristics of the drum are mechanical quantities that characterize its interactions with the surface of the terrain with which it comes into contact, highlighting the influence of these work tool - terrain type interactions on the evolution of the state of motion of the vibratory roller [3,4].

2. Methods and materials

The virtual modeling for a drum compactor begins with structural design using Computer-Aided Design (CAD) techniques to create a 3D digital representation of all components that will be imported in different software environments for advanced analysis. In Figure 2 the eccentric masses ensembles (developed with Inventor software) are connected in two positions by shaft for different compaction effects.

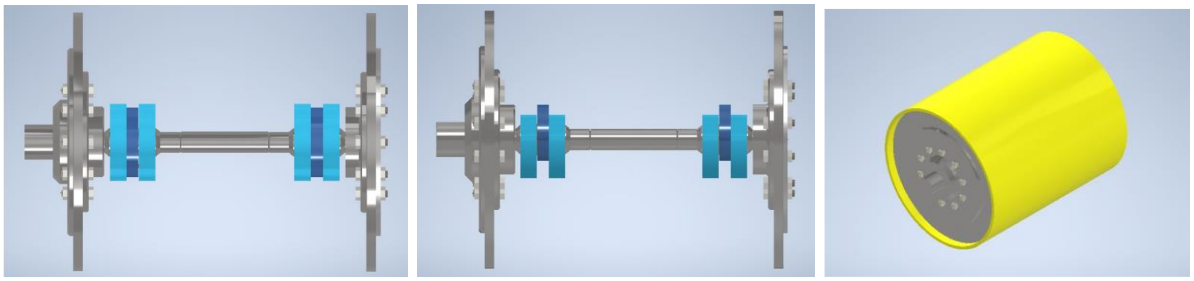

a) b) c)

Fig. 2. Assembly with eccentric masses into the drum:
a) in the same direction (case 1); b) in opposite directions (case 2); c) general view of the drum.

The static moment (M_{st}) of eccentric masses is calculated as the product of the unbalance mass (m_0) and its eccentricity (r) using the formula $M_{st} = m_0 r$. The resulting force amplitude F_0 is given by $F_0 = m_0 r \omega^2$, where ω is the angular velocity. To modify different operating modes (e.g. different vibration characteristics or transmitted forces), the vibrating device can have a different mechanical configuration because of combinations of eccentric masses. A dynamic rheological model with 2DOF (Figure 3) can be developed by using lumped parameters like springs and dampers to represent the material's behavior, where changing the working regime can be simulated by altering the model's parameters, such as stiffness and damping coefficients.

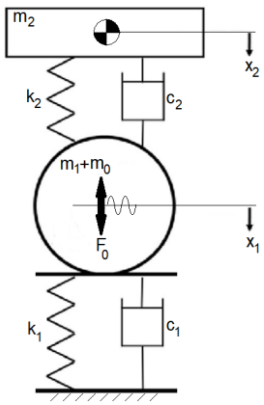

Fig. 3. Rheologic dynamic model of the vibratory roller

Adopting Newton's second law, the steady-state dynamic behavior of the vibratory roller during vibration due to the centrifugal force applied to the drum via rotating eccentric mass can be written as below [5]:

$$\begin{cases} (m_1 + m_0)\ddot{x}_1 + c_1\dot{x}_1 + k_1x_1 + c_2(\dot{x}_1 - \dot{x}_2) + k_2(x_1 - x_2) = m_0 r\omega^2 sin\omega t \\ m_2\ddot{x}_2 - c_2(\dot{x}_1 - \dot{x}_2) - k_2(x_1 - x_2) = 0 \end{cases} \quad (1)$$

where m_1 – chassis mass; m_2 – drum mass; m_0 – eccentric mases; k_1 – soil stiffness; k_2 – suspension stiffness; c_1 – damping soil; c_2 - damping suspension. The expression for the contact force that arises as a result of the interaction between the roller and the soil has the following expression [6]:

$$F_s = k_1x_1 + c_1\dot{x}_2, \quad (2)$$

which is applicable only if the condition $x_1 > 0$ is met, and if $x_1 < 0$ then the value of the force F_s is zero. The following data and information (Table 1) were used to create the case scenario for next analyses: terrain type: sandy soil; viscous-elastic characteristics of the soil: $k_1 = 35x10^7$ N/m; $c_1 = 10$ Ns/m; drum mass: $m_1 = 1158,7$ kg; chassis mass: $m_2 = 2500$ kg; viscous-elastic characteristics of the suspension: $k_2 = 45x10^5$ N/m; $c_2 = 5$ Ns/m; static moment: 7,5-10 kgm; frequency: f = 15-25 Hz

Table 1: Technical details for two operating regimes of the roller compactor

Constructive variants	Case 1	Case 2
Static moment of eccentric masses (M_{st})	7.5 kgm	10 kgm
Drum mass moment (I_Z)	111.005 kgm^2	111.026 kgm^2
Center of gravity (C_Z)	0.470 m	0.472 m

We implemented in MATLAB/Simulink a work scheme to illustrate roller movement by modeling a vibrator's eccentric masses, in two positions, and to put into evidence how changes to its parameters affect the vibration amplitude and impact force.

3. Simulation results

The results of simulations and plots showing how the roller's motion (in form of its vertical displacement) is influenced by the vibrator's operational settings. In this regard, the following graphs will be represented: the variation of the contact force that arises at the roller-ground interface (Figure 4), drum amplitude vs work frequency (Figure 5) and the movement in the phase plane (Figure 6).

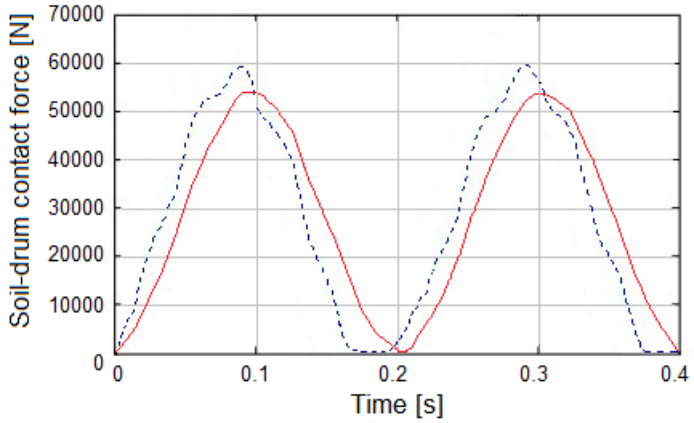

Fig. 4. Behavior of contact force between soil and vibratory drum on different work regimes: Red line – simulation case 1; Blue line – simulation case 2.

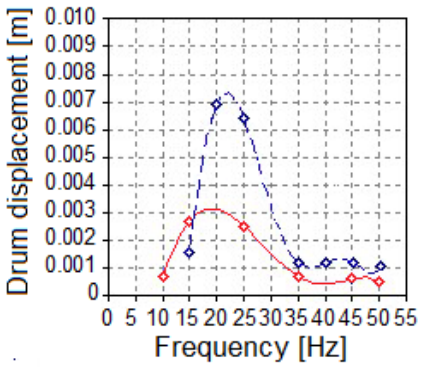

Fig. 5. Dependence of the amplitude of the drum vertical motion on the frequency: Red line – simulation case 1; Blue line – simulation case 2.

We have shown that the amplitude of the vertical motion of the vibratory drum increases with increasing frequency and is directly influenced by the static moment of the eccentric masses, which creates a larger impact force transmitted into the soil. For different static moments, the relationship between amplitude and frequency shows a unique curve, peaking at the resonant frequency of the system before decreasing again. Higher static moments lead to larger peak amplitudes and shift the resonant frequency to a higher value. The phase plane analysis for the roller motion shows the state of the system interpreted based on the velocity versus vertical position plot, focusing on the analysis of its sensitivity and stability over time. Thus, we can see how the phase plane trajectories diverge, indicating the sensitivity to the initial conditions and other parameters (frequency and eccentric masses), which can be visualized by changes in the shape of the phase plane, as shown in Figure 6. In addition, it is observed that the stable system has trajectories that converge towards a curve limit (cyclic), while the unstable system has trajectories that diverge or exhibit chaotic behavior.

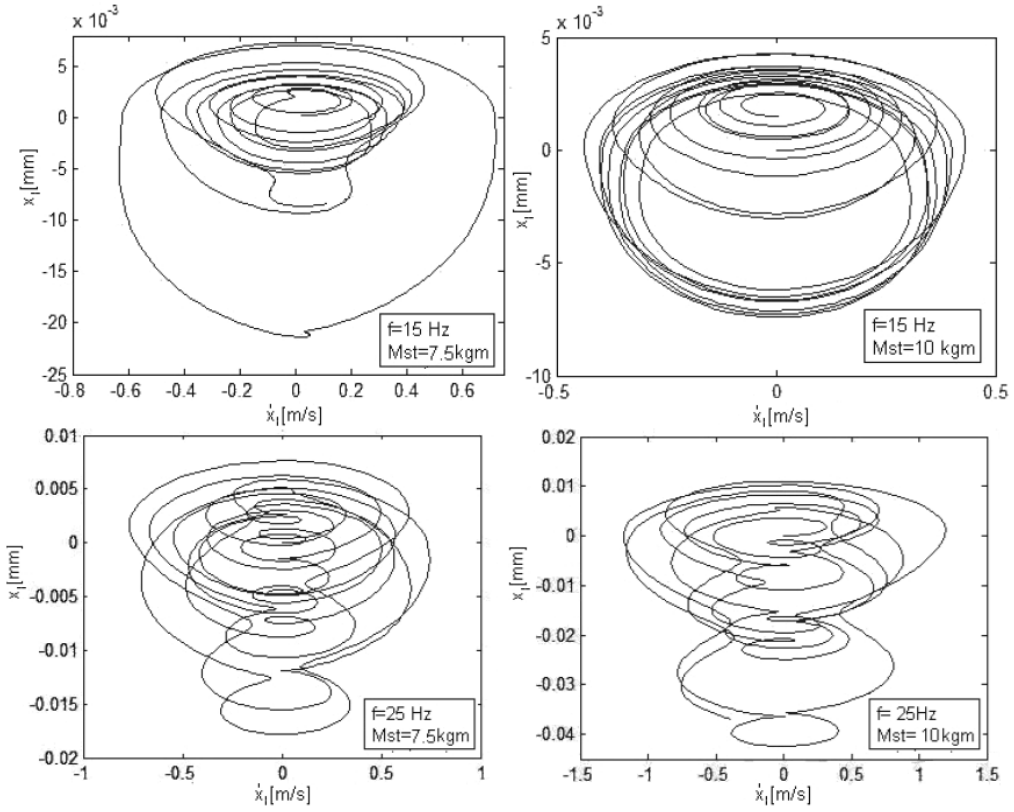

Fig. 6. Phase-plane representation for evaluating of stability motion of vibratory drum

4. Conclusions

Nonlinear dynamic behavior of the eccentric mass variation in vibratory roller compactors has been analyzed, revealing that it can lead to complex behaviors such as decoupling from the soil and different operating modes depending on factors like excitation amplitude and frequency. These analyses are supplied for understanding the roller's effectiveness and are based on models that include the coupling between the drum, frame, and soil, using lumped parameters.

References

[1] White, D.J., and P.KR. Vennapusa. "A Review of Roller-Integrated Compaction Monitoring Technologies for Earthworks". Final Report ER10-04, Earthworks Engineering Research Center (EERC), April 1, 2010.
[2] Popov, Y.G., and E.K. Chabutkin. "Increasing the Efficiency of Vibratory Rollers through Adjusting the Magnitude of the Disturbing Force". Paper presented at the 5th International Conference on Industrial Engineering (ICIE 2019), Sochi, Russian Federation, March 25–29, 2019.

[3] Debeleac, C.N., A. Buraga, and S.M. Nastac. "Experimental and Numerical Study in Dynamic Compaction of Weakly-Cohesive Soils." *Applied Sciences* 14, no. 22 (2024): 10129.
[4] Leopa, A., C. Debeleac, and S. Năstac. "Simulation of Vibration Effects on Ground Produced by Technological Equipments". Paper presented at the 12th International Multidisciplinary Scientific GeoConference SGEM2012, Albena, Bulgaria, June 17–23, 2012.
[5] Bratu, P., and C. Debeleac. “The analysis of vibratory roller motion.” Paper presented at the VII International Triennial Conference Heavy Machinery—HM 2011, Vrnjačka Banja, Serbia, June 29 – July 2, 2011.
[6] Debeleac, C.N., and A. Buraga. "Experimental Investigations and Numerical Simulations of Vibratory Compac-tion of Weakly Cohesive Soils". *Romanian Journal of Acoustics and Vibration* 19, no. 2 (2022): 143–148.

ISSN 1454 - 8003
Proceedings of 2025 International Conference on Hydraulics and Pneumatics - HERVEX
November 19-21, Băile Govora, Romania

DRYING THEORY AND CURRENT TRENDS IN CONVECTIVE AND SOLAR DRYING OF FOOD PRODUCTS

Ioan PAVEL[1], Gabriela MATACHE[1], Gheorghe ȘOVĂIALĂ[1], Marinela MATEESCU[2]

[1] National Institute of Research & Development for Optoelectronics/ INOE 2000 – Subsidiary Hydraulics and Pneumatics Research Institute / IHP, Bucharest, Romania; fluidas@fluidas.ro

[2] National Institute of Research-Development for Machines and Installations Designed to Agriculture and Food Industry INMA Bucharest, Romania

Abstract: *Population growth, climate change, and increasing pressure on energy resources make low-energy preservation technologies essential. Food drying—especially of fruits and vegetables—remains one of the oldest and most flexible preservation methods, yet the way it is carried out has changed radically: from traditional, uncontrolled sun drying to convective, solar, and hybrid systems optimized through automatic control and thermal energy storage.*
From a review perspective, this paper presents the theoretical fundamentals of convective drying (heat and mass transfer, internal diffusion, the crusting effect, and the role of temperature, relative humidity, and air velocity) and the critical technological parameters that determine product quality. It then synthesizes the common methods used to determine drying kinetics (drying curves and drying-rate curves, performance indicators) and provides a typical experimental example from the literature on apricot fruit drying.
In the trends section, the paper surveys the evolution of solar dryers (direct, indirect, tunnel-type, and greenhouse-type), the development of hybrid systems (solar–biomass, solar–electric, solar–heat pump), the integration of phase change materials (PCMs) for thermal energy storage, and the emergence of "smart" dryers equipped with IoT sensors and real-time monitoring. The socio-economic dimension is also discussed, highlighting the role of solar dryers in reducing post-harvest losses and supporting small-scale producers. Finally, conclusions and development directions are formulated for designers and manufacturers of drying equipment, with an emphasis on the convergence between classical drying theory and green, digital technologies.

Keywords: *Food drying, solar dryer, heat and mass transfer, convective drying, PCM, IoT, hybrid systems*

1. Introduction

Drying is one of the oldest methods of food preservation, initially practiced by directly exposing products to solar radiation. Removing water reduces microbiological activity and slows chemical reactions, enabling fruits and vegetables to be stored for long periods, with relatively low storage and transport costs.
Solar energy—an abundant renewable resource available throughout the year—is naturally associated with food drying. In recent decades, interest in solar drying has increased significantly, both due to the gradual depletion of fossil fuels and because of the pressure to reduce greenhouse-gas emissions. Recent studies and review papers show a steady increase in the number of publications dedicated to solar dryers for agri-food products, with a focus on energy efficiency, quality, and sustainability.
However, the traditional open sun-drying method has major limitations:

- limited control of temperature and humidity;
- risk of contamination by dust, insects, birds, or animals;
- high variability in product quality;
- significant thermal losses, since only a fraction of the incident radiation is effectively utilized.

To overcome these limitations, enclosed solar dryers (cabinet, tunnel, greenhouse) have been developed, where the product is protected from the outdoor environment and process parameters can be controlled more effectively. Recent developments include:

- indirect and hybrid solar dryers that combine solar energy with other sources (biomass, electric heaters, heat pumps) [1].

- integration of phase change materials (PCMs) for thermal energy storage [2].
- the use of sensors and IoT systems for real-time monitoring and control of the drying process [3].

In parallel, the literature emphasizes the need to more tightly link drying theory (describing heat and mass transfer at the product level) with the practical design of equipment: airflow distribution, channel geometry, product placement, integration of auxiliary heat sources, and thermal storage [4].
The purpose of this paper is to provide a focused review of the theoretical basis of convective drying of food products and to synthesize the main current technical trends in solar and hybrid drying, with direct implications for the design and optimization of drying equipment.

2. Method

2.1 The theoretical basis of convective drying

Drying fruits and vegetables is a heat and mass transfer process in which:

- hot air provides the energy required to evaporate water;
- water migrates from the interior of the product to the surface and is then removed by the airflow.

Internal diffusion and thermo-diffusion. At the beginning, free water on the surface evaporates rapidly. Subsequently, water from inner layers migrates toward the surface through internal diffusion, driven by concentration differences and osmotic pressure. At the same time, the temperature gradient between the exterior and the interior generates thermo-diffusion (water migration influenced by the thermal gradient). In convective drying practice, internal diffusion dominates the process, while thermo-diffusion plays a secondary role, because temperature differences inside the product are not very large.
Crust formation. If the evaporation rate at the surface is much higher than the internal diffusion rate of water, a crust (a dry, rigid surface layer) may form, blocking moisture migration from the interior. This phenomenon leads to:

- longer drying times;
- difficult rehydration;
- non-uniform texture and potential skin cracking (e.g., in plums, grapes).

To avoid crust formation, combined control of air temperature and relative humidity is essential, so that surface evaporation does not drastically exceed the internal diffusion capacity.

2.2. Process parameters and optimal conditions

For designers and operators, several parameters are critical:

- **Air temperature:**
  - for most fruits, the literature recommends dryer inlet temperatures of 70–72°C, decreasing to 40–45°C at the outlet;
  - exceeding these limits causes sugar caramelization, browning, loss of aroma and color, and degradation of certain heat-sensitive vitamins.
- **Air relative humidity:**
  - 20–25% at the system inlet, increasing to 60–70% at the outlet;
  - air that is too dry promotes crust formation; air that is too humid slows the process excessively.
- **Air velocity:**
  - it must be high enough to remove water vapor and maintain a moisture gradient between the product and the air;
  - in tunnel dryers, velocities in the 3–5 m/s range are frequently reported; values that are too low lead to rapid air saturation, while values that are too high increase energy losses.
- **Product size and geometry:**
  - reducing characteristic dimensions (thin slices, halves) shortens the diffusion path and increases the evaporation area;

- common examples: apricots as halves; apples and pears as slices; vegetables as rounds or cubes; grapes and plums as whole fruits.

Optimal process efficiency is achieved when the evaporation rate at the surface is approximately equal to the rate of water migration from the interior. This balance depends on the combination of temperature, relative humidity, air velocity, and the preparation method (cutting, blanching, osmotic pretreatments, etc.).

2.3. Moisture and performance indicators

In the analysis and control of drying processes, two main moisture-content indicators are used:

- Moisture content on a dry basis (dry-solid basis):

$$X_d = \frac{m_w}{m_{usc}}$$

where (m_w) is the mass of water, and (m_{usc}) is the mass of dry matter (dry solids).

- Moisture content on a wet basis (wet material basis):

$$X_u = \frac{m_w}{m}$$

where m is the total mass of the product (water + dry matter).

In addition, practical indicators are used:

- Drying yield – the ratio between the mass of dried product obtained and the mass of raw material used, expressed as a percentage.
- Drying ratio – the amount of raw material required to obtain 1 kg of dried product.

These measures support equipment sizing and enable comparisons between different technologies or process conditions.

2.4. Experimental methods for determining drying kinetics

Drying kinetics are typically determined from the mass–time variation curve. A common experimental setup includes:

- a drying chamber with a controlled hot-air supply (electric heaters or a conventional/solar heat source);
- a system for measuring product and air temperature (thermocouples, resistance temperature detectors);
- automatic control of air temperature (PID controller);
- air velocity measurement (anemometer, micromanometer);
- a precision balance, sometimes integrated into a suspension system that allows continuous monitoring of the sample mass without stopping the process.

From the measured data series m(t)m(t)m(t), moisture content is calculated and the following are plotted:

- the drying curve: moisture content vs. time;
- the drying-rate curve: the (numerical) derivative of moisture content with respect to time.

The analysis of these curves generally highlights three periods: initial heating, the constant-rate drying period, and the falling-rate period.

A frequently cited example in the literature concerns the convective drying of apricots with air heated to 60–100°C, at air velocities on the order of 0.5–1 m/s. In such studies, drying time decreases by several times when moving from moderate temperatures (e.g., 60°C) to higher temperatures (e.g., 100°C), and the maximum drying rate increases almost linearly with temperature up to a certain threshold, beyond which quality degradation becomes significant. Such results underpin practical recommendations for selecting the optimal temperature for each product.

3. Trends in food drying

In recent years, the literature has evolved from isolated descriptions of experimental cases to broader analyses of dryer typologies, methods for enhancing heat and mass transfer, and the integration of these technologies into agri-food value chains. Key directions are summarized below.

3.1. Evolution of solar dryers

Recent reviews show that solar dryers for food products can be grouped into several major categories: direct dryers (the product is exposed inside a glazed chamber), indirect dryers (the product does not “see” the sun directly; the air is preheated in a collector), tunnel-type dryers, and greenhouse dryers [5].
Observed trends include:

- a shift from direct drying to indirect and mixed configurations, to protect the product from direct radiation and to improve temperature control;
- optimization of collector geometry and airflow (guides, plenums, baffles) to ensure uniform air distribution and reduce “dead” zones;
- the use of photovoltaic-powered fans to maintain a constant air velocity, independent of wind variations.

Internationally, there is a shift from simple demonstration prototypes to pre-industrial equipment and solar dryers integrated into farms or cooperatives, with capacities ranging from a few tens to a few hundreds of kilograms per batch [4].
Solar dryers can be categorized based on size, structural/system configuration, and the way solar energy is utilized. Figure 1 presents all identified dryer types.

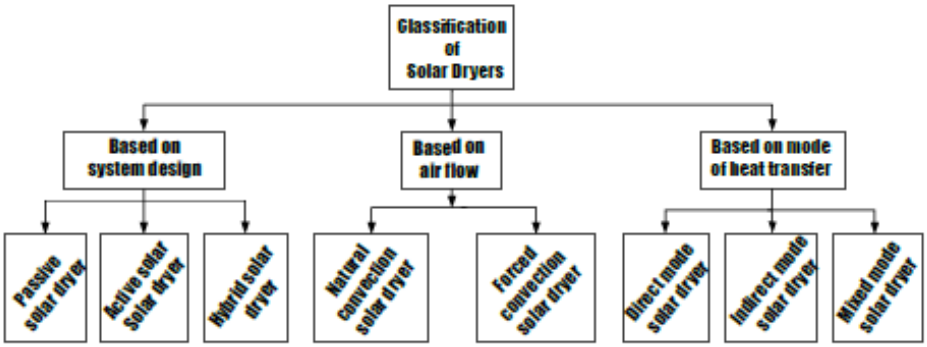

Fig. 1. Classification of solar dryers

The drying technology has seen a transition from the ancient open-air sun drying to the modern smart solar dryers as presented in Figure 2. The transition in the drying technology is as a result of continued increase in research activities in mechanical and electrical engineering (Renewable energy). Dryer designs, performance and efficiency have kept on improving within this transition.

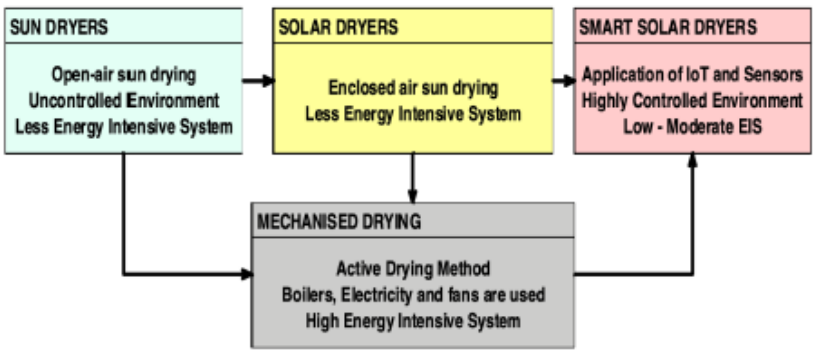

Fig. 2. Transition in solar drying technology

3.2. Hybrid systems: solar + biomass / electric / heat pump

An important direction is the development of hybrid dryers, which combine solar energy with other heat sources in order to ensure:

- process continuity (including during the evening or under low-radiation conditions);
- more precise and stable temperatures;
- shorter drying times and better product quality.

Reviews of hybrid dryers highlight the integration of four main types of sources: electric heaters, biomass (stoves, fire-to-air heat exchangers), thermal energy storage, and, more recently, solar-assisted heat pump (SAHP) systems [1].
Next, the operating modes of the three main drying systems are presented: direct drying (Fig. 3), indirect drying (Fig. 4), and hybrid (solar-thermal) drying (Fig. 5).

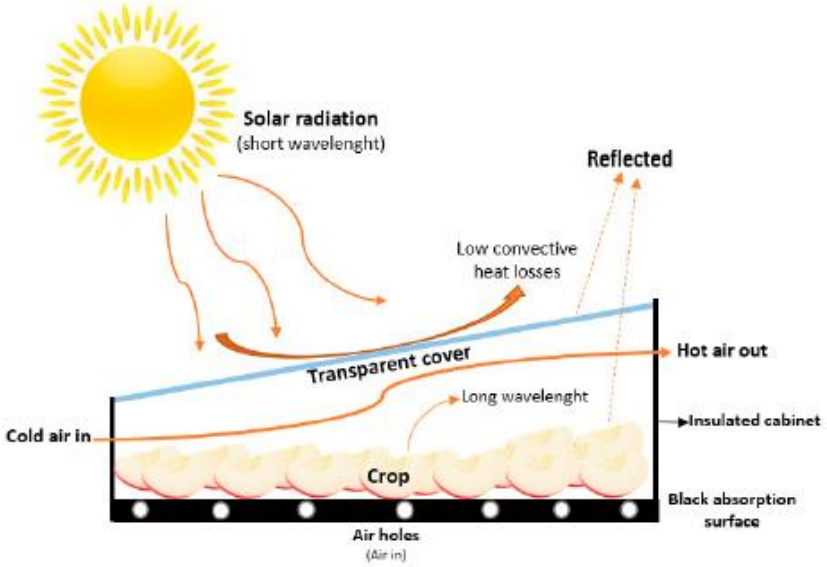

Fig. 3 Schematic of working principle of direct drying method

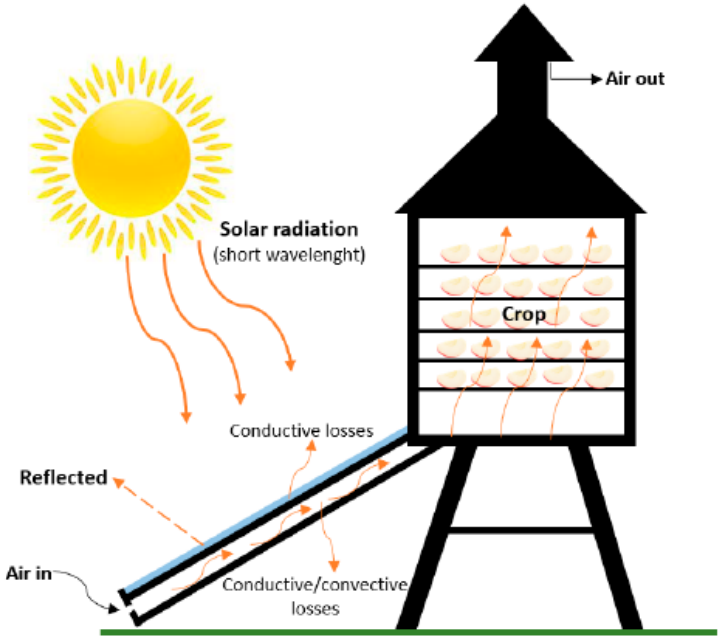

Fig. 4 Schematic of working principle of indirect drying method.

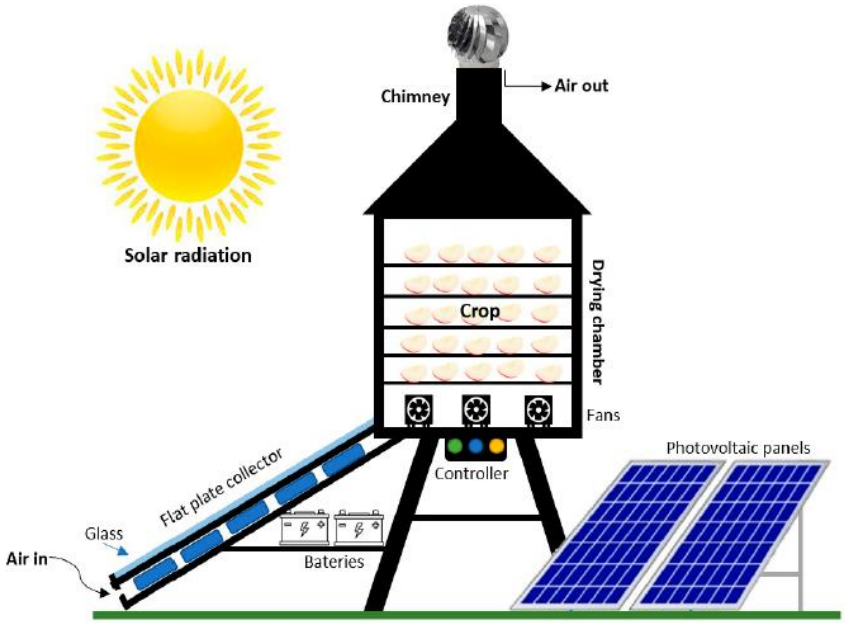

Fig. 5. Schematic of working principle of hybrid (solar–thermal) drying method

The advantages of hybrid systems include:

- increasing overall efficiency (solar energy covers part of the demand, while the remainder is supplied by the auxiliary source);
- reducing drying time by up to 30–50% compared with simple solar drying or natural drying;
- flexibility in adjusting process conditions for different product types.

At the same time, studies show that hybrid solutions must be carefully optimized to avoid overheating and to ensure they do not undermine the “low-carbon” advantage of solar drying.

3.3. Thermal storage using phase change materials (PCM)

The integration of phase change materials into solar dryers is one of the most visible trends in recent years. PCMs (paraffins, hydrated salts, eutectic mixtures, or experimentally, metal alloys) are used to:

- store thermal energy during periods of intense solar radiation;
- gradually release heat when radiation decreases (clouds, afternoon, evening), maintaining a more constant temperature inside the drying chamber.

Numerous studies and reviews show that using PCM in collectors or drying chambers can:

- reduce temperature fluctuations;
- extend the effective drying period by a few hours per day;
- increase overall thermal efficiency and shorten drying times [2].

From a design perspective, the main challenges relate to:

- selecting an appropriate melting temperature for the target product (typically 40–70°C);
- improving thermal conductivity (fins, metal inserts, microencapsulation);
- chemical compatibility and stability over repeated melting–solidification cycles.

3.4. “Smart” dryers: sensors, IoT, and advanced control

Advances in low-cost electronics and wireless communications have led to the concept of the “smart solar dryer”: a dryer equipped with sensors and microcontrollers (Arduino-, ESP-based systems, compact PLCs) capable of measuring and logging, in real time, parameters such as:

- air temperature and humidity at inlet and outlet;
- product temperature;
- air velocity or flow rate;
- solar radiation intensity.

Data can be transmitted to cloud platforms, where it is stored and analyzed, enabling:

- automatic control of fans and valves (on/off or PWM modulation);
- intelligent regulation of auxiliary heat sources (biomass/electric);
- optimization strategies (e.g., keeping the product as long as possible within the "optimal" temperature range for quality) [3].

Some papers even propose integrating radiation sensors or photodetectors into IoT schemes to better correlate atmospheric conditions with drying strategies and to reduce the risk of overheating or insufficient drying [6].

For manufacturers, this trend means that a modern dryer is no longer just a "box with hot air," but a mechatronic system in which thermal hardware (collector, chamber, fan) is tightly coupled with software (control algorithms, data logging, and potentially web interfaces or mobile apps).

3.5. The socio-economic dimension and small-scale adoption

Beyond technical performance, recent literature highlights the role of solar dryers in:

- reducing post-harvest losses in rural areas;
- increasing farmers' income by valorizing surplus production;
- diversifying products (dried fruits, dehydrated vegetables, herbs, spices) [7].

Socio-economic reviews show that successful implementation depends not only on thermal efficiency, but also on:

- initial cost and availability of locally sourced materials;
- ease of operation and maintenance (including for users without technical training);
- the existence of distribution networks for dried products;
- institutional support (funding programs, training, quality standards).

For Central and Eastern Europe, including Romania, the climate is favorable for seasonal solar drying, and integrating modern technologies (hybrid systems, PCM, IoT) into solutions affordable for small producers represents an important direction for research and technology transfer.

4. Conclusions and perspectives

Analyzing the theoretical basis and recent trends in food drying allows several conclusions and development directions to be formulated:

1. **Drying theory remains essential in design.** Even as "hardware" technology evolves (new dryer types, new materials, new configurations), sound design starts from understanding the roles of moisture and temperature gradients, internal diffusion, the risk of crust formation, and the relationship between temperature, relative humidity, and air velocity.
2. **Optimal parameters are product-specific.** Inlet ranges of 70–72°C and outlet ranges of 40–45°C, with relative humidities of 20–25% and 60–70%, should be seen as general benchmarks. To ensure maximum quality, each product (apricots, apples, vegetables, aromatic plants) requires fine tuning of temperature, air velocity, and slice thickness.
3. **Solar and hybrid systems are becoming the standard for sustainable applications.** Simple solar dryers are attractive due to low cost, but are limited by weather dependence. Hybrid systems—solar plus an auxiliary source—enable continuous operation, reduce drying time, and facilitate temperature control, with a lower carbon footprint than purely conventional systems.
4. **PCM and thermal storage improve process stability.** Integrating phase change materials into collectors or drying chambers has demonstrated higher energy efficiency and temperature stabilization, especially under variable radiation. Remaining challenges concern design (geometry, thermal contact, compatibility) and cost.
5. **IoT-driven digitalization is changing how dryers are operated.** Low-cost sensors, microcontrollers, and cloud platforms enable remote monitoring and control, batch traceability, real-time optimization, and even predictive algorithms to stop the process at the "optimal" moment in terms of quality versus energy consumption.

6. **Socio-economic impact reinforces the technology's relevance.** Solar and hybrid dryers can significantly reduce post-harvest losses and increase the incomes of small and medium producers, provided they are designed and implemented with careful attention to the local context (cost, technological culture, market).

Research and industry perspectives

- **Integrating numerical models and experiments.** Developing CFD and heat-and-mass-transfer models calibrated with experimental data will enable faster optimization of dryer configurations before physical prototyping, reducing development costs.
- **Standardization and design guidelines.** Creating design guidelines for different product categories (fruits, vegetables, medicinal plants) that combine drying theory with recommended design parameters (geometry, airflow, temperatures, control strategies) would support equipment manufacturers and end users.
- **Modular dryers for small farms.** Developing modular, scalable dryers that can be easily adapted to available volumes and product types is a promising direction for widespread adoption.
- **Integration into short agri-food supply chains.** Linking dryers with local distribution networks (local markets, cooperatives, traditional-product shops) can turn drying from a purely technological process into a tool for rural development.
- **Life-cycle environmental assessment (LCA).** LCA studies dedicated to solar and hybrid dryers can quantify real benefits in terms of avoided emissions and can guide choices of materials and structural configurations.

By combining a solid foundation in drying theory with recent technical innovations—solar, hybrid, PCM-based, and IoT-enabled—designers and equipment manufacturers can develop robust, efficient, and affordable solutions, suited both to industrial requirements and to the needs of small producers. This type of integrated approach is essential for food drying to remain, in the future as well, a central technology in the transition toward sustainable agri-food systems.

Acknowledgments

This work was supported by a grant of the Ministry of Research, Innovation and Digitization, CCCDI - UEFISCDI, project number PN-IV-P7-7.1-PTE-2024-0039, within PNCDI IV.

References

[1] Kong, Decheng, Yunfeng Wang, Ming Li, and Jingkang Liang. "A comprehensive review of hybrid solar dryers integrated with auxiliary energy and units for agricultural products." *Energy* 293 (April 2024): 130640.

[2] Krishna, Vedantam Sai, Sanjay Kumar Jain, Narayan Lal Panwar, and Rama Sree. "An overview on Phase Change Material incorporated in convective solar dryers." *Journal of Energy Storage* 131, Part A (September 2025): 117486. https://doi.org/10.1016/j.est.2025.117486.

[3] Nkolokosa, D. "The status of smart solar Dryers: Review." *Journal of Energy Storage* 14, no.1 (2023): 24-31.

[4] Shrivastava, Vipin, Pushpendra Singh, and Nitin Shrivastava. "A decade of progress in indirect solar drying: A review of systems for fruits, vegetables, and medicinal herbs (2015–2025)." *Renewable and Sustainable Energy Reviews* 226, Part C (January 2026): 116388. https://doi.org/10.1016/j.rser.2025.116388.

[5] Fernandes, Lisete, and Pedro B. Tavares. "A Review on Solar Drying Devices: Heat Transfer, Air Movement and Type of Chambers." *Solar* 4, no. 1 (2024): 15-42. https://doi.org/10.3390/solar4010002.

[6] Sharma, Brij Bhushan, Pankaj Vaidya, Nitin Kumar, Ankita Tiwari, Shonak Bansal, Mohammad Rashed Iqbal Faruque, and K. S. Al-mugren. "Enhancing post-harvest sustainability in temperate crops through smart IoT-integrated indirect solar dryer." *Scientific Reports* 15 (2025): 28608.

[7] Kimaro, D., A. Nyangarika, and T. Kivevele. "Uncovering socioeconomic insights of solar dryers for sustainable agricultural product preservation: A systematic review." *Heliyon* 10, no. 23 (2024): e40726.

ISSN 1454 - 8003
Proceedings of 2025 International Conference on Hydraulics and Pneumatics - HERVEX
November 19-21, Băile Govora, Romania

TECHNICAL AND ENVIRONMENTAL ASPECTS OF WIND FARM MAINTENANCE

Andrei-Cristian BĂDESCU[1], Bilghe SULIMAN[1]

[1] PhD Students, Faculty of Power Engineering, National University of Science and Technology POLITEHNICA Bucharest, 060042 Bucharest, Romania; andrei.badescu@stud.energ.upb.ro; bilghe.suliman@stud.energ.upb.ro

Abstract: *This paper provides a concise analysis of current trends in the maintenance of wind turbines and highlights how modern maintenance strategies contribute to operational sustainability and environmental protection. Based on extensive documentation and practical experience from wind energy projects, the main development directions are identified: the transition from corrective to predictive maintenance, process digitalization through SCADA systems and AI-based platforms, and the integration of circular economy principles in component management.*
In parallel, the study emphasizes the importance of environmental impact and life-cycle assessment (LCA) as integral parts of a sustainable maintenance strategy. The conclusions show that data-driven and predictive approaches can significantly reduce O&M (Operation and Maintenance) costs, increase equipment availability, and lower the ecological footprint of wind farms.

Keywords: *Predictive maintenance, wind energy, sustainability, environmental impact*

1. Introduction

Wind energy has become one of the main pillars of the global energy transition, contributing significantly to the reduction of greenhouse gas emissions and to the diversification of the energy mix. However, the operation of wind farms involves major challenges related to maintenance, reliability, and operational efficiency. Maintenance and repair costs can account for between 15% and 30% of the total Levelized Cost of Energy (LCOE) [1], [2].
In this context, companies and research centers continuously develop advanced maintenance methods aimed at minimizing unplanned downtime, extending equipment lifespan, and optimizing resource consumption. The current trend is toward intelligent, data-driven maintenance capable of anticipating failures before they occur and proposing optimal actions from both cost and environmental perspectives [3], [4].
Properly planned maintenance is no longer just a technical matter but also a key component of sustainability. Modern O&M strategies can directly reduce the carbon footprint by extending component lifetimes, reducing the need for new materials, and minimizing industrial waste [5]. Moreover, assessing the environmental impact of maintenance activities is becoming an integral part of decision-making, enabling simultaneous optimization of technical and ecological performance.

2. Current trends in wind farm maintenance

The evolution of maintenance in the wind sector has followed a clear trajectory—from corrective (reactive) maintenance to preventive, predictive, and finally prescriptive maintenance.

2.1 Corrective maintenance

This is the oldest form of maintenance, based on intervention only after a failure occurs. Although initially less costly, this approach carries high risks of unplanned downtime, production losses, and further damage to adjacent components [6].

In the wind industry—where access to turbines is often difficult due to remote locations and weather conditions—corrective maintenance is the most expensive long-term strategy.

2.2. Preventive maintenance

This strategy involves performing maintenance at regular intervals regardless of the actual condition of the equipment. While it reduces the risk of major failures, it can lead to premature replacements and inefficient use of resources. In recent years, preventive approaches have been refined through reliability analyses and historical data modeling to adjust maintenance intervals dynamically [7].

2.3. Predictive and prescriptive maintenance

The most advanced approach is predictive maintenance, based on real-time data from sensors, SCADA systems, and Condition Monitoring Systems (CMS). These monitor vibration, temperature, pressure, and oil quality to detect early signs of component degradation (gearbox, generator, bearings, blades).
By integrating artificial intelligence and machine learning algorithms, maintenance becomes prescriptive—not only predicting failures but also recommending the most efficient corrective actions based on cost, downtime, and ecological impact [8], [9].
Such systems are increasingly supported by digital twins and integrated analytics platforms that simulate the turbine's behavior under real conditions to guide optimal O&M decisions.

2.4. Reliability-Centered Maintenance (RCM)

The RCM approach relies on the functional analysis of each subsystem and the identification of critical components. Its purpose is to prioritize maintenance tasks based on risk level and operational importance. This methodology has become a standard tool for industrial-scale O&M optimization [10].

3. Correlation between maintenance and sustainability

The concept of sustainability in wind energy extends beyond the generation of clean electricity; it also encompasses how equipment is operated, maintained, and decommissioned. Therefore, maintenance activities play a crucial role in reducing environmental impact throughout the turbine's life cycle.

3.1. Impact of maintenance on the turbine life cycle

Life Cycle Assessment (LCA) analyses show that a significant portion of a turbine's environmental footprint is concentrated in the manufacturing and maintenance phases, rather than during operation [11].
Unplanned interventions often lead to additional material consumption, repeated transport to remote sites, and increased logistical emissions. Conversely, predictive maintenance mitigates these effects by enabling efficient planning and extending component lifetimes [12].

3.2. Resource optimization and waste reduction

In modern O&M strategies, resource optimization and spare parts management are key elements of sustainability. Scheduled replacements based on actual equipment condition enable reuse and refurbishment, minimizing waste generation.
For example, gearbox reconditioning and industrial oil filtration can lower environmental impact by up to 20%, according to NREL studies (2023) [13].

3.3. Digitalization and energy efficiency in maintenance

The digitalization of maintenance processes not only enhances reliability but also improves the overall energy efficiency of wind farm operations.

Modern SCADA platforms collect and process data from hundreds of turbines simultaneously, allowing for optimized crew routing, reduced travel times, and lower fuel consumption [14].
Furthermore, predictive analytics can evaluate cost-benefit ratios between replacing or continuing to operate a component based on current performance and environmental risk.

3.4. Circular economy strategies

An increasingly important aspect is the integration of circular economy principles. Instead of a linear model ("produce–use–discard"), sustainable maintenance encourages recycling, refurbishing, and material recovery.
Manufacturers and operators now collaborate on blade recycling programs, a key step toward achieving climate neutrality in the wind industry [15].
Thus, sustainable maintenance becomes a central pillar of the circular economy, directly contributing to the UN Sustainable Development Goals (SDGs).

4. Analysis and Discussion

4.1. Relevant technical indicators

Maintenance performance can be evaluated through indicators such as:

1. MTTF (Mean Time To Failure) – average time before a failure occurs;
2. MTTR (Mean Time To Repair) – average repair duration;
3. Availability (A) – proportion of operational time, calculated as:

$$A = \frac{MTTF}{MTTF+MTTR} \quad (1)$$

These indicators were applied in the author's previous case studies, showing that predictive maintenance can increase turbine availability from 92% to over 97%, while reducing annual maintenance costs by 10–15%.

4.2. Comparative analysis of maintenance strategies

Table 1: Comparative analysis of maintenance and environmental impact

Maintenance Type	Advantages	Disadvantages	Environmental Impact
Corrective	Low initial costs	High downtime, failure risks	High – frequent transport and replacements
Preventive	Operational stability	Premature replacements, fixed costs	Moderate – constant resource use
Predictive	High reliability, optimized cost	Requires sensor/AI investment	Low – optimized logistics and material

This comparison shows that, although predictive maintenance involves higher initial costs (monitoring equipment, software), its long-term benefits in energy efficiency and environmental performance make it the most economically and ecologically viable strategy [16], [17].

4.3. Correlation model between maintenance and environmental impact

Based on LCA methodology, a simplified risk matrix can be used to assess how maintenance affects environmental parameters:

Table 2: Risk matrix – assessment of maintenance impact of the environment

Evaluated Factor	Probability	Consequence	Risk Level
Hydraulic oil leakage	Medium	High	High
Frequent maintenance trips	High	Medium	High
Poor recycling of components	Medium	Medium	Medium
Continuous monitoring (CMS)	Low	Low	Low

Implementing CMS systems reduces both technical and ecological risks, confirming international findings (IRENA, 2024) and aligning with observations from the author's dissertation.

4.4. Economic considerations

From an economic perspective, predictive maintenance helps reduce the LCOE by minimizing production losses and improving maintenance scheduling.
Industry-wide data shows O&M cost savings of 10–20%, especially for wind farms above 100 MW [18].
Moreover, the reduction of waste and transport-related emissions supports ESG (Environmental, Social, and Governance) targets, increasingly required in energy sector reporting.

5. Conclusions

The analysis demonstrates that maintenance is a critical component for optimizing the performance, sustainability, and profitability of wind farms.
The transition from corrective to predictive and prescriptive maintenance has been driven by the need to enhance turbine availability, lower O&M costs, and align with global environmental goals.
The implementation of CMS systems and AI-based predictive models enables early fault detection and optimal intervention planning, directly reducing LCOE and the carbon footprint.
These technologies foster a sustainable approach by extending component lifetimes and minimizing resource consumption and waste generation.
The key outcomes are:

1. Predictive maintenance increases average turbine availability by up to 5 percentage points;
2. Annual maintenance costs can be reduced by 10–20%;
3. CO_2 emissions and waste from premature replacements can decrease by up to 25%.

Integrating circular economy principles and LCA-based decision-making provides a holistic perspective on wind farm sustainability.
In conclusion, the future of wind farm maintenance will be defined by:

1. Advanced digitalization – through data analytics and digital twins;
2. AI and machine learning integration – for prescriptive decision-making;
3. Operational sustainability – through reduced environmental impact and circular economy implementation.

These developments make maintenance not only a technical process but a strategic driver for clean, efficient, and sustainable energy.

References

[1] Stehly, Tyler, Patrick Duffy, and Daniel Mulas Hernando. "2022 Cost of Wind Energy Review." National Renewable Energy Laboratory (NREL), 2023. Accessed October 30, 2025. https://docs.nrel.gov/docs/fy24osti/88335.pdf.
[2] International Renewable Energy Agency (IRENA). "Renewable Power Generation Costs in 2023," 2024. Accessed October 30, 2025. https://www.irena.org/Publications/2024/Sep/Renewable-Power-Generation-Costs-in-2023.
[3] Ren, Zhengru, Amrit Shankar Verma, Ye Li, Julie J.E. Teuwen, and Zhiyu Jiang. "Offshore wind turbine operations and maintenance: A state-of-the-art review." *Renewable and Sustainable Energy Reviews* 144 (2021): 110886.

[4] Fox, Harriet, Ajit C. Pillai, Daniel Friedrich, Maurizio Collu, Tariq Dawood, and Lars Johanning. “A Review of Predictive and Prescriptive Offshore Wind Farm Operation and Maintenance.” *Energies* 15, no. 2 (2022): 504.
[5] Bădescu, A.-C. “Trends in the Evolution of Wind Turbine Maintenance. Case Study – Environmental Impact Assessment for a Wind Farm / Tendințe în evoluția întreținerii turbinelor eoliene. Studiu de caz – Evaluarea impactului asupra mediului pentru un parc eolian.” Master’s Thesis. Maritime University of Constanța, 2025.
[6] Carroll, J., A. McDonald, and D. McMillan. “Failure rate, repair time and unscheduled O&M cost analysis of offshore wind turbines.” *Renewable Energy* 19, no. 6 (2016): 1107–1119.
[7] Kusiak, A., and A. Verma. “A data-driven approach for monitoring blade pitch faults in wind turbines.” *IEEE Transactions on Sustainable Energy* 2, no. 1 (2011): 87–96.
[8] Ng, Eddie Yin-Kwee, and Jian Tiong Lim. “Machine Learning on Fault Diagnosis in Wind Turbines.” *Fluids* 7, no. 12 (2022): 371.
[9] Davidsson, S., M. Höök, and G. Wall. “A review of life cycle assessments on wind energy systems.” *The International Journal of Life Cycle Assessment* 17 (2012): 729–742.
[10] Atilgan Turkmen, Burcin, and Fatos Germirli Babuna. “Life Cycle Environmental Impacts of Wind Turbines: A Path to Sustainability with Challenges.” *Sustainability* 16, no. 13 (2024): 5365.
[11] Tchakoua, Pierre, René Wamkeue, Mohand Ouhrouche, Fouad Slaoui-Hasnaoui, Tommy Andy Tameghe, and Gabriel Ekemb. “Wind Turbine Condition Monitoring: State-of-the-Art Review, New Trends, and Future Challenges.” *Energies* 7, no. 4 (2014): 2595-2630.
[12] Tchakoua, P., R. Wamkeue, M. Ouhrouche, F. Slaoui-Hasnaoui, T. A. Tameghe, and G. Ekemb. “Wind turbine condition monitoring: State-of-the-art review, new trends, and future challenges.” *Energies* 7, no. 4 (2014): 2595–2630.
[13] National Renewable Energy Laboratory (NREL). “Gearbox Reliability Collaborative Update.” Technical Report, 2023.
[14] Jani, H. K., S. S. Kachhwaha, G. Nagababu, and A. Das. “A brief review on recycling and reuse of wind turbine blade materials.” *Materials Today: Proceedings* 62, Part 13 (2022): 7124-7130.
[15] Jensen, J. P., and K. Skelton. “Wind turbine blade recycling: Experiences, challenges and possibilities in a circular economy.” *Renewable and Sustainable Energy Reviews* 97 (2018): 165-176.
[16] García Márquez, F. P., A. M. Tobias, J. M. Pinar Pérez, and M. Papaelias. “Condition monitoring of wind turbines: Techniques and methods.” *Renewable Energy* 46 (2012): 169-178.
[17] Ding, F., Z. Tian, and T. Jin. “Maintenance modeling and optimization for wind turbine systems: A review.” Paper presented at the 2013 International Conference on Quality, Reliability, Risk, Maintenance, and Safety Engineering (QR2MSE), Chengdu, China, 15-18 July, 2013.
[18] WindEurope. *O&M and Asset Management Report 2023*. WindEurope, Brussels, 2023, 84 pp.

ISSN 1454 - 8003
Proceedings of 2025 International Conference on Hydraulics and Pneumatics - HERVEX
November 19-21, Băile Govora, Romania

EXPERIMENTAL RESEARCHES ON RHEOLOGICAL PROPERTIES OF BIOGREASES

Irina RĂDULESCU[1,*], Alexandru Valentin RĂDULESCU[1,*]

[1] Department of Machine Elements and Tribology, Faculty of Mechanical Engineering and Mechatronics, National University of Science and Technology POLITEHNICA Bucharest, Bucharest, Romania

* irina.radulescu@upb.ro; alexandru.radulescu@upb.ro

Abstract: *Currently, more and more manufacturers are producing biodegradable, high-performance soybean oil-based greases, available for various industrial and automotive applications. These products offer environmental benefits, such as non-toxicity and rapid biodegradability, as a sustainable alternative to conventional petroleum-based greases. This paper is focused on the rheological study of biodegradable greases based on soybean oil and aqueous sodium stearate, additivated with graphene or graphite nanoparticles in different concentrations. For this purpose, different biogrease samples have been prepared and each of them were thermal analysed in the range of 20^0C … 75^0C on a Brookfield CAP 2000+ viscometer, using Bingham rheological model. Finally, the thermal variation of the rheological parameters (yield stress and viscosity) was obtained, taking into account the presence of nano-additives.*

Keywords: *Rheology, biogreases, thermal, nano-additives*

1. Introduction

Biodegradable greases are semi-solid lubricants specifically formulated to be braked down by biological microorganisms in the environment, thereby reducing negative environmental impact [1]. They are used in applications where there is a risk of leakage or contamination of soil and water. They are minimally toxic to aquatic organisms, plants, and animals and do not bioaccumulate in the food chain. In case of spills or leaks (common in "total-loss" applications like chainsaws, food industry or rail curve grease), the environmental damage and associated clean-up costs are significantly lower than for petroleum-based products [2].
Currently, more and more manufacturers are producing biodegradable, high-performance soybean oil-based greases, available for various industrial and automotive applications [3].
Soybean oil-based greases are available in a variety of formulations, often incorporating different thickeners and additives to achieve performance comparable to traditional mineral oil products [4].
This paper proposes to study biodegradable greases based on soybean oil and aqueous sodium stearate as the thickener. Sodium stearate acts as a soap-based thickener, which forms a fibrous network within the soybean oil to create the grease structure [5], [6]. The use of an aqueous sodium stearate component facilitates the initial mixing and reaction. Water is typically heated and stirred with the sodium compound and stearic acid to dissolve the components and allow for the saponification reaction. The concentration of the sodium soap thickener in the base oil significantly impacts the final consistency of the grease. Ratios of oil-to-thickener are adjusted to achieve desired properties, typically within the 5-30% thickener range [7], [8].
The main advantage of using aqueous sodium stearate as the thickener is a high operating temperature range and a high level of biodegradability and non-toxicity.
Nanoparticles are highly effective as grease additives, significantly enhancing the grease's performance by reducing friction and wear, increasing load bearing capacity, and improving thermal stability and conductivity. They achieve this through several mechanisms at the microscopic level, such as: formation of the protective tribofilms at the surface level, rolling effect in the contact due to spherical nanoparticles etc. [9], [10].
In this paper, the nanoparticles used as additives for biodegradable greases are based on two allotropes of carbon with a hexagonal lattice structure: graphite and graphene. Graphite is a mineral that naturally occurs in metamorphic rock. It is formed as a result of the reduction of sedimentary

carbon compounds during metamorphism. Contrary to common belief, the chemical bonds in graphite are actually stronger. So, graphene is fundamentally one single layer of graphite; a layer of bonded carbon atoms arranged in a honeycomb (hexagonal) lattice. However, graphene offers some impressive properties that exceed those of graphite as it is isolated from its “mother material” [11], [12].

2. Experimental methodology

Biodegradable greases used for experiments were prepared using soybean base oil with aqueous sodium stearate thickener in concentration of 8% (wt). Four different types of samples have been tested, with the following composition:

- Pure grease (Fig. 1);
- Additivated grease, with antioxidant (1%) and antiwear (2%) additives (Fig. 2);
- Graphene grease, with antioxidant (1%), antiwear (2%) and graphene powder (0.3%) (Fig. 3);
- Graphite grease, with antioxidant (1%), antiwear (2%) and thermal expanded graphite (0.3%) (Fig. 4).

Fig. 1. Pure grease

Fig. 2. Additivated grease

Fig. 3. Graphene grease

Fig. 4. Graphite grease

The rheological measurements were performed on a Brookfield viscometer CAP2000+ equipped with four cone-and-plate geometry and using a Peltier system for controlling the temperature. The CAP 2000+ Series Viscometers are medium to high shear rate instruments with Cone Plate geometry and integrated temperature control of the test sample material, [13]. A typical view of the viscometer is presented in Fig. 5, with all the four geometries cone and plate.

Fig. 5. Geometry of Brookfield viscometer

Concerning the technical parameters of the viscometer, rotational speed selection ranges from 5 to 1000 RPM. Viscosity measurement ranges depend upon the cone spindle and the rotational speed (shear rate). Viscosity is selectively displayed in units of centipoise (cP), poise (P), or Pascal seconds (Pa•s). Temperature control of sample is possible between either 5°C (or 15°C below ambient, whichever is higher) and 75°C or 50°C and 235°C depending on viscometer model. The viscometer uses a CAPCALC32 software for complete control and data analysis. The geometry of testing cones and the viscosity range are presented in Table 1.

Table 1: Geometry and viscosity range of testing cones

Cone number	Cone radius, mm	Cone angle, degree	Viscosity range, Pa.s
3	9.53	0.45	0.083 ... 1.87
5	9.53	1.8	0.333 ... 7.50
6	7.02	1.8	0.833 ... 18.7
8	15.11	3	0.312 ... 3.12

A “velocity imposed gradient” test was used, with the temperature range between 20^0C and 75^0C and cone geometry number 8. The experimental results were numerically treated assuming the validity of Bingham rheological model:

$$\tau = \tau_0 + \eta \frac{\partial u}{\partial y} \quad (1),$$

where: τ – shear stress
τ_0 – yield stress
η – dynamic viscosity
$\frac{\partial u}{\partial y}$ – shear rate

3. Results

The experimental test consists of a load from the 10 s^{-1} to 2000 s^{-1} shear rate gradient, followed by an unload in order to highlight the thixotropy of the lubricant - "shear memory”. The test is repeated three times for each temperature (20^0C, 26^0C, 32^0C, 38^0C, 44^0C, 50^0C, 66^0C and 75^0C) and the duration of homogenization (soaking time) of the sample at a certain shear rate was 300 seconds. The rheograms are obtained by plotting shear stress as a function of the shear rate, as an average of 30 points, using the software Capcalc 32 specific for the viscometer. Fig. 6 shows a typical

rheogram at 20^{0}C, for all four types of greases: pure grease, additivated grease, graphene grease and graphite grease.

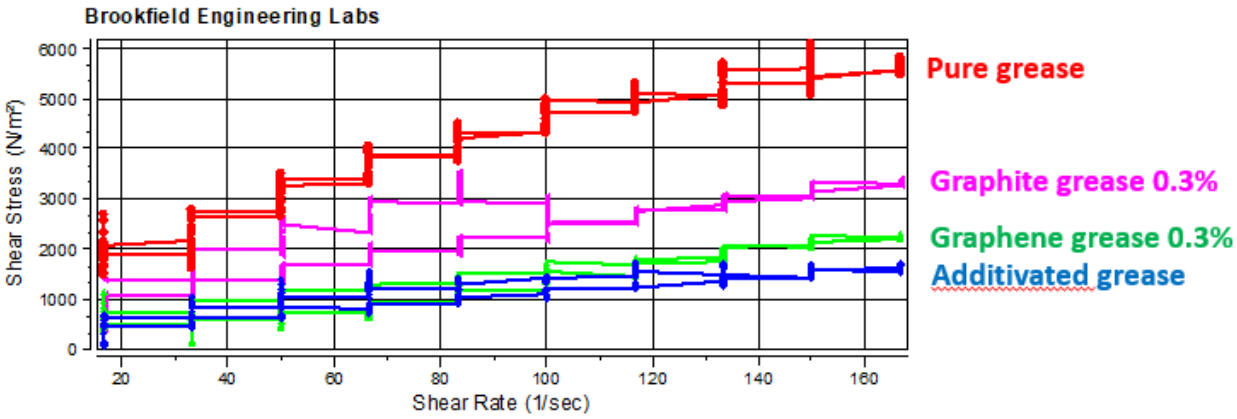

Fig. 6. Lubricant rheograms for the four greases, at 20^{0}C

Analysing the rheograms from Fig. 6 the following observations can be made:

- The grease in pure state has a homogenous structure, with a reduce thixotropy;
- The addition of antioxidant and antiwear additives to the grease decreases the values of the corresponding rheological parameters (yield stress and viscosity) by comparison with the pure grease;
- The supplementary addition of graphene nano-additive increases the values of rheological parameters by comparison with the additivated grease;
- The supplementary addition of graphite nano-additive increases the values of rheological parameters by comparison with the additivated grease with graphene, but it reduces the homogeneity of the grease structure.

The results regarding the variation of the rheological parameters (yield stress and viscosity) with the temperature are presented centralized in Tables 2, 3, 4 and 5.

Table 2: Rheological parameters for the pure grease

Temperature, ^{0}C	Yield stress (τ_o), Pa	Viscosity (η), Pa·s
20	2179	3.51
28	1857	1.98
37	1205	1.41
47	745	1.12
57	419	0.96
66	275	0.72
75	162	0.52

Table 3: Rheological parameters for the additivated grease

Temperature, ^{0}C	Yield stress (τ_o), Pa	Viscosity (η), Pa·s
20	532	1.83
28	337	1.24
37	197	1.10
47	125	0.93
57	112	0.66
66	60	0.57
75	41	0.31

Table 4: Rheological parameters for the graphene grease

Temperature, ^{0}C	Yield stress (τ_o), Pa	Viscosity (η), Pa·s
20	881	1.92
28	482	1.59
37	314	1.42
47	244	1.16
57	120	0.88
66	79	0.69
75	52	0.40

Table 5: Rheological parameters for the graphite grease

Temperature, ^{0}C	Yield stress (τ_o), Pa	Viscosity (η), Pa·s
20	1652	2.98
28	1483	1.46
37	1009	1.25
47	772	1.02
57	497	0.87
66	397	0.57
75	153	0.50

4. Discussions

Analyzing the experimental results concerning the variation of the rheological parameters with the temperature (Tables 2, 3, 4 and 5), it can be observed the influence of the additives and nanoparticles on the grease behavior.
The yield stress of the pure grease decreases by the temperature, considering the entire range of temperatures values: from 20^{0}C until 75^{0}C (Fig. 7). For the additivated grease, the yield stress at 20^{0}C is much smaller than the same value for the pure grease; over 20^{0}C, the yield stress is continuous decreasing, on the whole temperatures interval. The addition of the graphene nanoparticles increases the values for yield stress by comparison with the additivated grease, but they still remain smaller than for the pure grease. The greatest values for the yield stress are obtained for grease additivated with graphite particles.

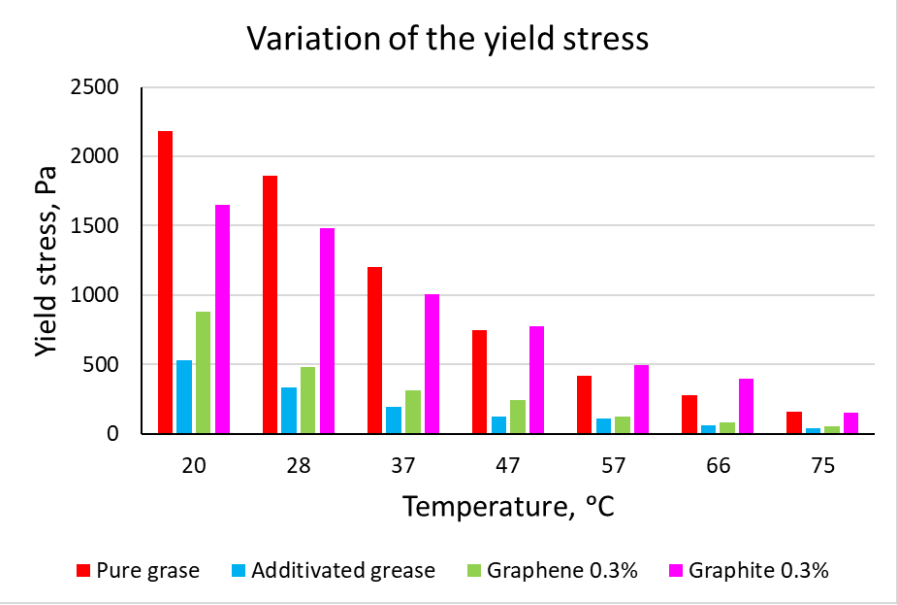

Fig. 7. Variation of the yield stress with temperature

The viscosity of the pure grease decreases by the temperature on whole interval of studied temperatures: from 20^0C until 75^0C (Fig. 8). The viscosity of the additivated grease decreases by the temperature and particularly - at 20^0C - this viscosity is half value of the pure grease viscosity.
Once with the increasing of temperatures, the difference between both grease viscosities is diminishing. The addition of the graphene nanoparticles increases a little bit the viscosity values - by comparison with the additivated grease, but the differences remain quite small.
The greatest values for the viscosity are obtained for grease additivated with graphite particles, even if they are always smaller than the corresponding pure grease. At the end of temperature interval (around 66^0C ... 75^0C) the differences between viscosities are almost insignificant.

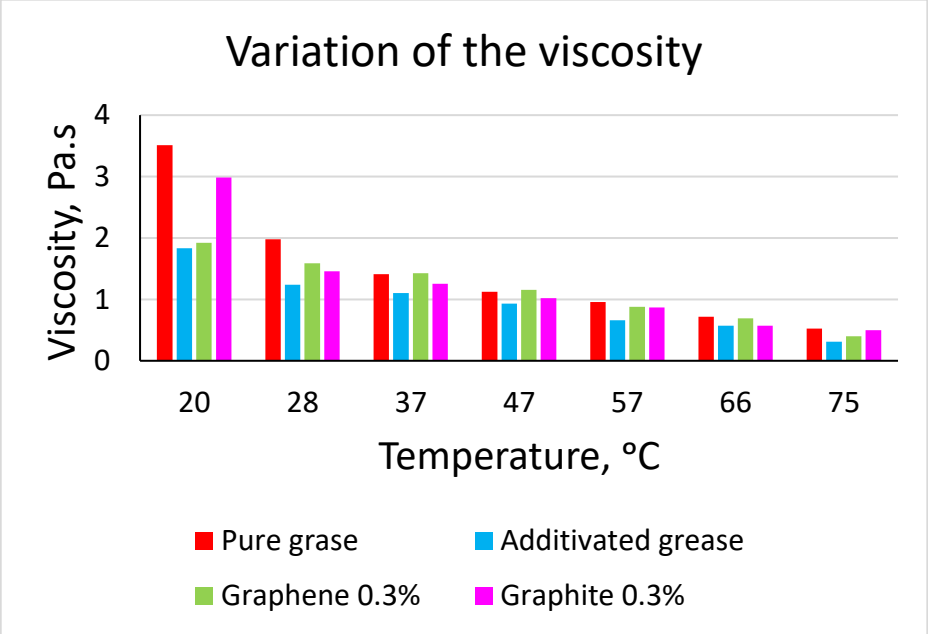

Fig. 8. Variation of the viscosity with temperature

4. Conclusions

1. The paper presents the study of the rheological properties (yield stress and viscosity) of biodegradable greases based on soybean oil with aqueous sodium stearate thickener, in concentration of 8%, additivated with 0.3% graphene or graphite nanoparticles.
2. The rheological properties were investigated in the range of temperature of 20^0C … 75^0C and the results were processed according to Bingham model.
3. It can be observed that the addition of the nanoparticles decreases the values of the rheological parameters (yield stress and viscosity), by comparison of the same values for pure grease.
4. The greatest values for the yield stress and for the viscosity are obtained for the grease additivated with graphite nanoparticles, by comparison with the grease additivated with graphene nanoparticles, but they still remain smaller, by considering the pure grease.
5. Supplementary investigations must be performed in order to study the tribological properties of these additivated grease with nanoparticles.

References

[1] Sánchez, Rafael, Concepción Valencia, and José María Franco. “Rheological and tribological characterization of a new acylated chitosan–based biodegradable lubricating grease: A comparative study with traditional lithium and calcium greases.” *Tribology Transactions* 57, no. 3 (2014): 445-454.

[2] Achanta, Satish, M. Jungk, and Dirk Drees. “Characterisation of cohesion, adhesion, and tackiness of lubricating greases using approach–retraction experiments.” *Tribology International* 44, no. 10 (September 2011): 1127-1133.
[3] Sánchez, Rubén, Jose María Franco Gómez, Miguel Ángel Delgado Canto**,** Concepción Valencia, and Críspulo Gallegos. “Thermal and mechanical characterization of cellulosic derivatives-based oleogels potentially applicable as bio-lubricating greases: Influence of ethyl cellulose molecular weight.” *Carbohydrate polymers* 83, no. 1 (2011): 151-158.
[4] Sharma, Brajendra K., Atanu Adhvaryu, Joe M. Perez, and Sevim Z. Erhan. “Soybean oil based greases: influence of composition on thermo-oxidative and tribochemical behavior.” *Journal of agricultural and food chemistry* 53, no. 8 (2005): 2961-2968.
[5] Núñez, N., Jose E. Martín-Alfons, Concepción Valencia, María Del Carmen Sánchez Carrillo, and José María Franco. “Rheology of new green lubricating grease formulations containing cellulose pulp and its methylated derivative as thickener agents.” *Industrial Crops and Products* 37, no. 1 (2012): 500-507.
[6] Saxena, Ankit, Deepak Kumar, and Naresh Tandon. “Development of eco-friendly nano-greases based on vegetable oil: An exploration of the character via structure.” *Industrial Crops and Products* 172 (2021): 114033.
[7] Dresel, Wilfried, and Rolf-Peter Heckler. “Lubricating greases.” In *Lubricants and Lubrication*. Wiley-VCH Verlag GmbH & Co. KGaA, February 2017, 781-842.
[8] Dube, Ndabezinhle Ngubhe, Hussien Noby, Mohamed G.A. Nassef, Abdelrahman Zkria, Hiroshi Naragino, and Marwa F. El Kady. “Extraction of Bio-Based Carbon Materials from Agricultural Waste as Additives for the Development of an Eco-Friendly Bio-Based Grease.” *Materials Science Forum* 1111 (December 2023): 97-103.
[9] Mas, Remy, and Albert Magnin. “Rheology of colloidal suspensions: case of lubricating greases.” *Journal of Rheology* 38, no. 4 (1994): 889-908.
[10] Salomonsson, Linda, Gunnar Stang, and Boris Zhmud. “Oil/thickener interactions and rheology of lubricating greases.” *Tribology Transactions* 50, no. 3 (2007): 302-309.
[11] Lin, Jinshan, Wang Liwei, and Chen Guohua. “Modification of graphene platelets and their tribological properties as a lubricant additive.” *Tribology letters* 41, no. 1 (2011): 209-215.
[12] Wong, H.-S. Philip, and Deji Akinwande. *Carbon nanotube and graphene device physics*. Cambridge University Press 2011.
[13] ***. Ametek Brookfield. “CAP 2000 Viscometer.” Accessed October 30, 2025. https://www.brookfieldengineering.com/products/viscometers/laboratory-viscometers/cap2000-viscometer.

ISSN 1454 - 8003
Proceedings of 2025 International Conference on Hydraulics and Pneumatics - HERVEX
November 19-21, Băile Govora, Romania

SWARM-BASED ROBOTIC INSPECTION AND FAULT DIAGNOSIS IN HEAVY-DUTY CONSTRUCTION MACHINERY

Ioan-Mihail SAVANIU[1], Aristia-Ioana POPOVICI[1]

[1] Technical University of Civil Engineering of Bucharest (UTCB) – Faculty of Mechanical Engineering and Robotics in Constructions

mihai.savaniu@utcb.ro, ioana.popovici@utcb.ro

Abstract: *This study presents the development of a collaborative robotic system, or robot swarm, equipped with video cameras and sensors for the periodic inspection of components in heavy-duty construction machinery. The primary aim is to detect cracks, abrasive-corrosive wear, and other defects, thereby preventing failures and/or accidents. By continuously monitoring large-scale construction equipment, the robots can transmit real-time data that can be analyzed using artificial intelligence. This enables prompt intervention in the event of anomalies and facilitates the prioritization of maintenance actions when significant wear is identified. This approach effectively reduces unplanned downtime and enhances operational safety by preventing major failures during machine operations.*

Keywords: *Robot swarm, inspection, wear, artificial intelligence, construction equipment*

1. Introduction

Construction equipment for earthmoving operations, such as excavators, bulldozers, and crawler loaders, functions under challenging conditions characterized by dust, mud, mechanical shocks, and significant load variations. Transmission and operational components, including tracks, carrier rollers, and idler wheels, are subjected to continuous abrasive and corrosive wear, and defects in these areas have a direct impact on the safety and availability of the equipment [1]. In practice, the financial implications of a major failure in the running gear can significantly surpass the costs associated with appropriate preventive maintenance.

Currently, inspections are predominantly conducted visually by specialized personnel while the equipment is not in operation. This method is time- consuming, relies heavily on the expertise of the operators, and generally precludes continuous monitoring during operation. Furthermore, certain areas are challenging to access without partial disassembly, thereby increasing maintenance costs. Modern predictive maintenance techniques, such as vibration analysis or oil analysis, serve as complements to visual inspection; however, they are not always capable of detecting all defects, such as cracks in the load-bearing structure, oil leaks, or foreign bodies [1] [2].

In recent years, advancements in computer vision and machine learning have significantly enhanced the efficiency of defect detection in mechanical components through the analysis of regions of interest (ROI) extracted from high-resolution images [2–4]. Concurrently, progress in mobile robotics, wireless communications, and artificial intelligence has facilitated the deployment of robotic swarms for the automated inspection of industrial equipment [5] [6]. Within such systems, multiple microrobots collaborate to distribute tasks related to exploration, data acquisition, and local preprocessing. This approach enables rapid coverage of extensive areas, enhances system redundancy and robustness, and provides flexibility in configuring monitoring missions.

In the context of inspecting and maintaining oversized construction machinery on-site, a significant challenge arises from the need to access multiple points within an unpredictable and hazardous environment. The deployment of multiple robots concurrently enhances the probability that at least one will successfully accomplish the task of inspecting or maintaining the construction machinery.

This paper aims to introduce an experimental platform for robotic inspection utilizing swarms of microrobots, specifically designed to diagnose defects in the running gear of heavy construction machinery. The paper details the hardware and software architecture, the method for generating

Regions of Interest (ROIs), and the testing scenarios, supported by actual images captured by the robots.

2. Implementation

The specialized literature documents numerous applications of automatic inspection of infrastructures and industrial equipment utilizing mobile robots or unmanned aerial vehicles (UAVs) [7], [8]. Predominantly, these methodologies concentrate on the inspection of power transmission lines and pipelines, the monitoring of civil structures, or the examination of rotating installations. In contrast, research concerning heavy construction machinery is comparatively limited, with a focus primarily on monitoring vibrations in bearings or conducting oil analysis for wear determination [1]. The automated visual inspection of tracks and rolling elements remains underexplored, despite these components being prone to a significant proportion of defects.
Robot swarms have been investigated for their potential applications in search and rescue operations, precision agriculture, and the exploration of uncharted environments [5], [6]. In this study, analogous principles are applied to the construction sector, characterized by intricate geometries where regions of interest (ROIs) are linked to specific mechanical components such as rollers, wheels, and track segments. An ROI, or region of interest, refers to a distinct area within an image or a three-dimensional model that the inspection system targets for analysis. Rather than processing the entire scene, algorithms prioritize these designated regions, which correspond to critical components (e.g., rollers, drive wheels, track segments), to identify cracks, wear, or other defects.
Figure 1 depicts examples of components subject to inspection, specifically detailing the running gear, including the wheels and rubber track, of an autonomous transport platform utilized in construction. Figure 2 presents the microrobots employed for inspection: the robotic platform equipped with omnidirectional wheels, based on Arduino and ESP32-CAM, and the STEM robot featuring LiDAR – MicroROS-Pi 5, positioned adjacent to the track section.

Fig. 1. Detail of the undercarriage of the construction machine: wheels and rubber track under inspection

The proposed system comprises a swarm of mobile microrobots designed to operate in proximity to a construction machine. The application discussed in the article is developed for students utilizing microrobots from the UTCB practice base, established under the CNFIS-FDI-2025-F-0289 project—RECIPA: Robotics and Ecology in Construction: Innovation and Applied Practice. Each robot is

tasked with exploring a predefined or dynamic area, acquiring images and/or LiDAR data, conducting preliminary identification of Regions of Interest (ROIs), and transmitting the data to a central processing station. The central station integrates data from the entire swarm and employs machine learning algorithms for defect detection.

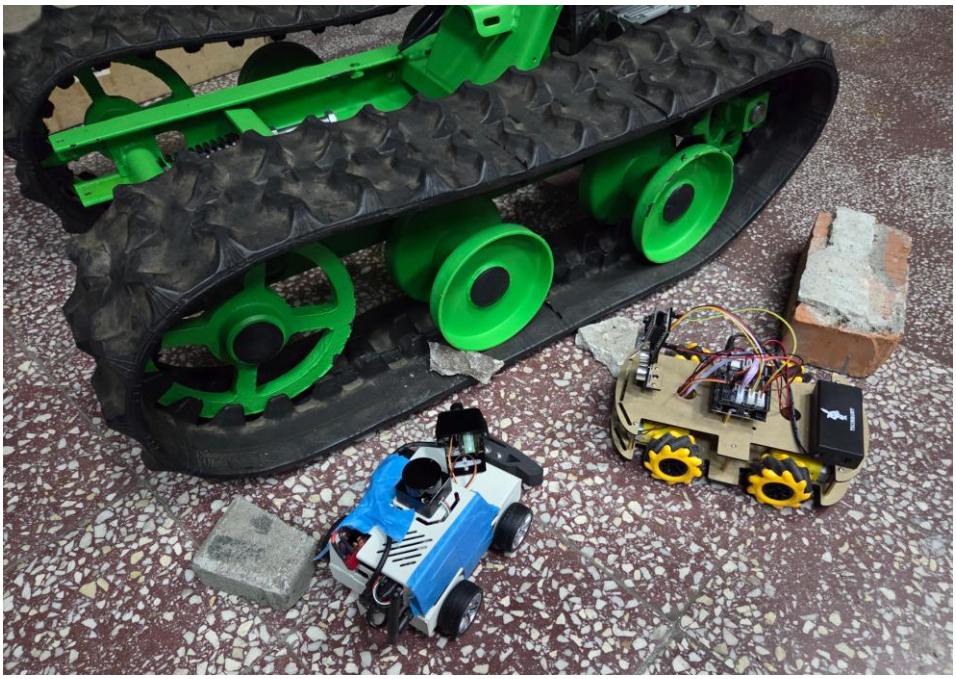

Fig. 2. Microrobots used in experiments: the omnidirectional wheeled platform with Arduino and ESP32-CAM (right) and the STEM robot with LiDAR – MicroROS-Pi 5 (left), positioned next to the track

The initial type of microrobot is equipped with a platform featuring four omnidirectional (Mecanum) wheels, facilitating movement in forward and backward directions, lateral shifts, and rotation around the vertical axis. The low-level control of movement and obstacle avoidance is managed through an Arduino microcontroller, while image acquisition is performed using an ESP32-CAM module mounted at the front. This robot is capable of approaching track elements and accurately repositioning itself in front of a region of interest (ROI) to capture high-resolution images. Its positioning, in conjunction with the STEM robot, adjacent to the train's running gear, is depicted in Figure 2.

The second category of robot serves as a STEM platform, featuring a four-wheel configuration and is equipped with a Raspberry Pi 5 computing unit. It incorporates MicroROS firmware to facilitate integration within the ROS2 ecosystem, a LiDAR sensor for both 2D and 3D mapping, additional proximity sensors, and a high-definition camera mounted on a gimbal with two degrees of freedom for viewing and video streaming. The primary function of this robot is to conduct volumetric mapping of the surrounding area and to detect obstacles or foreign objects.

Figure 3 illustrates a simulated critical scenario in which a concrete fragment becomes lodged between the roller and the track. Such scenarios are employed to assess the proposed system's capability to detect potentially hazardous anomalies.

The system components communicate through Wi-Fi, utilizing ROS2 protocols for message exchange. MicroROS nodes operate on the microrobots, tasked with raw data acquisition, filtering, and publishing. At the central station, ROS2 nodes are employed for data collection, synchronization, and processing, as well as for generating regions of interest (ROIs) and conducting preliminary defect detection, akin to industrial methodologies reported in [9].

Fig. 3. Detail capture: interaction between the roller and a piece of concrete caught in the track

The application development process employed a methodology based on Return on Investment (ROI) inspection, which adhered to the following procedural steps:
Step 1 - Identification of Regions of Interest
The regions of interest pertain to essential components of the undercarriage, including the support rollers, drive wheel, idler wheel, and segments of the track that are in contact with the ground or wheels. Based on the geometric model of the machine, these regions of interest can be delineated as projection areas within images (for video data) or as volumes in three-dimensional space (for LiDAR data).
Step 2 - Classification of Targeted Defects
The system is designed to detect the following categories of defects: longitudinal or transverse cracks on rollers and wheels, imperfections on the track surface, substantial abrasive wear on the roller flanks, the presence of foreign objects between the running elements, and indications of corrosion or material flaking.
Step 3 - Data Processing Flow
The data processing flow encompasses several stages: data acquisition; preprocessing, which includes noise reduction, illumination correction, and geometric calibration; segmentation of the region of interest (ROI); feature extraction; defect detection utilizing classifiers such as neural networks; and the reporting and formulation of maintenance recommendations.
Experimental Setup and Test Scenarios: To validate the concept, an experiment was conducted involving a track section equipped with a rubber track and green-painted metal rollers, simulating a component of a construction machine designed for heavy-duty operations. The details of this assembly are depicted in Figure 1.
In addition to the track, fragments of brick and concrete were strategically placed to simulate the presence of foreign objects on the running surface. Initially, the microrobots are positioned at a distance and subsequently move either autonomously or through teleoperation. The platform, equipped with omnidirectional wheels, approaches the edge of the track to conduct visual scans of the lower area. Concurrently, the STEM robot, which is equipped with LiDAR, traverses alongside the machine to map and identify priority Regions of Interest (ROIs) (Figure 2).
Figure 3 presents a detailed depiction captured by one of the robots, illustrating the interaction between a guide roller and a fragment of concrete lodged between the wheel and the track. This scenario poses a risk of damage if not promptly addressed.

3. Preliminary results and discussions

Preliminary evaluations have demonstrated that the microrobots are capable of accessing regions that are challenging for operators to observe directly. The omnidirectional wheeled platform

facilitates precise repositioning necessary for focusing on the region of interest (ROI), and the integration of images with LiDAR technology offers a more comprehensive depiction of the environment.
The images acquired provide detailed insights into the surfaces of the roller and track, revealing significant scratches and irregularities attributable to wear. In instances involving foreign objects, the system identifies abnormal interactions between the wheels and concrete fragments, which, if not promptly addressed, may result in damage. Additionally, limitations were noted concerning lighting conditions, potential Wi-Fi signal interference, and the necessity for precise calibration of LiDAR data integration with the images.

4. Conclusions

The paper delineates a system architecture for the robotic inspection of heavy construction machinery, utilizing a swarm of microrobots equipped with video cameras and LiDAR technology. By employing Regions of Interest (ROIs) defined on critical components of the undercarriage, the system facilitates detailed monitoring of areas susceptible to wear, early detection of defects, and identification of foreign objects in the operational area, thereby generating valuable data for predictive maintenance. Future research directions include the full integration of a real-time processing chain, the development and validation of deep learning models for automatic defect classification, the expansion of the swarm with additional robots (e.g., mini-drones), and the creation of standardized inspection and reporting protocols.

Acknowledgments

We express our gratitude for the opportunity to develop this application within the UTCB practice facility, established as part of the CNFIS-FDI-2025-F-0289 project—RECIPA: Robotics and Ecology in Construction, Innovation and Applied Practice.

References

[1] Randall, R. B. *Vibration-based Condition Monitoring: Industrial, Aerospace and Automotive Applications*. Wiley, 2011. Print ISBN:9780470747858, online ISBN:9780470977668. DOI:10.1002/9780470977668.
[2] Wang, Jinjiang, Peilun Fu, and Robert X. Gao. “Machine vision intelligence for product defect inspection based on deep learning and Hough transform.” *Journal of Manufacturing Systems* 51 (2019): 52-60. https://doi.org/10.1016/j.jmsy.2019.03.002.
[3] Özel, M. A., and M. Y. Gül. “Ensuring product detection and product counting on the assembly line using deep learning (YOLOv11).” *International Journal of Multidisciplinary Studies and Innovative Technologies IJMSIT* 9, no. 1 (2025): 53–58. DOI: 10.36287/ijmsit.9.1.8.
[4] LeCun, Y., Y. Bengio, and G. Hinton. “Deep learning.” *Nature* 521 (2015): 436–444. https://doi.org/10.1038/nature14539.
[5] Brambilla, M., E. Ferrante, M. Birattari, and M. Dorigo. “Swarm robotics: a review from the swarm engineering perspective.” *Swarm Intelligence* 7, no. 1 (2013): 1–41. https://doi.org/10.1007/s11721-012-0075-2.
[6] Şahin, E. “Swarm robotics: From sources of inspiration to domains of application.” Paper presented at the SAB 2004 International Workshop, Santa Monica, CA, USA, July 17, 2004. In Şahin, E., and W.M. Spears. (eds.) *Swarm Robotics*. SR 2004. *Lecture Notes in Computer Science* 3342 (2005): 10–20. https://doi.org/10.1007/978-3-540-30552-1_2.
[7] Nooralishahi, P., C. Ibarra-Castanedo, S. Deane, F. López, S. Pant, M. Genest, N.P. Avdelidis, and X.P.V. Maldague. “Drone-Based Non-Destructive Inspection of Industrial Sites: A Review and Case Studies.” *Drones* 5, no. 4 (2021): 106. https://doi.org/10.3390/drones5040106.
[8] Ambati, Prasanthi, K. M. Suman Raj, and A. Joshuva. “A review on pipeline inspection robot.” Paper presented at the 3rd International Conference on Frontiers in Automobile and Mechanical Engineering (FAME 2020), Chennai, India, August 7–9, 2020. *AIP Conf. Proc.* 2311 (2020): 060002. https://doi.org/10.1063/5.0033998.
[9] Bonci, A., F. Gaudeni, M. C. Giannini, and S. Longhi. “Robot Operating System 2 (ROS2)-Based Frameworks for Increasing Robot Autonomy: A Survey.” *Applied Sciences* 13, no. 23 (2023): 12796. https://doi.org/10.3390/app132312796.

ISSN 1454 - 8003
Proceedings of 2025 International Conference on Hydraulics and Pneumatics - HERVEX
November 19-21, Băile Govora, Romania

CONSIDERATIONS REGARDING HYDRAULIC PUMPS WEAR AND MODERN MANUFACTURING AND REMANUFACTURING TECHNIQUES

Cătălin DUMITRESCU[1], Cătălin VIȚELARU[2], Liliana DUMITRESCU[1], Ștefan-Mihai ȘEFU[1], Radu-Iulian RĂDOI[1], Adriana-Mariana BORȘ[1], Magdalena NEACȘU[1], Stefano-Andrea MANTOVANI[3]

[1] National Institute of Research & Development for Optoelectronics – Subsidiary Hydraulics and Pneumatics Research Institute (INOE 2000 – IHP)

[2] National Institute of Research & Development for Optoelectronics INOE 2000

[3] National Institute of Research & Development for Machines and Installations Designed to Agriculture and Food Industry – INMA

Abstract: *The wear of hydrostatic pumps negatively influences their operation and results in a decrease in volumetric efficiency, a reduction in service life and, ultimately, pump failure. The occurrence of the phenomenon of boundary or dry friction, at the contact between different component parts, extreme operating conditions, the lack of a lubricating film or fluid contamination increase pump wear. Currently, in order to improve the contact behaviour and increase the service life of a pump, new techniques and methods are used to treat the surfaces of the parts that intervene either in the manufacturing phase or in the maintenance phase.*
These techniques refer to the use of superior materials, the implementation of surface treatments (thin layer coatings), the use of machining processes (surface texturing) or 3D printing, and most of the time they are combined with each other to reduce the effect of wear.

Keywords: *Wear, hydrostatic pumps, metal coatings, thin layers*

1. General considerations regarding hydraulic pumps

Hydraulic pumps convert the mechanical energy generated by the drive motor into hydraulic energy. The transmission of energy from the motor to the pump is usually carried out through a flexible coupling that compensates for misalignment; in some cases, to make the drive speeds of the two components compatible, a gear or reduction unit must be interposed, especially in the case of endothermic engines. With a few exceptions, the standard rotational speeds for three-phase electric motors are compatible with direct connection to the pump; the speed is usually 1400 or 2800 rpm, but if the system is equipped with an electronic device known as an "inverter", the number of revolutions can be adjusted from the minimum limit (approx. 500 rpm) to the maximum. In the case of thermal engines, the drive speed is maintained within the same limits.
The pump receives energy to transfer a liquid; thus, a flow rate is generated at the pump outlet, which can be measured as a given volume passing through it per unit of time. In contrast, pressure results from the interaction of the pumped fluid with an obstacle, such as a reduction in the flow section, the piston of a cylinder or the blades of an engine. Pumps do not generate pressure, but are designed to support the pressure needed by the system. Hydraulic pumps, in general applications, are actually used either to move a fluid that encounters low resistance (e.g. systems that transfer water or similar fluids), or in systems where the fluid transmits energy, through its flow and pressure.
The most common types of pumps [1] are shown in Figure 1.

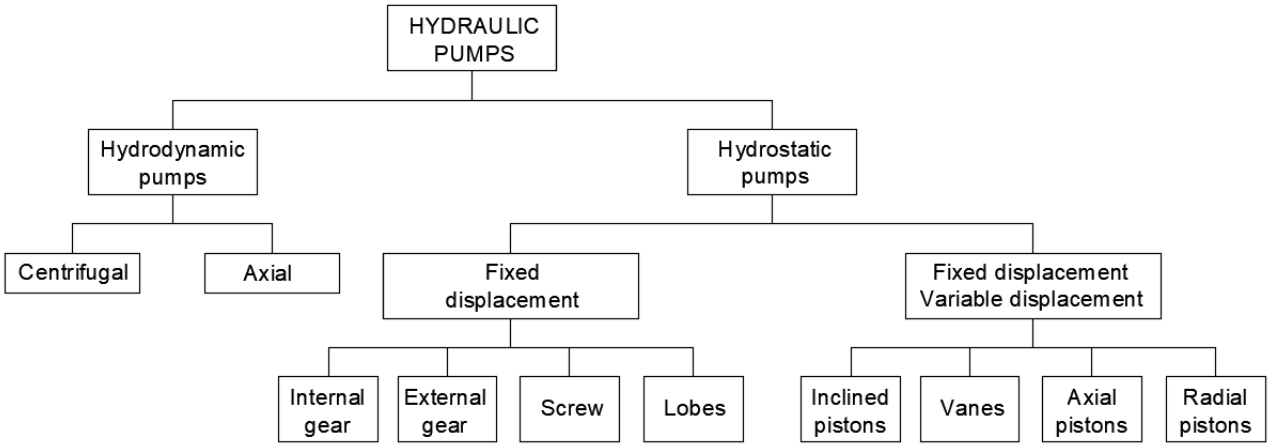

Fig. 1. The main types of hydraulic pumps

The physical principle falls under **hydrodynamics** in the first case, and **hydrostatics** in the second (Figure 1). Hydrodynamic pumps - usually called "rotodynamik pumps" - suck a liquid at rest and simply move it to another point; hydrostatic pumps - or "displacement pumps, volumetric pumps" - also suck a liquid from the tank, but move it to the drive system, characterized by high pressure. In this case the fluid is an intermediary through which energy is transferred, by means of the pressure that is installed in the system.
A major difference between the two types of pumps refers to the pressure level; if in hydrodynamic pumps the pressure that is installed in the circuit is of the order of a few bars, sufficient to move the fluid from one place to another, common hydrostatic pumps can support pressures of the order of a few hundred bars, and certain types of pumps can reach pressures of the order of thousands of bars.
When designing hydrostatic pumps, there are 2 important issues: the mechanical strength of the components, so that they operate at the pressures with which the pump is compatible, and respectively the tightness of the chamber in which the pressure is generated at the pump level.
Typically, hydrostatic pumps are based on the sealing of a chamber that reduces its volume; in this chamber the pumping effect is generated, the working fluid being forced by the tightness of the chamber to move towards the hydraulic circuit and thus transfer the energy generated at the pump level. Typically, in the hydraulic actuator (linear or rotary hydraulic motor) we also encounter one (e.g. hydraulic cylinder) or more sealed chambers (e.g. hydraulic piston motor).
Paradoxically, the tightness of a working chamber, which is key to the functioning of hydraulic systems and is achieved through the smallest possible clearances between the parts in contact, has a negative influence when the fluid in the system contains impurities; these reach the sealing area, where the clearances between the parts are very tight, and can damage the sealing surfaces.

2. Types of wear that occur in hydraulic systems

The main cause of wear in hydraulic systems is the absence of lubricant in the area where solid parts are in contact. Under the effect of pressing force, the parts come into contact and **adhesive wear** occurs. When there is a lubricant film, but it is insufficient, a less severe wear occurs, called **fatigue wear**. If the lubricant film loses some of its properties, **corrosive wear** can occur, and if the contact area of the parts comes into contact with oxygen, it evolves into **oxidative wear**.
If the lubricant contains hard particles that interpose between the two contacting surfaces, and the size of these particles is comparable to that of the distance between the parts, they produce **abrasive wear**. If the hard particles flow at a significant velocity and interact with the surfaces, they produce **erosive wear**.
Another type of wear, which occurs between parts with very small relative displacement, which can be from a few micrometers to a few millimeters, is **fretting wear**. In this case, under the action of

the load that brings the 2 parts into contact, local joining and detachment of the parts occur alternately, resulting in particles that subsequently lead to other types of wear. Depending on the contact pressure and the temperature in the interaction area, we can also have **impact wear** or **melting wear**.
Cavitation in hydraulic systems is an undesirable phenomenon that, among other inconveniences, causes **cavitational wear**; the result of operating in a cavitational mode is the detachment of particles from parts, which cause abrasive, erosive wear, etc. downstream.

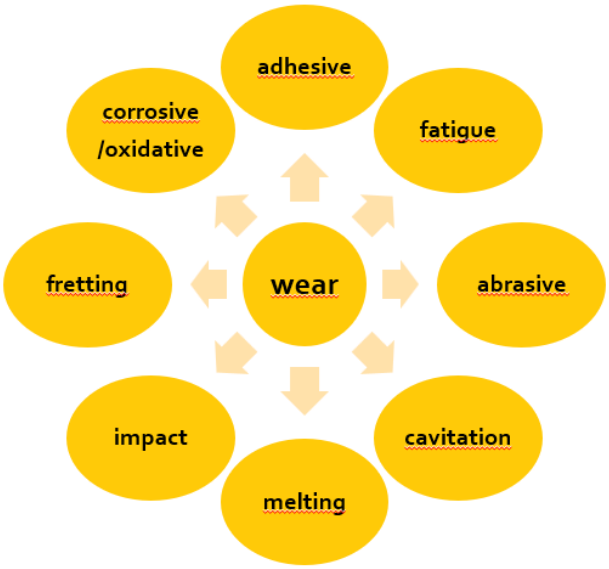

Fig. 2. Main types of wear in hydraulic systems

Figure 2 shows the main types of wear in hydraulic systems. Below are some considerations related to the wear of the most common types of pumps.

3. Wear in axial piston pumps

This type of pump is the most complex and therefore the most complex situations regarding wear and its effects can be encountered here. Wear in axial piston hydraulic pumps is caused by friction between components such as piston/cylinder, piston shoe/swash plate and cylinder block/valve (distribution) plate pairs, and is accelerated by factors such as abrasive contaminants in the hydraulic fluid, high operating pressure and poor lubrication. This wear can lead to decreased volumetric efficiency, reduced service life and, ultimately, pump failure. Reducing wear involves using appropriate materials, maintaining fluid cleanliness and ensuring adequate lubrication [2, 3].
The main wear mechanism is three-component abrasive wear between the piston block and the valve plate, due to the removal of coarse carbides from the valve plate surface. The removed carbides and debris contaminate the hydraulic fluid and cause significant wear on other components that are not designed to withstand such harsh abrasive particles.

3.1. Causes of wear

• Friction: The main source of wear is friction between moving parts in the absence of a consistent film of lubricating fluid, especially the piston-cylinder pair and the piston shoe/swash plate pair.
• Hydraulic fluid contamination: Abrasive particles such as sand or dirt in the hydraulic oil are a major cause of wear, as they can scratch surfaces and cause damage.
• High pressure: Excessive discharge pressure can lead to high contact pressures, which increases the wear of the piston/cylinder pair.
• Poor lubrication: Degraded oil does not create the necessary film between the surfaces; friction, corrosion, oxidation, etc. occur.

3.2. How wear and tear manifests itself

• Reduced efficiency: As a result of component wear, clearances between the contacting parts increase, increasing internal losses; therefore, the pump will deliver a reduced flow rate.
• Increased wear: The wear of a part with the detachment of particles can lead to accelerated wear of the part with which it is in contact, creating a cascading effect.
• Component failure: Severe wear can cause parts to jam or fail completely.
In axial piston pumps, hydraulic fluid fills the pump housing and acts as a lubricant for some components. The piston/shoe and shoe/swash plate contacts are better lubricated by a hole in the pistons and pads that allows a small amount of pressurized fluid to escape from the cylinder block and reach the pad/plate contact area.
Although these pumps have a high power density and relatively high efficiency, they can become unusable after a few thousand hours due to wear of their components, compared to a normal lifespan of 10...20,000 hours.

4. Wear in vane pumps

In high-pressure vane pumps, whether fixed or variable flow, wear occurs on the internal surface of the housing (stator ring), at the radial grooves of the rotor, as well as on the side and tip of the vanes, as a consequence of the sliding contact between the rotor, stator ring and the vanes (see Figure 3).

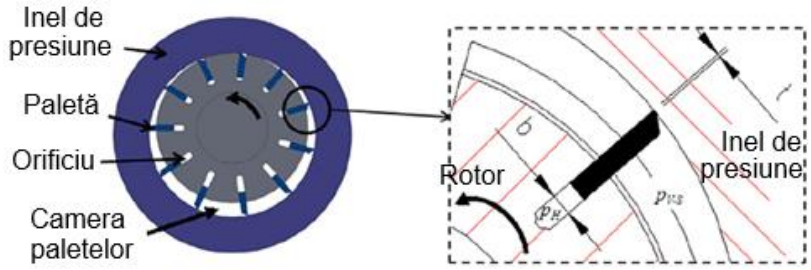

Fig. 3. Vane pump [4]

To achieve minimal wear, it is desirable to have an appropriate selection of materials and a design of the stator and blades taking into account the relative movement existing between them and the type of lubrication that exists in that area.
Thus, wear reduction can be achieved by improving the performance of the surface material if there is a boundary lubrication regime or by modifying the surface geometry in the case of a hydrodynamic lubrication regime.
As with other types of pumps, the parts in motion (impeller, vanes) wear out the most and are available in the form of repair (replacement) kits. Housing wear, which is slower but also more expensive, most often requires pump replacement, unless there is adequate remanufacturing technology.

5. Wear in gear pumps

The causes and effects of wear presented above (e.g. in axial piston pumps) are largely similar for all pump types; the most important difference is in the parts of the pump structure that wear out.
For **gear pumps**, the main wear occurs as a result of the pinion-housing and pinion-bearing block contact [5]; since the maximum pressure that develops in the pump housing is in the discharge area, a radial force occurs simultaneously and is transmitted through the driven pinion to the suction area of the housing. Since the pinion is in relative motion with respect to the housing, wear of the housing, which is most often made of aluminium alloy (duralumin, etc.), occurs in the contact area. Less wear is also found in the discharge area of the housing, as well as on the lateral faces of the bearing blocks. The side blocks can be replaced, their reconditioning not being economically

profitable. On the other hand, the wear of the casing most often requires the replacement of the pump; this is not possible in all situations, and when there is the option of remanufacturing the casing, this solution is preferable.

Fig. 4. Gear pump housing with wear evident in the suction and discharge area

In the case where the working fluid is heavily contaminated, wear occurs much faster than in the case of normal operation, and in this case it can also occur in the discharge area of the pump. The same phenomenon occurs in the case of long-term use, even if the conditions regarding oil quality, working pressure, etc. are met. Depending on the damage to the housing due to wear, the pump can be reconditioned or replaced.

6. Methods for increasing the service life and remanufacturing of hydraulic pumps

Recently, various methods have emerged to improve pump reliability, including the use of superior materials, surface treatments [6], or machining processes that improve contact behavior [7, 8]. These methods can be used in the initial design phase or for component reconditioning when economically justified. The category of surface treatments can include the deposition of thin layers, which is done in order to increase the resistance of the treated surfaces; the deposited film can have thicknesses from a few micrometers to a few tenths of a millimeter. If it is desired to compensate for wear occurring during operation, a previous deposition of a thicker layer can be made, over which the final film will be deposited.
The use of thin layers in hydraulics is in its infancy, this technique being used to date in other fields; however, it is starting to be found in this field as well, in response to requests for increasing the operating life or for remanufacturing some components [9] in order to reduce material consumption. The main methods of depositing thin layers:

a. Physical Vapour Deposition (PVD): thermal evaporation, sputtering, and vacuum ion plating.

b. Chemical Vapour Deposition (CVD): electrochemical deposition, chemical reduction, chemical vapour deposition, anodization

Depending on the state of aggregation of the deposition material and the physical and chemical processes of generation, transport and adhesion of the layers to the base material, there are different layer deposition technologies that use one or more methods.
Modern technologies used to deposit thin layers on metal surfaces are mainly: cathodic arc, magnetron sputtering (or DC-direct current)/ RF-radio frequency).
One of the more recent developments in magnetron sputtering is high-power pulsed sputtering, known as **High Power Impulse Magnetron Sputtering (HiPIMS)**, and is superior to DC magnetron sputtering techniques.

Another relevant technology for depositing starts is the one called **DLC (Diamond-Like Carbon) coatings** which consists of a PVD/CVD coating with exceptional hardness and lubrication properties.
To create extremely thin and uniform layers on surfaces, **ALD (Atomic Layer Deposition)** can be used, which takes place at the atomic level and is extremely precise.
Some of these processes are used in applications where the requirements are close to those in hydraulics; for example, the DLC process is currently adopted by most automotive manufacturers to create the working surface in engines, instead of the classic cylinder liners made of steel. In this case, the requirements are close to those of axial piston pumps: reduced roughness, resistance over time under friction conditions with a lubricant film, etc. The thickness of the deposited layer has values of 0.1...0.2 mm in this case.

7. Conclusions

Knowledge of the operation of hydraulic devices at the level of contact between the main parts, especially pumps, is essential for understanding the wear mechanism and, consequently, for obtaining the longest possible operating life for pumps, which represent the most important components of a hydraulic system. On the other hand, currently there are techniques that allow the remanufacturing of component parts whose failure, in the past, would have led to the complete replacement of the respective hydraulic device. The thin layer technique is one of these, which ensures the improvement of surface quality from the initial manufacturing phase or the reconditioning in the event of wear within certain limits. Even if this technique is still in its infancy in hydraulics, it is encountered in other fields, where it responds to similar requirements in terms of roughness, wear resistance under oil lubrication conditions, low friction coefficient, etc.

Acknowledgments

This work was supported by a grant of the Ministry of Research, Innovation and Digitization, CCCDI - UEFISCDI, project number PN-IV-P7-7.1-PTE-2024-0618, within PNCDI IV.

References

[1] Assofluid. *Hydraulics in Industrial and Mobile Applications*. Brugherio (Milano), Grafiche Parole Nouve s.r.l. Publishing House, 2007.
[2] Schuhler, Guillaume, A. Jourani, Salima Bouvier, and J.-M. Perrochat. “Multi technical analysis of wear mechanisms in axial piston pumps.” *IOP Conf. Series: Journal of Physics: Conf. Series* 843 (2017): 012077. doi :10.1088/1742-6596/843/1/012077.
[3] Liang, Yingna, Wei Wang, Miaomiao Shen, Zhepeng Zhang, Hao Xing, Cunyuan Wang, and Dianrong Gao. “Study on friction and wear characteristics of axial piston pump valve plate pairs modified with different surface energies.” *Coatings* 14, no. 3 (2024): 328. https://doi.org/10.3390/coatings14030328.
[4] Mucchi, Emiliano, Alessandro Agazzi, Gianluca D'Elia, and Giorgio Dalpiaz. “On the wear and lubrication regime in variable displacement vane pumps.” *Wear* 306, no. 1-2 (2013): 36–46. http://dx.doi.org/10.1016/j.wear.2013.06.025.
[5] Novak, Nejc, Ana Trajkovski, Marko Polajnar, Mitjan Kalin, and Franc Majdič. “Wear of hydraulic pump with real particles and medium test dust.” *Wear* 532-533 (2023): 205101. https://doi.org/10.1016/j.wear.2023.205101.
[6] Schuhler, Guillaume, A. Jourani, Salima Bouvier, and J.-M. Perrochat. “Efficacy of coatings and thermochemical treatments to improve wear resistance of axial piston pumps.” *Tribology International* 126 (2018): 376–385. https://doi.org/10.1016/j.triboint.2018.05.007.
[7] Schneider, Johannes, Daniel Braun, and Christian Greiner. “Laser Textured Surfaces for Mixed Lubrication: Influence of Aspect Ratio, Textured Area and Dimple Arrangement.” *Lubricants* 5, no. 3 (2017): 32. doi:10.3390/lubricants5030032.
[8] Antoszewski, Bogdan, and Piotr Kurp. “Effect of surface texture on the sliding pair lubrication efficiency.” *Lubricants* 10, no. 5 (2022): 80. https://doi.org/10.3390/lubricants10050080.
[9] Wang, Maolu, Xinjian Wang, Junyan Liu, Jiacheng Wei, Zhangwen Shen, and Yang Wang. “3-Dimensional ink printing of friction-reducing surface textures from copper nanoparticles.” *Surface & Coatings Technology* 364 (2019): 57–62. https://doi.org/10.1016/j.surfcoat.2019.02.080.

ISSN 1454 - 8003
Proceedings of 2025 International Conference on Hydraulics and Pneumatics - HERVEX
November 19-21, Băile Govora, Romania

VIBRATION BEHAVIOR IN HYDRAULIC DRIVE SYSTEMS: AN EXPERIMENTAL STUDY OF RIGID AND FLEXIBLE PIPE DYNAMICS

Carmen-Anca SAFTA[1], Nicolaie ORĂȘANU[1], Marian BLEJAN[2]

[1] National Institute of Science and Technology POLITEHNICA of Bucharest,

[2] Research Institute for Hydraulics and Pneumatics (INOE 2000 – IHP) Bucharest ROMANIA,

carmen.safta@upb.ro, nicolae.orasanu@upb.ro, blejan.ihp@fluidas.ro

Abstract: *The specialized literature in the field of hydraulic power drives reserves a generous space for the characteristic vibrations of these systems regardless of the application served by the hydraulic drives system. The present paper aims to make a comparative discussion between the vibrations measured on rigid pipes and those measured on flexible pipes of hydraulic drive systems. The vibration spectrum is highlighted over a range of 5000 Hz for rigid pipes and up to 2000 Hz for flexible pipes. The vibration spectrum is also accompanied by cepstrum representation with the help of which the defects in the analysed system can be highlighted.*

Keywords: *Cepstrum, hydraulic power drive, measurements, spectrum, vibration*

1. Introduction

A large debate in the scientifical and industrial community is the subject of vibrations in hydraulic systems [1-3]. Every component of a hydraulic drive system is a source of vibration and has its proper frequency. During operation the hydraulic power drive systems develop a wide frequency spectrum, from low frequencies (infrasonic frequencies [1]) to high frequencies (more than 1 kHz). In the technical literature is highlighted the influence of mechanical vibration on pressure pulsation spectrum of hydraulic systems, but there are some other papers with good practice examples of vibrations induced by the pulsation of pressure in the hydraulic systems known as flow-induced vibrations [1,2]. The sources of pressure fluctuations in the hydraulic system are: (a) transient states; (b) movement of the cinematic mechanism of positive displacements pumps, (c) mechanical vibrations of the mechanical parts in rotation (as gear box, bearings, rotors) and the waves in long hydraulic lines [4-6].
In the topic of vibrations in hydraulic power drive systems theoretical analysis, experimental and numerical simulation research were conducted to explain the vibration mechanism as Fluid-Structure Interaction (FSI) [1,3], to confirm the coincidence between pressure pulsation spectrum and vibration spectrum of hydraulic components [1,2], to minimize the impact of external vibrations on hydraulic valves [1,4], to demonstrate using Discrete Fourier Transformation (DFT) that non-synchronous vibration components dominate the dynamic behaviour of hydraulic system and have a significantly variation with flow rate [1,5], to find solutions to control and reduce vibrations in the hydraulic systems [1,3,4,6]. Also, it is well known that vibrations can cause operational instability of hydraulic components, reduce durability and seal failures, generate noise emissions in low-frequency range which affect human health [1-6].
This is the reason that we put a legitim question: what is the difference between vibration spectrum of a rigid pipe vs a flexible pipe in a hydraulic power drive system. The purpose of the work is to compare the spectrum of vibrations measured on rigid pipes with those measured on flexible pipes in hydraulic drive installations. With the measured vibrations, spectral representation is made to highlight the harmonic sidebands. The periodicities of harmonic sidebands are transformed into quefrency peaks obtained with cepstrum (the result of applying an inverse Fourier transform to the log magnitude spectrum) [7,8]. Usually, harmonic sidebands highlight certain faults in mechanical systems with rotating parts. In the case of hydraulic drive systems, the harmonic sidebands do not indicate necessarily a fault but seem to be a characteristic behavior of these systems.

2. Experimental setup

Two test stands were considered.
The shock absorber test stand, Figure 1, has the entire hydraulic drive system made with rigid pipes. The stand includes an electrohydraulic servomechanism supplied by a gear pump driven by an asynchronous electric motor with a speed of 1500 rpm.
The hydraulic equipment test stand, Figure 2, has flexible pipes in the system. The stand is intended for testing various types of hydraulic devices and equipment. Depending on the equipment being tested, different hydraulic circuits can be created. In this case, an axial piston pump and a swash plate were used and the load in the hydraulic circuit was created with a throttle valve.

Fig. 1. Shock absorbers test stand with rigid pipes

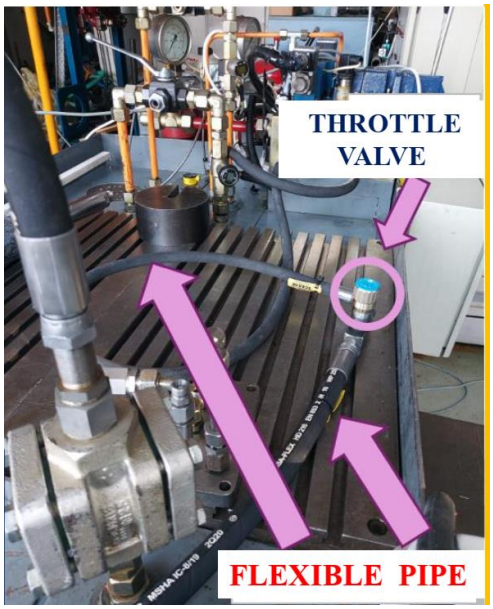

Fig. 2. Hydraulic equipment test stand having flexible pipes

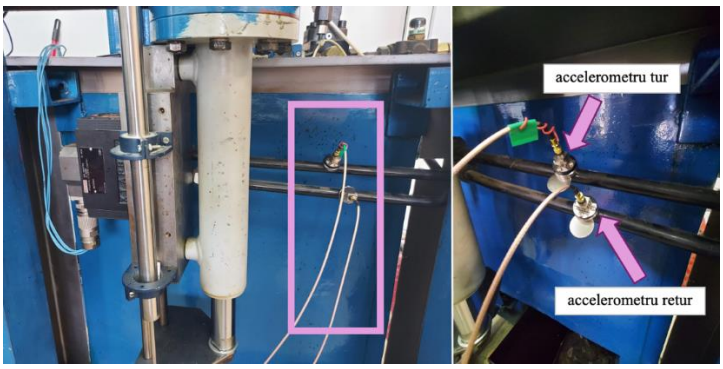

Fig. 3. Mounting accelerometers on the supply and return pipes (rigid pipes)

Fig. 4. Mounting accelerometers on the supply and return pipes (flexible pipes)

In the experiments, two CCLD piezoelectric accelerometers, type B&K 4507-B-001 with TEDS, sensitivity 10 mV/g, with a dynamic frequency range of 0.1 ÷ 6000 Hz, with operating temperatures

$(-54 \div 121)℃$, which were fixed on the pipes, were used. Acquisition rate was 50,000data/s (50 kHz).
The two accelerometers were mounted on the supply and return pipes. Thus, in the rigid pipe stand, an accelerometer was mounted on the inlet pipe into the actuator, respectively on the outlet pipe from the actuator, Figure 3. In the flexible pipe stand, the accelerometers were mounted on the upstream and downstream pipe of the throttle valve, Figure 4.
The accelerometers were connected to a computerized data acquisition system, the measurement chain consisting of:

- ❑ accelerometers,
- ❑ an NI-DAQ 9233 acquisition board (National Instruments) and
- ❑ specialized software for signal acquisition and processing dBFA Suite 4.8.1, developed by 01dB-METRAVIB (Areva Group).

The measurements were made for different operating conditions. Thus, for the stand with rigid pipes, the measurements were made for: (i) zero flow ($Q = 0$) when the electro-hydraulic servovalve has no control signal; (ii) flow $Q \neq 0$ for control the servovalve with a sinusoidal control signal with 1 Hz frequency; (iii) flow $Q \neq 0$ for control the servovalve with a sinusoidal control signal with 2 Hz frequency. For the stand with flexible pipes, the measurements were made at pressures of (j) 50 bar; (jj) 70 bar.

3. Measurements and results

With the two accelerometers mounted perpendicular to the pipe walls, therefore perpendicular to the flow direction in the pipes, the accelerations were measured. The signals were filtered and integrated, determining the velocities, respectively the displacements. From a physical point of view, the displacements are displacements (deformations) in the radial direction of the pipe.
Figure 5 shows the displacement spectrum for the rigid supply and return pipes in the case of zero flow at the actuator, when the servovalve does not receive a command signal. The harmonic sidebands that form at different frequencies are observed on 2,000 Hz frequency range. The result was obtained using the subroutines of the dBFA Suite 4.8.1 program.

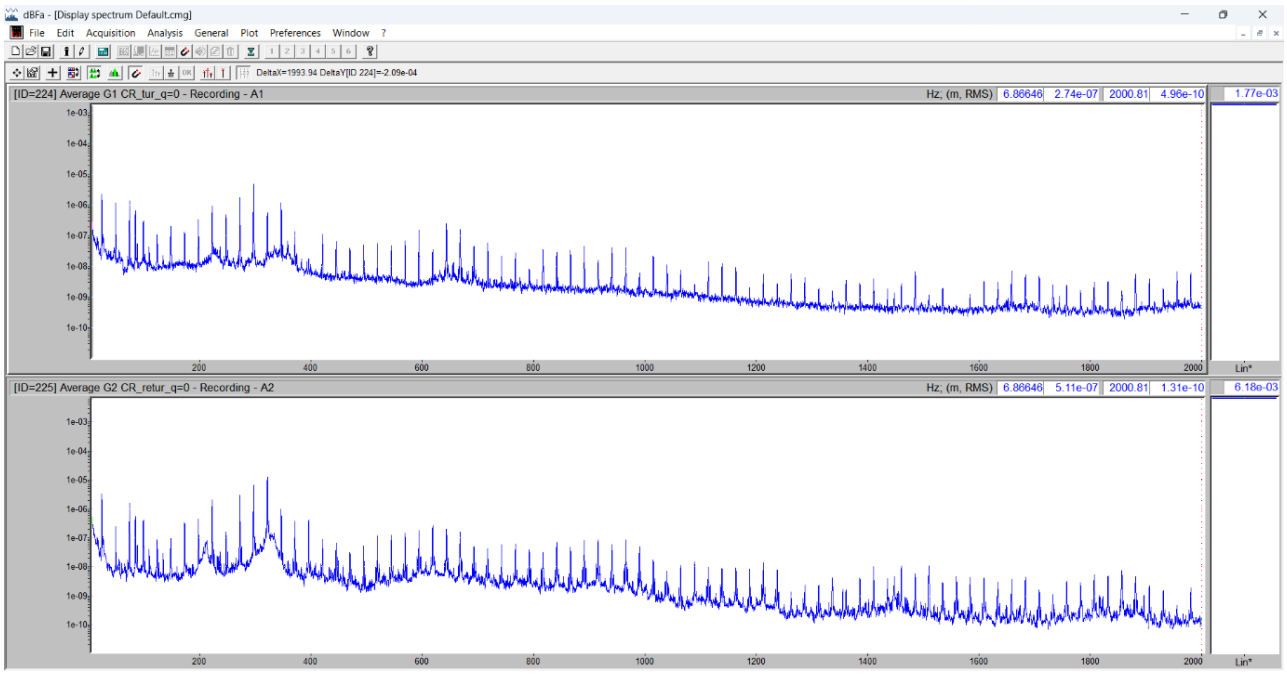

Fig. 5. Displacements spectrum and harmonics of the rigid supply and return pipes, $Q = 0$.

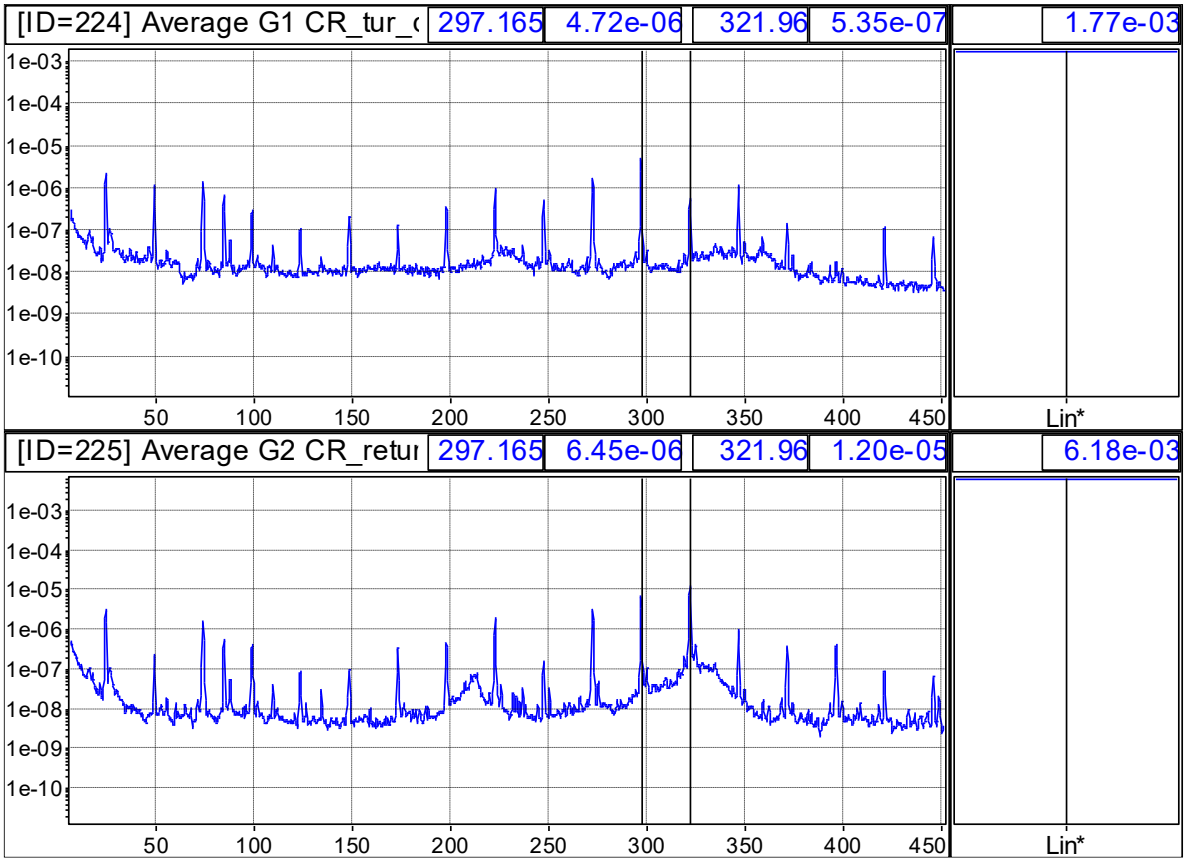

Fig. 6. Displacements spectrum of the rigid supply (top image) and return pipe, $Q = 0$, on first 450 Hz

Table 1: Displacement values for the first harmonics of the rigid pipes, supply and return, $Q = 0$

Harmonics	Frequency (Hz)	Rigid pipe radial displacement (μm)	
		Supply pipe	Return pipe
f_1	24.8	2,2	3,21
f_2	49.6	1,17	0,236
f_3	74,4	1,38	1,57
f_4	99,2	0,296	0,413
f_5	124	0,1	0,084
$f_{6\text{-}11}$	…	…	…
f_{12}	297,2	**4,72**	6,45
f_{13}	321,96	0,54	**12,0**

In Figure 6 the displacement spectrum is plotted on first 450 Hz from the frequency range plotted in Figure 5 and the harmonics of the fundamental frequency f_1 are given in Tabel 1 together with the radial displacements on the supply and return rigid pipes.
The fundamental frequency $f_1 = 24{,}8$ Hz is given on the electric motor of the gear pump used in the shock absorbers test stand. The maximum radial displacement of the supply pipe is on harmonics f_{12} and on return pipe on harmonics f_{13}. Note that the displacements on the return pipe are greater than the displacements on the supply pipe for the mentioned harmonics.
Figures 7 and 8 show the displacement spectrum for the rigid supply and return pipes over the first 450 Hz of the frequency range when the actuator is supplied with a flow rate Q≠0 for controlling the servovalve with a sinusoidal control signal with a frequency of 1 Hz (Figure 6) and in the case of a sinusoidal control signal with a frequency of 2 Hz (Figure 7).

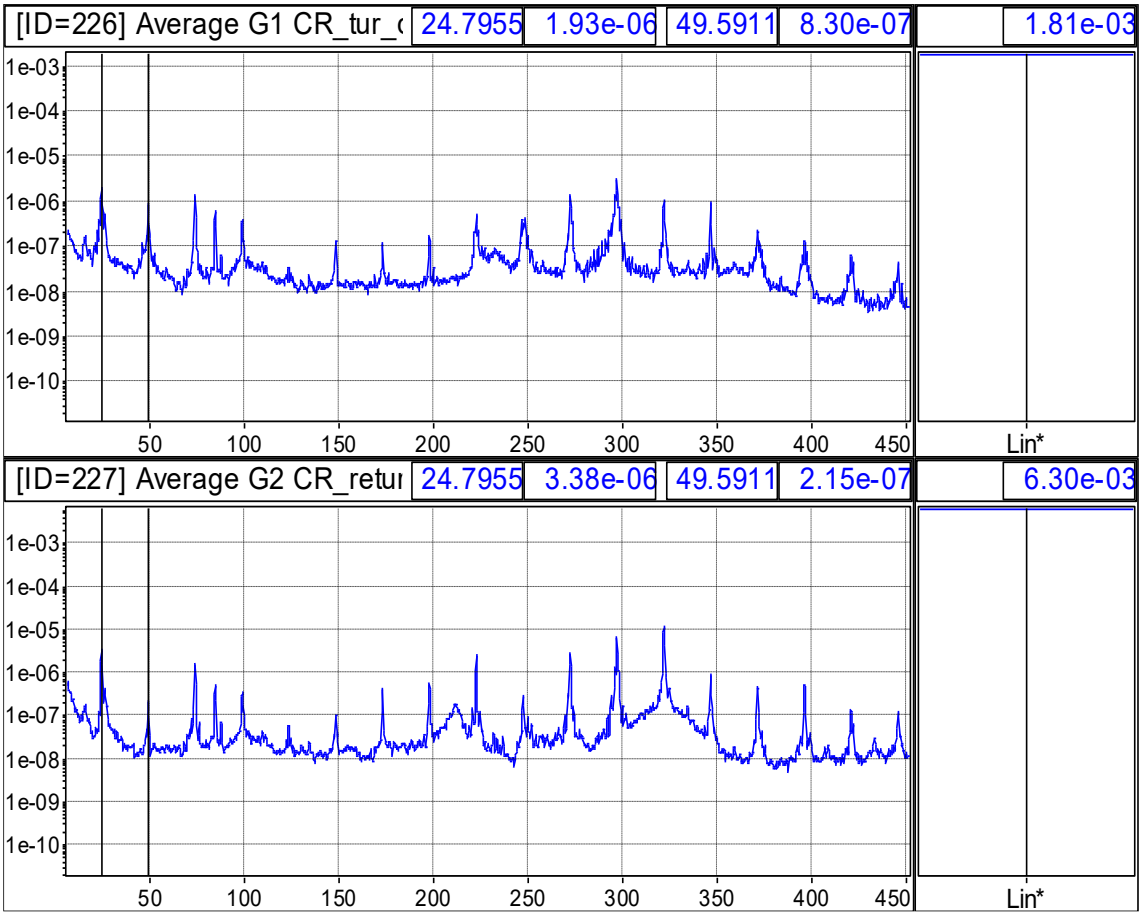

Fig. 7. Displacements spectrum on rigid pipes, supply and return, $Q \neq 0$ and 1 Hz frequency

Table 2: Displacement values of the first harmonics on rigid pipes, $Q \neq 0$ and 1 Hz frequency

Harmonics	Frequency (Hz)	Rigid pipe radial displacement (μm)	
		Supply pipe	Return pipe
f_1	24.8	1,93	3,38
f_2	49.6	0,83	0,215
f_3	74,4	1,4	1,55
f_4	99,2	0,39	0,32
f_5	124	0,03	0,06
$f_{6\text{-}11}$	…	…	…
f_{12}	297,2	**2,9**	6,5
f_{13}	321,96	0,99	**11,5**

The maximum radial displacement of the supply pipe is on harmonics f_{12} and on return pipe on harmonics f_{13}, and the displacements on the return pipe are greater than the displacements on the supply pipe for the mentioned harmonics.

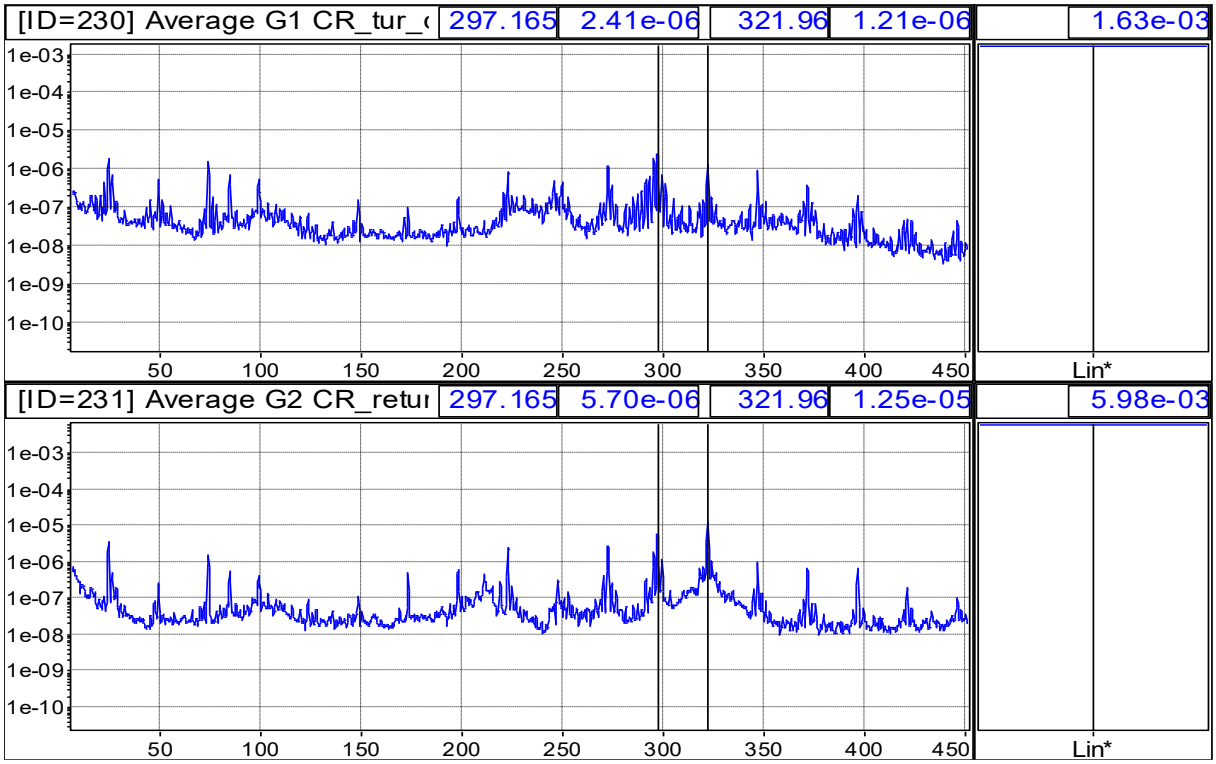

Fig. 8. Displacements spectrum of the rigid pipes, supply and return, $Q \neq 0$ and 2 Hz frequency

Table 3: Displacement values of the first harmonics on rigid pipes, $Q \neq 0$ and 1 Hz frequency

Harmonics	Frequency (Hz)	Rigid pipe radial displacement (μm)	
		Supply pipe	Return pipe
f_1	24.8	1,8	3,46
f_2	49.6	0,52	0,24
f_3	74,4	1,54	1,55
f_4	99,2	0,52	0,41
f_5	124	0,066	0,088
$f_{6\text{-}11}$	…	…	…
f_{12}	297,2	**2,4**	5,7
f_{13}	321,96	1,21	**12,5**

As in the previous case it is observed that the maximum radial displacement of the supply pipe is on harmonics f_{12} and on return pipe on harmonics f_{13}. Also, the displacements on the return pipe are greater than the displacements on the supply pipe.
If we return to Figure 5, we notice that the harmonic sidebands highlight not only the frequency of the electric motor driving the volumetric pump. There are also frequencies of other equipment within the driving scheme that we should identify in the spectrum. For example, the frequency of the electrohydraulic servovalve (if it is known from the catalog data).
Figure 9 is the cepstral representation of the spectrum in Figure 8.
In the cepstral representation, the abscissa (x-axis) is represented in seconds and is called the quefrency and the coordinate (y-axis) represents the amplitude of the cepstral components. From the physical point of view, the x-axis indicates the repetition period of the structures in the spectrum (Figure 8), and the y-axis indicates how strong the periodicity detected at a given quefrency is.

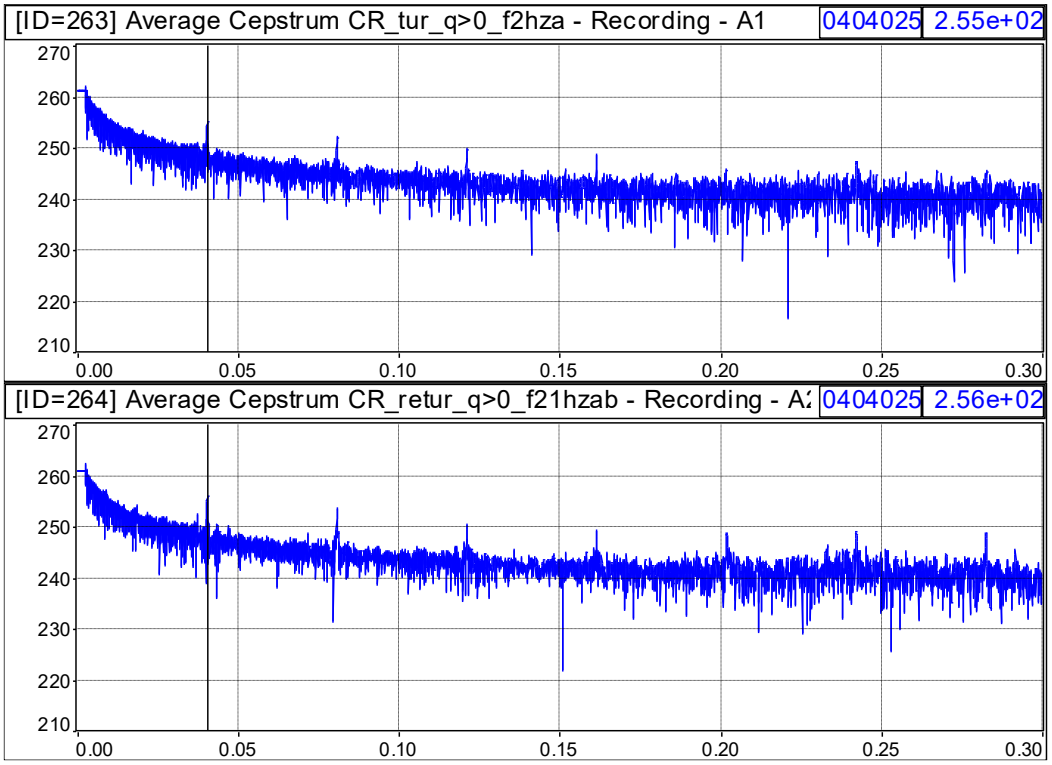

Fig. 9. Displacements cepstrum on rigid pipes, supply and return, $Q \neq 0$ and 2 Hz frequency

Figures 10 and 11 show the displacements spectrum for the installation with flexible pipes (Figure 2). The spectrum shows the frequencies and amplitudes (displacements along the pipe radial direction) in the case of a pressure of 70 bar (Figure 10) and 50 bar (Figure 11) in the adjustable throttle circuit.

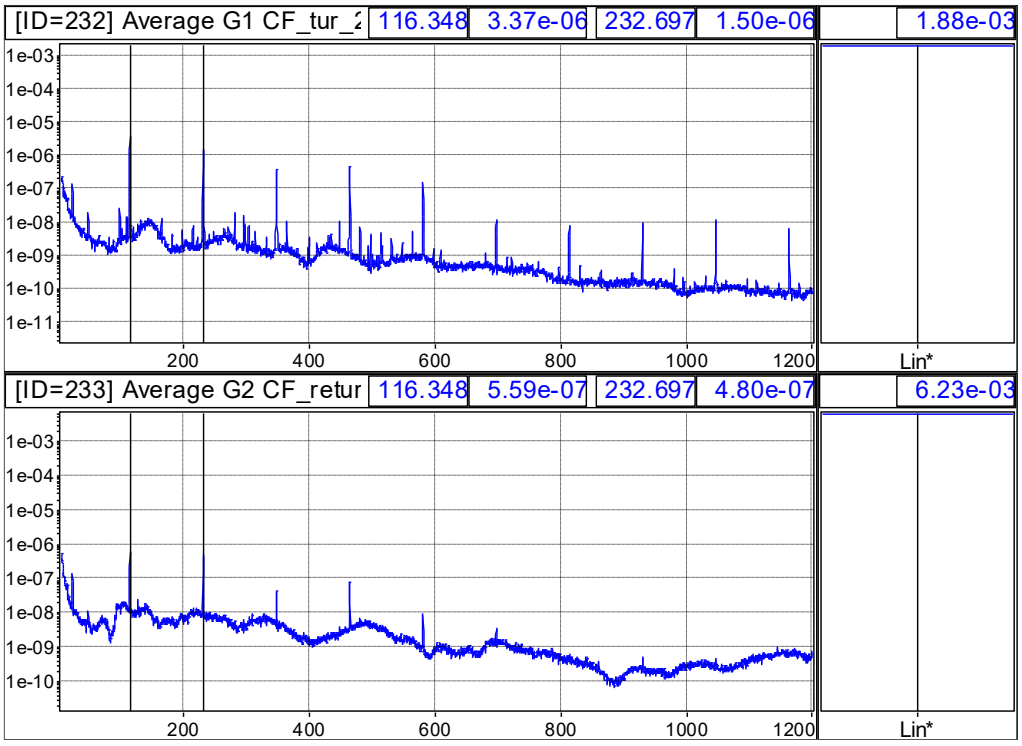

Fig. 10. Displacements spectrum on flexible pipes, supply and return, with 70 bar pressure

Table 4: Displacements values on flexible pipes, supply and return, with 70 bar pressure

Harmonics	Frequency (Hz)	Rigid pipe radial displacement (μm)	
		Supply pipe	Return pipe
f_1	116,35	3,37	0,56
f_2	232,7	1,5	0,48
f_3	349,05	0,36	0,46
f_4	465,8	0,46	0,08
f_5	582,1	0,15	0,009
f_6	698,5	0,012	0,003

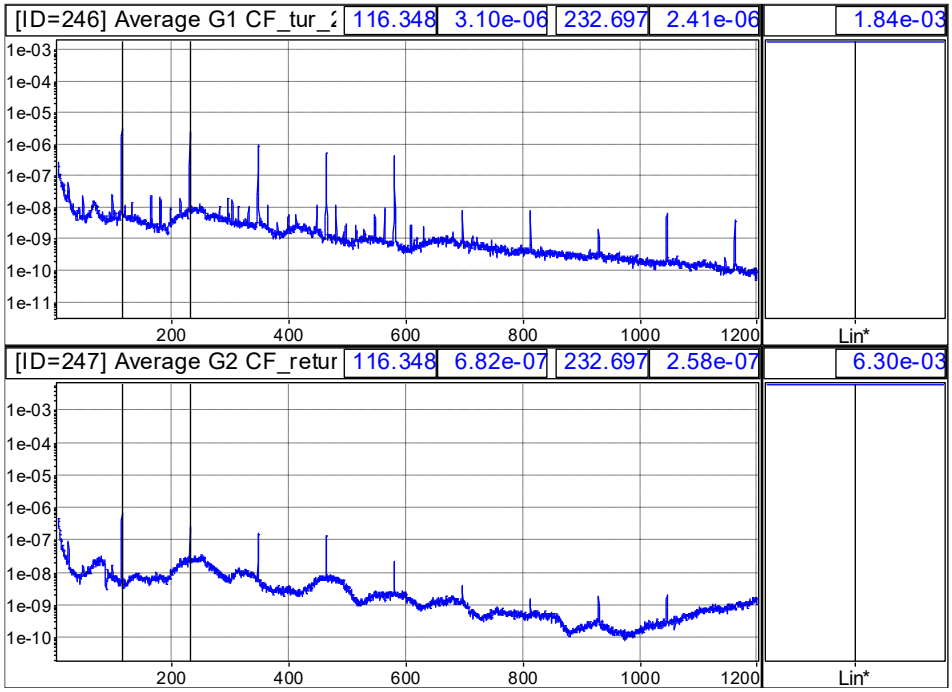

Fig. 11. Displacement spectrum on flexible pipes, supply and return, with 50 bar pressure

Table 5: Displacement values on flexible pipes, supply and return, with 50 bar pressure

Harmonics	Frequency (Hz)	Rigid pipe radial displacement (μm)	
		Supply pipe	Return pipe
f_1	116,35	3,10	0,67
f_2	232,7	2,41	0,26
f_3	349,05	0,95	0,16
f_4	465,01	0,53	0,14
f_5	581,4	0,42	0,002
f_6	697,7	0,004	0,004

In the displacement spectrum it is observed that the harmonics do not have those sidebands highlighted in the case of the hydraulic drive installation with rigid pipes, Figure 5. In the case of the displacement spectrum for flexible pipes, a damping of the vibrations is observed even if harmonics can be highlighted for the fundamental frequency $f_1 = 116.35$ Hz whose amplitude decreases with increasing frequency. Tables 4 and 5 show the values of the displacements at the harmonics in the spectrum characteristic of the hydraulic flow and return circuit in the two operating variants 70 bar and 50 bar. Also, the values of displacement are greater on the flexible supply pipe than on the return pipe.

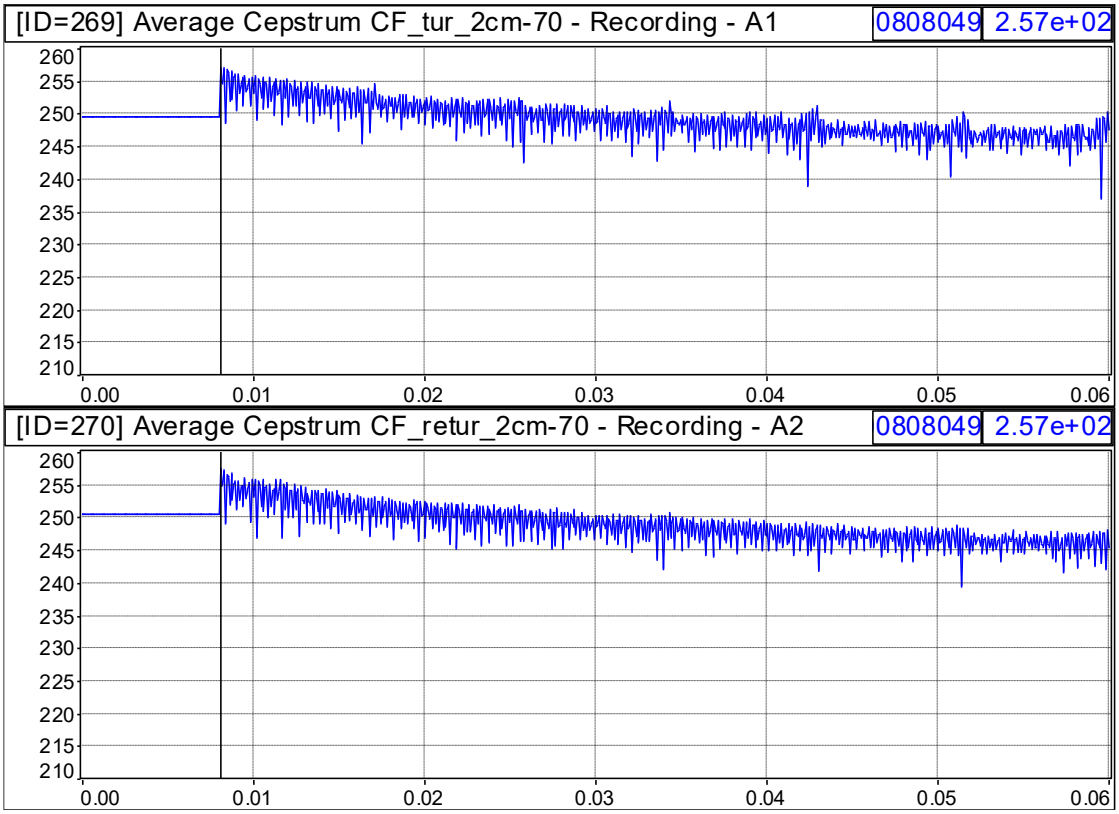

Fig. 12. Cepstrum on flexible pipes, supply and return, with 70 bar pressure

Figure 12 shows the cepstral displacement characteristic for the flexible flow and return pipe for the operation of the adjustable throttle at 70 bar. Even if in the spectral representation the frequency bands do not have the same consistency as the vibrations measured on the rigid pipes, the periodic character of the vibrations in the drive system can be observed from the cepstrum.

4. Conclusions

In this paper vibration measurements were performed on hydraulic drive systems incorporating two pipe configurations: rigid and flexible. The experimental setups differed substantially in the hydraulic structure system designed. One configuration consisted of a shock absorber test stand equipped with an electrohydraulic servomechanism, where measurements were taken on rigid pipes. The second configuration involved a test stand for various hydraulic components, where measurements were conducted on flexible pipes.

Accelerometers were mounted on the supply and return lines associated with specific devices or sections of the hydraulic circuit in each stand. In the rigid-pipe configuration, additional measurements were acquired under zero-flow conditions through the servomechanism, with the servovalve in an inactive state. The recorded vibration spectrum encompassed low-frequency components (<10 Hz) and extended to high-frequency ranges—up to 5000 Hz for rigid pipes and 2000 Hz for flexible pipes. Fundamental frequencies and harmonics up to the 10th order were identified in displacement spectrum.

Frequencies observed in flexible pipes exhibited significant damping relative to those in rigid pipes. The amplitude levels were extremely small (in both cases), in the order of micrometers, corresponding to radial displacements of pipe walls. Accelerometers were oriented perpendicular to the pipe axis and flow direction. The presence of numerous harmonics suggests a potential risk of resonance phenomena.

For flexible pipes, vibration amplitudes were consistently higher on supply lines compared to returned lines, a trend that persisted under elevated pressures (50 bar, 70 bar). The harmonic content on flexible return lines was lower than on supply lines.
Cepstral analysis reveals harmonic periodicity in rigid and flexible pipes; however, graphical cepstrum representations highlighted multiple harmonics and periodic components of modulated signals.
These findings provide a basis for developing methodologies to support predictive maintenance programs for hydraulic drive systems.

References

[1] Stosiak, M., and M. Karpenko. *Dynamis of Machines and Hydraulic systems. Mechanical Vibrations and pressure pulsations*. Part of *Synthesis Lectures on Mechanical Engineering (SLME)*. Springer, 2024. https://doi.org/10.1007/978-3-031-55525-1.
[2] Stosiak, M., M. Karpenko, and A. Deptuła. “Coincidence of pressure pulsations with excitation of mechanical vibrations of hydraulic system components. An experimental study.” *Cognitive Sustainability* 1, no. 2 (2022). https://doi.org/10.55343/CogSust.12.
[3] Gao, P., T. Yu, Y. Zhang, J. Wang, and J. Zhai. “Vibration Analysis and control technologies of hydraulic pipeline system in aircraft: A review.” *Chinese Journal of Aeronautics* 34, no. 4 (2021): 83-114. https://doi.org/10.1016/j.cja.2020.07.007.
[4] Stosiak, Michał, Mykola Karpenko, Adam Deptuła, Kamil Urbanowicz, Paulius Skačkauskas, Anna Małgorzata Deptuła, Algimantas Danilevičius, Šarūnas Šukevičius, and Mariusz Łapka. “Research of Vibration Effects on a Hydraulic Valve in the Pressure Pulsation Spectrum Analysis.” *Journal of Marine Science and Engineering* 11, no. 2 (2023): 301. https://doi.org/10.3390/jmse11020301.
[5] Dobšáková, L., N. Nováková, V. Habán, M. Hudec, and P. Jandourek. “Vibrations of hydraulic pump and their solution.” Paper presented at The 11th International Conference „Experimental Fluid Mechanics 2016”, Marienbad, Czech Republic, November 15-18, 2016. *EPJ Web of Conferences* 143 (2017): 02017.
[6] Dhameliya, K., U. Shah, and I. Upadhyay. “Vibration analysis of a hydraulic cylinder – a review.” *International Journal of Engineering Development and Research - IJEDR* 4, no. 1 (2016): 556-562.
[7] Randall, R. B. *Application Notes*. *Cepstrum Analysis and Gearbox Fault Diagnosis*. Edition 2. Bruel & Kjaer. Accessed November 7, 2025. https://www.bksv.com/media/doc/233-80.pdf.
[8] Oppenheim, A.V., and Ronald W. Schafer. “From Frequency to Quefrency: A History of the Cepstrum.” *IEEE Signal Processing Magazine* 21, no. 5 (October 2004): 95 – 106. DOI: 10.1109/MSP.2004.1328092.

ISSN 1454 - 8003
Proceedings of 2025 International Conference on Hydraulics and Pneumatics - HERVEX
November 19-21, Băile Govora, Romania

AUTOMATED HYDRAULIC SYSTEM FOR ON-LINE MONITORING OF TREATED WASTEWATER QUALITY

Radu RĂDOI[1], Polifron CHIRIȚĂ[1], Adriana BORȘ[1], Ioana ILIE[1], Costin GÂNDESCU[2]

[1] National Institute of Research & Development for Optoelectronics – Subsidiary Hydraulics and Pneumatics Research Institute (INOE 2000 – IHP)

[2] Lightning Net S.R.L.

Abstract: *Wastewater monitoring is the process of examining sewage to gain insight into conditions within a community. It supports public health, environmental stewardship, and the management of water infrastructure. Monitoring includes gathering samples from sewer systems - such as the influent to treatment plants or points within the sewer network - and analyzing them for: chemical markers like pharmaceuticals and pesticides; Industrial contaminants; nutrient levels, including nitrogen and phosphorus. The article presents an automated wastewater quality monitoring installation. A system of electrically controlled valves directs water from the discharge of a hospital treatment system to a sensor module that analyzes a series of parameters based on an algorithm.*

Keywords: *Wastewater sampling, on-line monitoring, sensors module*

1. Introduction

In order not to exceed the limits imposed by national and European legislation for waters discharged from factories, hospitals, or municipal wastewater treatment plants, periodic monitoring of the efficiency of treatment processes is required.
Monitoring the quality of treated wastewater at the outlet of a city's wastewater treatment system represents an essential step in environmental protection and the maintenance of public health, given the large volume of wastewater generated by the population, industry, and commercial activities.
Monitoring the quality of treated wastewater at the outlet of a hospital treatment system is an essential process for protecting the environment and public health, considering that wastewater from healthcare facilities may contain pathogenic microorganisms, pharmaceutical residues, chemical substances, heavy metals, and other specific contaminants. This monitoring aims to verify the efficiency of treatment processes and ensure compliance with current regulatory standards through the analysis of physico-chemical parameters such as pH, temperature, conductivity, turbidity, nitrogen, and phosphorus, as well as microbiological parameters such as *E. coli* and enterococci. For contaminants specific to the hospital environment, pharmaceutical residues, disinfectants, heavy metals, or other elements are monitored.
Sampling is carried out using automatic or composite methods in order to realistically reflect daily variations, and the equipment used includes online sensors, automatic analyzers, and sampling stations. The results are reported periodically (daily, monthly), and their analysis allows for the rapid identification of potential malfunctions in the treatment installation and the protection of natural receiving waters or the sewer network. Thus, systematic monitoring ensures strict control of discharged water quality and contributes to reducing environmental impact.
A number of authors have conducted reviews or studies on wastewater monitoring. For example, Moretti, A. et al., in paper [1], review classical laboratory methods versus innovative real-time solutions, providing a practical comparison of automatic analyzers, the limitations of laboratory methods, and the potential of online sensors for traditional parameters and emerging indicators.
Li, X. et al., in paper [2], provide a detailed analysis of emerging contaminants (pharmaceuticals, personal care products, endocrine disruptors), their sources, modern analytical methods, and existing gaps in monitoring practices.

Chen, H. et al., in [3], present recent advances in optical sensors, remote sensing, and multi-scale data integration (satellites, drones, and shoreline sensors), and discuss the applicability of these technologies for monitoring the quality of urban effluents.
Kreuter, M. W. et al., in [4], discuss the expansion of wastewater monitoring in the context of public health surveillance (wastewater-based epidemiology), the lessons learned during the COVID-19 pandemic, and the implications for continuous monitoring of pathogens and antimicrobial resistance (AMR).
Antonini, G. et al., in [5], present a concrete example of innovation: an image-analysis-based sensor combined with machine learning for the real-time detection of secondary effluent characteristics.
In the technical report [6], the prevalence of emerging contaminants in wastewater streams, their occurrence frequency, and recommendations for practical monitoring at the regional level are identified.
Santhosini, R. et al., in [7], analyze IoT-based implementations for continuous monitoring (low-cost sensors, communication systems, and data management), highlighting the advantages for detecting rapid variability as well as limitations related to accuracy and calibration.
Karim, M. S. et al., in [8], review electrochemical, optical, and bioreceptor-based sensors for wastewater assessment, discussing their robustness in complex environments and the need for calibration under real-world conditions.

2. Automatic monitoring system

The general block diagram of the monitoring system is shown in Fig. 1. It includes a series of functional modules comprising solenoid valves, manual valves, solution reservoirs, pumps for water circulation, and a clean water pump used for water jet washing of the measurement chambers that contain the sensors. The diagram also includes a Command and Control Module (CCM), consisting of a programmable controller and a computer.

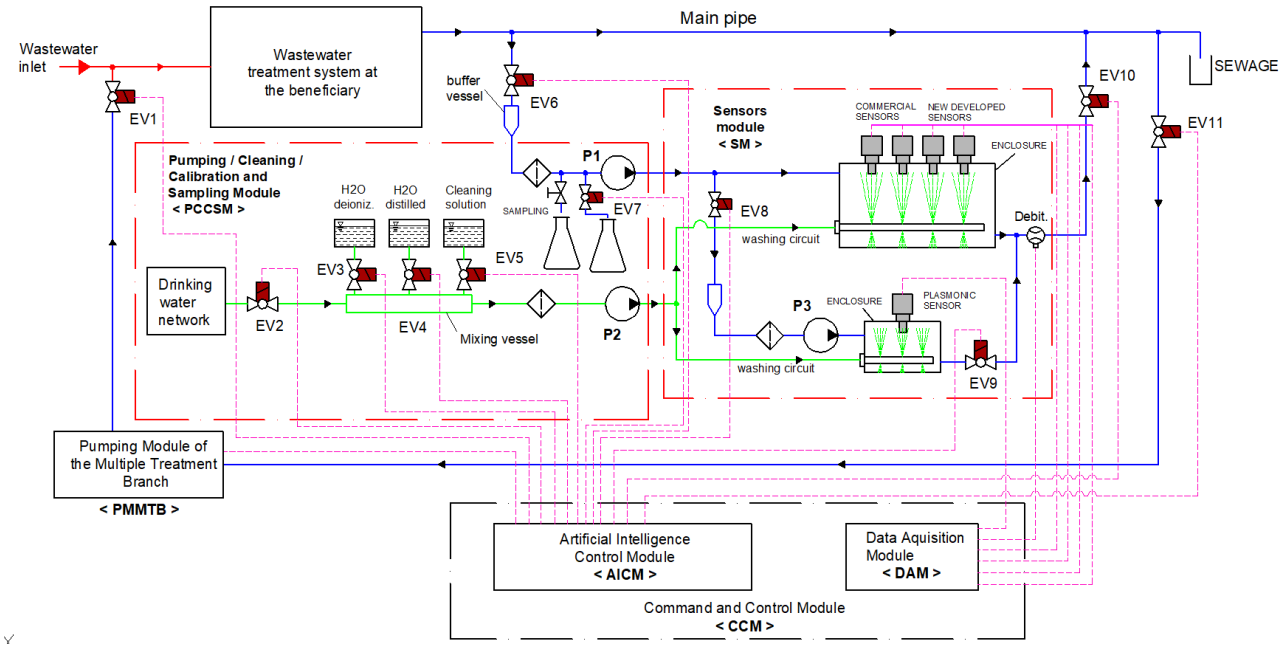

Fig. 1. General block diagram

2.1 Pumping cleaning calibration and sampling module (PCCSM)

The module receives treated wastewater from the output of treatment system at the beneficiary through a T-fitting. Pump P1 draws liquid from a preloaded buffer vessel through valve EV6 and sends it to the Sensors Module (SM). The module also receives clean water through solenoid valve EV2 for the preparation of the washing solution, which is pumped by P2 to the pipes with nozzles

that spray the sensors in the measuring chambers after each sample measurement. Through solenoid valves EV2 to EV5, a recipe for the washing solution can be loaded into a mixing vessel.

2.2 Sensors module (SM)

The module contains two measuring chambers: one with electrochemical sensors and one with a measurement system using a plasmonic sensor that can identify a specific compound that needs to be specially detected. Through solenoid valve EV8, the buffer vessel can be supplied, from which pump P3 can feed the plasmonic sensor chamber. The plasmonic sensor chamber also has an integrated pipe with pressurized washing nozzles for cleaning after each processed water sample.
Figure 2a shows the schematic of the measuring chamber with electrochemical sensors. The chamber has an inlet port, an outlet port, a pipe with washing nozzles, full and empty level switches, and an automatic air bleeder. The sensors are mounted in housings according to the 3D drawing (Fig. 2b). The electrochemical sensor plate (Fig. 2c) is mounted with the electric terminals facing the electronic amplifier and is sealed with resin. The worn-out sensors can be replaced, as the housing can be dismantled.

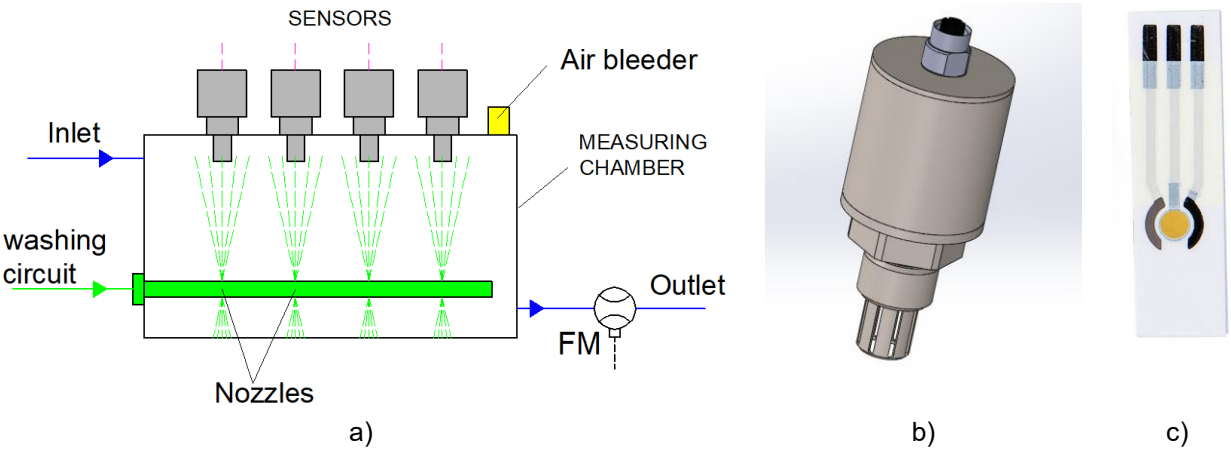

Fig. 2. Measurement chamber with sensors:
a) Measurement chamber schematic;
b) – housing for the electrochemical sensor and electronic amplifier;
c) – electrochemical sensor model.

2.3 Command and Control Module (CCM)

The CCM module includes an Artificial Intelligence Control Module (AICM), implemented using a computer running AI algorithms, and a Data Acquisition Module (DAM), implemented with a programmable logic controller (PLC). Control signals for solenoid valves, pumps, and functional sensors (water level and flow) are managed by the programmable controller, which communicates with the artificial intelligence module. The sensors are connected to the analog inputs of the programmable controller, while the solenoid valves are actuated via digital outputs.
The artificial intelligence control module is designed to significantly improve the accuracy, consistency, and reliability of the data acquired by the wastewater monitoring system. It operates as an intelligent advanced processing layer integrated on top of the existing sensor infrastructure.

The module aims to increase the measurement accuracy of physico-chemical parameters by implementing advanced data processing methods, to automatically detect and correct measurement errors, and to reduce the influence of noise, sensor drift, and anomalous values. In addition, it seeks to ensure data continuity in the event of temporary equipment failures, so that the acquired information remains reliable and complete, effectively supporting operational decision-making.
The module also provides decision support by generating intelligent alerts based on the identification of trends and true anomalies within the data streams.

3. Automated on-line water sample measurement

Automated algorithm for on-line water sample measurement refers to the use of intelligent computational methods integrated with real-time sensors to continuously monitor water quality parameters. These algorithm automatically collect, process, and analyze data such as pH, turbidity, conductivity, temperature, and contaminant concentrations, enabling rapid detection of anomalies or pollution events. By operating on-line, the system eliminates the need for manual sampling and laboratory analysis, reducing response time and human error. Furthermore, automated algorithms can apply data filtering, calibration, and predictive models to improve measurement accuracy and support decision-making in water treatment plants, environmental monitoring, and smart water management systems [9, 10].
The structure of the algorithm for automated water sample measurement can take the form shown in figure 3.

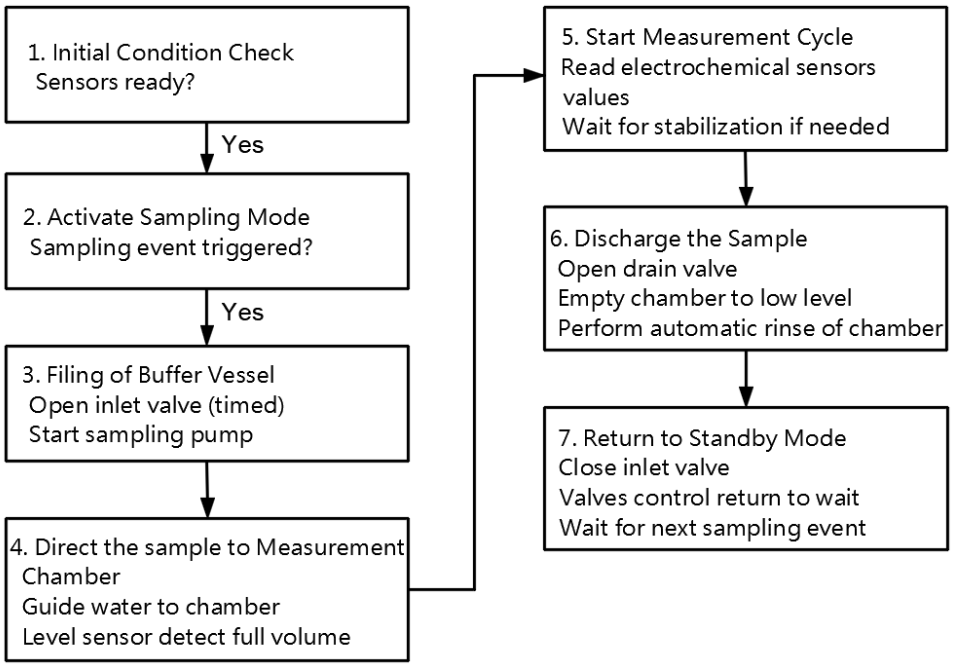

Fig. 3. Structure of the algorithm for automated water sample measurement

The data management system represents an essential component of the data acquisition system, with the role of archiving the collected information for subsequent analysis and compliance with reporting requirements. Data can be stored locally on the acquisition controller or on dedicated servers or network-attached storage (NAS) systems, in various formats such as CSV, TXT, binary files, or SQL databases. Through specialized software connectors, the system integrates with the existing IT infrastructure, enabling the organization, filtering, searching, and visualization of historical data. This approach facilitates continuous monitoring, performance analysis, and pattern identification, contributing to the development of a robust and efficient solution.

Synchronization and Sampling

When multiple sensors are used, it is important to ensure their proper synchronization so that the acquired data are coherent. This can be achieved by configuring the sampling rate such that all channels acquire data at the same frequency.
The sampling rate represents how often data are read from the sensors. It must be adjusted according to the nature of the signal and the specific application. For example, for slow-varying

signals (such as temperature), the sampling rate can be lower, whereas for fast signals (such as vibrations or acoustic waves), a much higher sampling rate is required.

Error Handling and Data Security

Within a data acquisition system, it is essential to implement mechanisms capable of identifying and managing potential errors occurring during data reading or transmission.
Communication errors may arise due to interruptions in the connection between sensors, the acquisition board, and IT systems. To prevent data loss, the software should include data integrity verification functions and generate alerts when anomalies or gaps in the data stream are detected.
Measurement errors may result from sensor hardware failures, unfavorable environmental conditions, or sensor aging. For this reason, it is necessary to implement plausibility validation methods for the measured values, such as comparison with reference values or automatic identification of values exceeding allowable limits.
Data security measures must be adopted, such as data encryption, to prevent unauthorized access and accidental or intentional data modification.

4. Conclusions

Online systems provide frequent or continuous data that enable early detection of anomalies and pollution events, supporting fast and effective decision-making.
Continuously monitored parameters (pH, turbidity, conductivity etc.) allow automatic or informed adjustments in treatment processes, reducing energy use, chemicals, and operating costs.
Sensors may experience clogging or signal drift; sensitivity to organic matter or particles can reduce accuracy without regular maintenance and cleaning.
System benefits are maintained only through consistent calibration, cleaning, inspection and component replacement.
Alarm thresholds and notification workflows (SMS, email) ensure quick reactions from operators and response teams.

Acknowledgments

The research work contained in this paper was supported within the frame of the project ”AI-based system using optical, photonic, and electrochemical sensors for wastewater monitoring in high-risk environments – SISMED”, Project Code 331741, Funding Contract No. 390052 / 03.09.2025.

References

[1] Moretti, Alessandro, Heidi Lynn Ivan, and Jan Skvaril. “A review of the state-of-the-art wastewater quality characterization and measurement technologies. Is the shift to real-time monitoring nowadays feasible?” *Journal of Water Process Engineering* 60 (2024): 105061. https://doi.org/10.1016/j.jwpe.2024.105061.
[2] Li, Xingyu, Xiaojing Shen, Weiwei Jiang, Yongkai Xi, and Song Li. “Comprehensive review of emerging contaminants: Detection technologies, environmental impact, and management strategies.” *Ecotoxicology and Environmental Safety* 278 (2024): 116420. https://doi.org/10.1016/j.ecoenv.2024.116420.
[3] Chen, Huilun, Xilan Gao, and Rongfang Yuan. "Advances in Remote Sensing and Sensor Technologies for Water-Quality Monitoring: A Review." *Water* 17, no. 20 (2025): 3000. https://doi.org/10.3390/w17203000.
[4] Kreuter, M.W., R. Garg, A.K. Marsh, A. Olagoke, O. Weng, V. De La Vega, C. Dunn, and K.J. Johnson. “Wastewater Monitoring: Improving Public Awareness and Understanding in the United States, May 2024.” *Public Health Reports*® (2025): 00333549251359177 (in press). https://doi:10.1177/00333549251359177.
[5] Antonini, Giorgio, Joshua M. Pearce, Franco Berruti, and Domenico Santoro. “A novel camera-based sensor for real-time wastewater quality monitoring.” *Water Practice and Technology* 19, no. 9 (2024): 3778-3793. https://doi.org/10.2166/wpt.2024.211.
[6] Tan, Hung, Phoebe Lewis, and Minna Saaristo. *Emerging contaminants in wastewater and receiving surface water environments*. Technical Report. Environment Protection Authority Victoria, Melbourne, May 2025.

[7] Santhosini, R., U.K. Subhiksha, and V.E. Jayanthi. “Review on Evaluation and Analysis of Water Quality Monitoring Systems Using IoT.” *International Research Journal on Advanced Engineering Hub (IRJAEH)* 2, no. 9 (2024): 2331-2341. https://doi.org/10.47392/IRJAEH.2024.0320.

[8] Abdul Karim, M.S., Nurhafizah Yusof, Norazwina Zainol, and Nor Aziz. “Potential of wastewater quality assessment using electronic sensors: A review.” *Research Journal of Chemistry and Environment* 29, no. 4 (2025): 119-131. https://doi.org/10.25303/294rjce1190131.

[9] Burnet, J.B., K. Demeter, S. Dorner, A.H. Farnleitner, F. Hammes, A.J. Pinto, E.I. Prest, M. Prévost, R. Stott, and N. van Bel. “Automation of on-site microbial water quality monitoring from source to tap: Challenges and perspectives.” *Water Research* 274 (2025): 123121. https://doi.org/10.1016/j.watres.2025.123121.

[10] Guang, D., D.E. Wiley, M. Hlavacek, and A.G. Fane. "On-line automatic sampling for real time monitoring of wastewaters.” *Water Research* 30, no. 11 (1996): 2651-2654. https://doi.org/10.1016/S0043-1354(96)00171-6.

https://hervex.ro